Jonathan Kingslake

Department of Geography

University of Sheffield

Modelling Ice-Dammed Lake Drainage

PhD Thesis

Submitted in accordance with the requirements

for the degree of Doctor of Philosophy

9th January 2013

Abstract

The drainage of ice-dammed lakes produces floods that can pose hazards, waste water resources and modulate ice flow. In this thesis I investigate several aspects of ice-dammed lake drainage through the development and analysis of mathematical models.

After an introduction in the first chapter and a description of the mathematical background to the thesis in the second, the third chapter investigates the mechanisms behind observed variability in the size and timing of subglacial floods from ice-dammed lakes. In particular, I examine how environmental controls like the weather and the shape of glaciers affect floods.

In the next chapter, I quantify how well simple models can predict the dates of floods from an ice-marginal lake in Kyrgyzstan. I find that incorporating environmental controls into models improves their prediction ability.

Next I investigate the coupling between subglacial drainage and glacier motion during ice-dammed lake drainage by developing and analysing a model which couples a marginal lake, glacier sliding, subglacial drainage through a channel and subglacial drainage through a distributed system of cavities. I show how changes in lake level cause the rate at which a glacier slides to increase during the first half of floods and decrease during the second half.

The next two chapters are concerned with two lake-drainage scenarios that involve water flowing as an open stream: firstly, the subglacial open-channel flow that occurs after a marginal lake drains completely during a flood, and secondly, the drainage of supraglacial lakes across the surface of ice sheets.

I end the thesis with a summary of my findings and some suggestions of theoretical and field-based investigations that are worthwhile pursing in the future.

Acknowledgements

Contents

Chapter 1 **Introduction**

Interactions between water and ice result in many interesting phenomena. A classic example, well-studied by glaciologists, is the formation and drainage of ice-dammed lakes. Ice-dammed lakes form next to, on the surface of, and beneath glaciers and ice sheets. Some lakes drain catastrophically, producing high-magnitude floods (e.g. Björnsson, 2002; Hewitt and Liu, 2010; Liestøl, 1956; Post and Mayo, 1971; Roberts, 2005; Thorarinsson, 1953; Tweed and Russell, 1998). People care about this because floods pose hazards (e.g. Richardson and Reynolds, 2000), waste water resources (Mamatkanov and Mingtszyan, 2011) and can modulate the flow of the adjacent ice (Anderson et al., 2005; Bartholomaus et al., 2011; Das et al., 2008; Magnusson et al., 2011; Mayer and others, 2008; Sugiyama et al., 2008).

Studying this phenomenon helps us better understand other ice-water interactions such as glacier surging (Björnsson, 1998), seasonal evolution of drainage systems (Bartholomaus et al., 2011; Bartholoemew et al., 2012; Nienow et al., 1996) and drainage through vertical conduits in glaciers called moulins. This is important because glacial meltwater is a vital resource for millions of people worldwide (e.g. Barnett et al., 2005; Kehrwald et al., 2008) and contributes to sea-level rise (Bindoff et al., 2007). Glaciers and ice sheets are currently responding to a changing climate and a better understanding of ice-water interactions is needed if we are to predict the future of this response.

Thus, in this thesis I aim to increase our understanding of ice-dammed lake drainage, aiding efforts to mitigate its negative consequences and contributing to global efforts to understand how water and ice interact in glacial systems. I start with an overview of what we already know about ice-dammed lake drainage and how to mathematically model it before outlining this thesis' contributions and structure.

Fig. 1.1 illustrates several ways in which ice-dammed lakes form in and around mountain glaciers (Costa and Schuster, 1988; Tweed and Russell, 1998; Roberts, 2005). At the glacier terminus, proglacial lakes can form when glacier runoff is dammed by a moraine (e.g. Richardson and Reynolds, 2000). Hence, the observed proliferation of such lakes is associated with mountain glacier retreat (e.g. Bajracharya and Mool, 2009; Komori, 2008). These lakes can drain catastrophically through mechanical and thermal erosion of their moraine dams (Ding and Liu, 1992; Richardson and Reynolds, 2000) and the resultant floods can have peak water discharges in excess of 30000 $m^3\ s^{-1}$ and propagate hundreds of kilometres down-valley (Richardson and Reynolds, 2000). These floods pose

significant hazards (e.g. Bajracharya et al., 2007; Vuichard and Zimmermann, 1986), but they tend to be one-off events because they completely destroy the moraine dam.

In contrast, some lakes drain via the enlargement of pathways through or over glacier ice. Because ice flows under its own weight, these pathways can close after lake drainage, allowing regularly repeating floods to emanate from the same lake. The other three kinds of lake shown in Fig. 1.1 – subglacial, marginal and supraglacial lakes – can behave in this way and it is these I focus on in this thesis.

Subglacial lakes form between the bottom surface of a glacier and its substrate – usually bedrock or glacial till. Because subglacial water usually flows from high to low hydraulic potential and this potential is determined by the ice thickness and the bed elevation (e.g. Cuffey and Paterson, 2010; Shreve, 1972), subglacial lakes generally form in bedrock depressions or in regions where the ice surface is locally depressed (Björnsson, 2002; Clarke, 2005; Livingstone et al., 2012). The latter can result from locally increased basal melting due to geothermal heating, which also provides a source of water. While so-called subglacial lakes in alpine systems can often be partially open to the atmosphere (e.g. Björnsson, 2002; Capps et al., 2010), true subglacial lakes, isolated from the atmosphere by the overlying ice, are common beneath modern ice sheets (e.g. Carter et al., 2007; Fricker et al., 2011; Siegert et al., 2005; Smith et al., 2009; Wright and Siegert, 2011) and are hypothesised to have been common beneath past ice sheets (e.g. Evatt et al., 2006, Livingstone et al., 2012).
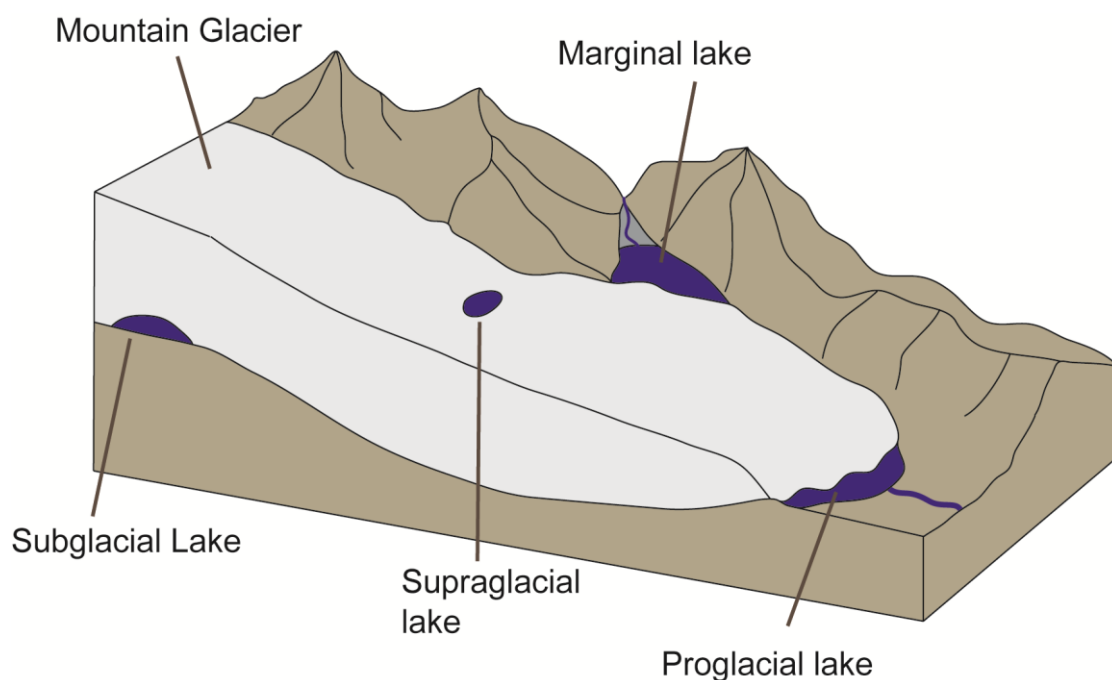
Fig. 1.1. Several kinds of ice-dammed lakes. Adapted from Roberts (2005).

Marginal lakes can form at the confluence of two glaciers, or, as shown in Fig. 1.1, in an ice-free tributary valley against a glacier that occupies a main valley. An example of a lake in the former setting is Gornersee in Switzerland that forms at the confluence of Gornergletscher and Grentzgletscher (Huss et al., 2007). Examples of lakes in the latter setting are: Hidden Creek Lake, Alaska (Anderson et al., 2003), Grænalón, Iceland (Roberts et al., 2005), Merzbacher Lake, Kyrgyzstan (Mayer et al., 2005;Ng and Liu, 2009), Hazard Lake, Canada (Collins and Clarke, 1977), Summit Lake, Canada (Clarke, 2003; Mathews, 1973; Post and Mayo, 1971), Strupvatnet, Norway (Aitkenhead, 1960; Liestøl, 1956; Whalley, 1971) and Øvre Messingmalmvatn, Norway (Engeset et al., 2005).

All the marginal lakes mentioned above are particularly well-studied because they have been observed to drain. Drainage can occur subglacially. Because subglacial floods are common in Iceland they are often referred to by their Icelandic name *jökulhlaups*. Fig. 1.2 displays a water discharge time series observed during a typical subglacial jökulhlaup from a lake called Grimsvötn in Iceland. Grimsvötn forms in a subglacial caldera beneath Vatnajökull ice cap. It is fed by meltwater produced in an adjacent volcanically active area and, although usually referred to as a subglacial lake, it is only partially covered by a thick floating ice shelf (Björnsson, 1992, 2002; Ng and Björnsson, 2003; Nye, 1976).
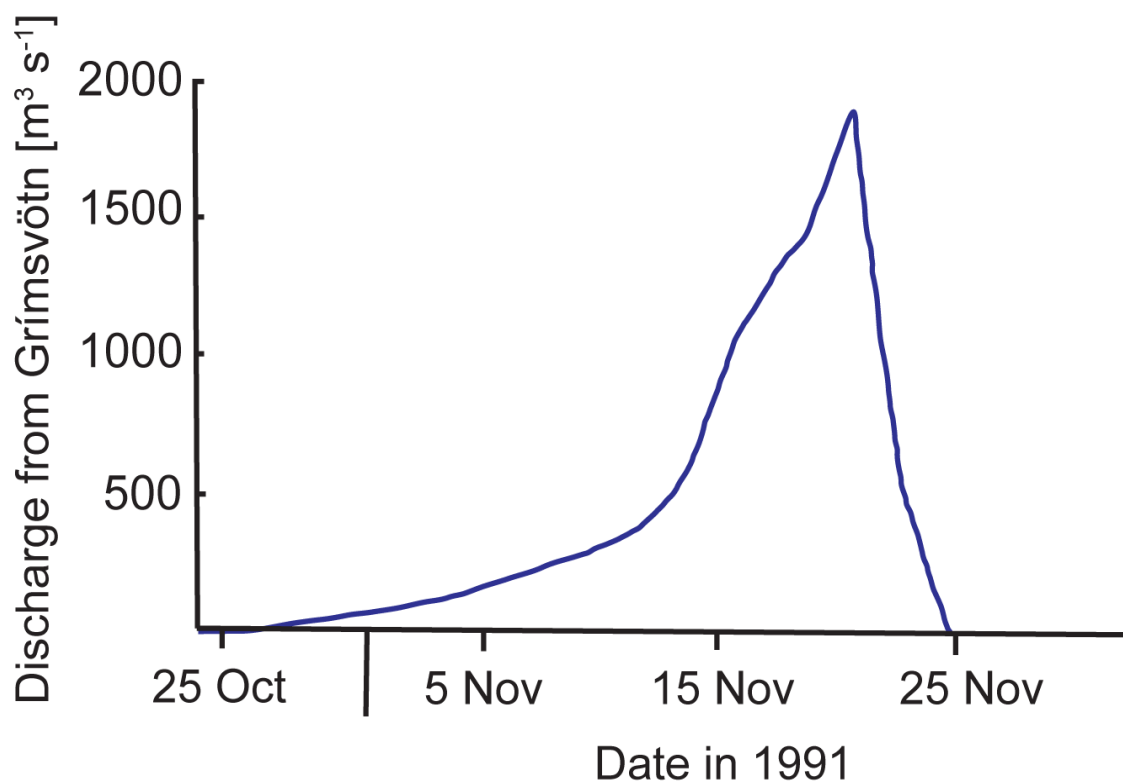
Fig. 1.2. Hydrograph of a jökulhlaup from subglacial lake Grimsvötn, Iceland in 1991. Reproduced from Björnsson (1998). Accuracy is 10 %. This hydrograph is typical in shape for subglacial jökulhlaups, with a relatively slow exponential rising limb and a rapid falling limb.

Floods are thought to almost always occur through ice-walled channels at the ice-cap's bed. The jökulhlaup hydrograph in Fig. 1.2 is typical of subglacial floods from marginal and subglacial lakes in magnitude and shape (Roberts, 2005); discharge increases approximately exponentially over one or two weeks and decreases relatively rapidly following a peak of up to several thousand cubic metres per second. Theory suggests that this shape results from the way in which the size of an ice-walled subglacial channel, assumed to convey the floods, evolves over time through a competition between enlargement through melt caused by the flowing water and closure due to the flow of ice (Nye, 1976).

Lake drainage affects the dynamics of glaciers (e.g. Magnusson et al., 2011). Glaciers slide over their beds at a rate that depends on the basal water pressure. Many large glaciers permanently have water at their beds, but changes in subglacial water flux associated with lake drainage can alter water pressure and sliding. This is interesting for glaciologists trying to understand how longer-term changes in water flux might affect ice dynamics. Excitingly, this coupling between ice dynamics and lake drainage, already known about in alpine glaciers (e.g. Anderson et al., 2005; Magnusson et al., 2011; Mayer et al., 2008; Riesen et al., 2010; Sugiyama et al., 2010) has recently been observed in Greenland (Das et al., 2008; Zwally et al., 2002) and Antarctica (Stearns et al., 2008).

In Greenland, this coupling is between ice dynamics and supraglacial lakes (Fig. 1.1). Supraglacial lakes form in topographic depressions on the Greenland Ice-sheet's surface (e.g. Echelmeyer et al., 1991; Lüthje et al., 2006; Sundal et al., 2009; Selmes et al., 2011; Reynolds, 1981) and are often observed to drain through hundreds of metres of ice to the ice-sheet's bed (e.g. Das et al., 2008). Drainage results in an increase in basal water pressure and in the ice-sheet's sliding velocity. These observations have led some to hypothesise that a positive feedback – between surface melt, lake drainage to the ice-sheet's bed, enhanced sliding and dynamic ice-sheet thinning – has the potential to cause significant mass loss in Greenland (e.g. Pritchard et al., 2009; Rignot and Kanagaratnam, 2006).

Jökulhlaup-like drainage occurs beneath Antarctica and may have occurred beneath paleo–ice-sheets (e.g. Evatt et al., 2006; Fricker et al., 2007, Livingstone et al., 2012; Wingham et al., 2006). Antarctic subglacial lakes were first discovered in the 1970's using airborne radio-echo sounding and satellite altimetry (e.g. Robin et al., 1970; Siegert, 2000; Siegert et al., 1996; Siegert et al., 2005), but little was known about their time evolution until Wingham et al. (2006) detected temporal changes in the elevation of the East Antarctic Ice Sheet near Dome C (135°E, 74°S). He concluded that these

changes were the result of corresponding changes in the volume of water impounded in a small group of subglacial lakes in the Adventure Subglacial Trench. Evatt et al. (2006) modelled this hypothesised jökulhlaup-like drainage and concluded that lakes beneath ice sheets can drain via large periodic floods, lasting years, rather than weeks as is observed in smaller alpine jökulhlaup systems. With lake drainage appearing inherently unstable and episodic in their model, they suggested that jökulhlaup-like drainage is common today beneath Antarctica. Since their modelling study, numerous observations have confirmed this suggestion (e.g. Fricker et al., 2007; Fricker et al., 2009; Fricker et al., 2010; Smith et al., 2009; Winberry et al., 2009). Furthermore, just as in mountain glaciers, lake drainage has been observed to affect the dynamics of the overlying ice (Stearns et al., 2008).

Observations show that lake drainage can be a recurring phenomenon. Returning to jökulhlaups from mountain glaciers and ice caps, Fig. 1.3 shows time series of lake level (above sea level, Fig. 1.3a) and lake depth (above the lake bed; Fig. 1.3b) from two jökulhlaup lakes. The data in the top panel is from Grimsvötn (reproduced from Björnsson, 2002) and the data in the bottom panel is from Merzbacher Lake (Ng and Liu, 2009) – a marginal lake in Kyrgyzstan that I describe in detail in Chapter 4. At both lakes, periods of lake filling are separated by floods, seen in the time series records as abrupt drops in the lake level and depth. Hydrographs from floods from both systems usually have a shape similar to that displayed in Fig. 1.2. In both panels the horizontal dashed lines indicate the height (Fig. 1.2a) and depth (Fig. 1.2b) the lakes need to reach in order to cause their ice dams to float. This 'flotation depth' is roughly equal to the ice-dam's height above the lake's bed multiplied by the ratio of the densities of ice and water, ≈9/10 (Tweed, 2000).

With regard to these time series, several observations are revealing of important differences and similarities between the two systems. Firstly, the 'shoulders' visible in Fig. 1.3b, indicating times when lake-depth rise is temporarily slower than at other times, are absent from Fig. 1.3a. They correspond to the winter months and their absence in Fig. 1.3a alludes to an important difference between the systems. Both lakes are filled by meltwater but the sources of heat used in melting ice to produce this meltwater are different in each case. At Grímsvötn this heat source is predominantly geothermal (Nye, 1976), the rate at which the lake fills is therefore almost independent of the seasons. In contrast, Merzbacher Lake is filled by runoff from an up-valley glacier which melts at a rate predominantly determined by weather conditions. Hence the slow filling during the winter when sub-melting-point temperatures mean that the only input to the lake is from ice calving off the ice-dam, which is assumed constant for this reconstruction.

a Observed Grímsvötn surface level time series

b Reconstructed Merzbacher Lake depth time series
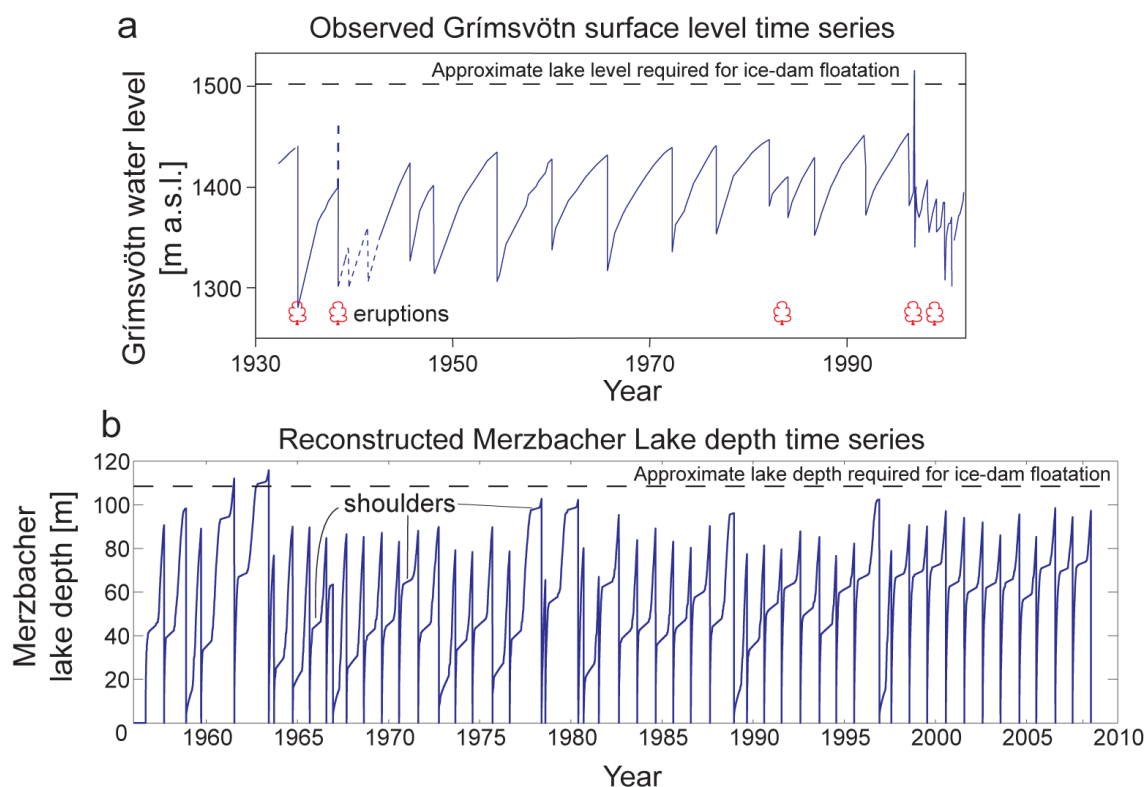
Fig. 1.3. Time series of (a) the observed lake level above sea level of Grímsvötn subglaial lake, Iceland, and (b) the reconstructed (see chapter 4) depth of Merzbacher Lake, Kyrgyzstan. The timeseries in (a) is taken from Björnsson (2002), who reconstructed lake level from observations of the surface of the water and ice shelf. The red clouds indicate the approximate timing of subglacial volcanic eruptions. The time series in (b) is reconstructed following the methods of Ng and Liu (2009), described later in section 4.3.4. In both panels, the dashed horizontal lines represent the lake level and depth the lakes must reach to float their ice dams. They are placed approximatly based on Björnsson's (2002; 2009) statements that Grimsvötn jökulhlaups typically start when the lake is 60–70 m below the flotation level and Ng and Liu's (2009) estimate of 120 m for the height of Merzbacher Lake's ice dam.

Secondly, although this is not made obvious by the vertical scale in Fig. 1.3a, Grímsvötn does not empty during floods; floods terminate while there is still water in the lake. In contrast, Merzbacher Lake does empty (Ng and Liu, 2009). This is reflected in the reconstruction; after each flood the lake depth begins increasing from zero. This is common in marginal lakes in alpine systems (e.g. Bartholomaus et al., 2011; Collins and Clarke, 1977; Huss et al., 2007).

Lastly, floods are fairly regular, but in both systems there is variability in the length of lake-filling periods, in the maximum depth each lake reaches before floods begin and, allthough not visible in the figure, in the peak discharge of floods. At Merzbacher Lake (Fig. 1.3b) there is inter-flood variability that Ng et al. (2007) linked to variations in the weather and its effect on meltwater input to the lake. Ng and Liu (2009) investigated the

temporal dynamics of Merzbacher Lake floods further and found that they could explain many features of the sequence of flood dates using the concept of a 'flood initiation threshold'. At Grímsvötn (Fig. 1.3a), filling periods that usually last 5-10 years are sometimes interrupted by floods caused by subglacial volcanic eruptions, indicated in the figure by the red clouds. The increase in meltwater input associated with these eruptions clearly has a dramatic effect on the size of floods. Moreover, Fig. 1.3a shows how the lake reached the flotation depth (dashed line) just once during the period shown. This occurred in November 1996, just before the largest flood ever recorded from Grimsvötn and after a month of rapid lake filling caused by a large subglacial volcanic eruption (Björnsson, 2002; Gudmundson et al., 1997). This flood was not only larger than any other ever observed from Grimsvötn, peaking at ~40000 m^3 s^{-1}, it also reached its peak unusually rapidly. Hence, this flood's hydrograph was very unlike the typical jökulhlaup hydrograph (Fig. 1.2). The unusual hydrograph, the lake reaching the flotation depth (Fig. 1.3a) and other observational evidence indicating widespread over-pressurisation (basal water pressure that exceeds the overburden pressure of the ice) suggest that this flood started and developed in a very different manner than typical Grimsvötn floods and floods from other systems (e.g. Merzbacher Lake (Björnsson, 2002; Flowers et al., 2004; Jóhannesson, 2002).

This anomalous Grimsvötn flood stimulated research into a long-standing unresolved question: how do jökulhlaups begin? Answering this would constitute a significant step towards an ability to predict flood size and timing. Initially, when people observed these floods from downstream, they were unsure if they occurred subglacially; Kerr (1934) and Maag (1963) hypothesised that ice-marginal lakes overtopped their ice dams and drained by incising a channel in the ice surface. This style of drainage is observed from supraglacial lakes (e.g. Raymond and Nolan, 2000) and occasionally from marginal lakes (Werder et al., 2009), but many other observations show that marginal and subglacial lakes often drain subglacially (e.g. Collins and Clarke, 1977; Higgins, 1970; Liestøl, 1956; Whalley, 1971). With the most common style of drainage established as being subglacial, the question of how subglacial drainage starts remained. Thorarinsson (1953) supposed that lakes reach the flotation level, lifting the ice dam and allowing water to drain beneath it. Glen (1953) and Liestøl (1956) pointed out that, as such flotation-initiated drainage progresses, it would lower the lake's level and the ice dam would come to rest on its bed again, halting drainage; the result being steady drainage controlled by the input to the lake. But Aitkenhead (1960) thought that the bed was unlikely to come to rest in exactly the same place on its bed and so water flow could continue to flow through gaps between the ice and rock, enlarging a channel by friction as was also suggested by Liestøl (1956). Glen (1953) proposed a different mechanism.

When water pressure is sufficiently greater than the ice overburden pressure at the base of an ice-dam the ice will flow in response to the unbalance in horizontal stresses, slowly opening a drainage pathway. This mechanism requires that the ice dam does not float when the lake depth exceeds the flotation depth. This seems improbable given observations of floating portions of ice dams (e.g. Marcus, 1960; Mayer et al., 2005; Walder et al. 2006) and floods that have certainly been initiated by ice-dam flotation (Björnsson, 2002, 2009; Jóhannesson, 2002). Floatation could be prevented if the density of the ice dam were larger than that of pure ice, perhaps due to a high content of rock (Tweed, 2000). How floods start remains a gap in our understanding (Ng et al., 2007; Ng and Liu, 2009). With the exception of Fowler (1999), who built on seminal theoretical work by Nye (1976), few people have developed theoretical models which try to fill this gap.

Nye's (1976) theory represented a step-change in our understanding of jökulhlaups. He built on Röthlisberger's (1972) theory of steady-state water flow through an ice-walled channel to model lake drainage through a time-evolving channel at the glacier bed. Nye's model, described in detail in the next chapter, successfully explained the shape of the rising part of floods from Grimsvötn, showing that it arises through a feedback between channel enlargement by frictional dissipation of heat in the flowing water, the size of the channel and the water flux.

Nye's theory has been the basis for all subsequent theoretical jökulhlaup work. Studies have tried to improve the model – by removing simplifying assumptions, improving how the model describes processes and adding descriptions of new processes – and have aimed to apply the model to numerically simulate observed floods (e.g. Björnsson, 1992; Clarke, 1982, 2003; Evatt, 2006; Evatt et al., 2006; Flowers et al., 2004; Fowler, 1999, 2009; Ng, 1998; Ng et al., 2007; Spring and Hutter, 1981, 1982; Pimental and Flowers, 2011).

Nye assumed a straight, uniform channel and that the water in the lake is at the melting point. Also, he ignored heat conduction in the water and through the surrounding ice, and the water's kinetic energy. Spring and Hutter (1982) developed a more general model of water flow through an ice-walled channel from first principles of continuum mechanics, which made none of these simplifications. In particular, their model allowed the channel's size and curvature to vary in space and time and the lake water to be warmer than the melting point. This general model was simplified by Spring and Hutter (1981) to numerically simulate jökulhlaups through a straight, stationary channel, but despite their simplifications, numerical stiffness posed difficulties in their investigations (Clarke, 2003).

Like Spring and Hutter (1982), Clarke (1982) set out to improve Nye's model, but he took a simpler approach. He too removed Nye's assumption that the lake is at the melting temperature, but his approach separated the heat that melts the channel walls into two contributions: one from the heat dissipated in the turbulently flowing water and another from the sensible heat of the lake. Unlike Spring and Hutter (1981), he assumed that floods are throttled by one spatially-fixed constriction in the channel near the lake. Hence, after also assuming the water pressure gradient in the channel can be represented by its spatially-averaged value, spatial dependence could be removed and the model could be reduced to two ordinary differential equations. These could be solved without numerical difficulty to simulate floods from Hazard Lake, Canada.

Later, Clarke (2003) combined his separation of heat sources idea with Spring and Hutter's (1981) spatially dependent model to simulate floods from Grimsvötn, Iceland, Hazard Lake, Canada and Summit Lake, Canada. He found that the numerical difficulties experienced by Spring and Hutter were due to multiple wave solutions to the equations having vastly different propagation speeds. He allowed the water in the channel to be slightly compressible, damping out the rapidly propagating wave solutions which had caused the problems. Although this modification is unphysical, it was found to have no discernable effect on simulations. He concluded that previous models which assume flow is controlled by a spatially-fixed channel constriction (Clarke, 1982; Ng, 1998; Ng and Björnsson, 2003), do not adequately capture many of the dynamics of jökulhlaups.

One of Clarke's (2003) aims was to investigate how best to parameterise water-to-ice heat transfer in the channel, particularly when the lake is warmer than the melting point. He used his separation-of-heat-sources approach to tackle this, but others have taken different approaches. Originally Nye (1976) used the empirical Dittus-Boelter equation to parameterise water-to-ice heat transfer. Björnsson (1992) and Jóhannesson (2002) suggest that this underestimates the rate at which the sensible heat of the lake's water is transferred to the channel walls. Evatt (2006) points out that the heat transfer coefficient in the Dittus-Boelter equation used by Nye was derived from experiments with Reynolds number ~10^5 (McAdams, 1951). Perhaps, Evatt suggests, heat transfer is more efficient at the much higher Reynolds numbers expected during jökulhlaups ~10^7. Using results from newer experiments (Insenko et al., 2005), Evatt (2006) modifies Nye's (1976) heat equation to try and improve its representation of heat transfer. Simulations made with the modified model suggest that lake temperature plays only a minor role in controlling jökulhlaup size which led Evatt et al. (2006) and Fowler (2009) to ignore this parameter. In contrast, Ng et al.'s (2007) investigation of the climatic controls on jökulhlaups showed that warmer weather increases the size of floods in several ways, one being the extra heat contained in warm lake water contributing to channel

enlargement. Their work reveals a link between weather conditions and flood size, and they suggest that a key control on the variability in floods from Merzbacher Lake (Fig. 1.3b) is the weather.

The complication of a deformable bed in glacial drainage was considered by Walder and Fowler (1994) and Ng (2000), and sediment transport during floods was modelled by Fowler and Ng (1996). Fowler and Ng (1996) also removed the assumption of a circular (or semi-circular) ice-walled channel. This allowed a spatially varying channel shape and showed that with high water pressure, a wide, low roofed canal cut into a till substrate can exist.

All the thermo-mechanical jökulhlaup models mentioned so far have followed Nye (1976) in side-stepping the question of how floods start. They assume the existence of a small channel from the beginning of simulations whose evolution controls the simulated flood. One shortcoming of this approach is that, for a particular initial lake depth, the initial size of this channel must be chosen arbitrarily. Because initial channel size strongly affects the size and timing of a simulated flood, these models are useless for predicting the dates of floods. Indeed, Ng (1998) and later Ng and Björnsson (2003) have shown that the Nye (1976) model formulated with time dependence only and no space dependence – like Clarke's (1982) model – simulates repeating floods but their size grows unstably with time. The channel gets increasingly miniscule between floods and the peak discharge of each flood is larger than the last's. This behaviour is unphysical and not observed in real systems. For example, the size of floods from Grimsvötn varies but does not appear to grow unstably over time. Clearly, if one aims to understand why a flood begins when it does or how environmental conditions between floods affect their size, models need to be able to simulate complete cycles of lake filling, flood initiation, flood development and flood termination in a physically plausible way.

Fowler (1999) tackled this by making some modifications to Nye's model, most important of which was allowing the discharge to become negative between floods – that is, allowing water to flow upglacier towards the lake. I describe this in more detail during the next two chapters. In brief, this modification allows a water divide to form beneath the ice dam when the lake level is low. This suppresses the unstable growth of floods found by Ng (1998) and the divide's dynamics control the size of floods. In the model, floods initiate because this divide moves towards the lake in response to lake filling. When the divide reaches the lake a flood initiates and grows through Nye's feedback mechanism. Fowler's (1999) aim was to explain why Grimsvötn reached the flotation depth in November 1996 whereas it typically starts to drain before it reaches this depth. It turns out that Fowler's (1999) ideas can be extended to studying variability in the size and timing of 'typical' floods.

I have outlined what we already know about ice-dammed lake drainage; observations and modelling studies of the phenomenon have uncovered much of its governing physics. However, in key areas – like flood initiation and termination, prediction of flood timing and magnitude, and the interaction between floods and glacier motion – understanding is lacking. Understanding can be improved through further mathematical modelling of the mechanisms that underlie lake drainage and I pursue this in this thesis.

By focussing on several aspects of this large topic, I aim to push forward our understanding of ice-dammed lake drainage in general and contribute to answering some specific questions along the way. Throughout I ignore the complication of a lake with a temperature warmer than the melting point. As discussed above, this interesting topic has been investigated thoroughly and I choose to focus on other mechanisms.

The approach I take throughout is to setup models of physical systems and analyse them to reveal and explain physically qualitative features of the system's behaviour. Therefore, except during an optimisation exercise in Chapter 4, I avoid fitting model results to observations. It has been established by others that this is possible for jökulhlaup hydrographs using various forms of Nye's equations (e.g. Björnsson, 1992; Clarke, 2003; Fowler, 2009; Ng et al., 2007).

The thesis is organised as follows. In Chapter 2 I outline the models (conceptual and mathematical) of water flow beneath ice masses that underpin my investigations in the following four chapters, where I examine specific aspects of subglacial drainage of lakes. In another chapter I apply similar concepts to surface drainage. At the start of each of these five chapters I introduce each aspect of ice-dammed lake drainage in more detail than I have above.

In Chapter 3 I investigate what physically controls the size and timing of floods. The size of modelled jökulhlaups turns out to be closely linked to flood initiation and varies in unexpectedly complex ways depending on the rate at which meltwater is input to the system, where meltwater is input and how this input varies with time.

Continuing my investigation of jökulhlaup timing, in Chapter 4 I use insight gained during Chapter 3's physical modelling to see how well I can predict the timing of floods from Merzbacher Lake, Kyrgyzstan. Meteorological and hydrological data pertaining to jökulhlaups from this lake are available and I optimise a suite of 'flood-date prediction models' – of lower order than the lake-drainage models that I employ in other chapters – against this data to maximise their ability to predict floods. In doing so, I take the first steps towards operational flood forecasting and uncover aspects of jökulhlaup physics.

Returning to fully thermo-mechanical jökulhlaup modelling in Chapter 5, I extend Chapter 3's model to include a second drainage system and glacier sliding. I solve the model numerically to investigate in more detail than in Chapter 3 how meltwater input affects floods and the coupling between floods and glacier motion. My results introduce the intriguing possibility that subglacial floods can, under some circumstances, cause a glacier to speed up and slow down to equal extents.

A frequent issue that arises during Chapters 3 and 5 is the fact that current jökulhlaup models cannot describe the physics of subglacial water flowing as an open stream. Hence, they cannot simulate full flood cycles from the majority of jökulhlaup lakes because they empty completely during floods. In Chapter 6 I address this shortcoming by developing a model of open-channel flow after jökulhlaups. I use the model to analyse how open-channel flow begins and how long it lasts. Numerical simulations show how periods of open-channel flow allow one flood to affect the next; a 'memory-effect' that could explain previously unexplained aspects of the reconstructed Merzbacher Lake depth time series (Fig. 1.3b).

Chapter 7 stands alone in this thesis, in that it is concerned with the surface drainage of supraglacial lakes. This work has its place in this thesis because in essence surface drainage is similar to subglacial jökulhlaups; both phenomena involve a positive feedback between melt enlargement and discharge. I show theoretically what controls whether a lake will drain over the surface catastrophically or steadily. This is important because surface drainage moves water from high to low elevations on ice sheets, affecting where lakes are available to drain to the bed and influence ice dynamics.

Finally, in Chapter 8, I summarise my findings and highlight some key areas where future work is worthwhile.

Chapter 2 **Mathematical background**

2.1   Introduction

In this thesis I build on existing models of subglacial-hydrological processes to better understand the subglacial drainage of ice-dammed lakes. The purpose of this chapter is to describe these models and the methods I use to solve them numerically.

The material is divided into two parts, the first much weightier than the second. The first part, section 2.2, covers models of water flow through ice-walled subglacial channels, the jökulhlaup model I use in later chapters and the methods I use to solve this model. In the second part I summarise models of basal sliding and drainage through 'linked-cavity' systems that underlie my study of the coupling between lake drainage and ice motion, presented in Chapter 5.
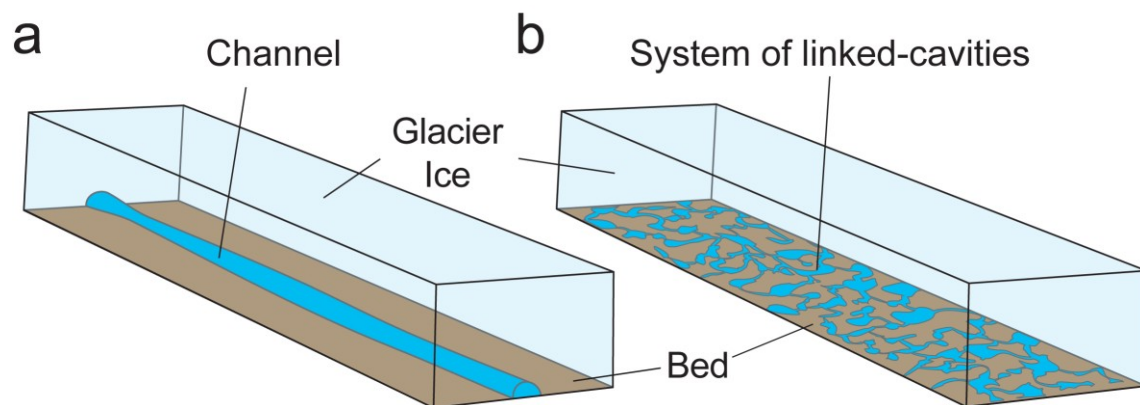
Fig. 2.1. Subglacial drainage through (a) a channel and (b) a system of linked-cavities.

2.2   Channels

Röthlisberger (1972) developed one of the first theories of water flow through ice-walled channels. In Röthlisberger's theory, energy dissipated by water flowing turbulently through an ice-walled channel (Fig. 2.1a) is used to melt the channel walls and this enlargement is balanced by inward viscous deformation of the surrounding ice, which acts to close the channel. Restricting his analysis to the steady-state case, where melt enlargement balances creep closure, Röthlisberger (1972) showed that channels tend to coalesce to form upglacier-branching drainage networks. Nye (1976) extended the theory to allow melt and viscous deformation to be out of balance and used his time-dependent model to explain the time evolution of jökulhlaups from Grimsvötn subglacial lake, Iceland.

I outline these studies in sections 2.2.1 and 2.2.2. I then describe Fowler's (1999) modification of Nye's model in section 2.2.3. Fowler's model is slightly modified and non-dimensionalised in section 2.2.4 so as to apply it to an alpine marginal lake system. In section 2.2.5 I describe three numerical methods I use to solve the new model that I refer to as the Nye-Fowler jökulhlaup model.

2.2.1   Steady-state drainage through an ice-walled channel

Röthlisberger (1972) envisaged a water discharge, Q, flowing through an ice-walled circular channel. Distance along the channel is denoted by s and time is denoted by t. Fig. 2.2 shows a short section of the channel of length ds with arrows indicating the direction of water flow (blue), the inward creep closure of the ice (red) and the water pressure exerted at the section's ends (green).
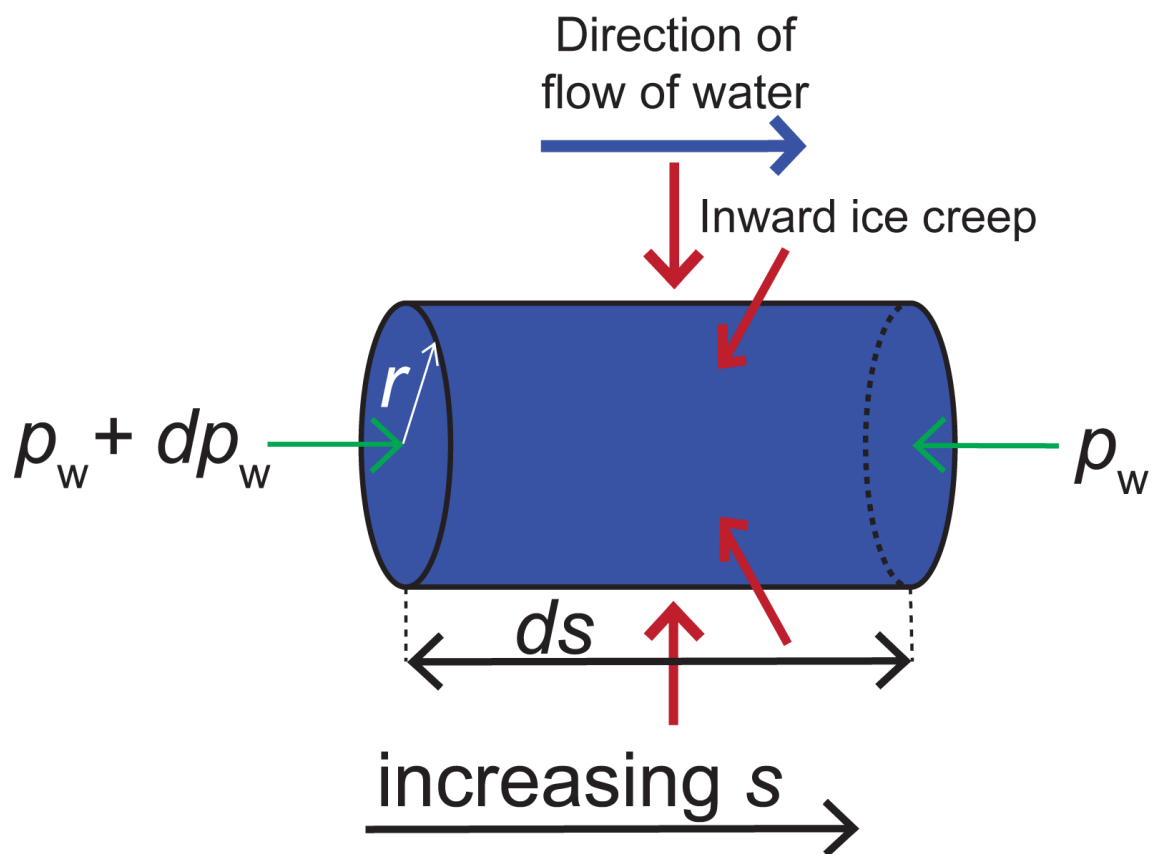
Fig. 2.2. A short section of a horizontal subglacail channel. Reproduced from Röthlisberger (1972). The spatial coordinate s increases from left to right. This is also the assumed direction of the flow of the water in the channel and of the glacier.

In every unit time a volume of water Q moves from the left-hand end of the channel section in Fig. 2.2 (where the water pressure is $p_w + dp_w$) to the right-hand end (where the water pressure is p_w). The water gains some energy as it moves because it moves through a potential gradient. The water is assumed to be at the melting temperature at all times and this temperature changes with pressure, so some of the energy the water

gains in moving from left to right in Fig. 2.2 is used in changing the water's temperature to match the new pressure-dependent melting-point. The leftover energy, $0.684Qdp_w$, is used in melting the following volume of ice per unit time in the channel element:

$$\frac{0.684\, Q\, dp_{\mathrm{w}}}{L\rho_{\mathrm{i}}}.$$

2-1

where L is the latent heat of fusion of water and ρ_i is the density of ice ($\approx$900 kg m^3). Based on measurements of the closure rate of boreholes in ice made by Nye (1953), Röthlisberger (1972) uses the following phenomenological expression for the rate of inward viscous deformation of the ice, expressed as a volume per unit time in the channel element:

$$\pi r^2 K_0 (p_{\mathrm{i}} - p_{\mathrm{w}})^n ds\,.$$

2-2

In this expression, r is the cross-sectional radius of the channel (Fig. 2.1), p_i is the overburden pressure of the ice and n and K_0 are ice flow parameters (these are related to A, the flow parameter used in Röthlisberger's original paper by K_0 = $2/(nA)^n$). Assuming that the evolution of the channel is in a steady state, Röthlisberger (1972) equated eqns. 2-1 and 2-2 and rearranged for the spatial pressure gradient, dp_w/ds, to yield

$$\frac{dp_w}{ds} = \frac{2\pi L\rho_{\mathrm{i}}}{0.684(nA)^n}\frac{1}{Q}(p_{\mathrm{i}} - p_{\mathrm{w}})^n r^2.$$

2-3

The balance of momentum between the flowing water and the channel's walls can be described by Manning's equation (e.g. Chow, 1959; Henderson, 1966; Yen, 2002). This phenomenological equation describes the mean flow velocity v of water moving through a total potential gradient, G, along a channel with a hydraulic roughness parameterised by the Manning roughness coefficient, n', as follows:

$$v = \frac{R_{\mathrm{H}}^{\frac{2}{3}}}{n'}\left[\frac{1}{\rho_{\mathrm{w}}g}G\right]^{\frac{1}{2}},$$

2-4

where g is the acceleration due to gravity ($\approx$10 m s^{-2}), ρ_w is the density of water ($\approx$1000 kg m^3). R_H is the channel's hydraulic radius defined by

$$R_{\mathrm{H}} = \frac{S}{P_{\mathrm{w}}},$$

2-5

where S and P_w are the channel's cross-sectional area and wetted perimeter respectively. In a full-flowing circular channel $S = \pi r^2$ and $P_w = 2\pi r$, so $R_H = r/2$. The total hydraulic potential gradient G is the sum of two terms, one associated with the slope of the channel ϕ and the other is the negative of the spatial gradient of water pressure:

$$G = \rho_w g \sin \phi - \frac{dp_w}{ds}$$

2-6

(e.g. Cuffey and Paterson, 2010). With the sign convention I have chosen, water flows in the direction of increasing s when G is positive. In the special case of a horizontal channel, which Röthlisberger considered first, $\phi = 0$, so $G = -dp_w/ds$. Using this expression for G and the fact that the discharge Q through a full-flowing circular channel is related to the channel's cross-sectional radius r and the mean flow velocity v by $v = Q/\pi r^2$, Manning's equation can be rearranged for r^2 to give

$$r^2 = \left(\frac{2^{\frac{4}{3}}\rho_w g}{\pi^2} \right)^{\frac{3}{8}} n'^{\frac{3}{4}} Q^{\frac{3}{4}} \left(-\frac{dp_w}{ds} \right)^{-\frac{3}{8}}.$$

2-7

Eliminating r between this expression and eqn. 2-3, and rearranging for $-dp_w/ds$ yields an expression for the water pressure gradient in a horizontal steady-state channel:

$$-\frac{dp_w}{ds} = \left(\frac{2^{\frac{3}{2}}\pi^{\frac{2}{8}}L\rho_i}{0.684(nA)^n} \right)^{\frac{8}{11}} (\rho_w g)^{\frac{3}{11}} n'^{\frac{6}{11}} Q^{-\frac{2}{11}} (p_i - p_w)^{\frac{8n}{11}}.$$

2-8

Assuming the roughness and flow properties of the ice are constant,

$$-\frac{dp_w}{ds} \propto Q^{-\frac{2}{11}} (p_i - p_w)^{\frac{8n}{11}}.$$

2-9

Hence, Röthlisberger's (1972) theory shows that, in a steady-state channel, the magnitude of the water pressure gradient decreases with increasing water flux Q. This has consequences for the large-scale behaviour of channelised drainage systems. If two subglacial channels join at some point beneath the glacier, integrating eqn. 2-9 from the point they join, in an upglacier direction (i.e. in the direction of decreasing s) along each of the channels, shows that the channel with the higher discharge will be at a lower pressure. Hence, if water can be exchanged between them, through a permeable substrate or along the ice-rock interface, this channel will capture water from the other. In steady state, smaller channels will tend to shrink at the expense of larger ones and

channelised drainage systems will tend to consist of one or several large upglacier-branching channels.

2.2.2 Time-dependent drainage through an ice-walled channel: Nye's model

Nye (1976) built on Röthlisberger's (1972) model, removing his steady-state assumption, to explain the time evolution of jökulhlaups from Grimsvötn, Iceland. Nye's model consists of four coupled differential equations describing the evolution of an ice-walled channel at the glacier bed that is pressure-coupled to a lake, and the conservation of mass, momentum and energy in the water that flows along the channel. The situation is illustrated in Fig. 2.3. These four equations, along with an algebraic fifth equation that describes the transfer of heat from the water to the ice, relate five variables: channel cross-sectional area, water discharge, water pressure, channel wall melt rate and water temperature. I describe each of the five equations in turn.
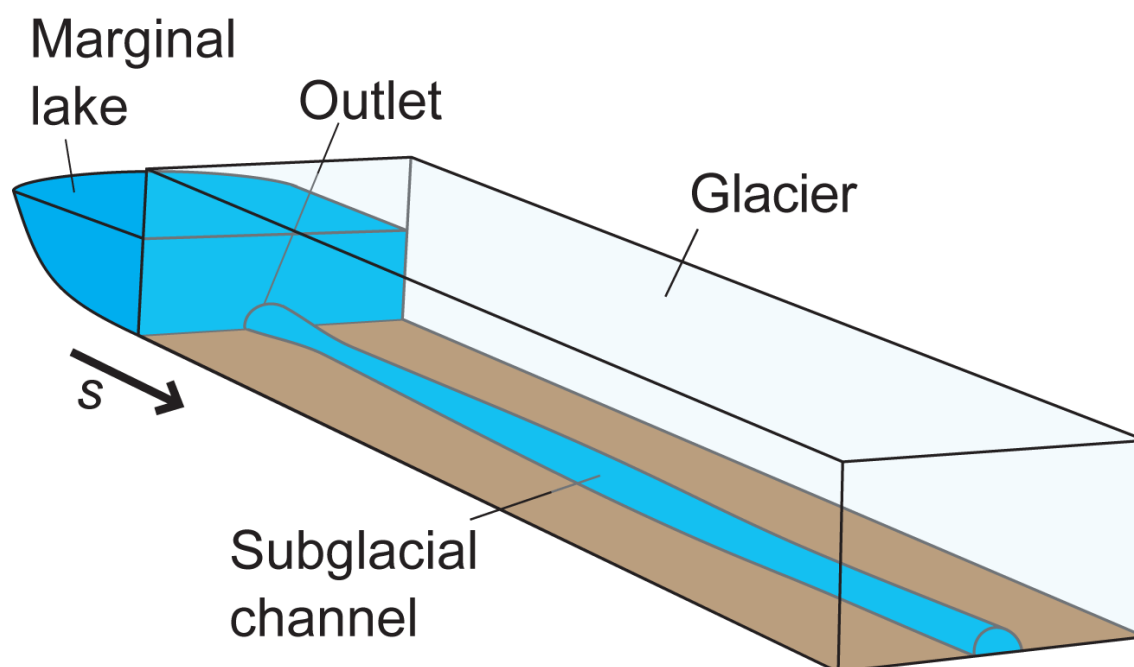
Fig. 2.3. Channelised subglacial drainage of a marginal lake

Channel geometry evolution

Just as Röthlisberger (1972) did, Nye (1976) supposed that ice-walled channels enlarge by melting and close due to inward creep flow of the ice. Unlike Röthlisberger, Nye allowed the rates at which these processes alter channel size to be out of balance. He described the rate of change of channel cross-sectional area, S, with time, t, as the sum of two terms:

$$\frac{\partial S}{\partial t} = \frac{m}{\rho_i} - K_0 S (p_i - p_w)^n,$$

<div align="right">**2-10**</div>

where p_i and p_w are still the water and ice pressures respectively and K_0 and n are the same ice flow parameters as above. The first term on the right represents channel enlargement through melting due to the dissipation of heat in the turbulently flowing water. The melt rate m is expressed as a mass per unit length of the channel per unit time. The second term represents channel closure due to the viscous flow of the ice (only valid when $p_w \leq p_i$).

Mass conservation

The spatial gradient in the discharge, Q, is equal to the water produced by melting at the channel walls minus the local rate of change of S:

$$\frac{\partial Q}{\partial s} = \frac{m}{\rho_w} - \frac{\partial S}{\partial t},$$

<div align="right">**2-11**</div>

where s is the distance along the glacier, which increases downglacier (Fig. 2.3).

Momentum balance

Like Röthlisberger (1972), Nye (1976) used Manning's equation to relate the channel cross-sectional area, the water's flow velocity, v, and the potential gradient driving this flow. Using the definition of G (eqn. 2-6) with Manning's equation (eqns. 2-4) eqn. 2-5, and $v = Q/S$ yields

$$G = \rho_w g \sin \phi_b - \frac{\partial p_w}{\partial s} = \mathcal{N} \frac{Q^2}{S^{\frac{8}{3}}},$$

<div align="right">**2-12**</div>

where $\mathcal{N}$ is a function of hydraulic roughness n' and the channel's shape:

$$\mathcal{N} = \left(\frac{S}{R_H^{\,2}} \right)^{\frac{2}{3}} \rho_w g n'^2 \, .$$

<div align="right">**2-13**</div>

Note that the channel slope ϕ in eqn. 2-4 has been replaced by the slope of the glacier bed ϕ_b because I assume the channel is located at the bed. Nye assumed that channel shape does not change, so $\mathcal{N}$ is constant. Using eqn. 2-5, $S/R_H^{\,2} = 2(2+\pi)^2/\pi \approx 16.8$ for a semi-circular channel and $S/R_H^{\,2} = 4\pi \approx 12.6$ for a circular channel. Nye (1976) assumed the latter.

Energy balance

Nye then applied the 1st law of thermodynamics to a cylindrical volume whose ends move with the flowing water and whose longitudinal axis runs along that of the channel .

This volume also includes ice that is about to be melted from the channel walls. This is the result:

$$Q\left(\rho_w g \sin\phi_b - \frac{\partial p_w}{\partial s}\right) = mL + m\sigma(\theta_w - \theta_i) + \rho_w \sigma S \frac{\partial \theta_w}{\partial t}.$$

2-14

In this expression θ_w and θ_i are the water and ice temperatures and σ is the specific heat capacity of water. It describes a balance between the energy gained as a volume Q of water moves through the potential $G = \rho_w g \sin\phi_b - \partial p_w/\partial s$ every unit time (the left-hand side), and the change in the internal energy of the water and ice in the cylindrical volume (the right-hand side). This change in internal energy is apportioned between melting a mass m of ice per unit time per unit length (the first term on the right), bringing this newly produced water to the bulk temperature of the water (second term) and changing the bulk water temperature of the water (third term). This assumes that the ice surrounding the channel is at the pressure melting point and that the energy used in accelerating the newly produced water to the velocity of the bulk water is negligible. It also assumes, because the water is flowing turbulently, the flow is well mixed and the bulk temperature is uniform except for a boundary layer at the channel walls where the water temperature adjusts to the ice temperature.

Heat transfer

Equation 2-14 defines the overall energy balance but does not determine how energy gained by the water as it moves through the potential gradient is apportioned between the three internal energy terms on the expression's right-hand side. To complete the model Nye (1976) uses the empirical Dittus-Boelter equation (McAdams, 1953) to construct an expression that relates the Reynolds number (a function of discharge and channel size), the temperature excess $(\theta_w - \theta_i)$ and the heat used in melting the walls of the channel (the sum of the first two terms on the right of eqn. 2-14; this includes the heat used in bringing newly produced meltwater to the bulk water's temperature because this temperature change occurs in the boundary layer). This leads to the following algebraic expression relating Q, S, $(\theta_w - \theta_i)$ and m:

$$0.205\left(\frac{2Q\rho_w}{\pi^{\frac{1}{2}}S^{\frac{1}{2}}\eta_w}\right)^{0.8} \kappa_w(\theta_w - \theta_i) = mL + m\sigma(\theta_w - \theta_i),$$

2-15

where η_w and κ_w are the viscosity and thermal conductivity of water.

Equations 2-10 to 2-15 complete Nye's model of time-dependent channelised drainage. He used it to explain the shape of jökulhlaup hydrographs during their rising stages

when discharge is increasing with time (see Fig. 1.2). He suggested that, during this stage of flood development, the viscous creep and temperature excess terms in eqns. 2-10, 2-14 and 2-15 and the contribution to the discharge from the melting of the channel walls can be neglected. He also supposed that the potential gradient can be represented by its spatially-averaged value. Neglecting the temperature excess is equivalent to assuming that the water temperature is always very close to the ice temperature and that all the heat generated in the flow is used instantaneously and locally in melting the walls of the channel. Hence, the second and third terms on the right of eqn. 2-14 are neglected and eliminating Q between eqns. 2-12 and 2-14 and assuming a constant potential gradient (left hand side of eqn. 2-12) yields the following expression for the melt rate m in terms of the channel cross-sectional area S and the total potential gradient, G:

$$m = \frac{S^{\frac{4}{3}}G^{\frac{3}{2}}}{\mathcal{N}^{\frac{1}{2}}L}.$$

2-16

Combining eqn. 2-16 with eqn. 2-10 (with the viscous creep term neglected) yields

$$\frac{\partial S}{\partial t} = \frac{G^{\frac{3}{2}}}{\rho_i \mathcal{N}^{\frac{1}{2}}L} S^{\frac{4}{3}},$$

2-17

which describes the time evolution of the channel cross-sectional area. Nye (1976) then differentiated both sides of eqn. 2-12 with respect to t and eliminated $\partial S/\partial t$ and S from the resulting expression using eqns. 2-17 and 2-12 respectively to arrive at the following expression for the rate of change of discharge during the rising stage of a flood:

$$\frac{\partial Q}{\partial t} = \frac{4G^{\frac{11}{8}}}{3\rho_i \mathcal{N}^{\frac{3}{8}}L} Q^{\frac{5}{4}}.$$

2-18

Integrating this expression shows that discharge increases as $Q = \mathcal{N}(-1/t)^4$, where $t = 0$ is the time at which the discharge theoretically goes to infinity. Physically, Nye's theory suggests that discharge through a channel, that is pressure-coupled to a lake, grows through a positive feedback between melt enlargement of the channel, channel size and water discharge. Melt increases the channel size (described by the channel evolution equation; eqn. 2-10), a larger channel can convey a larger discharge (via the momentum balance equation; eqn. 2-12), and this leads to a higher rate of melting (through the energy balance equation; eqn. 2-14).

Nye showed that his model's prediction of the time evolution of discharge during jökulhlaups closely agreed with reality by fitting eqn. 2-18 to the rising stage of an observed hydrograph recorded during a flood from Grimsvötn in March 1972. This success was used as a justification for assumptions made during the model's development: that floods occur through channels, that viscous creep is negligible during the rising stages of floods, that the along-channel hydraulic potential gradient can be approximated by its spatially-averaged value and that heat dissipated by water flow is used instantaneously in melting the channel walls.

Nye (1976) also considered the termination of floods. As the lake empties, the potential gradient driving water flow decreases and the difference between the ice and water pressures at the lake increases. This leads to the closure term in the channel geometry equation exceeding the melt-opening term and the channel closes.

Nye (1976) had demonstrated that the main features of jökulhlaups from Lake Grimsvötn were due to water flowing through a subglacial channel whose geometry evolves in time as a result of the two opposing processes of melt enlargement and viscous ice creep closure. This was an important step in the development of theoretical subglacial hydrology and Nye's (1976) model has been the basis for all subsequent theoretical investigations of jökulhlaups and most theoretical work on 'everyday' subglacial drainage.

2.2.3   Fowler's modification of Nye's model

Fowler (1999) modified Nye's (1976) model with the aim of explaining how jökulhlaups from Grimsvötn initiate and repeat. This was the first model to simulate stably repeating flood cycles and to explain how the rapid lake input the preceded the large 1996 Grimsvötn flood caused the lake to fill to the flotation level when floods usually start when the lake level is 60-70 m lower than this. The significance of this is discussed further in the introduction of Chapter 3. Here I describe Fowler's (1999) model.

A concept borrowed from studies of basal sliding and friction between glaciers and their bed is the basal effective pressure. Effective pressure is the difference between the ice overburden pressure, p_i, and the basal water pressure, p_w, in this case, in a channel:

$$N = p_i - p_w.$$

2-19

Fowler (1999) recast Nye's (1976) equations in terms of N. Differentiating the above expression with respect to distance along the channel, s, and eliminating $\partial p_w / \partial s$ between the result and eqn. 2-6 yields

$$G = \rho_w g \sin \phi_b - \frac{\partial p_i}{\partial s} + \frac{\partial N}{\partial s}.$$

2-20

This expresses the total potential G in terms of glacier geometry (first two terms on the right) and the gradient of the effective pressure (the last term). Fowler (1999) defined the basic hydraulic gradient, ψ, as the sum of the two glacier-geometry-related terms:

$$\psi = \rho_w g \sin \phi_b - \frac{\partial p_i}{\partial s}.$$

2-21

Total potential gradient could then be expressed in terms of ψ and N,

$$G = \psi + \frac{\partial N}{\partial s}.$$

2-22

Substituting this expression and the definition of hydraulic radius (eqn. 2-5) into Manning's equation (eqn. 2-4) yields Fowler's momentum balance equation:

$$\psi + \frac{\partial N}{\partial s} = f \rho_w g \frac{Q^2}{S^{\frac{8}{3}}}.$$

2-23

The friction factor f is related to Nye's (1976) parameter $\mathcal{N}$ and the Manning roughness coefficient by

$$f = \frac{\mathcal{N}}{\rho_w g} = \left(\frac{S}{R_H^{\,2}}\right)^{\frac{2}{3}} n'^2.$$

2-24

For a semi-circular channel, $f = (2(\pi+2)^2/\pi)^{2/3} n'^2 \approx 6.6 n'^2$. In a significant departure from Nye's model, Fowler (1999) modified his momentum balance equation to deal realistically with a total potential gradient (the left-hand side of eqn. 2-23) that is negative. A negative total potential gradient, which can be due to glacier geometry or an adverse water pressure gradient, drives water flow upglacier towards the lake. Upglacier water flow corresponds to a negative discharge, so to deal with this mathematically Fowler (1999) added a modulus sign to eqn. 2-23, yielding

$$\psi + \frac{\partial N}{\partial s} = f \rho_w g \frac{Q|Q|}{S^{\frac{8}{3}}}.$$

2-25

Hence, as S is always positive, when total potential gradient is negative, Q is also negative as required. Nye's (1976) channel closure equation was also expressed in terms of the effective pressure:

$$\frac{\partial S}{\partial t} = \frac{m}{\rho_\text{i}} - K_0 S N^3.$$

<div align="right">**2-26**</div>

Fowler (1999) adopted Nye's water mass conservation equation but added a supply term *M*. This term represents water entering the channel along its length and has units of mass per unit distance-along-the-channel per unit time. It can be a function of time and space. Mass continuity is thus given by

$$\frac{\partial S}{\partial t} + \frac{\partial Q}{\partial s} = \frac{m}{\rho_\text{w}} + M.$$

<div align="right">**2-27**</div>

After assuming the temperature of the water in the lake and the channel is always equal to the melting point, energy conservation leads to a balance between the channel-wall melt-rate and the rate of energy dissipated in the water as a volume *Q* moves through the potential *G* per unit time:

$$mL = Q\left(\psi + \frac{\partial N}{\partial s}\right).$$

<div align="right">**2-28**</div>

In summary, the equations Fowler used to describe channel evolution and the conservation of mass, momentum and energy in the channel are respectively:

$$\frac{\partial S}{\partial t} = \frac{m}{\rho_\text{i}} - K_0 S N^3,$$

<div align="right">**2-29**</div>

$$\frac{\partial S}{\partial t} + \frac{\partial Q}{\partial s} = \frac{m}{\rho_\text{w}} + M,$$

<div align="right">**2-30**</div>

$$\psi + \frac{\partial N}{\partial s} = f \rho_\text{w} g \frac{Q|Q|}{S^{\frac{8}{3}}},$$

<div align="right">**2-31**</div>

$$mL = Q\left(\psi + \frac{\partial N}{\partial s}\right).$$

<div align="right">**2-32**</div>

Fowler (1999) coupled his channel to a lake in terms of both effective pressure and water discharge. According to this coupling the effective pressure at the lake changes due to an environmental meltwater input to the lake and discharge into, or out of, the channel at the lake outlet (Fig. 2.3) and the effective pressure at the lake dictates the effective pressure in the channel at the lake outlet (Fig. 2.3).

2.2.4   The Nye-Fowler jökulhlaup model

In this section I present the model I use in Chapter 3 to simulate jökulhlaups and develop further in Chapters 5 and 6. It consists of Fowler's (1999) channel equations coupled to a marginal lake and scaled according to the typical size of marginal lakes and their floods. For the rest of the thesis, I refer to this model as the Nye-Fowler jökulhlaup model.

Coupling the channel to a lake

The depth of a marginal lake, h_L, and the effective pressure in a subglacial channel immediately adjacent to the lake (labelled the outlet in Fig. 2.3), N_L are related linearly by

$$N_L = N(0,t) = \rho_i g H_D - \rho_w g h_L,$$

2-33

where H_D is the height of the ice dam. The volume of the lake, V_L, changes with time due to water input from its surroundings, Q_{in}, and water exchange with the channel. The latter is equal to the discharge through the channel at the outlet, $Q(0,t)$. So the rate of change of lake volume is given by

$$\frac{dV_L}{dt} = Q_{in}(t) - Q(0,t).$$

2-34

How lake depth and lake volume are related depends on lake hypsometry. I follow previous work (e.g. Clarke, 1982; Ng and Björnsson, 2003; Walder and Costa, 1996) to parameterise hypsometry using the following expression:

$$\left(\frac{h_L}{h_{Li}}\right)^{p_L} = \frac{V}{V_{Li}},$$

2-35

where h_{Li} is the reference lake depth, V_{Li} is the reference lake volume and p_L is a dimensionless parameter that can be derived from hypsometry data. Using the chain rule with eqn. 2-35 yields the relationship between dV_L/dt and dh_L/dt:

$$\frac{dV}{dt} = \frac{dV}{dh_L}\frac{dh_L}{dt} = \frac{p_L V_{Li}}{h_{Li}^{p_L}} h_L^{p_L-1} \frac{dh_L}{dt}.$$

2-36

Combining this with eqn. 2-34 yields the dimensional lake-depth evolution equation,

$$\frac{dh_L}{dt} = \frac{h_{Li}^{p_L}}{p_L V_{Li} h_L^{p_L-1}}[Q_{in}(t) - Q(0,t)].$$

2-37

Equations 2-29–2-33 and 2-37 complete the dimensional form of the model that I refer to hereafter as the Nye-Fowler model.

Non-dimensionalisation

To non-dimensionalise the Nye-Fowler model, I define scales for the variables *S*, *N*, *Q*, *M*, ψ, *t*, *m*, h_L and Q_{in} as follows:

$$S = S_0 S^*, \qquad N = N_0 N^*, \qquad Q = Q_0 Q^*, \qquad M = M_0 M^*, \qquad \psi = \psi_0 \psi^*,$$
$$t = t_0 t^*, \qquad m = m_0 m^*, \qquad h_L = h_{L0}\, h_L^*, \qquad Q_{in} = Q_{in0}\, Q_{in}^*.$$

<div align="right">

2-38

</div>

where the asterisks denote dimensionless variables. The scales for *s* and *Q* are defined as s_0 = 10 km and Q_0 = 1500 m³ s⁻¹ respectively. These are reasonable values for channel length and the peak discharge for floods from marginal lakes. Replacing dimensional variables in eqn. 2-29 with the corresponding products of scales and dimensionless variables from eqn. 2-38 gives

$$\frac{S_0}{t_0}\frac{\partial S^*}{\partial t^*} = \frac{m_0 m^*}{\rho_i} - K_0 S_0 N_0^3 S^* N^{*3}.$$

<div align="right">

2-39

</div>

Equating the coefficients of the three terms in the above expression gives,

$$\frac{S_0}{t_0} = \frac{m_0}{\rho_i} = K_0 S_0 N_0^3,$$

<div align="right">

2-40

</div>

which defines the scales for the effective pressure and time:

$$N_0 = (K_0 t_0)^{-\frac{1}{3}},$$

<div align="right">

2-41

</div>

$$t_0 = \frac{\rho_i S_0}{m_0}.$$

<div align="right">

2-42

</div>

This leaves the non-dimensional channel geometry equation:

$$\frac{\partial S^*}{\partial t^*} = m^* - S^* N^{*3}.$$

<div align="right">

2-43

</div>

Next, replacing the dimensional variables in eqn. 2-30 with eqn. 2-38 yields

$$\frac{S_0}{t_0}\frac{\partial S^*}{\partial t^*} + \frac{Q_0}{s_0}\frac{\partial Q^*}{\partial s^*} = \frac{m_0}{\rho_i} r m^* + M_0 M,$$

<div align="right">

2-44

</div>

where $r = \rho_i/\rho_w$. Substituting eqn. 2-42 into this expression and defining

$$\epsilon_R = \frac{s_0 m_0}{Q_0 \rho_i}, \qquad M_0 = \frac{Q_0}{s_0},$$

<div align="right">

2-45

</div>

yields the non-dimensional mass conservation equation

$$\epsilon_R \frac{\partial S^*}{\partial t^*} + \frac{\partial Q^*}{\partial s^*} = \epsilon_R r m^* + M^*.$$

2-46

Replacing variables in eqn. 2-31 and equating the coefficients from the right-hand terms with the coefficient of the first term on the left yields

$$\psi_0 = f\rho_w g \frac{Q_0^2}{S_0^{\frac{8}{3}}}.$$

2-47

This leaves the non-dimensional momentum conservation equation:

$$\psi^* + \delta \frac{\partial N^*}{\partial s^*} = \frac{Q^*|Q^*|}{S^{*\frac{8}{3}}},$$

2-48

where

$$\delta = \frac{N_0}{s_0 \psi_0}.$$

2-49

Finally for the channel equations, replacing dimensional variables in eqn. 2-32 gives

$$Q_0 Q^* \left(\psi_0 \psi^* + \frac{N_0}{s_0} \frac{\partial N^*}{\partial s^*} \right) = m_0 m^* L.$$

2-50

Equating the right-hand coefficients with the coefficient of the first term on the left yields

$$m_0 = \frac{Q_0 \psi_0}{L},$$

2-51

and the non-dimensional energy balance equation:

$$Q^* \left(\psi^* + \delta \frac{\partial N^*}{\partial s^*} \right) = m^*.$$

2-52

Moving onto the lake-depth evolution equation, the lake-depth scale, h_{L0}, is chosen as the flotation depth:

$$h_{L0} = \frac{\rho_i}{\rho_w} H_D.$$

2-53

Eliminating H_D between this and eqn. 2-33, then replacing the dimensional lake depth and the dimensional effective pressure at the outlet in the resulting expression with the corresponding scales and dimensionless variables from eqn. 2-38, yields

$$N_0 N_L^* = \rho_w g h_{L0}[1 - h_L^*].$$

2-54

Defining

$$\beta_R = \frac{\rho_w g h_{L0}}{N_0}$$

<div align="right">**2-55**</div>

leaves the non-dimensionalised equation relating the effective pressure at the outlet to lake depth:

$$N_L^* = \beta_R[1 - h_L^*].$$

<div align="right">**2-56**</div>

Finally, substituting 2-38 into 2-37 yields the non-dimensional lake depth evolution equation:

$$\frac{dh_L^*}{dt^*} = \frac{\lambda_L}{h_L^{*p_L - 1}}[Q_{in}^* - Q(0,t)^*],$$

<div align="right">**2-57**</div>

where

$$\lambda_L = \frac{t_0 h_{Li}^{p_L} Q_0}{p_L V_{Li} h_{L0}^{p_L}}.$$

<div align="right">**2-58**</div>

Boundary conditions

A pair of boundary conditions is required to solve the channel equations. As already described, at the lake, the effective pressure boundary condition is given by the lake depth and eqn. 2-56. At the glacier terminus ($s = s_0$) a second boundary condition is needed. I use a constant dimensionless effective pressure at the terminus, N_T^*. Two reasonable choices for N_T^* are $N_T^* = 0$ (Ng, 1998), corresponding to the ice thickness and the water pressure going to zero at the terminus, and $N_T^* = N_a/N_0 = \rho_i g H(s = s_0)/N_0$, corresponding to zero water pressure and an ice thickness of H at the terminus. Initially I use the former ($N_T^* = 0$).

Summary

Box 2-1 contains the non-dimensional Nye-Fowler model.

Box 2-1. The Nye-Fowler Model (asterisks dropped).

The channel

Channel evolution

$$\frac{\partial S}{\partial t} = \frac{|Q|^3}{S^{\frac{8}{3}}} - SN^3$$

2-59

Mass continuity

$$\frac{\partial Q}{\partial s} = \epsilon_\mathrm{R}(r-1)\frac{|Q|^3}{S^{\frac{8}{3}}} + \epsilon_\mathrm{R} SN^3 + M$$

2-60

Conservation of momentum

$$\frac{\partial N}{\partial s} = \frac{1}{\delta}\left(\frac{Q|Q|}{S^{\frac{8}{3}}} - \psi\right)$$

2-61

Boundary conditions and the lake

Channel effective pressure at the lake

$$N(s=0,t) = N_\mathrm{L} = \beta[1 - h_\mathrm{L}]$$

2-62

Lake depth evolution

$$\frac{dh_\mathrm{L}}{dt} = \frac{\lambda_\mathrm{L}}{h_\mathrm{L}^{p_\mathrm{L}-1}}[Q_\mathrm{in} - Q(0,t)]$$

2-63

Effective pressure at the terminus

$$N(s=1,t) = N_\mathrm{T} = 0$$

2-64

Model parameters

$$\epsilon_\mathrm{R} = \frac{s_0 m_0}{Q_0 \rho_\mathrm{i}}, \qquad r = \frac{\rho_\mathrm{i}}{\rho_\mathrm{w}}, \qquad \delta = \frac{N_0}{s_0 \psi_0}$$

$$\beta_\mathrm{R} = \frac{\rho_\mathrm{w} g h_\mathrm{L0}}{N_0}, \qquad \lambda_\mathrm{L} = \frac{t_0 h_\mathrm{Li}^{p_\mathrm{L}} Q_0}{p_\mathrm{L} V_\mathrm{Li} h_\mathrm{L0}^{p_\mathrm{L}}}.$$

2-65

Scales

$$S_0 = \left(\frac{f\rho_\mathrm{w} g Q_0^2}{\psi_0}\right)^{\frac{3}{8}}, \qquad N_0 = \left(\frac{K_0 \rho_\mathrm{i} S_0 L}{\psi_0 Q_0}\right)^{-\frac{1}{3}}, \quad m_0 = \frac{Q_0 \psi_0}{L},$$

$$t_0 = \frac{\rho_\mathrm{i} S_0 L}{\psi_0 Q_0}, \qquad M_0 = \frac{Q_0}{s_0}, \qquad h_\mathrm{L0} = \frac{\rho_\mathrm{i}}{\rho_\mathrm{w}} H_\mathrm{D}.$$

2-66

2.2.5 Numerical methods

Here I describe the numerical methods used to solve the Nye-Fowler model. The spatial and temporal domains are discretised into n space grid points and m time steps. The space grid points are referred to by the index $j = 1$ to n and separated by grid spacing Δs. Time steps are referred to by the index $i = 1$ to m and separated by time steps of size Δt. At time step i the Euler method is used with eqn. 2-63 to evolve the lake level forward in time:

$$h_L^{i+1} = h_L^i + \Delta t \frac{\lambda_L}{h_L^{i\,p_L-1}} \left[Q_{in}{}^i - Q_1^i \right].$$

2-67

The same method is used with eqn. 2-59 to evolve the channel cross-sectional area, S, forward in time at all grid points

$$S_j^{i+1} = S_j^i + \Delta t \left[\frac{\left| Q_j^i \right|^3}{S_j^{i\frac{8}{3}}} - S_j^i N_j^{i\,3} \right], \quad j = 1, \dots, n.$$

2-68

The forward evolution of these variables depends on the discharge and the effective pressure at time step i, Q_j^i and N_j^i. These can be found by simultaneously solving the mass and momentum conservation equations (eqns. 2-60 and 2-61) using a numerical method I call the relaxation method. This is described first below. However, the relaxation method is computationally demanding, so simplifying the model allows two more efficient methods to be used: Newton's method, described by Ng (1994), and what I refer to as the boundary layer method, used by Fowler (1999), Evatt (2006) and Evatt et al. (2006). I also describe these two alternative methods below.

Relaxation method

My aim is to find the set of values for N^i and Q^i that obey: (i) the mass and momentum conservation equations (eqns. 2-60 and 2-61):

$$\frac{\partial Q^i}{\partial s} = \epsilon_R (r-1) \frac{\left| Q^i \right|^3}{S^{i\frac{8}{3}}} + \epsilon_R S^i N^{i\,3} + M^i,$$

2-69

$$\frac{\partial N^i}{\partial s} = \frac{1}{\delta} \left(\frac{Q^i |Q^i|}{S^{i\frac{8}{3}}} - \psi \right);$$

2-70

(ii) the boundary condition at the lake,

$$N_1^i = \beta_R \left[1 - h_L^i \right];$$

2-71

and (iii) the boundary condition at the glacier terminus,

$$N_n^i = 0.$$

2-72

The channel's area S_j^i and lake's depth h^i are known from the previous timestep, the basic hydraulic gradient ψ is constant and only a function of space, and the meltwater input to the channel along its length M can be a function of space, time or other model variables.

The relaxation method operates at two levels. An inner loop is supplied with a guess at the lake discharge Q_1^i that will yield Q^i and N^i profiles that obey the model equations and both boundary conditions. The inner loop uses this guess to produce Q^i and N^i profiles that match the lake discharge supplied to it and obey eqn. 2-69, eqn. 2-70 and the boundary condition at the terminus (eqn. 2-72), but not the effective pressure boundary condition at the lake (eqn. 2-71). An outer loop then tunes Q_1^i until the Q^i and N^i profiles produced by the inner loop also match the effective pressure required by the boundary condition at the lake (eqn. 2-71).

The inner loop works by iteratively relaxing towards a solution which obeys the desired equations. The following description of the inner loop is summarised in Fig. 2.4.

A derivative of Q with respect to a new independent variable ζ is added to the left-hand-side of the mass conservation equation to give

$$\frac{\partial Q^i}{\partial \zeta} + \frac{\partial Q^i}{\partial s} = \epsilon_R (r - 1) \frac{|Q^i|^3}{S^{i\frac{8}{3}}} + \epsilon_R S^i N^{i3} + M^i.$$

2-73

The added term has no physical meaning, but by treating the new variable ζ in the same way as one treats time in a physical model, eqn. 2-73 can be seen as a wave equation which describes waves travelling in the positive s direction as 'time' ζ passes. Using this wave-equation analogy, eqn. 2-73 and eqn. 2-70 can be simultaneously evolved forward using a Forward Time Upwind Difference scheme to simulate waves moving downglacier as 'time' passes. Crucially, in most cases, the waves tend to die out as 'time' passes and the system approaches a 'steady state'. Reaching such a steady state is equivalent to my unphysical addition – the ζ-derivative – disappearing. The result is a pair of Q^i and N^i profiles that obey the eqns. 2-69 and 2-70 as required (note that eqn. 2-73 with $\partial Q_j^i / \partial \zeta = 0$ is identical to eqn. 2-69).
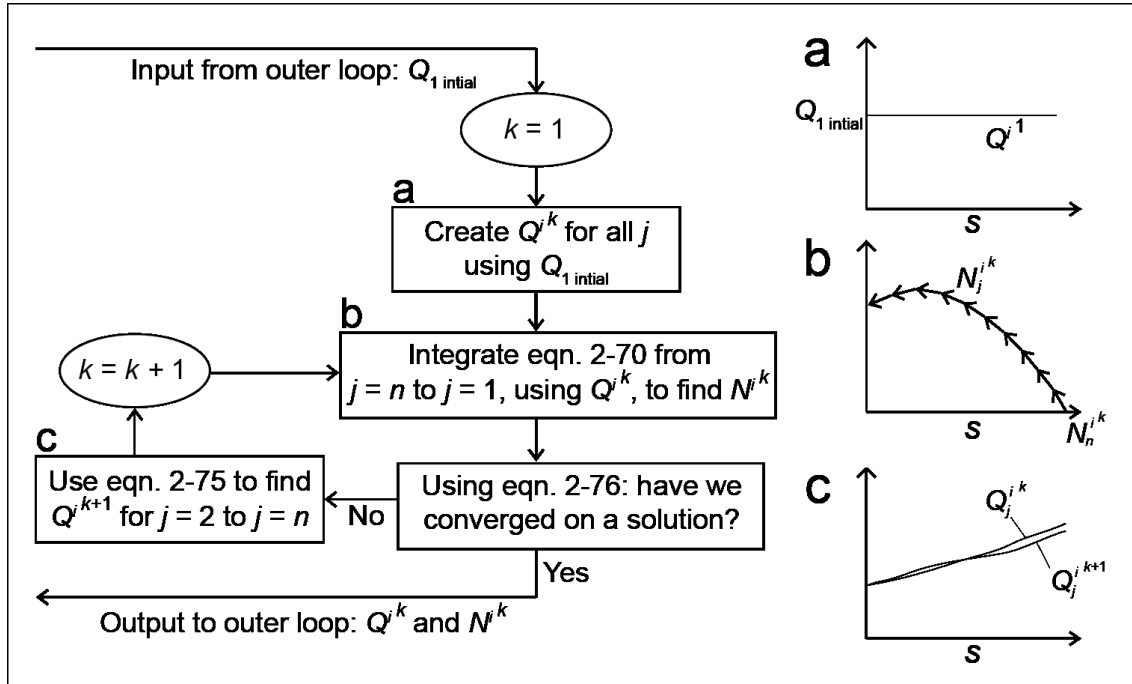
Fig. 2.4. The inner loop of the relaxation method. The algorithm that operates in the inner loop of the relaxation method is summarised in the flow diagram on the left. The three panels on the right, (a), (b) and (c), illustrate three stages of the algorithm labelled in the flow diagram accordingly.

I have also found that introducing a damping term to the equation which is proportional to the product of S^i and the ζ-derivative of N^i, greatly decreases the time it takes the system to reach a steady state. With this addition eqn. 2-73 has the following form:

$$\frac{\partial Q^i}{\partial \zeta} + \frac{\partial Q^i}{\partial s} = \epsilon_R(r-1)\frac{\left|Q^i\right|^3}{S^{i\frac{8}{3}}} + \epsilon_R S^i N^{i3} + M^i + \mu\frac{\partial N^i}{\partial \zeta}S^i,$$

2-74

where μ is a numerical constant ~0.01–0.5. The physical interpretation of the damping term is that it makes the water slightly compressible, thereby damping the propagation of waves. When $\partial N^i/\partial \zeta < 0$ the water pressure is increasing, the water is compressed and takes up less volume, hence the damping term is proportional to $\partial N^i/\partial \zeta$. The effect is larger where the channel is larger because the same fractional change in the compression of the water has a larger effect on the volume, hence the damping term is proportional to S^i. A similar approach was taken by Clarke (2003) in decreasing the numerical stiffness of Spring and Hutter's (1981) model equations. My approach has one advantage over his. My unphysical damping term, ($\mu\ \partial N^i/\partial \zeta\ S^i$) is guaranteed to disappear, because I seek a solution that is steady in the ζ-dimension, $\partial N^i/\partial \zeta = \partial Q^i/\partial \zeta = 0$ (in fact the damping term's disappearance is used as the criterion by which the steady state is detected numerically). In general, Clarke's (2003) unphysical damping term does not disappear, because it contains a derivative of the water's pressure in terms of real time t.

Applying the Forward Time Upwind Difference scheme to eqn. 2-74 gives

$$
{}^{k+1}Q_j^i = {}^kQ_j^i + \Delta\zeta\left[\frac{{}^kQ_j^i - {}^kQ_{j-1}^i}{\Delta s} + \epsilon_R(r-1)\frac{\left|{}^kQ_j^i\right|^3}{S_j^{i\frac{8}{3}}} + \epsilon_R S_j^i\,{}^kN_j^{i\,3} + {}^kM_j^i + \mu\frac{{}^kN_j^i - {}^{k-1}N_j^i}{\Delta\zeta}S_j^i\right].
$$

2-75

The k superscripts that appear to the left of the terms Q_j^i, N_j^i and M_j^i in the above expression refer to the grid points along the ζ dimension. Note that S_j^i is not a function of ζ and so does not require a k-superscript and, because M can be a function of Q, N or S, it can change with space, real time and ζ, so it does need a k superscript.

Given a guess at the discharge at the lake, $Q_{1\text{ initial}}$, the inner loop constructs an initial Q-profile for all j, ${}^1Q^i$ (uniform ${}^1Q^i$ is used for simplicity). This profile and eqn. 2-70 are used to find the corresponding ${}^1N^i$ by starting at $j=n$, where eqn. 2-72 defines N_n, and integrating back to the lake using quadrature. ${}^1Q^i$ and ${}^1N^i$ are then used in eqn. 2-75 to find ${}^2Q^i$ for $j=2$ to n. This process iterates until the rate of change of ${}^kN^i$ with ζ is small, This is detected numerically when the following criteria is met:

$$
\max\left(\left|\frac{{}^kN_j^i - {}^{k-1}N_j^i}{{}^kN_j^i}\right|\right) < \Upsilon_{\text{Re}},
$$

2-76

where the max function returns the largest value its argument has over the range $j=1$ to n and Υ_{Re} is a tolerance which is set to a small value ($\sim10^{-7}$). The results of this process are Q^i and N^i profiles that (i) match the initial guess at the lake discharge supplied to the inner loop's algorithm, $Q_{1\text{ initial}}$, (ii) obey the mass and momentum conservation equations and (iii) obey the boundary condition at $j=n$. The calculated profiles do not however match the boundary condition on the effective pressure at the lake (eqn. 2-71). The initial guess, $Q_{1\text{ initial}}$, is tuned until the effective pressure at $j=1$ matches the boundary condition dictated by the lake. This is done in the outer loop using the Newton-Raphson root-finding algorithm (not to be confused with Newton's method described next).

Newton's method

In some cases Q is everywhere positive. The modulus signs in eqns. 2-60 and 2-61 can be removed, leaving

$$
\frac{\partial Q^i}{\partial s} = \epsilon_R(r-1)\frac{Q^{i\,3}}{S_j^{i\frac{8}{3}}} + \epsilon_R S^i N^{i\,3} + M^i,
$$

$$\frac{\partial N^i}{\partial s} = \frac{1}{\delta}\left(\frac{Q^{i^2}}{S^{i\frac{8}{3}}} - \psi\right).$$

These equations can be solved using an implicit numerical method called Newton's method (Ng, 1994), so-called because it is analogous to the Newton-Raphson root-finding algorithm. It operates as follows. Initial guesses are made at discharge and pressure profiles that obey eqns. 2-77 and 2-78 and the imposed boundary conditions. A series of small corrections are made to these guesses with the aim of bringing them closer to the true solutions. At each iteration the next set of these corrections is calculated using the current iteration's guesses at the discharge and pressure profiles.

The previous time step's discharge profile is used as the initial guess at the discharge profile:

$$^1Q_j^i = Q_j^{i-1}, j = 1, \dots, n.$$

Now the superscript to the left of the term Q_j^i refers to the current iteration within Newton's method. The i superscript still refers to the time step and the j subscript still refers to the spatial grid point. The initial guess at the N profile is arranged so that it obeys the boundary conditions at the lake, $N(0,t)^i = N_L{}^i$, and the terminus, $N(s=s_0,t) = N_T$, using the following function:

$$^1N_j^i = \sin\left[(1 - s_j)(\pi - \sin^{-1}N_L{}^i)\right] + s_jN_T, \qquad j = 1, \dots, n.$$

At the kth iteration of Newton's method the aim is to use the current guesses at the correct discharge and effective pressure profiles, $^kQ^i$ and $^kN^i$, to find new guesses that better approximate the solutions to eqns. 2-77 and 2-78, $^{k+1}Q^i$ and $^{k+1}N^i$. The equations are applied at the next iteration,

$$\frac{\partial}{\partial s}\left[^{k+1}Q^i\right] = \epsilon_R(r - 1)\frac{^{k+1}N^{i^3}}{S^{i\frac{8}{3}}} + \epsilon_R S^i{}^{k+1}N^{i^3} + M^i,$$

$$\delta\frac{\partial}{\partial s}\left[^{k+1}N^i\right] = \left(\frac{^{k+1}N^{i^2}}{S^{i\frac{8}{3}}} - \psi\right),$$

and spatial derivatives are approximated using central difference,

$$\frac{^{k+1}Q^i_{j+1} - {}^{k+1}Q^i_{j-1}}{2\Delta s} = \epsilon_R(r-1)\frac{^{k+1}Q^{i^3}_j}{S^{i\frac{8}{3}}_j} + \epsilon_R S^i_j{}^{k+1}N^{i^3}_j + M^i_j,$$

$$\delta\frac{^{k+1}N^i_{j+1} - {}^{k+1}N^i_{j-1}}{2\Delta s} = \frac{^{k+1}Q^{i^2}_j}{S^{i\frac{8}{3}}_j} - \psi_j$$

2-83

(note that I am also assuming that the supply term M is constant and uniform, Newton's method can still be used if this assumption is not made, I make it for simplicity). The next iteration's guesses, $^{k+1}Q^i$ and $^{k+1}N^i$, are found by replacing these terms by the sum of the previous iteration's guesses and two sets of spatially-dependent correction terms, $^kdQ^i$ and $^kdN^i$, defined as follows:

$$^{k+1}Q^i = {}^kQ^i + {}^kdQ^i,$$

$$^{k+1}N^i = {}^kN^i + {}^kdN^i.$$

2-84

Substituting eqn. 2-84 into eqn. 2-83 gives

$$\frac{^kQ^i_{j+1} + {}^kdQ^i_{j+1} - {}^kQ^i_{j-1} - {}^kdQ^i_{j-1}}{2\Delta s}$$

$$= \epsilon_R(r-1)\frac{\left({}^kQ^i_j + {}^kdQ^i_j\right)^3}{S^{i\frac{8}{3}}_j} + \epsilon_R S^i_j\left({}^kN^i_j + {}^kdN^i_j\right)^3 + M^i_j,$$

$$\delta\frac{^kN^i_{j+1} + {}^kdN^i_{j+1} - {}^kN^i_{j-1} - {}^kdN^i_{j-1}}{2\Delta s} = \frac{\left({}^kQ^i_j + {}^kdQ^i_j\right)^2}{S^{i\frac{8}{3}}_j} - \psi_j.$$

2-85

Next, expanding the brackets, neglecting terms containing higher orders of $dQ^{i\,k}$ and $dN^i_{\;k}$, and dropping the i and k indexes for clarity, leaves

$$\frac{Q_{j+1} + dQ_{j+1} - Q_{j-1} - dQ_{j-1}}{2\Delta s}$$

$$= \epsilon_R(r-1)\frac{Q^3_j + 3Q^2_j dQ_j}{S^{\frac{8}{3}}_j} + \epsilon_R S_j\left(N_j{}^3 + 3N^2_j dN_j\right) + M_j,$$

2-86

$$\delta\frac{N_{j+1} + dN_{j+1} - N_{j-1} - dN_{j-1}}{2\Delta s} = \frac{Q^2_j + 2Q_j dQ_j}{S^{\frac{8}{3}}_j} - \psi_j.$$

2-87

Equations 2-86 and 2-87 represent a set of 2n linear simultaneous equations where the only unknowns are the two sets of n correction terms dN and dQ. They can be solved as

a matrix equation. The coefficients of the correction terms are gathered on the left-hand side:

$$
\begin{bmatrix} -\dfrac{1}{2\Delta s} & 0 & -\dfrac{3\epsilon_R(r-1)Q_j^2}{S_j^{\frac{8}{3}}} & -3\epsilon_R S_j N_j^2 & \dfrac{1}{2\Delta s} & 0 \end{bmatrix}
\begin{bmatrix} dQ_{j-1} \\ dN_{j-1} \\ dQ_j \\ dN_j \\ dQ_{j+1} \\ dN_{j+1} \end{bmatrix}
$$

$$
= \left[M_j + \frac{\epsilon_R(r-1)Q_j^3}{S_j^{\frac{8}{3}}} + \epsilon_R S_j N_j^3 - \delta\frac{Q_{j+1}-Q_{j-1}}{2\Delta s} \right],
$$

2-88

$$
\begin{bmatrix} 0 & -\dfrac{\delta}{2\Delta s} & -\dfrac{2Q_j^2}{S_j^{\frac{8}{3}}} & 0 & 0 & \dfrac{\delta}{2\Delta s} \end{bmatrix}
\begin{bmatrix} dQ_{j-1} \\ dN_{j-1} \\ dQ_j \\ dN_j \\ dQ_{j+1} \\ dN_{j+1} \end{bmatrix}
= \left[\frac{Q_j^2}{S_j^{\frac{8}{3}}} - \psi_j - \delta\frac{N_{j+1}-N_{j-1}}{2\Delta s} \right].
$$

2-89

Combining these two expressions forms a block matrix equation of the form $\Xi.x = v$:

$$
\begin{bmatrix} b_1 & c_1 & 0 & 0 & 0 & 0 \\ a_2 & b_2 & c_2 & 0 & 0 & 0 \\ 0 & a_3 & b_3 & c_3 & 0 & 0 \\ 0 & 0 & \ddots & \ddots & \ddots & 0 \\ 0 & 0 & 0 & a_{n-1} & b_{n-1} & c_{n-1} \\ 0 & 0 & 0 & 0 & a_n & b_n \end{bmatrix}
\begin{bmatrix} x_1 \\ x_2 \\ x_3 \\ \vdots \\ x_{n-1} \\ x_n \end{bmatrix}
= \begin{bmatrix} v_1 \\ v_2 \\ v_3 \\ \vdots \\ v_{n-1} \\ v_n \end{bmatrix},
$$

2-90

where

$$
a_j = \begin{bmatrix} -\dfrac{1}{2\Delta s} & 0 \\ 0 & -\dfrac{\delta}{2\Delta s} \end{bmatrix}, \quad
b_j = \begin{bmatrix} -3\epsilon_R(r-1)Q_j^2 S_j^{-\frac{8}{3}} & -3\epsilon_R S_j N_j^2 \\ -2Q_j^2 S_j^{-\frac{8}{3}} & 0 \end{bmatrix}, \quad
c_j = \begin{bmatrix} \dfrac{1}{2\Delta s} & 0 \\ 0 & \dfrac{\delta}{2\Delta s} \end{bmatrix},
$$

$$
x_j = \begin{bmatrix} dQ_j \\ dN_j \end{bmatrix}, \quad
v_j = \begin{bmatrix} M_j + \epsilon_R(r-1)Q_j^3 S_j^{-\frac{8}{3}} + \epsilon_R S_j N_j^3 - \delta\frac{Q_{j+1}-Q_{j-1}}{2\Delta s} \\ Q_j^2 S_j^{-\frac{8}{3}} - \psi_j - \delta\frac{N_{j+1}-N_{j-1}}{2\Delta s} \end{bmatrix}.
$$

2-91

At the boundaries, the coefficients *a*, *b*, *c* and *v* must be altered to obey the boundary conditions on the effective pressure *N* (eqns. 2-62 and 2-64). The initial guess at the *N* distribution was chosen to obey the boundary conditions (using eqn. 2-80) and the

effective pressure correction terms at $j=1$ and $j=n$ are fixed at zero so the effective pressure at the boundaries never gets updated, i.e. at the boundaries eqn. 2-89 is replaced by $dN_1 = 0$ and $dN_n = 0$. The equivalent replacement for eqn. 2-88 is found by applying eqn. 2-86 at the top ($j=1$) and bottom ($j=n$) of the domain, which yields, respectively

$$\frac{Q_2 + dQ_2 - Q_1 - dQ_1}{\Delta s} = \epsilon_R(r-1)\frac{Q_1^3 + 3Q_1^2 dQ_1}{S_1^{\frac{8}{3}}} + \epsilon_R S_1\left(N_1^{\ 3} + 3N_1^2 dN_1\right) + M_1$$

<div align="right">2-92</div>

$$\frac{Q_n + dQ_{n-1} - Q_n - dQ_{n-1}}{\Delta s} = \epsilon_R(r-1)\frac{Q_n^3 + 3Q_n^2 dQ_n}{S_n^{\frac{8}{3}}} + \epsilon_R S_n\left(N_n^{\ 3} + 3N_n^2 dN_n\right) + M_n.$$

<div align="right">2-93</div>

This is rearranged and combined with $dN_1 = 0$ and $dN_n = 0$ into matrix equations as before:

$$\begin{bmatrix} -\dfrac{1}{\Delta s} - 3\epsilon_R(r-1)Q_1^2 S_1^{-\frac{8}{3}} & -3\epsilon_R S_1 N_1^2 & \dfrac{1}{\Delta s} & 0 \\ 0 & 1 & 0 & 0 \end{bmatrix}\begin{bmatrix} dQ_1 \\ dN_1 \\ dQ_2 \\ dN_2 \end{bmatrix}$$
$$= \begin{bmatrix} M_1 + \epsilon_R(r-1)Q_1^3 S_1^{-\frac{8}{3}} + \epsilon_R S_1 N_1^3 - \delta\dfrac{Q_2 - Q_1}{\Delta s} \\ 0 \end{bmatrix}$$

<div align="right">2-94</div>

and

$$\begin{bmatrix} -\dfrac{1}{\Delta s} & 0 & \dfrac{1}{\Delta s} - 3\epsilon_R(r-1)Q_n^2 S_n^{-\frac{8}{3}} & -3\epsilon_R S_n N_n^2 \\ 0 & 0 & 0 & 1 \end{bmatrix}\begin{bmatrix} dQ_{n-1} \\ dN_{n-1} \\ dQ_n \\ dN_n \end{bmatrix}$$
$$= \begin{bmatrix} M_n + \epsilon_R(r-1)Q_n^3 S_n^{-\frac{8}{3}} + \epsilon_R S_n N_n^3 - \delta\dfrac{Q_n - Q_{n-1}}{\Delta s} \\ 0 \end{bmatrix}.$$

<div align="right">2-95</div>

These two expressions define the values of the coefficients of the matrix Ξ at the top and bottom of the domain, b_1, c_1, a_n, b_n, v_1 and v_n:

$$b_1 = \begin{bmatrix} -\dfrac{1}{\Delta s} - 3\epsilon_R(r-1)Q_1^2 S_1^{-\frac{8}{3}} & -3\epsilon_R S_1 N_1^2 \\ 0 & 1 \end{bmatrix}, \quad c_1 = \begin{bmatrix} \dfrac{1}{\Delta s} & 0 \\ 0 & 0 \end{bmatrix}, \quad a_n = \begin{bmatrix} -\dfrac{1}{\Delta s} & 0 \\ 0 & 0 \end{bmatrix}$$

$$b_n = \begin{bmatrix} \dfrac{1}{\Delta s} - 3\epsilon_R(r-1)Q_n^2 S_n^{-\frac{8}{3}} & -3\epsilon_R S_n N_n^2 \\ 0 & 1 \end{bmatrix},$$

$$v_1 = \begin{bmatrix} M_1 + \epsilon_R(r-1)Q_1^3 S_1^{-\frac{8}{3}} + \epsilon_R N_1^3 - \delta\frac{Q_2 - Q_1}{\Delta s} \\ 0 \end{bmatrix},$$

$$v_n = \begin{bmatrix} M_n + \epsilon_R(r-1)Q_n^3 S_n^{-\frac{8}{3}} + \epsilon_R S_n N_n^3 - \delta\frac{Q_n - Q_{n-1}}{\Delta s} \\ 0 \end{bmatrix}.$$

2-96

Equation 2-90, with terms defined by eqns. 2-91, 2-93 and 2-96, defines a linear tri-diagonal block matrix equation of the form $\Xi.x = v$. This block matrix equation can be solved for the block vector x, which contains the correction terms dQ and dN (see eqn. 2-91), using a modified version of the Thomas Algorithm.

First the Thomas Algorithm modifies the coefficients (eqns. 2-93 and 2-96) in a 'forward sweep' from $j=1$ to n:

$$c_j = b_j^{-1}c_j \quad \text{and} \quad v_j = b_j^{-1}v_j, \qquad j = 1$$

$$\begin{cases} B = b_j - c_{j-1}a_j \\ c_j = B^{-1}v_j \\ v_j = B^{-1}(v_j - v_{j-1}a_j) \end{cases}, \qquad j = 2, \dots, n.$$

2-97

Then the algorithm calculates the solution by back substitution from $j=n$ to 1:

$$x_j = v_j, \qquad j = n$$

$$x_j = v_j - c_j x_{j+1}, \qquad j = n - 1, \dots, 1.$$

2-98

Discharge and effective pressure profiles at the $k+1^{\text{th}}$ iteration, $^{k+1}Q^i$ and $^{k+1}N^i$, are then calculated by adding the correction terms to $^kQ^i$ and $^kN^i$ (eqn. 2-84). The whole process iterates until $^kQ^i$ and $^kN^i$ converge on a solution. This is detected numerically when no correction term exceeds a small tolerance $Y_{\text{Ne}} = 10^{-9}$:

$$\max\left(^k dQ^i, {}^k dN^i\right) < Y_{\text{Ne}}.$$

2-99

The result is discharge and effective pressure profiles that obey the mass and momentum conservation equations (eqns. 2-77 and 2-78) and the effective pressure boundary conditions (eqns. 2-62 and 2-64).

Boundary layer method

By making further simplifications, model equations can be solved using the computationally efficient boundary layer method (Evatt, 2006; Fowler, 1999, 2009). Assuming the source term M is uniform in space and that the parameter ϵ_R is small

enough that terms containing it in the mass conservation equation (eqn. 2-60) are negligible compared to M simplifies this equation to

$$\frac{\partial Q(s,t)}{\partial s} = M(t).$$

2-100

I will show in Chapter 3 that this is appropriate for reasonable values of model scales and parameters. Also, by replacing the effective pressure boundary condition at the terminus (eqn. 2-64) with a Neumann boundary condition,

$$\frac{\partial N(1,t)}{\partial s} = 0,$$

2-101

the complications of solving the full boundary value problem with either of the two methods I have described above can be avoided. By using this boundary condition I assume the primary mechanisms that control flood dynamics operate beneath the ice dam. The details of the channel hydraulics further down the channel are assumed to play only a secondary role.

Substituting eqn. 2-101 into eqn. 2-61 and rearranging yields an expression for the discharge at the terminus, $Q(1,t)$, in terms of the channel area, S, and the hydraulic gradient, ψ, at the terminus:

$$Q(1,t) = \sqrt{S(1,t)^{\frac{8}{3}} \psi(1)}.$$

2-102

Integration of eqn. 2-100 from some position along the channel s to the terminus, $s = 1$, yields

$$\int_{Q(s,t)}^{Q(1,t)} dQ = M(t) \int_s^1 ds,$$

$$Q(1,t) - Q(s,t) = M(t)[1 - s].$$

2-103

Combining eqns. 2-102 and 2-103 results in an expression for $Q(s,t)$ in terms of $S(1,t)$, $\psi(1)$, s and $M(t)$:

$$Q(s,t) = \sqrt{S(1,t)^{\frac{8}{3}} \psi(1) - M(t)[1 - s]}.$$

2-104

At each grid point I calculate this discharge profile using the following expression:

$$Q_j^i = \sqrt{S_n^{i\frac{8}{3}} \psi_n - M^i[1 - s_j]}.$$

2-105

Finally, starting from the known lake effective pressure N_L, I calculate the effective pressure profile by numerically integrating eqn. 2-61 by iterating the following expression from $j = 1$ to n:

$$N_{j+1}^i = N_j^i + \frac{\Delta s}{\delta} \left(\frac{Q_j^i |Q_j^i|}{S_j^{i\frac{8}{3}}} - \psi_j \right).$$

2-106

Summary

The numerical methods described above and their key characteristics are summarised in Table 2-1.

Table 2-1. Summary of my numerical methods.

Method	Relative computation efficiency	Equations solved by this method	Can $\partial Q/\partial s$ = f(N,S,Q)?	Can Q be negative?	Boundary condition at terminus
Euler	-	Channel evolution	-	Y	-
Relaxation	Low	Mass and momentum conservation	Y	Y	$N(1.t) = $ const.
Newton's	Moderate	Mass and momentum conservation	Y	N	$N(1.t) = $ const.
Boundary Layer	High	Mass and momentum conservation	N	Y	$\frac{\partial N(1.t)}{\partial s} = $ const.

The relaxation method is the only one of the three methods used to solve the mass and momentum conservation equations that can solve them in full as they appear in Box 2-1. However, it is the most computationally demanding and so in situations where the channel discharge remains positive everywhere the more efficient Newton's method can be used. Furthermore, when the focus of a numerical investigation is on a boundary layer near the lake and $\partial Q/\partial s$ is assumed to be uniform, the boundary layer method provides an even more computationally efficient alternative.

2.3   Cavities

Theory suggests that subglacial channels are spatially-localised features (section 2.2.1; Röthlisberger, 1972). But observations and theory suggest that water can also flow at the ice-bed interface through spatially-distributed hydrological systems (e.g. Kamb, 1987; Fountain and Walder, 1998; Lliboutry, 1958; Walder, 1986; Walder and Hallet, 1979). Hypothesised distributed drainage systems include: thin water films between ice and bedrock or between ice and till (e.g. Walder, 1982), water flow through porous till (Flowers and Clarke, 2002a), subglacial ground-water flow (Boulton et al, 2007a,b), systems of anastomosing canals incised in till (Walder and Fowler, 1994), macro-porous water sheets supported by clasts (Creyts and Schoof, 2009) and linked systems of cavities (e.g. Kamb, 1987; Walder, 1986; Fountain and Walder, 1998). The last of these – the linked-cavity system – is the distributed system I consider here. It is the most widely studied, both observationally and theoretically, and because cavities are maintained by ice flow they provide a useful link between basal hydrology and ice dynamics. This link also means that this section's summary of the theories of subglacial cavitation and linked-cavity drainage that underlie Chapter 5's modelling must be preceded by an introduction to basal sliding. I start with Weertman's (1957) work that introduced two mechanisms: enhanced creep and regelation.

2.3.1 Enhanced creep and regelation

In Weertman's theory of basal sliding the ice is always in contact with a rough bedrock surface and a basal shear stress τ_b drives sliding with a velocity u_b. The roughness of this bedrock surface is characterised by the ratio between the typical height and typical spacing of bedrock bumps, R_a. Sliding occurs through two mechanisms: enhanced creep and regelation.

Both mechanisms are due to the comparatively high normal stress at the ice-rock interface on the upglacier side of the bedrock bumps. This provides the upglacier force which resists glacier flow and causes enhanced creep flow of ice around the bumps. The other mechanism – regelation – is due to the pressure-dependence of the melting temperature of ice. The higher the pressure the lower the melting temperature. The ice is assumed to be at the pressure-melting point everywhere. So on the upglacier side of each bump – where the pressure is higher – the ice temperature is lower than on a bump's downglacier side – where the pressure is lower. Hence, there is an along-glacier temperature gradient. This induces heat flow through the bedrock bump and the surrounding ice in an upglacier direction. Water formed from melting of ice at the upglacier side of the bump flows in a thin film between the ice and the bed to the downglacier side of the bump where it refreezes due to the higher melting point there.

Kamb and LaChapelle (1964) found observational evidence for these two processes at Blue Glacier, Washington, USA.

Theoretically, regulation operates effectively for small bumps and enhanced creep is most effective for large bumps, suggesting that bumps of intermediate size will control basal motion. Using this argument Weertman (1957) derived the following expression relating u_b to τ_b and R_a:

$$u_b = c_w \left(\frac{\tau_b^{\frac{1}{2}}}{R_a} \right)^{n+1},$$

<div align="right">**2-107**</div>

where c_w is a constant and n is an ice rheology constant (≈ 3; Glen, 1955).

2.3.2 Sliding with cavitation

Many revisions to Weertman's (1957) theory were made (e.g. Lliboutry, 1958; Lliboutry, 1964; Lliboutry 1968; Weertman, 1962; Weertman, 1967). These include Lliboutry's (1958) suggestion of subglacial cavitation. The idea is, as the ice flows over an uneven bedrock surface, the normal pressure of the ice acting on the lee-side of bedrock bumps is reduced. If this is sufficiently low the ice separates from the rock and cavities form. Cavity formation reduces basal friction and speeds-up sliding. Crucially, because cavities are likely to be water-filled and hydraulically connected to one another, changes in the pressure of this water p_w may change the size of cavities and the speed at which the ice slides over the bedrock surface.

For ice sliding over a glacier bed that undulates sinusoidally with a wavelength λ and an amplitude a_b, a balance of the forces acting at the bed shows that cavities form if the basal effective pressure, N_C (= p_i - p_w, where p_i is the ice overburden pressure and p_w is the water pressure), is less than a critical value called the separation effective pressure, N_{Sep}:

$$N_{Sep} = \frac{\tau_b}{\pi R_a}$$

<div align="right">**2-108**</div>

where the ratio R_a from the previous section is more precisely defined as $R_a = a_b/\lambda$ (e.g. Bindschadler, 1983; Cuffey and Paterson, 2010). Cavities influence u_b by reducing the ice-rock contact area. Bindschadler (1983) used the theory behind eqn. 2-108 to introduce the bed separation index, $I_b = \tau_b/N_C$, as a measure of the "relative amount of bed separation occurring" across the glacier bed. Larger I_b is associated with higher τ_b

and/or lower N_C and faster sliding. Bindschadler (1983) multiplied eqn. 2-107 sliding law by the bed separation index to include this effect in Weertman's (1957) theory:

$$u_b = c_s \frac{\tau_b^{p_b}}{N_C^q},$$

2-109

where p_b and q are positive and the constant c_s is inversely related to R_a. With p_b = 2.95, c_s = 84 m yr^{-1} bar$^{1-p_b}$ and q = 1, Bindschadler (1983) found that this sliding law matched observations from Variegated Glacier, Alaska, more closely than Weertman's original theory eqn. 2-107. Budd et al. (1979) tested a sliding law of this form against the results from an experiment which involved dragging ice over surfaces of different roughnesses. They found, for a wide range of sliding velocities, q = 1 and $1 \leq p_b \leq 3$ provided the best match between eqn. 2-109 and their observations.

Iken and Truffer (1997) and Anderson et al. (2004) built on the separation effective pressure concept and the latter authors suggested the following sliding law:

$$u_b = c_s \tau_b \left[\frac{1}{N_C^q} - \frac{1}{N_{Sep}^q} \right], \qquad N_C < N_{Sep},$$

$$u_b = 0, \qquad N_C > N_{Sep}.$$

2-110

Iken (1981) applied a force balance argument to an idealised, 'tilted-staircase' bed to suggest a second critical effective pressure, N_u:

$$N_u = \frac{\tau_b}{2\pi R_a}.$$

2-111

When $N_C \leq N_u$, ice moves up the upglacier sides of bedrock bumps, basal friction ceases to increase with u_b, and sliding becomes unstable. Truffer and Iken (1998) found a similar result for a sinusoidally undulating bed and Schoof (2005), building on these ideas and other theoretical work (Fowler, 1986; Fowler, 1987a), solved a linear ice rheology model analytically with a generalised bed topography and proposed a generalised coulomb-friction sliding law. Finite-element modelling using non-linear ice rheology by Gagliardini et al. (2007) showed that Schoof's (2005) sliding law can be generalised to include more realistic ice rheology.

From the theories discussed here, one is left with the following picture of basal sliding over rough bedrock: (i) when effective pressure is high, no cavities form and sliding occurs through Weertman's (1957) mechanisms of regelation and enhanced creep (eqn. 2-107); (ii) as effective pressure is reduced below a critical value called the separation effective pressure, cavities form, increasing the velocity of basal sliding (eqn. 2-109 or

eqn. 2-110); and (iii) as effective pressure is reduced further, below a second critical value, ice begins to move up the upglacier sides of bedrock bumps and sliding becomes unstable as friction does not increase with sliding velocity.

2.3.3 Linked-cavity drainage

In addition to influencing glacier sliding, cavities are thought to form part of the hydrological system (Kamb, 1987; Walder, 1986). Theory suggests these linked-cavity drainage systems behave fundamentally differently to channelised drainage systems. Röthlisberger (1972) found that, in a steady-state channel, water pressure gradient, $\partial p_w/\partial s$, and discharge, Q, are negatively related (section 2.2.1). Walder (1984) developed a model of steady state cavity drainage that suggests in linked-cavity systems these quantities are positively related.

Walder (1986) balanced cavity enlargement and closure to derive the following expression for the steady-state cross-sectional area of a cavity, S_C:

$$\frac{4}{\pi} K_0 S_C \left[\frac{N_C}{n}\right]^n = R u_b + (1 - \gamma) \frac{Q_C}{Lk\rho_i} G.$$

2-112

The cavities close due to the inward creep of ice, represented by the left-hand side of eqn. 2-112. They open due to basal sliding over bedrock bumps of typical height R and melting of ice caused by heat dissipated in water that flows through the system. These processes are represented by the first and second term on the right of eqn. 2-112. In this expression Q_C is the water discharge, N_C is the effective pressure in the cavities, G is the total hydraulic potential and γ and k are constants. Walder (1986), following Nye (1976), used Manning's equation (eqn. 2-4) to relate S_C to Q_C:

$$Q_C = \left(\frac{\pi R}{4k}\right)^{\frac{2}{3}} (\rho_w g)^{-\frac{1}{2}} \frac{1}{n'} S_C G^{\frac{1}{2}}.$$

2-113

Eliminating S_C between these two equations and solving for Q_C yields

$$Q_C = \frac{R u_b G^{\frac{1}{2}}}{\frac{4}{\pi c_m} K_0 \left[\frac{N_C}{n}\right]^n - (1 - \gamma) \frac{Q_C G^{\frac{3}{2}}}{Lk\rho_i}}.$$

2-114

Walder (1986) showed that the term representing melt in eqn. 2-114 (second term in the denominator) is negligible. On neglecting the melt term in eqn. 2-114, the relationship between Q_C, u_b, G and N_C has the form

$$Q_{\mathrm{C}} \propto \frac{u_{\mathrm{b}} G^{\frac{1}{2}}}{N_{\mathrm{C}}{}^{n}}.$$

2-115

As *G* is a positive function of the water pressure gradient $\partial p_{\mathrm{w}}/\partial s$, this equation implies that the cavity discharge increases with $\partial p_{\mathrm{w}}/\partial s$. This is in contrast to the equivalent relationship in channels, where discharge decreases with $\partial p_{\mathrm{w}}/\partial s$.

This disparity between channels and cavity systems is due to the different mechanisms that maintain water flowpaths in each case. Channels are maintained by melting due to heat dissipated in the turbulent water flow. An increase in discharge leads to increased melt and a decrease in the magnitude of $\partial p_{\mathrm{w}}/\partial s$ (see section 2.2.1; eqns. 2-3 and 2-9). In contrast, cavities are predominantly maintained by ice flow over bedrock bumps – assumed to be independent of water flow. Consequently, higher water pressure gradient drives a higher discharge.

This theoretical result suggests that when two cavities drain to a common location at a glacier bed, the one with the lower discharge will have a lower pressure and will tend to capture water from the other, equalising the discharges and the pressures. Unlike a channel that is larger than its neighbouring channels, a large cavity does not have a tendency to capture water from its smaller neighbours. Hence, this theory suggests that a distributed system of hydraulically-linked cavities can be a stable configuration for a subglacial drainage system. (e.g. Fountain and Walder, 1998; Cuffey and Paterson, 2010; Benn and Evans, 2008).

In a more complete analysis, Kamb (1987) found a similar result while modelling sliding velocity using eqn. 2-109. Furthermore, invoking concepts of unstable sliding when effective pressure is low, discussed in the previous section, he suggested the transition from a low-pressure channel system to a high-pressure cavity system as an explanation for the onset of glacier surges, an idea that has been extended by many studies (e.g. Björnsson, 1998; Eisen et al., 2005; Fowler, 1987b; Fowler and Schiavi, 1998; Mayer et al., 2011).

2.4   Summary and outlook

I have presented the theories of subglacial drainage through channels and linked cavities that underlie my modelling during the next four chapters. I have described how Röthlisberger's (1972) steady-state channel model was developed into a time-dependent model by Nye (1976) to explain the shape of jökulhlaup hydrographs. I have also covered Fowler's (1999) modification to this model and in the next chapter I will demonstrate how these modifications impact on the behaviour of the model. To do this I

will be solving model equations numerically and I have described three alternative methods that I use to achieve this. Finally, I introduced the concepts of basal sliding and subglacial cavitation that underlie my investigation of the coupling between jökulhlaups and glacier motion in Chapter 5. With the mathematical background covered, I am ready to proceed with these investigations.

Chapter 3   **Environmental controls on flood cycles**

3.1   Introduction

Observations show that the size and timing of jökulhlaups vary, both between systems and between repeat floods from the same system (see the time series of lake depth in Fig. 1.3). A proper understanding of the controls on such variability is lacking and could help to mitigate jökulhlaup hazards, inform the design and operation of hydroelectric power plants and predict future change in jökulhlaup systems.

Previous authors have identified various environmental controls on the size and timing of jökulhlaups. These include glacier shape, which affects jökulhlaups through its effect on the basic hydraulic potential of the glacier (see eqn. 2-21; Fowler, 1999), and air temperature, which affects jökulhlaups through its control on the rate of water input to the lake (Ng et al., 2007; Ng and Liu, 2009). In this chapter I use the Nye-Fowler model to further investigate these two environmental controls. I also consider a third: the rate of water input to the channel along its length.

My approach throughout this chapter is to use the Nye-Fowler model to numerically simulate periodic cycles of lake filling and drainage and investigate how changing environmental controls between simulations affects the size of these flood cycles and the timing of floods. Hence, the first part of the investigation is concerned with assessing under what conditions the Nye-Fowler model can simulate repeating flood cycles.

Ng (1998) was first to show that the size of floods simulated using Nye's jökulhlaup model (see section 2.2.2), formulated with only time dependence (and no spatial dependence), increase indefinitely with time (see also Ng and Björnsson, 2003). Tackling this problem, Fowler (1999) showed that retaining a spatial dimension in Nye's (1976) model, introducing a region of negative hydraulic gradient just downglacier of the lake and supplying the channel with water along its length (see section 2.2.3) allows a water divide to form near the lake between floods. Upglacier (lake-ward) of the divide, water supplied to the channel flows into the lake and downglacier of the divide water flows to the glacier's terminus. As the lake fills between floods, this divide, or 'seal', migrates towards the lake in response to increasing lake water pressure. When it reaches the lake, the channel grows through a feedback between frictional melting of the channel walls and water discharge, and a flood initiates (Nye, 1976). Divide formation in Fowler's (1999) model stabilises the unstable growth of flood cycles found by Ng (1998). This is significant because, as discussed in Chapter 1, unstable growth of flood cycles is not observed in reality. Hence it is desirable to have a model, like Fowler's (1999), which can

simulate stably repeating cycles. Here, I further explore what controls the stability of the size of flood cycles using the spatially-dependent Nye-Fowler model. Specifically, I investigate whether a region of negative basic hydraulic gradient near the lake and an input of water to the channel along its length are necessary conditions for divide formation and whether divide formation is necessary to stabilise the growth of flood cycles.

In addition to proposing divide formation as a stabilising mechanism, Fowler (1999) showed that, in his model, when the prescribed lake water input is increased dramatically lake level can reach the 'flotation level' – the level at which the ice-dam becomes afloat on the lake water. This finding is consistent with observations of Lake Grimsvötn, Iceland made in 1996 (see Fig. 1.3). Usually this lake begins to drain when its level is ~60 m below the flotation level. But in November 1996, rapid lake water input caused by a subglacial volcanic eruption caused the lake level to reach the flotation level (e.g. Björnsson, 2002). The ensuing flood reached its peak discharge of $\sim 4 \times 10^4$ m^3 s^{-1} in around 16 hours, more rapidly than any other observed flood from Grimsvötn. Such rapid flood development cannot be explained by Nye's discharge-melt feedback (e.g. Björnsson, 2002; Jóhannesson, 2002). However, building on the Nye equations, Fowler (1999) explained how a lake can reach the flotation level when the rate of lake water input is sufficiently high. In his model, as the lake fills, the subglacial divide in the channel migrates towards the lake due to the increasing lake water pressure, but it lags behind this forcing. This lag increases with the rate of lake-level change. Hence, when the lake fills rapidly the lake level can reach the flotation level before the divide arrives at the lake.

My hypothesis here is that these ideas about the lag time of the divide's migration can be extended from Fowler's (1999) investigation of the 1996 Grimsvötn flood to explain variability in 'typical' jökulhlaups, that is, jökulhlaups that initiate before the lake level reaches the flotation level. Hence, I extend Fowler's (1999) work to investigate the physics of divide migration in detail. In particular I show that these physics can explain how environmental factors, like the shape of the glacier near the lake, the rate of water input to the lake and the rate of water input to the channel along its length, may control the size of flood cycles and play a crucial role in jökulhlaup variability.

Ng and Liu (2009) used a simple model based on flood-initiation thresholds (see Chapter 4) with a periodic temperature forcing to show how aspects of the temporal dynamics of jökulhlaups can be explained by considering the interaction between temporal variations in one environmental factor – the melt water input to the lake – and the flood initiation threshold. I extend this work by investigating the behaviour of the Nye-Fowler model when it is forced with a seasonally-varying melt water input to the lake. I show

that interactions between the timing of floods and the seasons lead to several kinds of complex behaviour in the model: mode-locking, where the repeat time of floods is locked to integer numbers of years; resonance, where small changes in the amplitude of the temporally-varying lake water input cause large changes in the peak discharge of floods; and chaos, where flood cycles never settle into a steadily-repeating pattern and are sensitive to initial conditions. My analysis of this model behaviour is guided by studies of dynamical systems.

This chapter is organised as follows. In section 3.2 I investigate the ability of the Nye-Fowler model to simulated stable flood cycles. In section 3.3 the dependences of the size of flood cycles and flood repeat time on three environmental factors – the meltwater input to the lake, the meltwater input to the channel, and the glacier's shape near the lake – are investigated and explained in terms of the physics of divide migration. In section 3.4 results of model runs with seasonally-varying meltwater inputs are presented and results are discussed in section 3.5.

3.2   Flood cycles

3.2.1 Model setup

Fig. 3.1 shows the model jökulhlaup system used throughout this chapter. A marginal lake, with hypsometry defined by $V_{Li} = 5 \times 10^8$ m^3, $h_{Li} = 100$ m and $p_L = 1$, drains through a 10 km long, semi-circular channel with hydraulic roughness $n' = 0.1$ m$^{-1/3}$ s (from eqn. 2-24 this corresponds to $f \approx 0.07$ m$^{-2/3}$ s^2). The glacier's thickness H is constant and uniform (=100 m). These values pertain to Merzbacher Lake and South Inylchek Glacier, Kyrgyzstan (Ng and Liu, 2009). The channel's evolution and the flow of water through the channel are described by eqns. 2-59–2-61:

$$\frac{\partial S}{\partial t} = \frac{|Q|^3}{S^{\frac{8}{3}}} - SN^3,$$

3-1

$$\frac{\partial Q}{\partial s} = \epsilon_R(r-1)\frac{|Q|^3}{S^{\frac{8}{3}}} + \epsilon_R SN^3 + M,$$

3-2

$$\frac{\partial N}{\partial s} = \frac{1}{\delta}\left(\frac{Q|Q|}{S^{\frac{8}{3}}} - \psi\right).$$

3-3

The lake's evolution is described by eqn. 2-63:
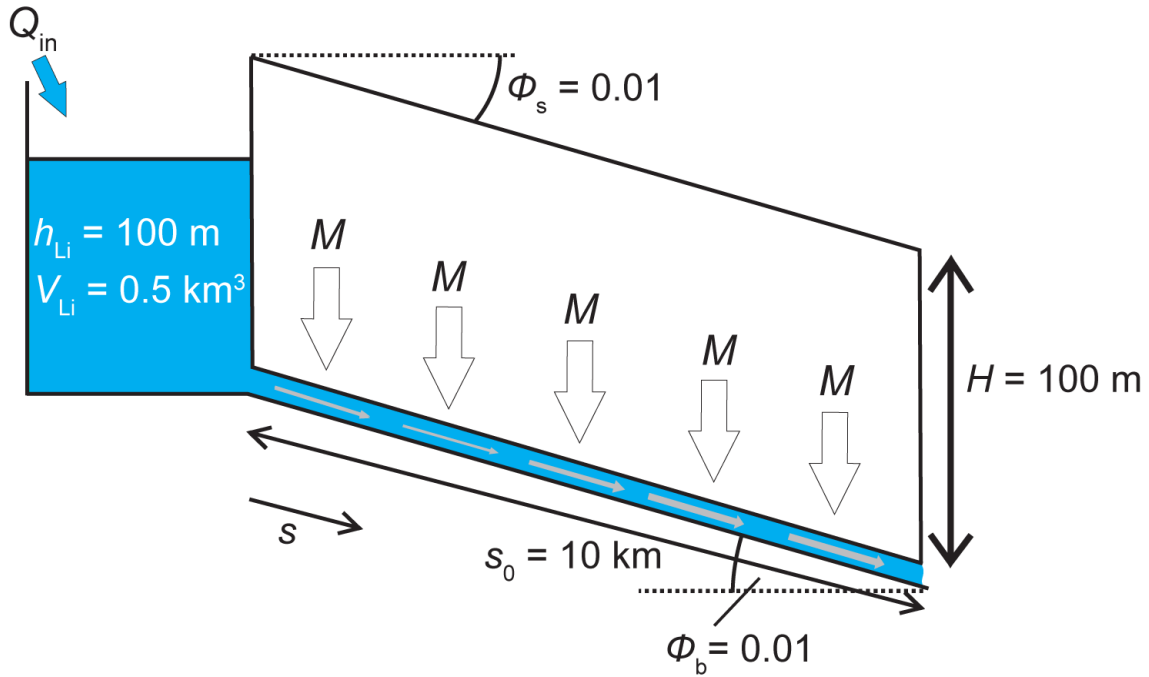
Fig. 3.1. My model jökulhlaup system.

$$\frac{dh_{\mathrm{L}}}{dt} = \frac{\lambda_{\mathrm{L}}}{h_{\mathrm{L}}^{p_{\mathrm{L}}-1}}[Q_{\mathrm{in}} - Q(0,t)]$$

3-4

and the lake level h_{L} defines the boundary condition on the channel's effective pressure at the lake outlet via eqn. 2-61:

$$N(s = 0, t) = N_{\mathrm{L}} = \beta[1 - h_{\mathrm{L}}].$$

3-5

Initially, the hydraulic gradient, ψ, is kept constant, uniform and positive (=1), however later it will be parameterised by an exponential function (eqn. 3-9) that allows it to be negative near the lake. The surface slope, ϕ_s = 0.01, supplies the basic hydraulic gradient scale, $\psi_0 = \rho_w g \phi_s \approx 100$ Pa m^{-1}, and the discharge scale is chosen as a typical peak discharge, Q_0 = 1500 m^3 s^{-1}. These scales are used with eqns. 2-65 and 2-66 and the following physical constants,

$$g = 10 \text{ m}^2 \text{ s}^{-1}, \qquad L = 3.3 \times 10^5 \text{ J kg}^{-1}, \qquad \rho_w = 1000 \text{ kg m}^{-3},$$

$$\rho_i = 900 \text{ kg m}^{-3}, \qquad K_0 = 10^{-24} \text{ Pa}^{-3} \text{ s}^{-1},$$

3-6

to calculate the remaining scales,

$$S_0 \approx 490 \text{ m}^2, \ N_0 \approx 1 \times 10^6 \text{ Pa}, t_0 \approx 1 \times 10^6 \text{ s},$$

$$m_0 \approx 0.45 \text{ kg m}^{-1} \text{ s}^{-1}, M_0 \approx 0.15 \text{ m}^2 \text{ s}^{-1}, h_{\mathrm{L}0} = 90 \text{ m},$$

and dimensionless parameters,

$$\epsilon_R \approx 0.0034, \qquad r = 0.9, \qquad \delta \sim 1,$$
$$\beta_R \approx 0.9, \qquad \lambda_L \approx 3.2 \; .$$

In agreement with previous work (Evatt et al., 2006; Fowler, 1999; 2009; Ng, 1998; Ng and Björnsson, 2003), ϵ_R is small. This shows that the contribution to channel water balance from melting of the channel walls and creep closure of the channel is small compared to Q.

For the effective pressure boundary condition at the terminus, I use $N(s = s_0, t) = 0$. An alternative boundary condition is $N(s = s_0, t) = N_a = \rho_i g H$, but the choice does not qualitatively affect my results. Initially I retain terms containing ϵ_R, in anticipation that they may be significant between floods. The relaxation method is used to solve the mass and momentum conservation equations, while Forward Euler time-stepping is used to evolve the lake level and the channel area in time (section 2.2.5). I use time steps of 0.01, a grid spacing of 0.01, an initial lake depth of 1/3 and an initial discharge at the lake of 5×10^{-4} (all non-dimensional).

3.2.2 Control simulation: unstable growth in flood-cycle size

Fig. 3.2 displays the results of a control model simulation during which the lake is filled with a constant water input Q_{in} = 10 m^3 s^{-1} and drains through a channel that receives no water input along its length, M = 0 m^2 s^{-1}, beneath a uniform slab glacier, $\psi(s) = \psi_0$. The plot displays simulated time series of lake depth (Fig. 3.2a), discharge at the lake outlet (Fig. 3.2b) and the cross-sectional area of the channel at the lake outlet (Fig. 3.2c).

Oscillatory filling and drainage of the lake is evident in all three time series. For the purposes of explaining the physical origin of the cycles, key points in the second cycle displayed in Figs. 3.2a–3.2c have been labelled A, B, C and D. The line labelled A marks the lowest lake depth reached after the first simulated flood, this depth is called the flood's lowstand. Following this lowstand the lake fills (between A and B) which causes the effective pressure at the lake outlet to decrease (according to eqn. 3-5). This decrease in effective pressure has two effects: one, it decreases the rate at which the channel closes through creep flow of the ice (according to eqn. 3-1) and two, it increases the total potential gradient ($\delta \partial N / \partial s + \psi$) by reducing the magnitude of $\partial N / \partial s$ which is negative at this stage of the flood cycle. During this lake-filling period, initially discharge decreases as the channel shrinks following the previous flood (between 1 and 1.5 years), but at ~1.5 years the increasing total potential gradient and the decreasing creep closure

of the channel (associated with increasing lake level) result in the discharge beginning to increase.

A higher discharge increases the rate at which the channel is enlarged by melt and the channel's cross-sectional area begins to increase ~1 day after the discharge begins to increase (Fig. 3.2c). A larger channel allows a higher discharge, which further increases the rate of channel enlargement by melting. This positive feedback between discharge and channel cross-sectional area is the mechanism introduced by Nye (1976) to explain the shape of jökulhlaup hydrographs. The feedback continues and at point B the discharge out of the lake equals the water input to the lake ($Q(0,t) = Q_{in}$); the lake reaches its highest depth – its highstand – and begins to drain. As the lake drains, the discharge continues to increase via Nye's feedback. However, as the lake depth decreases, the channel closure rate increases through eqns. 3-1 and 3-5. This acts to
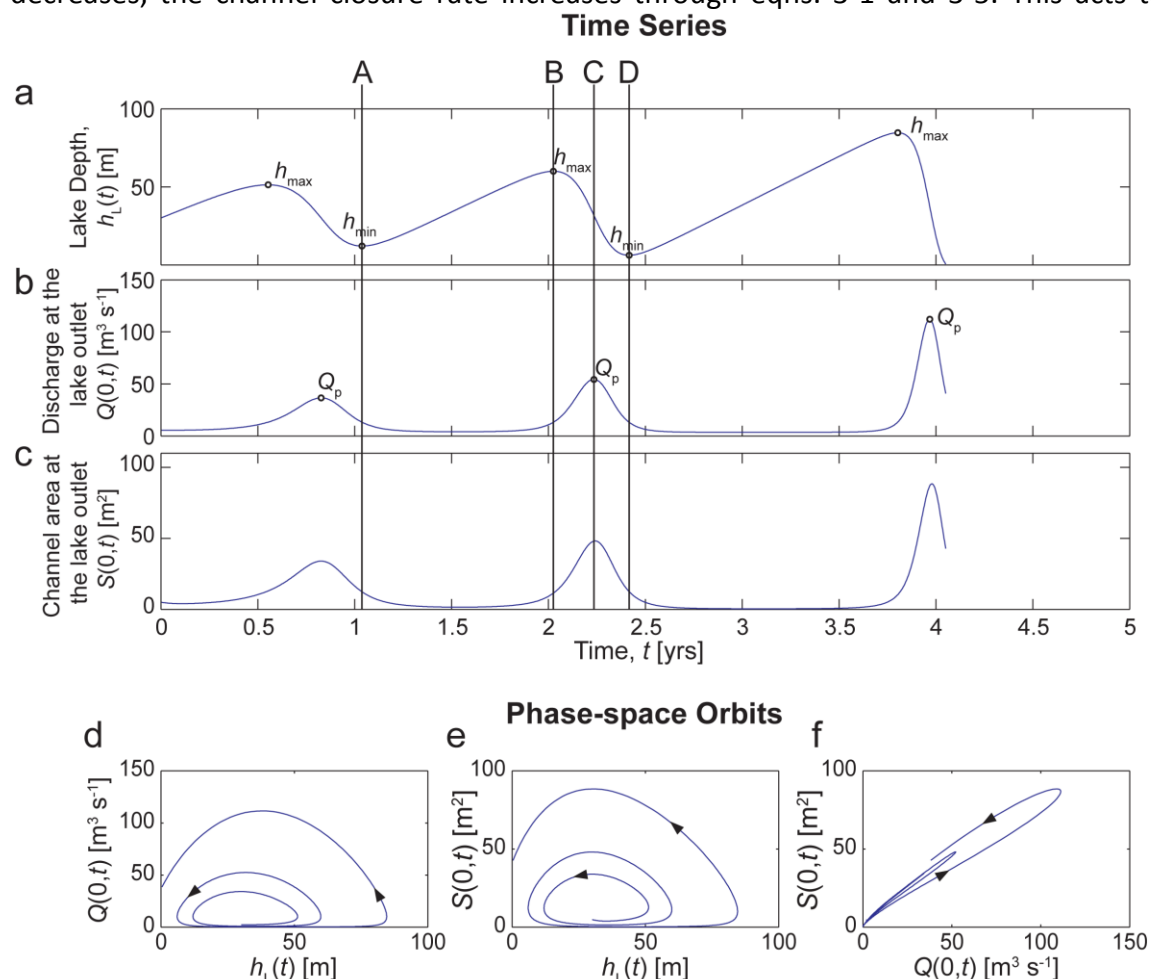
Fig. 3.2. Flood cycles simulated using the Nye-Fowler model. The lake is filled with input Q_{in} = 10 m^3 s^{-1}, and drains through a channel that receives no input of water along its length, M = 0 m^2 s^{-1}, beneath a uniform, slab glacier with a = 0. Time series of (a) lake depth, $h_L(t)$, (b) discharge in the channel at the lake outlet, $Q(s = 0,t)$, and (c) the area of the channel at the lake outlet, $S(s = 0,t)$; and orbits in the (d) $Q(s = 0,t)–h_L(t)$, (e) $S(s = 0,t)–h_L(t)$, and (f) $S(s = 0,t)–Q(s = 0,t)$ phase spaces.

suppress Nye's feedback and, at point C, the flood reaches its peak and discharge begins to decrease. Between point C and point D the discharge decreases until at D the input to the lake exceeds the outflow through the channel and the lake begins to fill. This marks the start of the next flood cycle. These cycles are also evident in the solution's oscillatory orbits in Q–h_L, S–h_L and S–Q phase-spaces, plotted in Fig. 3.2d, 3.2e and 3.2f respectively.

The highstand and peak discharge increase, and the lowstand decreases, from each flood cycle to the next until, during the third flood, the lake empties (at $t \approx 4$ years). Here the simulation terminates because the open-channel flow that would occur in reality after the lake empties cannot be simulated by the Nye model (this problem is tackled in Chapter 6). This growth in the size of flood cycles is reminiscent of that demonstrated by Ng (1998) using a reduced model formulated with time dependence only. The reason for the similarity between the full model and Ng's reduced model is the nearly spatial uniform discharge in my simulations due to $M = 0$ m^2 s^{-1}, $\epsilon_R \ll 1$ and $\psi = \psi_0$.

3.2.3 Stable flood cycles

I now demonstrate how two environmental parameters in the Nye-Fowler model can be changed to suppress the unstable growth in the size of flood cycles. The first is the basic hydraulic potential gradient ψ. The second is the supply of water to the channel along its length M.

Negative basic hydraulic gradient near the lake suppresses flood cycle growth
Following Fowler (1999), I parameterise the basic hydraulic gradient, ψ, with

$$\psi = \psi_0 \left[1 - a \exp\left(-b \frac{s}{s_0} \right) \right].$$

3-9

The parameter b is kept constant at 20, and I vary how much ψ is decreased relative to ψ_0 near the lake by increasing a from zero. When $a > 1$, ψ is negative at the lake. Negative ψ acts to drive water upglacier towards the lake, possibly discouraging the lake from draining. Hence, I refer to such a negative ψ near the lake as a topographic seal. A lake-ward dipping glacier surface could cause this and is observed in real systems (e.g. Lake Grimsvötn; Fowler, 1999).

Fig. 3.3 displays time series of lake depth, discharge at the lake outlet and the cross-sectional area of the channel at the lake outlet from a simulation that used $a = 3$. All other parameters are unchanged from the control simulation (previous section). The growth in the size of the flood cycles is suppressed by the negative basic hydraulic gradient near the lake. This prevents the lake emptying and the system approaches limit
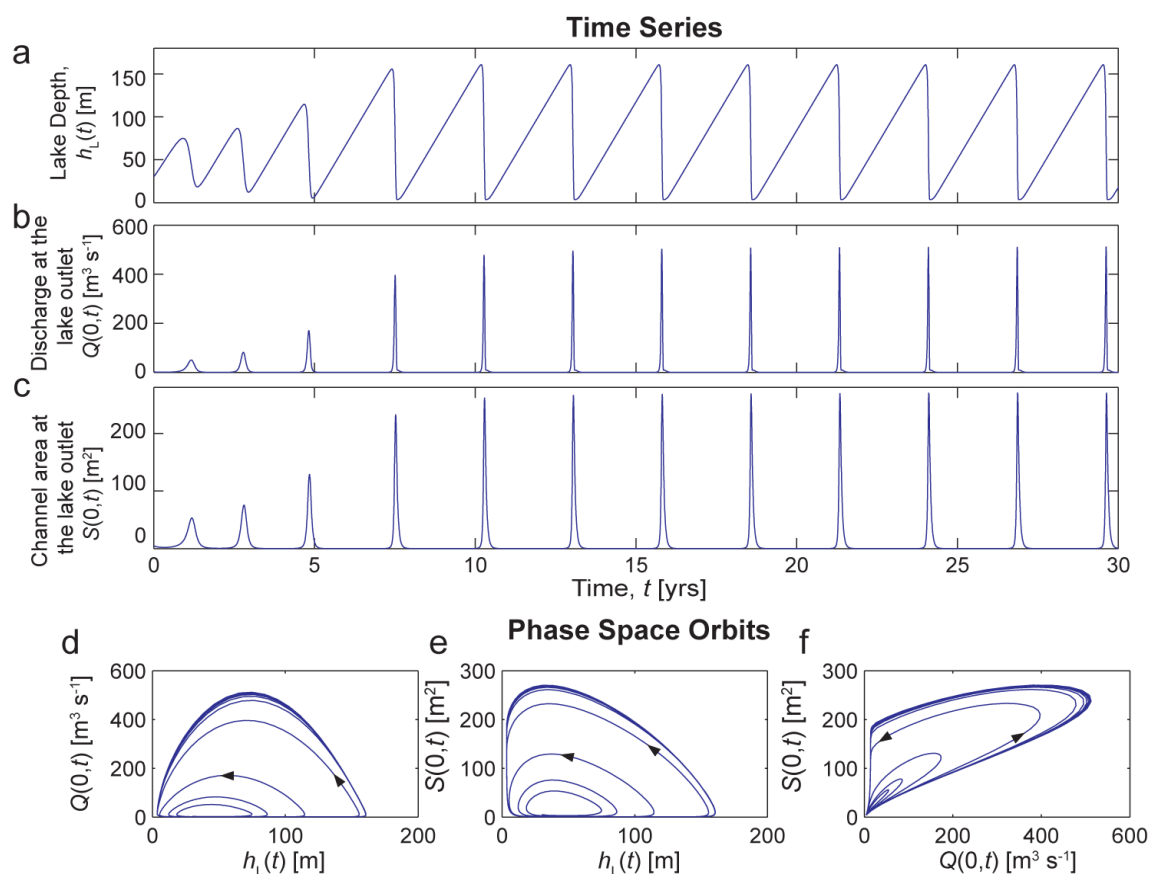
Fig. 3.3. Stable flood cycles simulated using the Nye-Fowler model. Negative basic hydraulic gradient near the lake, a = 3. Channel receives no input of water along its length, M = 0 m^2 s^{-1}. p_L = 1 and Q_{in} = 10 m^3 s^{-1}. Layout is identical to Fig. 3.2.

cycles in the phase-spaces in Figs. 3.3d–3.3f. In this simulation, lake level often exceeds the flotation depth (90 m). In reality this would lead to a flood being immediately initiated as the ice dam is lifted, but this process is not modelled here. Instead, negative effective pressure causes unrealistic channel enlargement through ice creep.

Increasing a, corresponding to an increasingly negative ψ near the lake, reduces the highstand and peak discharge of floods, and, crucially for preventing the lake emptying during simulations, increases the lowstand of floods. These trends can be seen in Fig. 3.4, which plots the long-time solution orbits in $Q(0,t)$–$h_L(0,t)$ phase space of seven simulations. Each simulation used a different value for a.

The discharge at the lake outlet is positive throughout all seven simulations, so Fowler's (1999) divide formation and migration mechanisms are not operating here. By definition, for a divide to form, the discharge needs to change spatially. In these simulations the channel is not supplied with water along its length (M = 0) and the parameter ϵ_R is small, so discharge is almost spatially uniform. Hence, a divide cannot form.
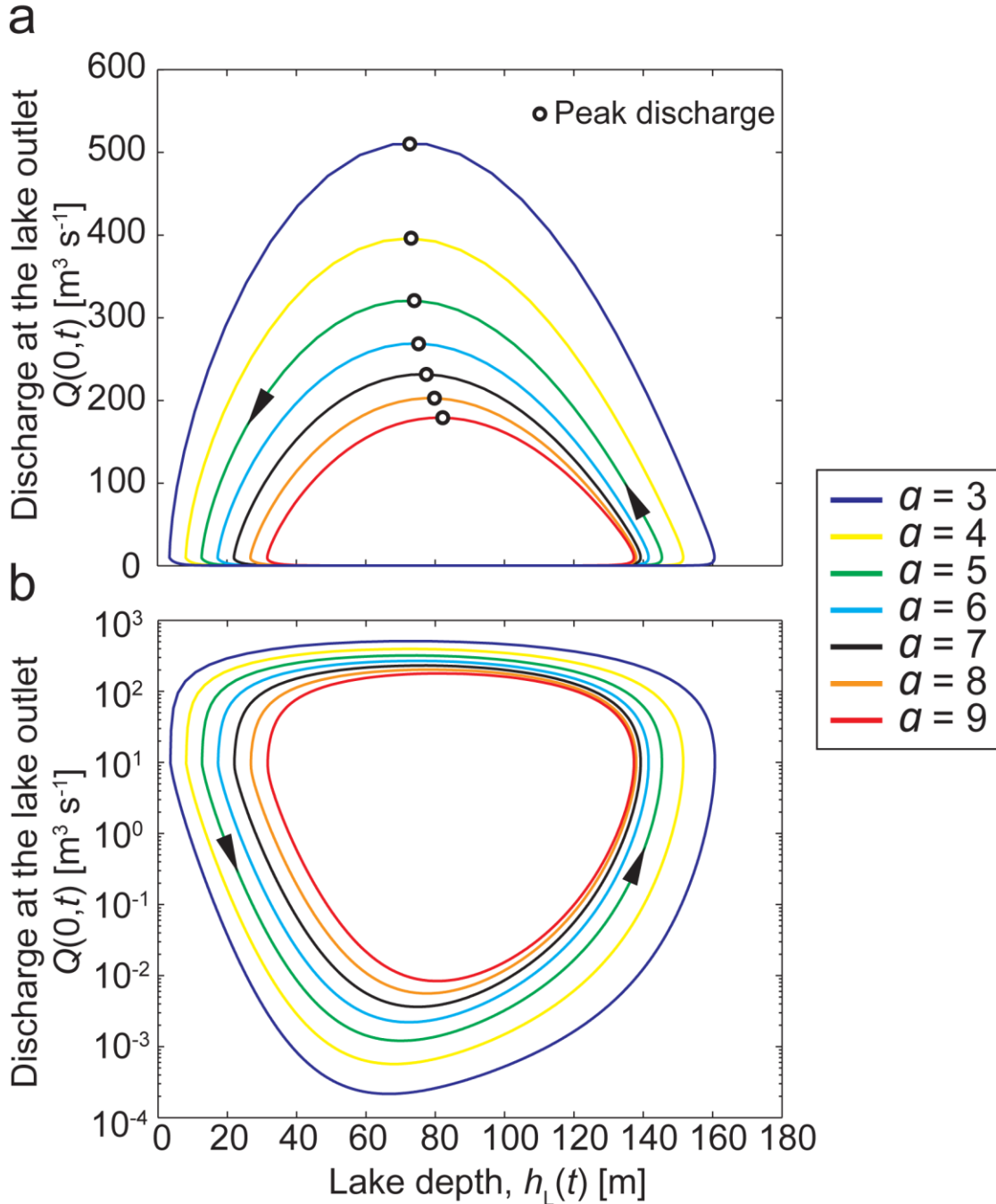
Fig. 3.4. The long-time orbits in $Q(0,t)$–$h_L(0,t)$ phase space of the Nye-Fowler model with basic hydraulic gradient parameter a = {3, 4, 5, 6, 7, 8, 9}, Q_{in} = 10 m³ s⁻¹ and M = 0 m² s⁻¹. The plots show one complete limit cycle in each case and have linear $h_L(0,t)$ axes and (a) linear and (b) logarithmic $Q(0,t)$ axes.

Physically, one expects an increase in a to decrease the water discharge through the channel because the total potential gradient ($\delta \partial N / \partial s + \psi$) near the lake approximately decreases with a. This expectation is fulfilled when the lake is draining, i.e. when $Q(s = 0,t) > Q_{in}$. In each simulated flood cycle, after the lake reaches its highstand, larger values of a result in a lower peak discharge and induce the discharge to peak when the lake has a higher depth. These two effects cause the lowstand to increase with a.

Contrary to the expectation of a decrease in discharge with increasing a is the fact that discharge through the channel during lake-filling periods (when $Q(s = 0,t) < Q_{in}$) increases with a. An examination of the numerical results, in more detail than can be shown graphically here, reveals why this occurs. It occurs because the size of the channel at the lake outlet, at the moment the lake reaches its lowstand, increases with a. This numerical observation can be approximately explained by examining the momentum balance (eqn. 3-3) in the lake outlet at the moment the lake reaches its lowstand. From eqn. 3-3 this balance is

$$G(s = 0) = \frac{Q_{in}{}^{2}}{S(s = 0)^{\frac{8}{3}}},$$

<div align="right">**3-10**</div>

where $S(s = 0)$ is the channel cross-sectional area at the lake outlet and $G(s = 0)$ is the total hydraulic potential gradient at the lake outlet,

$$G(s = 0) = \delta \left.\frac{\partial N}{\partial s}\right|_{s=0} + \psi(s = 0)$$

<div align="right">**3-11**</div>

All other things remaining equal, $G(s=0)$ decreases with a (because $\psi*(s=0) = 1 - a$). Hence, from eqn. 3-10, $S(s = 0)$ increases with a. Physically this means that, because Q_{in} is constant across all the simulations, the simulations with a lower basic hydraulic gradient to help drive downglacier water flow, need a larger channel to maintain the same discharge Q_{in}. After lowstand the lake-filling period begins. Hence simulations with a larger channel at the start of this period (i.e. those with higher a) have a higher discharge throughout this period.

Supplying the channel with water along its length suppresses flood cycle growth

Flood cycle growth can also be suppressed in simulations by supplying the channel with water along its length. I assume that this meltwater input comes from an adjacent distributed drainage system with a higher water pressure than the channel and that this input is constant and uniform. The possibility that it can vary in space and time as the two drainage systems coevolve is considered in Chapter 5. In the present chapter this input is represented by the term, M, in the mass conservation equation (eqn. 3-2). Fig. 3.5 displays results from a simulation with $a = 0$ and $M = 2.5 \times 10^{-4}$ m^2 s^{-1}. The lake level never exceeds the flotation depth or empties and the system approaches limit cycles. The same hydrographic sequence as I described with reference to Fig. 3.2 operates during this simulation with one difference beging that, in this simulation, discharge at the lake outlet becomes negative between floods – a divide forms.

Fig. 3.6 shows long-time solution orbits in $Q(0,t)$–$h_L(0,t)$ phase space of seven simulations. Each simulation used a different value for the supply of water to the channel along its length M. The results show that, between floods, water flows out of the channel into the lake, $Q(0,t) < 0$. As the channel is supplied with water along its length and ϵ_R is small, discharge in the channel increases with distance down glacier. This, coupled with the fact that $Ms_0 \approx 5$ m^3 s^{-1} is larger than the magnitude of the negative discharge at the lake outlet between floods (< 0.5 m^3 s^{-1}; Fig. 3.6b), indicates that when $Q(0,t) < 0$ there must exist a position in the channel with zero discharge. This is Fowler's (1999) water divide. If water enters the channel upglacier of the divide's position, it flows towards the lake, if water enters the channel downglacier of the divide's position, it flows towards the glacier's terminus. With $a = 0$, the basic hydraulic gradient is positive everywhere, so divide formation is caused only by low water pressure at the lake outlet.

During lake filling periods, the divide migrates in response to changing lake water pressure and the time evolution of the channel's cross-sectional area. I will explain how this migration is visible in the phase-plane plot in Fig. 3.6b. As ϵ_R is small,
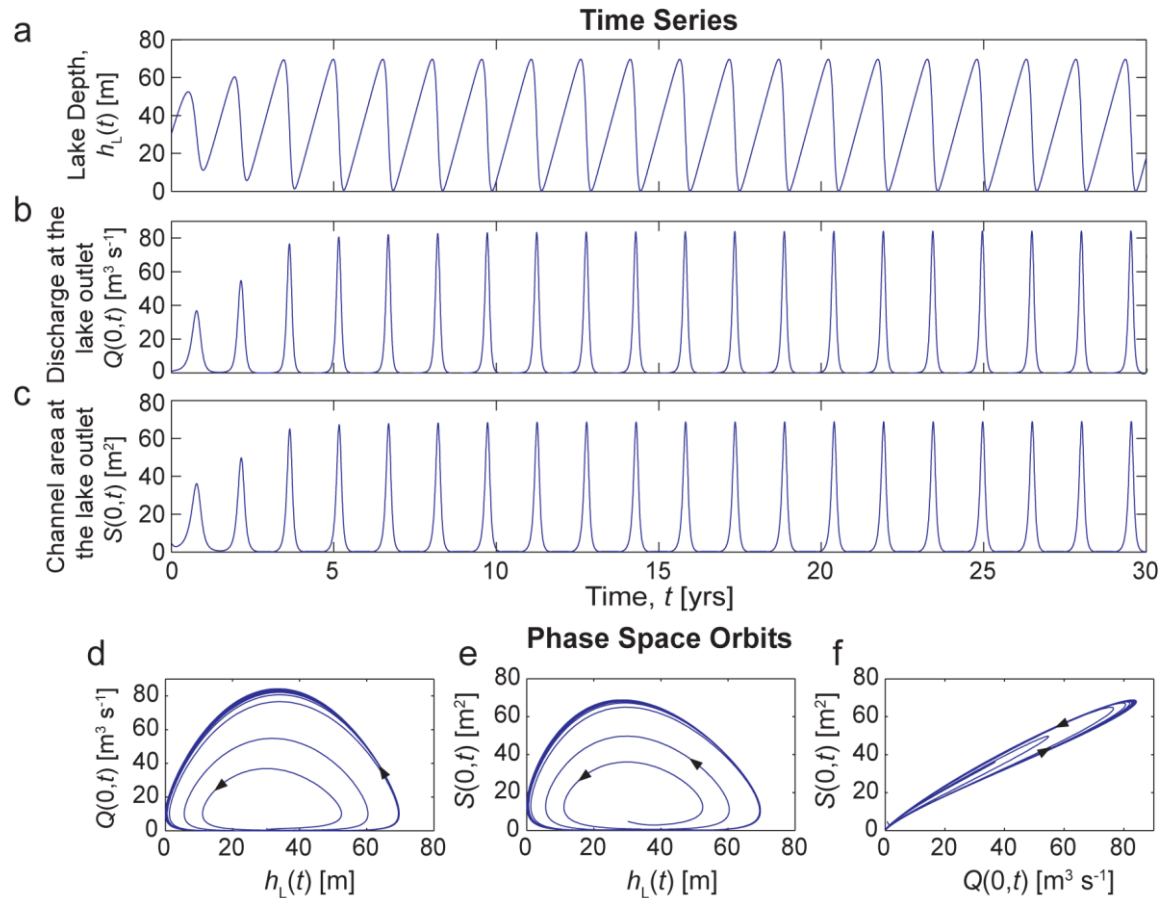
Fig. 3.5. Repeating flood cycles caused by non-zero meltwater input to the channel, $M = 2.5 \times 10^{-4}$ m^2 s^{-1}, beneath a uniform glacier, $a = 0$. $Q_{in} = 10$ m^3 s^{-1} and $p_L = 1$. The layout is identical to Figs. 3.2 and 3.3.
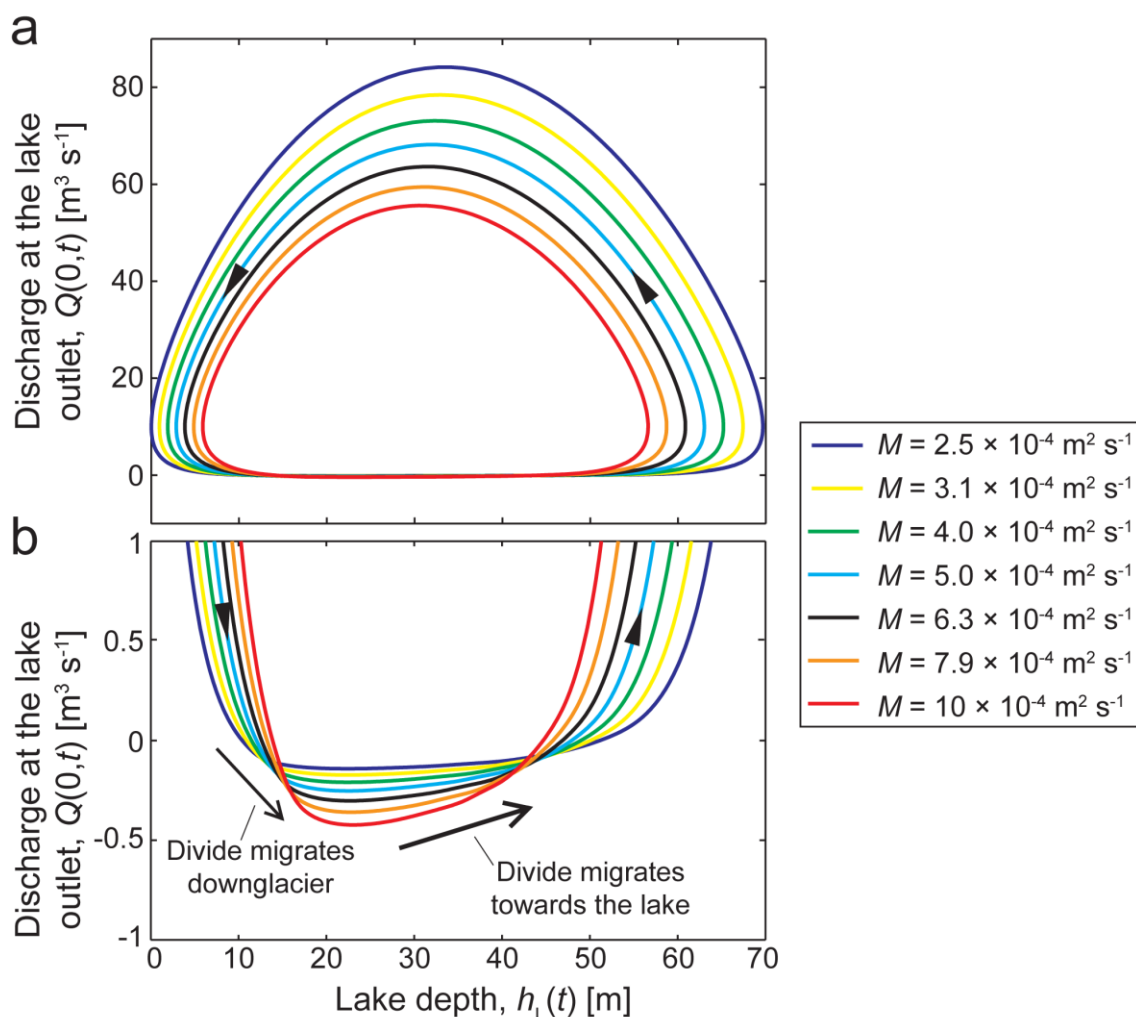
Fig. 3.6. The orbits in $Q(0,t)$–$h_L(0,t)$ phase-space of limit cycles with background water supply to the channel, M = {2.5, 3.1, 4.0, 5.0, 6.3, 7.9, 10} × 10^{-4} m^2 s^{-1}. Q_{in} = 10 m^3 s^{-1} and a = 0. (b) shows the same results as (a) but focuses on the details of the lake filling period, note the two different vertical axes.

$\partial Q/\partial s \approx M$, so when Q is negative its magnitude is approximately proportional to the distance between the lake and the divide. With this in mind, the divide's migration is visible in the phase-plane plot in Fig. 3.6b as the changing magnitude of $Q(0,t)$ (the vertical axis) while it is negative. Immediately after the divide forms (i.e. after $Q(0,t)$ becomes negative) it migrates downglacier into $s > 0$, then it turns and migrates slowly towards the lake. These migrations are labelled in Fig. 3.6b. When the divide reaches the lake, the channel can grow through Nye's melt–discharge feedback and a flood starts.

Increasing M from zero allows the water divide to form and divide formation suppresses growth in the size of flood cycles by increasing the size of the channel during lake-filling periods (Fig. 3.6b), expediting flood development and decreasing highstand. Increasing M further decreases the size of floods further (Fig. 3.6). This is

58

due to the dynamics of the divide's migration. I defer a full physical explanation of these dynamics to the next section.

Summary

In the simulations discussed in this section (whose results are displayed in Figs. 3.3–3.6), increasing either of two environmental parameters, a and M, produced superficially similar results: a decrease in the highstand and the peak discharge of floods, and an increase in the lowstand of floods. Consequently, increasing either parameter stabilises flood cycles and promotes the simulation of periodic floods. The Nye-Fowler model does not need both a topographic seal ($a > 1$) and the channel to be supplied with water along its length ($M > 0$) in order to simulate periodic stable flood cycles.

Although increasing a and increasing M have similar effects on flood cycles, in each case the physical explanation of these effects is entirely different. When no water is supplied to the channel ($M = 0$), no water divide forms and increasing a changes the size of simulated flood cycles through its effect on the total hydraulic potential gradient in the channel. In contrast, when water is supplied to the channel along its length ($M > 0$), a water divide does form and it is the dynamics of the divide's movement that explain the dependence of the size of flood cycle on the parameter M. These dynamics are discussed in detail in the next section.

3.3 Controls on the characteristics of flood cycles

Stable recurring flood cycles provide a basis for investigating physically why the characteristics of flood cycles depend on environmental factors – like the meltwater input to the lake Q_{in}, the meltwater input to the channel along its length M and the basic hydraulic gradient parameter a – without the obstacles associated with arbitrarily chosen initial conditions.

I restrict this section's investigation to cases where $M > 0$ and a subglacial water divide forms between floods. Of the two sets of simulations examined in the previous section, the second set, which used $M > 0$ and $a = 0$, yielded the more realistic flood cycles (with a highstand lower than the flotation depth). Also, in reality, channels are unlikely to be hydraulically isolated from their subglacial surroundings.

In section 3.3.1 I explore the dependence of the size of flood cycles on the environmental parameters Q_{in}, M, and a by conducting a sensitivity analysis of the model. I explain this dependence physically in section 3.3.2 by analysing the spatial

distribution of model variables along the channel during a lake-filling period when a subglacial water divide is migrating towards the lake.

3.3.1 Sensitivity analysis of the reduced Nye-Fowler Model

First, I follow Fowler (1999) in neglecting terms in the Nye-Fowler model that contain ϵ_R and using $\partial N/\partial s = 0$ as the terminus boundary condition. The resulting reduced version of the Nye-Fowler model is:

$$\frac{\partial S}{\partial t} = \frac{|Q|^3}{S^{\frac{8}{3}}} - SN^3,$$

3-12

$$\frac{\partial Q}{\partial s} = M,$$

3-13

$$\frac{\partial N}{\partial s} = \frac{1}{\delta}\left(\frac{Q|Q|}{S^{\frac{8}{3}}} - \psi\right).$$

3-14

The evolution of the lake level h_L is still described by eqn. 3-4 and the effective-pressure boundary conditions on the channel are given by

$$N(s = 0, t) = \beta[1 - h_L]$$

3-15

and

$$\left.\frac{\partial N}{\partial s}\right|_{(s=s_0)} = 0.$$

3-16

The computationally efficient boundary layer method (section 2.2.5) can be used to solve the reduced model, making an exploration of Q_{in}–M–a parameter space feasible. My preliminary numerical explorations, unreported here, show that these choices of boundary conditions at the terminus and the numerical method used do not affect the qualitative features of divide physics. These choices do however affect my results quantitatively. Hence, the results displayed in Figs. 3.3–3.6 in the previous section are not directly comparable to the results of the sensitivity analysis presented below.

Using the same time step, grid spacing, initial lake depth, initial discharge and system geometry as I used in the previous section, eqns. 3-4 and 3-12–3-16 are integrated forward in time until (i) the lake empties, (ii) the channel closes anywhere along its length, $S(s,t) = 0$, or (iii) limit cycles are reached. Limit cycles are detected and recorded when the lowstand, highstand and peak discharge of a cycle are all within 0.05 % of their respective quantities recorded during the previous two cycles. Between multiple
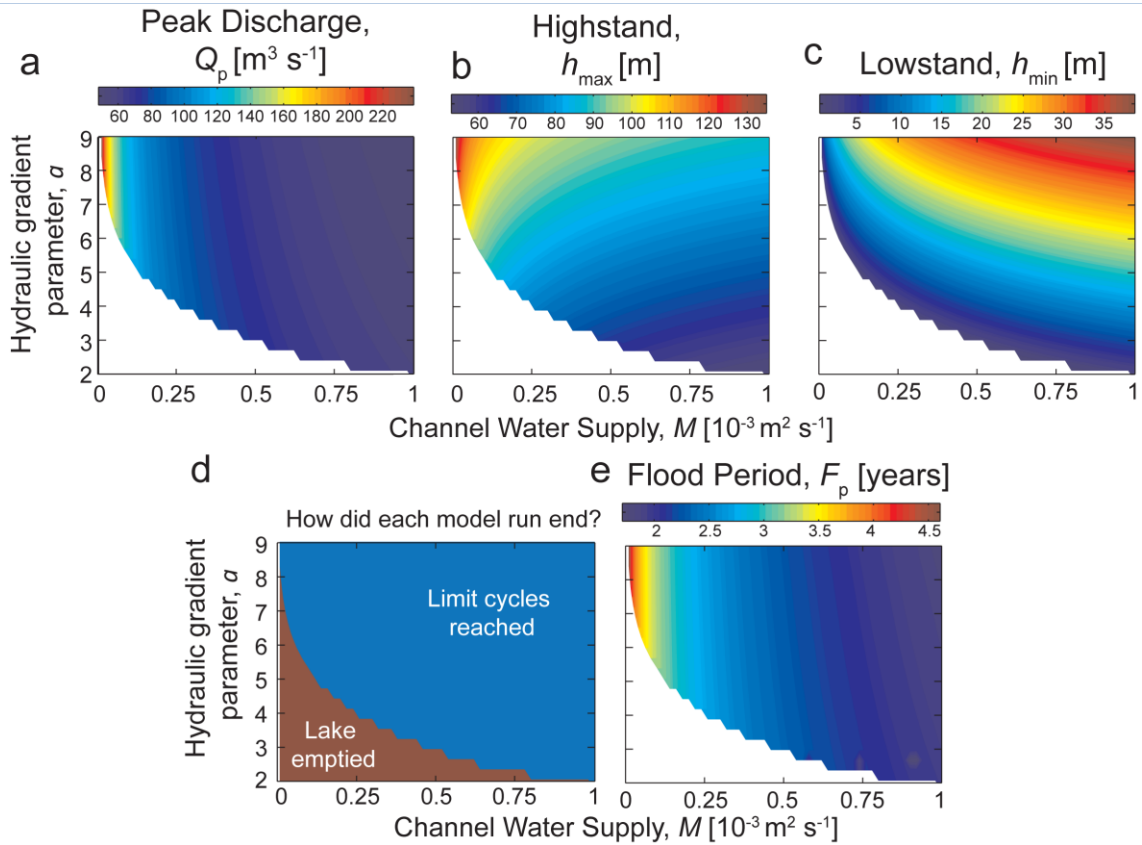
Fig. 3.7. The control of the environmental parmeters *a* and *M* on flood-cycle characteristics. Results of a sensitivty analysis of the reduced Nye-Fowler model presented as filled contour maps showing (a) the peak discharge, (b) the highstand, (c) the lowstand and (e) repeat time, of long-time flood cycles vary with the hydraulic gradient parameter *a* and the channel's meltwater input *M*. (d) indicates whether each pair of parameters lead to the lake emptying or to limit cycles. In all simulation lake input, Q_{in} = 5 m³ s⁻¹.

simulations, I vary the environmental parameters Q_{in}, M and a and at the end of each simulation that resulted in the system reaching limit cycles, the following characteristics pertaining to the size and timing of the limit cycles are recorded: their highstand, their lowstand, their peak discharge and the time interval between their peak discharges (hereafter, their repeat time).

Fig. 3.7 displays these characteristics recorded from a set of simulations during which the hydraulic gradient parameter a and the channel meltwater input M were varied over plausible ranges, $2 \le a \le 9$ and $10^{-5} \le M \le 10^{-3}$ m² s⁻¹ respectively. The results are displayed as contour maps that show how the peak discharge, Q_p, the highstand, h_{max}, the lowstand, h_{min}, and the repeat time, F_p, of limit cycles varies with a and M. The rate of water input to the lake is kept constant in all simulations, Q_{in} = 5 m³ s⁻¹. As indicated by Fig. 3.7d, limit cycles are reached during the majority of model runs and higher channel inputs and hydraulic gradient parameters favour this. In the minority of model runs the lake emptied, ending the simulation. The serration of the line separating the

two regions in parameter space in Fig. 3.7d is an artefact of the resolution of the parameter sweep.

Fig. 3.7a shows that, as expected from the results in section 3.2, peak discharge decreases with the supply of water to the channel M and the hydraulic gradient parameter a (although the dependence on the latter is weak for this choice of lake input and boundary condition). From Fig. 3.7c, the lowstand increases with M and a, as seen in the results of earlier simulations (Figs. 3.4 and 3.6). From Fig. 3.7b, the highstand decreases with M, but, unlike during earlier simulations which used $M = 0\ \mathrm{m^2\,s^{-1}}$ (Fig. 3.4), highstand increases with a. This is because in the earlier simulations, whose results are shown in Fig. 3.4 (section 3.2.3), $M = 0\ \mathrm{m^2\,s^{-1}}$ and no divide formed between floods. Now, with $M \neq 0\ \mathrm{m^2\,s^{-1}}$, a divide does form and its dynamics dominate the mechanisms discussed in section 3.2.3 which caused the highstand to decrease with a when no divide formed. The time between floods is almost independent of a and decreases with M (Fig. 3.7e).

Fig. 3.8 plots the same limit-cycle characteristics as Fig. 3.7 but shows how they vary over the lake-input–channel-input (Q_{in}–M) parameter space. The hydraulic gradient is kept constant in all simulations ($a = 5$). Lower lake input and higher channel supply favour the establishment of limit cycles (Fig. 3.8d). The green regions in Fig. 3.8d indicate the simulations during which the channel closed completely. This occurs at the divide when it moves slowly compared to the rate at which the channel closes through ice creep. By definition the discharge in the channel is zero at the divide, so the channel is always closing here. However, because the closure rate in the model is proportional to the channel's cross-sectional area (S; eqn. 3-1), the channel should theoretically never close completely. The closure detected in these numerical solutions is an artefact of the discretisation of the time domain during the numerical solution of the model.

As before (see the discussion of the results presented in Fig. 3.7), the size of flood cycles decreases with the rate of water input to the channel M. The strength of this effect decreases as the rate of water input to lake Q_{in} increases (c.f. the slope of contours in lower-right and upper-right of Figs. 3.8a, 3.8b and 3.8c). Peak discharge and highstand increase, and lowstand decreases with Q_{in}. The repeat time of flood cycles decreases with both Q_{in} and M.

In summary, increasing the rate of water input to the lake increases the size of flood cycles and causes them to repeat more often. Increasing the rate of water input to the channel also causes flood cycles to repeat more often, but decreases their size.
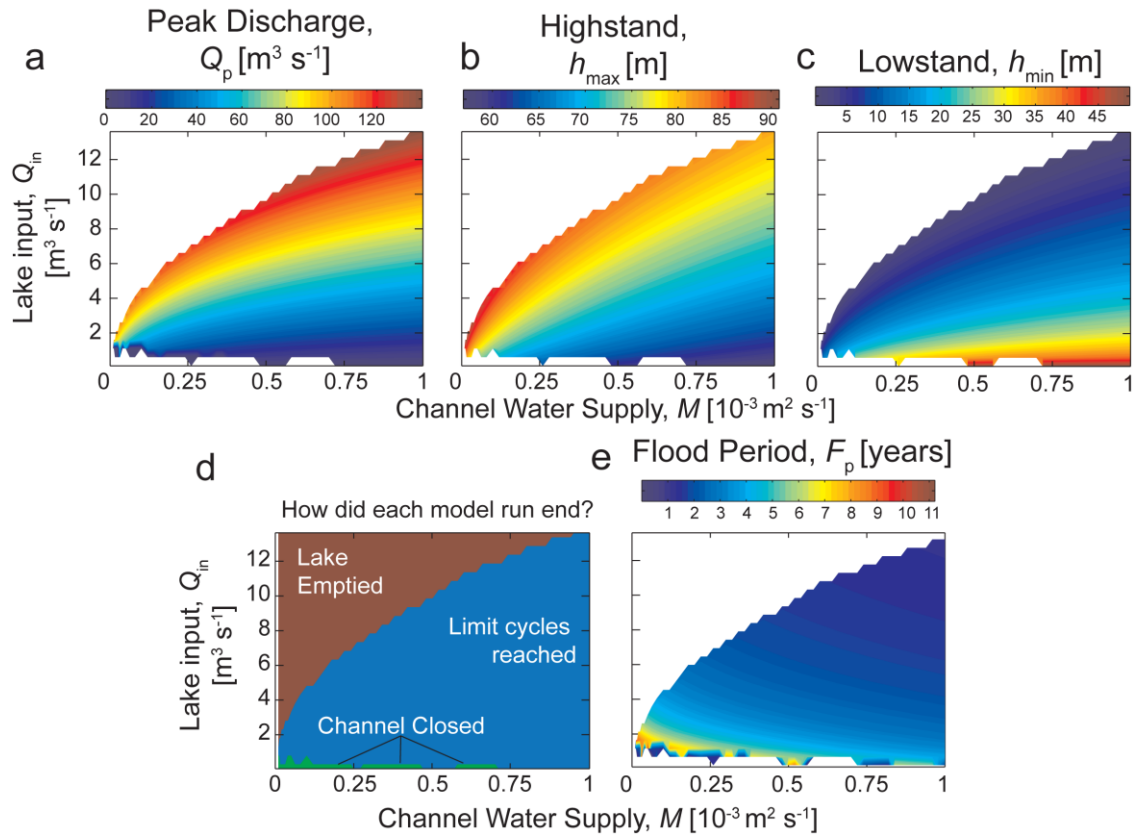
Fig. 3.8. Controls on flood cycles of lake input Q_{in} and the input to he channel M (with a = 5). The variation of (a) peak discharge, (b) highstand, (c) lowstand and (e) flood period, over Q_{in}–M parameter space, displayed as filled contour maps. (d) indicates whether each pair of parameters lead to the lake emptying, the channel closing or limit cycles.

3.3.2 Physics of the divide's migration

The way in which flood cycles change with the hydraulic gradient and the two types of meltwater inputs is due to the dynamics of the subglacial water divide that formed between floods during all the simulations analysed in section 3.3.1. I examine these dynamics next.

Fig. 3.9 shows the spatial variation in channel area (green), discharge (blue) and effective pressure (red) near the lake, extracted from one of the simulations discussed above, during a lake-filling period. The simulation used a = 5 so, from eqn. 3-9 with a = 5 and b = 20, the basic hydraulic potential gradient is negative in a region that extends from the lake to a point where ψ = 0 at 805 m from the lake. This point is indicated in Fig. 3.9a by the dashed black line. The divide is downglacier of this point and moving upglacier (as indicated by the blue arrows) in response to decreasing effective pressure at the lake (red arrow).

Fig. 3.9b shows a close-up of the divide's position. Three moving points, labelled A, B and C in Fig. 3.9, are important for divide migration: (A) the position the divide is

migrating towards due to the lake pressure forcing, this moves upglacier as the lake fills (the black arrow); (B) the divide's current position, which moves upglacier towards point A; and (C) a constriction in the channel, where the channel area is at its minimum value, created by formerly low Q at this location. All three points are migrating upglacier, with B lagging behind A and C lagging behind B. If the lake were to stop filling at this moment, points B and C would relax towards point A, which would stop moving upglacier at the instant the lake filling stopped.
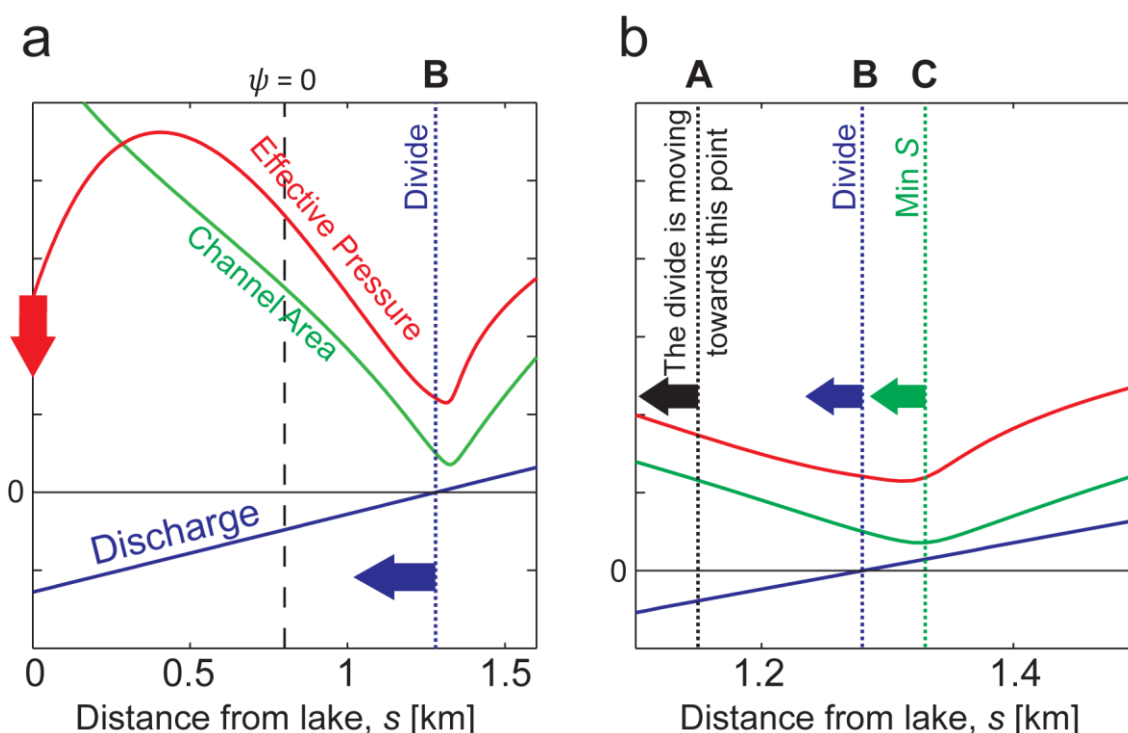
Fig. 3.9. The mechanics of divide migration. The spatial variation of the effective pressure (red), the discharge (blue) and the channel area (green) profiles during a lake-filling period, extracted from a simulation that used $a = 5$. $\psi > 0$ at the divide. Both panels show the same moment in the filling period. Note the different horizontal scales.

Under steady-state conditions, the constriction point would coincide with the divide, however, when conditions are not steady, the divide is migrating towards point A and the channel takes time to evolve in response to this migration. Hence, a steady state is never reached. Instead the constriction point C lags behind the divide position B. Divide migration is impeded by the relatively slow evolution of the channel because, as the divide moves away from the constriction point, the discharge through the constriction increases. Because it is difficult to force water through such a constriction (see the momentum balance equation; eqn. 3-3), the divide can only move so far away from the constriction point before the water pressure in the constriction is increased (i.e. the effective pressure in the constriction is decreased) sufficiently to stop any further

movement of the divide relative to the constriction. Hence, the divide's continued lake-ward migration relies on the relatively slow evolution of the channel – the point B in Fig. 3.9b lags behind point A. Due to these mechanisms the divide's arrival at the lake is delayed with respect to the lake pressure forcing and the highstand is larger than it would be if these mechanisms did not operate.

These delaying mechanisms can explain the increase in highstand with the hydraulic gradient parameter a and the lake input Q_{in}, and the decrease in highstand with the water input to the channel M, observed in the results displayed in Figs. 3.7 & 3.8. If all other variables remained equal, a uniform decrease in the basic hydraulic gradient (ψ) reduces the total hydraulic gradient ($\delta \partial N / \partial s + \psi$) and the discharge uniformly (see the momentum balance equation; eqn. 3-3). From the blue curve in Figs. 3.9a and 3.9b it can be seen that this corresponds to a downglacier shift in the divide's position. Increasing the parameter a decreases ψ near the lake, hence the divide's movement is impeded in its migration through this region when $a > 0$, and impeded more severely a is higher. This increases the delay in the divide's arrival at the lake which increases the flood cycle's highstand. Increasing the lake input also increases the delay and the highstand because point A moves upglacier more rapidly, increasing the lag between A and B.

Finally, increasing M increases the discharge through the constriction for a given lag between C and B (because $\partial Q / \partial s = M$). This increase in discharge speeds-up the evolution of the channel – specifically, by increasing the rate at which the constriction is enlarged through melt – for a given lag between C and B. This reduces the constriction's inhibiting effect on divide migration and acts to decrease the delay in the divide's arrival at the lake.

3.4   Mode-locking, resonance and chaotic dynamics of the Nye-Fowler model

The mechanisms discussed above provide a link between meltwater input to jökulhlaup systems and the size and timing of jökulhlaups. However, the discussion was based on results from simulations that used constant meltwater inputs to the lake and the subglacial channel. This is unrealistic. Real meltwater production depends on weather conditions or geothermal activity, both of which vary with time. Here I explore the behaviour of the Nye-Fowler model when the meltwater input to the lake varies seasonally.

3.4.1 Model setup: time-varying model forcings
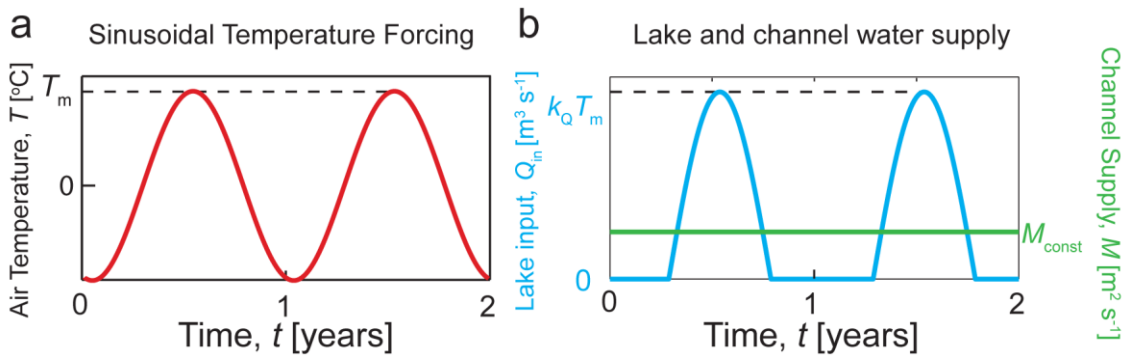
Fig. 3.10. Seasonally varying forcings. (a) Synthetic sinusiodal air temperature time series given by eqn. 3-17. (b) Lake and channel water supply given by eqn. 3-18.

I use a synthetic, sinusoidal air temperature time series (Fig. 3.10a), defined by

$$T = T_\mathrm{m}\sin[2\pi(t - 0.2877)],$$

3-17

to simulate seasonal variability in weather conditions. In this expression the time t has units of years and integer t corresponds to the beginning of each calendar year. T is the air temperature in degrees Celsius and T_m is the maximum air temperature reaching during the annual cycle. The offset of 0.2877 years ensures this maximum air temperature occurs in midsummer. I model meltwater input to the lake Q_in as directly proportional to T:

$$Q_\mathrm{in} = \max(0, k_\mathrm{Q}T),$$

3-18

where $\max(X_1, X_2)$ returns the larger of X_1 and X_2. This expression simply captures the ideas that the rate of meltwater production increases with the temperature of the air and is zero when this temperature is lower than 0 °C. For simplicity I have assumed that meltwater production and air temperature above 0 °C are linearly related and their constant of proportionality is k_Q. Also for simplicity, I keep the rate of meltwater input to the channel constant: $M = M_\mathrm{const}$.

Assuming the same glacier and lake geometries as in previous sections (but now with $a = 8$), an initial lake depth of 0.44 (or 40 m dimensionally) and an initial discharge at the lake outlet of $Q(0,0) = 5 \times 10^{-4}$, model equations are integrated for 120 model years using the boundary layer method (section 2.2.4). The value chosen for k_Q (= 2 m^3 s^{-1} K^{-1}) is close to the value of a similar melt model parameter derived empirically in the next chapter (see Table 4-2, section 4.3.3). The constant input to the channel $M_\mathrm{const} = 7 \times 10^{-4}$ m^2 s^{-1} was chosen through trial-and-error as a value that yields periodic flood

cycles for a wide range of values for T_m. The approach I take in investigating the Nye-Fowler model when it is forced with the time-varying lake water input defined by eqns. 3-17 & 3-18 is to run multiple simulations while varying the climate between them by changing the environmental parameter T_m.
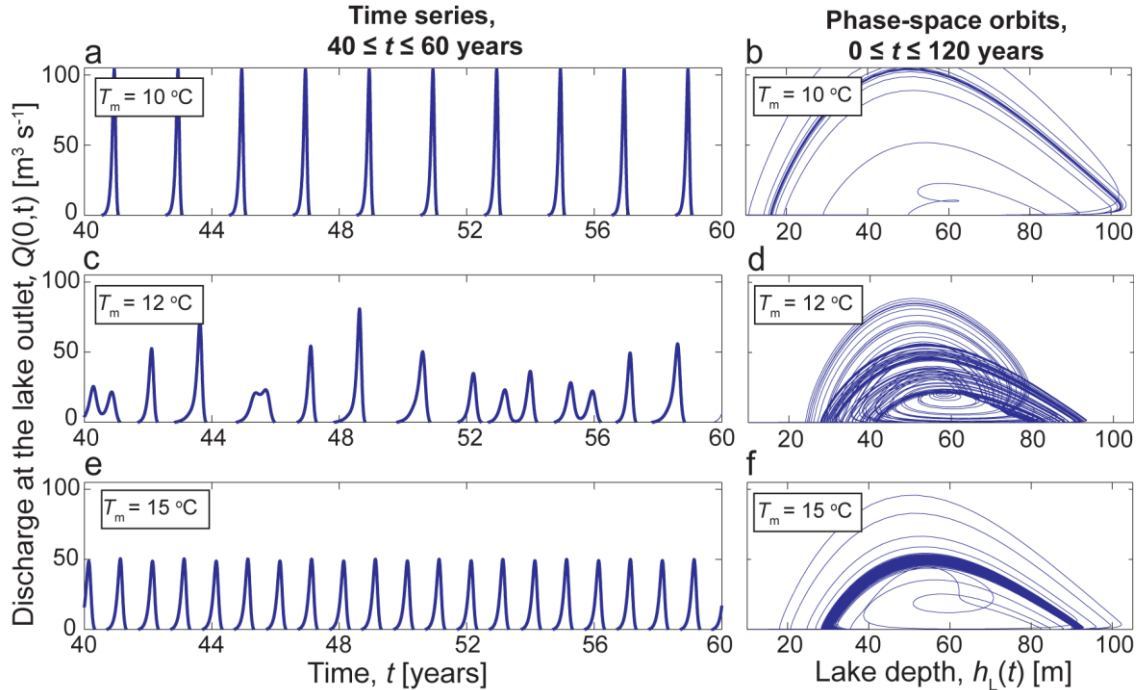
Fig. 3.11. Results of simulations using seasonally-varying air temperature to drive lake input, with (a–b) T_m = 10 ºC, (c–d) T_m = 12 ºC and (e–f) T_m = 15 ºC. (a, c & e). Time series of discharge at the lake outlet $Q(0,t)$ for 20 model years in the middle of the simulations after transients have ended and (b, d and f) solution orbit in $Q(0,t)$–$h_L(t)$ phase-space for the whole of the 120-year-long model runs.

3.4.2 Results

The discharge time series and phase-plane orbits plotted in Fig. 3.11 provide the first hints that the relationship between flood cycles and lake input are more complicated when the input to the lake varies with time than when it is constant. The figure plots results from model runs with T_m = 10 ºC, T_m = 12 ºC and T_m = 15 ºC. When T_m = 10 ºC and 15 ºC, after transients the system approaches limit cycles with repeat periods of two years and one year respectively. Contrary to expectations based on the analysis in section 3.3, the warmer simulation, with the higher mean lake input, yields flood cycles with a lower peak discharge (c.f. Figs. 3.11a & 3.11e). Another unexpected result is seen in Figs. 3.11c & 3.11d; when T_m = 12 ºC, flood cycles are simulated, but they neither grow unstably in size nor approach limit cycles. Instead the flood cycles seem random, never reaching a periodic orbit in $Q(0,t)$–$h_L(t)$ phase-space (Fig. 3.11d).

To investigate these phenomena further, I conduct multiple simulations, that each use a different value for T_m. I record the peak discharge of each simulated flood after the first ten floods and the mean time between floods during the second 60 years of each 120-year-long simulation (these choices of which floods to use in the recording of results were made to avoid transients dominating the plot of the results, they are arbitrary and do not affect my findings). Fig. 3.12 plots the results. Each point on Fig. 3.12a plots one flood's peak discharge Q_p (vertical axis) against the value of T_m used in the simulation
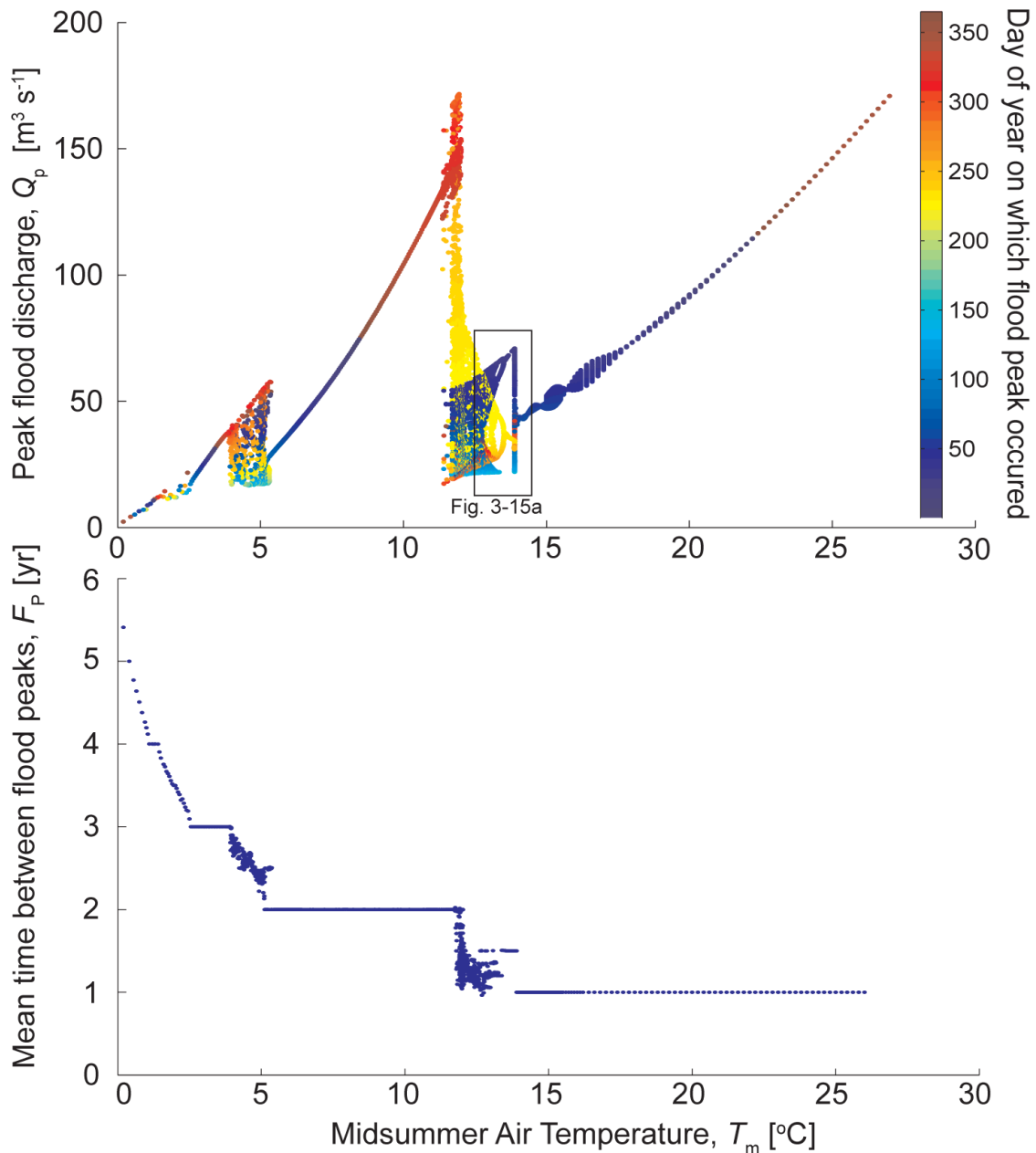
Fig. 3.12. (a) Peak discharge of all flood (bar the first 10 floods) in 120-year simulations plotted against the value of T_m used in the simulation. The black box indicates the region of the plot shown in more detail in Fig. 3.15a. (b) The mean time between flood peaks during the second half of each model run, F_p. In both panels the variable increment in T_m is manifests itself as the variable horizontal distance between points.

that produced that flood (horizontal axis). The colour of each point indicates the day of the year on which the flood peak occurred. Lines of points that are one point in vertical extend (e.g. $6 \leq T_m \leq 11$ ^{0}C and $T_m > 19$ ^{0}C) correspond to limit cycles, where all the recorded floods have the same peak discharge; slightly thicker lines of points (e.g. $14 \leq T_m \leq 17$ ^{0}C) correspond to simulations during which transients lasted longer than the first 10 floods (because I excluded the first 10 floods); and large blocks of points indicate chaotic, dense orbits, an example of which is shown in Figs. 3.11c & 3.11d. Fig. 3.12b shows the mean time between flood peaks during the second half of each simulation, F_P.

Fig. 3.12 puts into context the results displayed in Fig. 3.11. The simulations with $T_m =10$ ^{o}C and $T_m = 15$ ^{o}C lie in two regions of T_m parameter space where peak discharge, Q_p, increases with T_m (Fig. 3.12a) and the mean time between floods, F_P, is locked to integer numbers of years, 2 years and 1 year respectively (Fig. 3.12b). In both regions, as T_m and the total annual lake input decrease, instead of floods occurring less often, the mean time between floods F_P remains constant and floods shrink to compensate for the decrease in lake input. Although the colour scheme does not make it clear, in these regions the floods occur progressively later in the calendar year as T_m is decreased. This behaviour is analogous to 'mode-locking' of forced non-linear oscillators, where the frequency of an oscillator's response is locked to that of its forcing.

As noted above, decreasing T_m from 15 ^{o}C to 10 ^{o}C increases the peak discharge of floods, Q_p. These two values of T_m were chosen to demonstrate this change in Q_p in Fig. 3.11, but Fig. 3.12 shows where $T_m = 15$ ^{o}C and $T_m = 10$ ^{o}C fit into rest of my results. Between $T_m \approx 15$ ^{o}C and $T_m \approx 10$ ^{o}C, the peak discharge of floods increases roughly three-fold and there is an associated and abrupt shift in the timing of floods in the calendar year (see differently coloured points in Fig. 3.12).

This counterintuitive increase in Q_p as T_m and the total annual meltwater input to the lake decrease can by understood using another concept from studies of non-linear oscillators: resonance. When the total annual input to the lake is too large to allow it to last two years before draining ($T_m > 14$ ^{0}C), floods occur every year ($F_p = 1yr$). As T_m is reduced, floods get smaller because the total annual input to the lake gets smaller. However, when T_m is sufficiently small, the lake can last two years before draining (e.g. $T_m = 10$ ^{o}C). The total input to the lake during each flood's filling period (which is now roughly twice as long as when the mean flood repeat time $F_p = 1$ yr) is larger than it was before when T_m was slightly larger (e.g. $T_m = 15$ ^{o}C) and the peak discharge of floods is correspondingly larger. This behaviour is, in some ways, analogous to the behaviour of forced damped oscillators that respond more strongly when they are driven at their resonant frequency. A lake's "resonant climatic forcing" is any value of T_m that results in

the lake completely filling (that is, the lake level reaching roughly the flotation level) in an integer number of years. There are therefore multiple resonant values of T_m corresponding to the total annual input to the lake being equal to $1/n$ (where n = 1, 2, 3,…) multiplied by the volume of the lake when it is completely full. This is reflected in Fig. 3.12a by a second resonance peak at $T_m \approx 5.5$ °C and a third, hardly visible at the plots resolution, at $T_m \approx 2$°C.
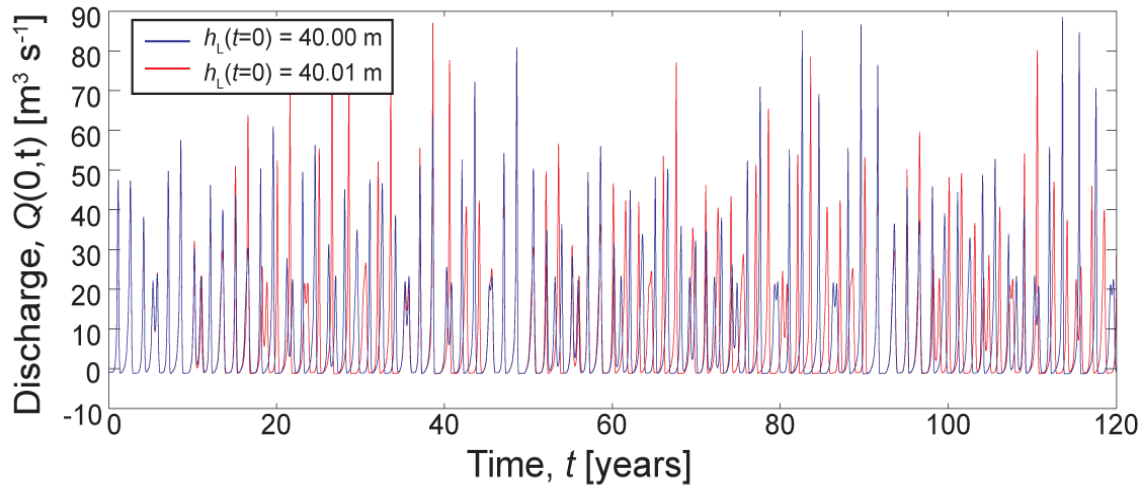
Fig. 3.13. Sensitivity of the model simulations to initial conditions. Time series of discharge at the lake outlet during two simulations that used T_m = 12 °C and two slightly different initial lake depths, 40.00 m and 40.01 m.

These resonant T_m values can be approximated analytically by integrating eqns. 3-17 and 3-18 over one year, to show that the total input to the lake during that time is $3.51 \times 10^8 k_Q T_m / \pi$. I then assume the lake empties after each flood and take the reference lake volume, V_{Li}, as the volume of the lake when it is 'full'. Equating the total annual input to the lake to the volume V_{Li} yields an expression for the nth resonant value of T_m: $\pi V_{Li}/(3.51 \times 10^8 \, n \, k_Q)$ = {24.9, 12.5, 8.3, 6.2, …} °C. Comparing these values to the locations along the T_m axis of the resonance peaks in Fig. 3.12 shows that the second resonant T_m value ($\approx$12.5 °C) matches well with the numerically simulated resonance peak. However, because a significant volume of water is left in the lake after floods simulated with $T_m < 10$ °C, the third and fourth analytically-derived resonant T_m values (at $\approx$8.3°C and $\approx$6.2 °C) do not match the simulated resonance peaks.

Mode-locked regions are separated by densely populated regions corresponding to flood cycles that display characteristics of chaotic systems. The high density of the orbits is evident in the example plotted in Figs. 3.11d and the time series of the results suggest that no repeating pattern emerges over the 120-year simulations (e.g. Fig. 3.13). Like other chaotic systems (e.g. Drazin, 1992) the model is sensitive to initial conditions. Fig. 3.13 plots the time series of discharge at the lake outlet $Q(0,t)$ from two simulations that used T_m = 12 °C, with two slightly different initial lake depths, 40.00 m and 40.01 m. The

solutions track each other for around 10 years but after this they begin to diverge. After 20 model years the solutions no longer resemble one another.
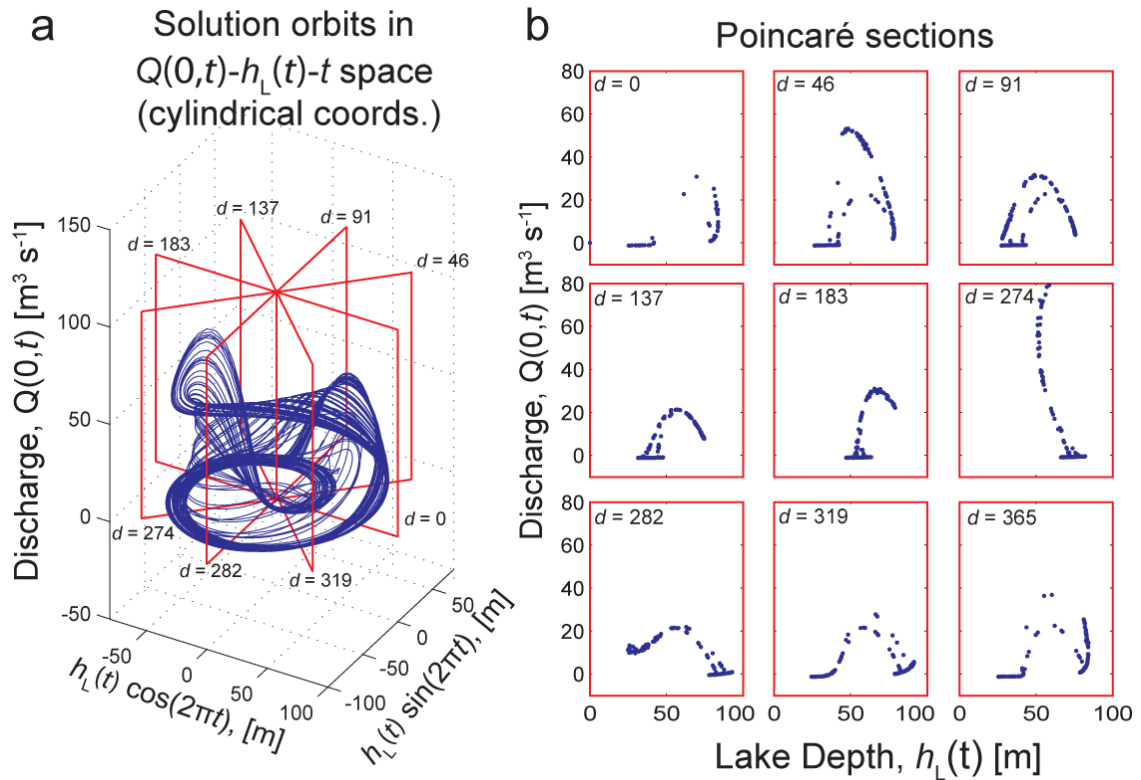
Fig. 3.14. Topological mixing of Q-h_L phase space. (a) Solution orbit in Q-h_L-t space of simulation with T_m = 12 °C and $h_L(t=0)$ = 40 m, plotted in cylindirical coordinates. The curve's distance from the vertical axis denotes the lake's depth, its position along the vertical axis denotes the discharge at the lake outlet and its rotation around the vertical axis denotes progression through the annual cycle of lake filling. (b) Poincaré sections taken through this space, perpendicular to the t-dimension, at nine different stages of the year. Each section's location in Q-h_L-t phase space is indicated by the red boxes in (a) and denoted by the day of the year, d.

Topological mixing of phase space is another characteristic of chaotic systems evident in the results. When topologically mixed, any region of phase space will eventually overlap with every other region. To demonstrate this, in Fig. 3.14 I have re-plotted the results of the simulation that used T_m = 12 °C (previously plotted in Fig. 3.11d) in a slightly different way. Fig. 3.14a displays the simulation's orbit in Q-h_L-t phase space using a cylindrical coordinate system. The blue curve's distance from the vertical axis denotes the lake's depth, its position along the vertical axis denotes the discharge at the lake outlet and its rotation around the vertical axis (its azimuthal coordinate) denotes progression through the annual cycle of lake filling. In addition, Fig. 3.14b displays nine 2-dimensional Poincaré sections taken along Q-h_L planes, perpendicular to the time-dimension, at nine points in the annual cycle denoted by the day of the year d. Time t

has units of years, so *d* is the fractional part of *t* multiplied by 365. The blue points in each plot in Fig. 3.14b locate the intersection of the blue curve from Fig. 3.14a with each Poincaré section. Plotting the results in this way shows how the shape of the simulation's orbit, that initally appears random, posseses structure; together the points form a shape. This 'Nye-Fowler attractor' rotates, bifurcates and folds over on itself as the plots progress through the annual cycle. This is topological mixing. The pattern is reminiscent of similar plots from studies of non-linear oscillators (e.g. the Duffing oscillator; Novak and Frehlich, 1982).

The transition from limit cycles to chaotic cycles as T_m decreases from 14 ^{o}C to 13 ^{o}C involves two types of bifurcation. Fig. 3.15a shows this region of T_m in detail. The first bifurcation, at $T_m \approx 13.88^o$C, is an abrupt transition from period-1 cycles, where all floods have the same peak discharge, to period-2 cycles, where the system alternates between large and small floods. Figs. 3.15b & 3.15c display results from simulations from both
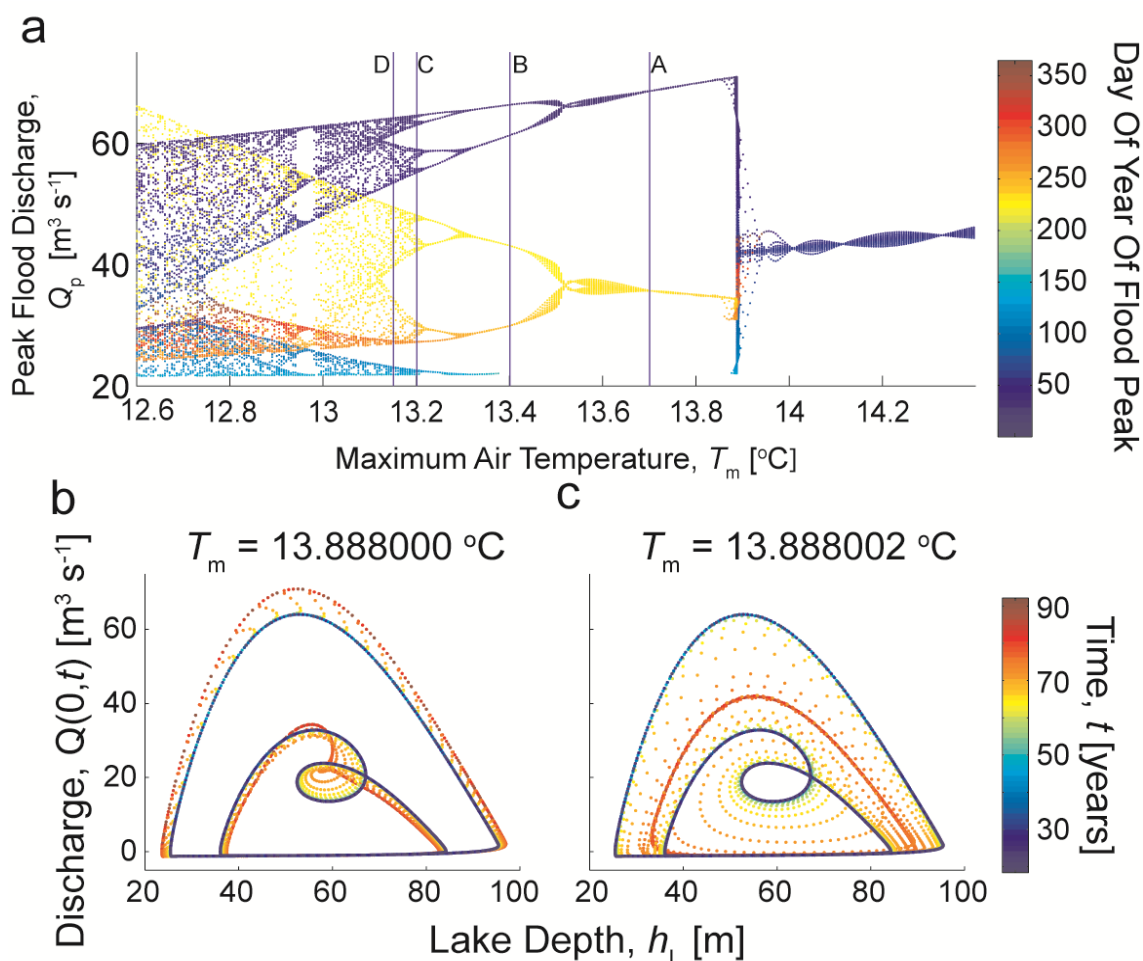
Fig. 3.15. Transition from limit cycles to chaos occurs via two types of bifurcation. (a) close-up view of Fig. 3.12 in the region 12.6 ≤T_m≤ 14.4 ^{0}C. Orbits in Q-h_L phase-space of solutions with (b) T_m = 13.888000 ^{o}C and (c) T_m = 13.888002 ^{o}C – either side of the abrupt transition from period-1.5 floods to period-1 floods visible in (a). Dots are separated by ~4.5 model days.
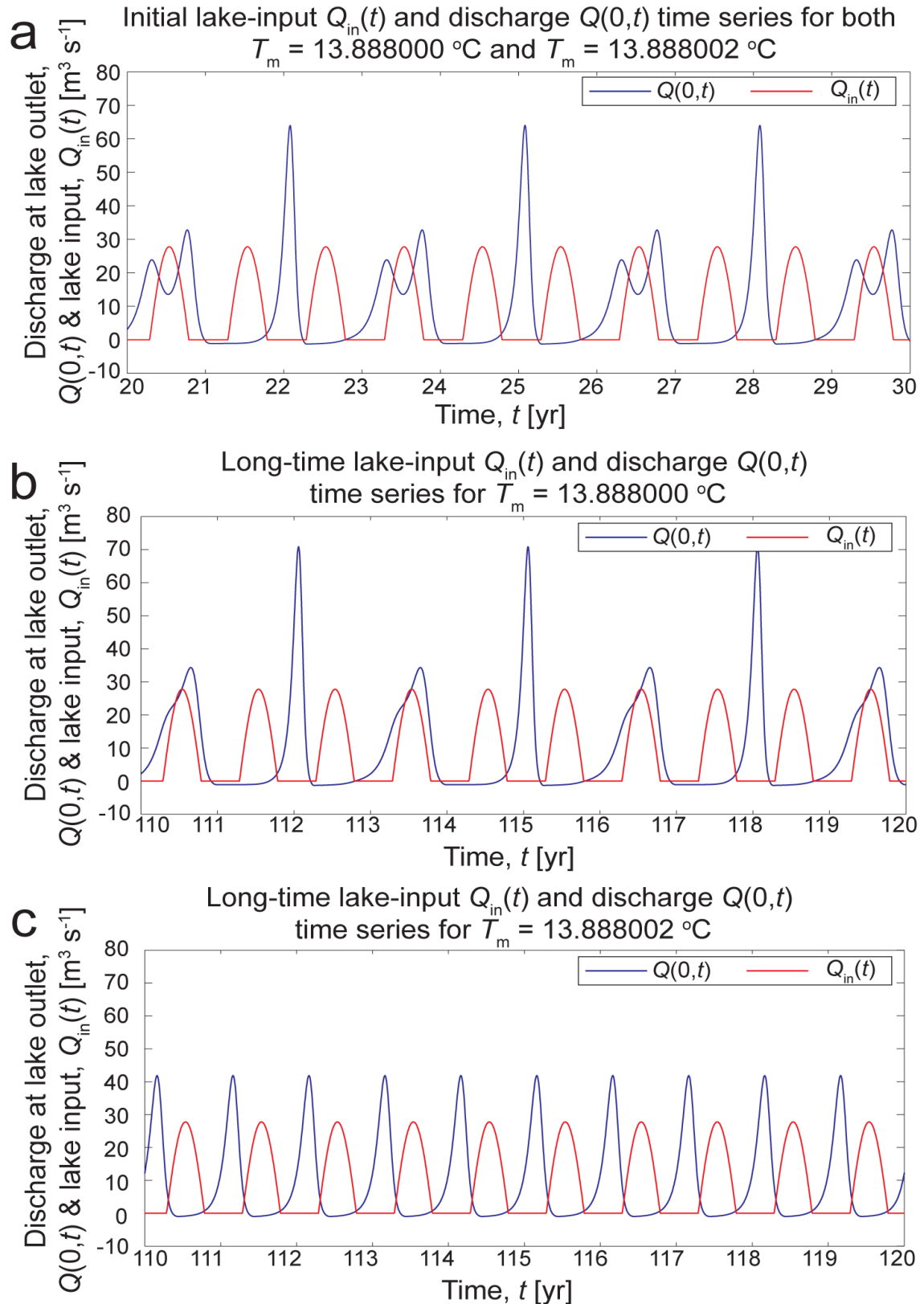
Fig. 3.16. Time series of discharge at the lake outlet, $Q(0,t)$ (blue curves), and the water input to the lake, $Q_{in}(t)$ (red curves) corresponding to (a) the initial unstable time series of two simulations, one with T_m = 13.888000 °C and another with T_m = 13.888002 °C;, (b) the final time series of the simulation with T_m = 13.888000 °C; and (c) the final time series of the simulation with T_m = 13.888002 °C.

sides of this abrupt transition (with T_m = 13.888000 °C and T_m = 13.888002 °C). The figures show solution orbits in Q–h_L phase space as a series of point representing each solution's location in the phase space every ~4.5 days. The colour of the points denotes progression through the simulation. Corresponding time series of discharge and lake input are plotted in Fig. 3.16.

Both solutions start on almost identical unstable period-2 orbits. These orbits are shown as blue points in Figs. 3.15b–3.15c and the corresponding time series of Q_{in} and Q are shown in Fig. 3.16a (note that the four time series are identical on this scale, so they appear as only two curves in Fig. 3.16a). On this oribit, the timing of floods is such that every other flood is double-peaked. The onset of melt in Spring occurs just after the first peak and instigates the second (Fig. 3.16a). Larger floods occur every third winter. As each simulation progresses, the solution orbits leave this unstable orbit in one of two ways. During the warmer run (T_m = 13.888002 °C; Figs. 3.15c and 3.16c), floods occur
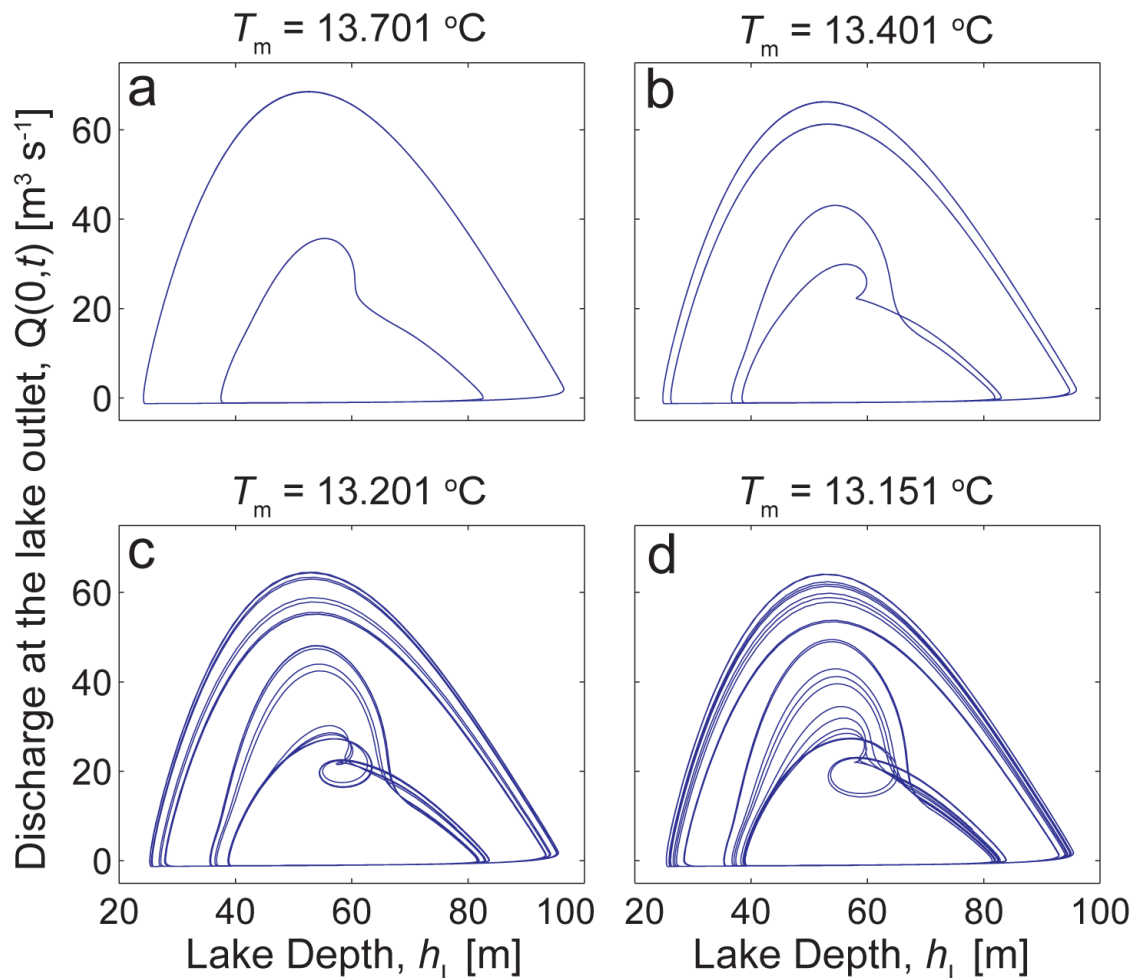
Fig. 3.17. A cascade of period-doubling bifurcations. Long-time solution orbits in Q–h_L phase space of four simultations that used (a) T_m = 13.701 °C, (b) T_m = 13.401 °C, (c) T_m = 13.201 °C, (d) T_m = 13.151 °C. The panels a, b, c and d, correspond to the positions in T_m-parameter space indicated in Fig. 3.15a by the vertical lines A, B, C and D, respectively.

progressively earlier each year and the double-peaked flood evolves into two floods of equal size. Meanwhile, the originally-larger flood shrinks. The long-term result is period-1 limit cycles with a mean flood repeat time of F_P = 1 year. These cycles are shown as red points in Fig. 3.15c and their corresponding discharge time series are shown in Fig. 3.16c.

In contrast, during the cooler run (T_m = 13.888000 ^{o}C; Figs. Fig. 3.15b and Fig. 3.16b) floods occur progressively later until the first peak of the double-peaked flood shrinks and disappears. The long-term result is period-2 limit cycles with a mean flood repeat time of F_P = 1.5 years. These cycles are shown as red points in Fig. 3.15b and their corresponding discharge time series are shown in Fig. 3.16b.

Further decrease in T_m leads to a cascade of bifurcations of the second type. Fig. 3.17 plots four solution orbits in Q–h_L phase space that use T_m values that bracket several of these period-doubling bifurcations. As T_m is decreased past each bifurcation point (see biurcations in Fig. 3.15, for example between the vertical lines labelled A and B), the orbits split into two branches and solutions that formerly repeated themselves, for example, every two floods now repeat every four years. The result of many of these bifurcations is the densely populated, chaotic region on the left of Fig. 3.15.

Both types of bifurcation demonstrated in the these results have been observed before in studies of other systems of equations. In particular, cascades of period-doubling bifurcations are common (e.g. May, 1976; Parlitz and Lauterborn, 1987) This supports the idea that the Nye-Fowler model can produce truly chaotic dynamics when driven by a time-varying forcing.

3.5   Discussion

Before embarking on an investigation of the environmental controls on flood cycles, in section 3.2 I focused on determining the conditions under which the Nye-Fowler model can simulate a subglacial water divide between floods and stable periodic flood cycles. The results of numerical simulations suggest a divide will not form when the channel is not supplied with water along its length (when M = 0 m^2 s^{-1}). A small contribution to the spatial gradient in the discharge in the channel from the evolving channel cross-sectional area and the water melted from the channel's walls ($\epsilon_R \neq 0$) is insufficient to allow divide formation. Conversely, when the channel is supplied with water along its length, a divide can form. This can occur even when the surface of the glacier has a uniform slope – i.e. when no topographic seal exists. In this case when the depth of a marginal lake is low, water can flow uphill (and 'up–basic-hydraulic-gradient') into the lake. One implication of these findings is that assuming water always flows down basic hydraulic gradients, as

is often done (e.g. Carter and Fricker, 2012; Flowers, 2003), may not always be appropriate. Indeed, in some systems, such as jökulhlaup systems, 'up–basic-hydraulic-gradient' water flow may be crucial to their behaviour.

Divide formation is important for jökulhlaup dynamics because it suppresses unstable growth in the size of flood cycles and allows Nye's (1976) equations to simulate periodic floods (Fowler, 1999). Investigating further, I have found that divide formation is not in fact a necessary condition for the simulation of periodic floods. When the channel is not supplied with water along its length, using a non-zero ϵ_R and a topographic seal suppresses flood cycle growth without a divide forming. In reality, the channel is unlikely to be hydraulically isolated from the rest of the bed and may be supplied with water by an adjacent distributed drainage system along its length.

Next, I addressed the main goal of this chapter: to investigate how environmental factors control the size and timing of floods. Simulations showed that when a divide forms, the meltwater input to a jökulhlaup system controls flood size through the dynamics of subglacial water-divide migration. In the model, meltwater can be input to the system in two ways: into the lake from its subaerial surroundings or into the channel along its length from the adjacent subglacial environment. An increase in meltwater production in a jökulhlaup system could be due to warm weather or increased geothermal activity, and, depending on the system, could result in an increase in the input to the lake, an increase in the input to the channel, or both. It turns out that, in the model, exactly how meltwater is apportioned between the lake and the channel, determines how warm weather or increased geothermal activity affects the size of flood cycles. Increasing the input to the lake increases flood size (increasing highstand and peak discharge, and decreasing lowstand) and increasing the input to the channel decreases flood size (decreasing highstand and peak discharge, and increasing lowstand).

These findings may have consequences for real jökulhlaup systems. Before the unusually large flood that emanated from Lake Grimsvötn in 1996, a subglacial volcanic eruption dramatically increased meltwater production. Observations show that this caused the lake input to increase and the lake to reach the flotation level (Gudmundsson et al., 1997; Björnsson, 2002). Fowler's (1999) modification of Nye's equations was motivated by these observations, however, they are only reproducible in simulations using the Nye-Fowler model if the increase in the lake input is not accompanied by a significant increase in the background supply of water to the channel along its length (*M*). Physically, in the model, increased input to the channel counteracts the increase in flood size associated with increased input to the lake, because the divide can migrate more easily when the channel input is larger. These considerations suggest that, at Grimsvötn

in November 1996, any increase in the input to the channel associated with increased subglacial geothermal heating during the eruption was small compared to the observed increase in lake input.

Similar considerations apply to glaciers where meltwater production is linked to air temperature (not geothermal heating). Warm weather could lead to an increase in lake input and flood size. Alternatively, flood size could decrease during warmer weather if the local meteorology and topography means these conditions cause a larger increase in meltwater reaching the glacier's bed than in meltwater reaching the lake.

Because the topography and the spatial and temporal distribution of weather and geothermal heating in jökulhlaups systems is highly variable, my modelling results suggest that the way in which changes in the weather and geothermal activity affect the size and timing of floods will also be variable and system-specific.

The relationship between meltwater input to the lake and flood size is more complex when this input varies seasonally. Interactions between the timing of lake drainage and the seasonal cycle of lake filling results in several interesting behaviours: mode locking, where the mean time between floods is locked to an integer number of years; resonance, where larger floods occur when the total annual input of meltwater to the lake is an integer fraction of the lake's volume when full; and chaos, where flood cycles are highly sensitive to initial conditions and never repeat.

All three of these model behaviours can be understood by considering the model jökulhlaup system as a periodically-forced nonlinear oscillator. In many situations the response of an oscillator to a periodic driving force can have the same frequency as that of the driving force. This mode locking occurs between many coupled oscillatory systems, such as between the moon's rotation on its axis and its orbit round the Earth. Also, when an oscillator is driven by a forcing with a particular frequency, the timing of the driving force and the oscillations can coincide in such a way as to produce a large response in the oscillator (e.g. Young and Freedman, 2006). This is termed resonance and I have used the same term to describe similar behaviour exhibited by the Nye-Fowler model. Simulated floods are larger when the model is driven by a forcing with a particular amplitude. My analysis showed that the peaks in the size of floods are associated with climatic regimes (parameterised in the model by T_m) that allow the lake to fill to a depth approaching the flotation depth in an integer number of years. Chaotic dynamics such as those demonstrated here have been observed in studies of oscillators with nonlinear damping, for example the Van der Pol oscillator, or a nonlinear restoring force, for example the Duffing oscillator (Drazin, 1992, Kanamaru, 2007; Novak and Frehlich, 1982).

The way the Nye-Fowler jökulhlaup model behaves when it is forced with a time-varying meltwater input to the lake may have consequences for future changes in real jökulhlaup systems. Sustained changes in environmental factors (such as the meltwater input to an ice-dammed lake) can be expected to change the size and timing in the calendar year of floods. But while a jökulhlaup system remains mode-locked these changes may occur in a gradual and predictable manner. Gradual changes in timing have been observed at Merzbacher Lake, Kyrgyzstan (Ng and Liu, 2009) and Gornersee, Switzerland (Huss et al., 2007). At these systems, floods that occur on average once a year have been occurring progressively earlier each year. According to my model results this shift in flood timing is consistent with long-term warming; in regions of T_m parameter space corresponding to mode-locked flood cycles, increasing T_m shifts the dates of flood peaks to earlier in the calendar year (see page 69). If changes like those observed in these real systems continue, my results suggest that jökulhlaup systems are also capable of undergoing more abrupt changes in both the timing and peak discharge of floods.

Related to this is the question of jökulhlaup predictability. My findings suggest that the timing and magnitude of jökulhlaups may be unpredictable in the long term. In the model, even when the only time-varying forcing is the smoothly-varying lake input, the long-term evolution of the system can be sensitively dependent on initial conditions: initial conditions that someone wanting to predict floods cannot know. In reality, the fact that the weather fluctuates chaotically makes long-term prediction even harder. However, a sensitive dependence on initial conditions only manifests in some regions of parameter space. In other regions, the system reaches limit cycles independent of initial conditions, and floods remain regular despite large changes in climate forcing. Hence, predicting the timing of an imminent flood may sometimes be possible. This is pursued in the next chapter using a suite of lower-order 'threshold' models.

Several extensions to my investigation of the Nye-Fowler model forced with time-varying inputs are worthwhile. Firstly, the stability of the chaotic dynamics demonstrated here could be investigated – both in terms of initial conditions and the model's structure. Quantitatively, the bifurcations described in section 3.4.2 are certainly dependent on initial conditions and structure. An investigation of the system's stability would aim to confirm my suspicion that the qualitative features of the bifurcation diagram (Fig. 3.12) and the existence of the 'Nye-Fowler attractor' do not depend on model structure and initial conditions. Varying the model's structure could entail changing or removing terms, or changing the model's forcings. One such change, that has already been investigated, is the substitution of the constant channel input used here, with a temperature-dependent channel input. This emulates an annual shut-

down of the drainage system during the winter. The results of a parameter search show that the chaotic dynamics seen at the transition between one-year-long flood cycles and two-year-long flood cycles (11.5 $<T_m<$ 13.8 ^{o}C; Fig. 3.12) are replaced by a single period-doubling bifurcation. This change is associated with the winter drainage system shutdown. The chaotic dynamics that separate other mode-locked regions (e.g. two-year-long cycles and three-year-long cycles) remain. Further work could investigate how other changes, such as removing the exponents of some nonlinear terms affect the model's chaotic dynamics.

Secondly, further work could extend my parameter search. The highest midsummer air temperature, T_m, I reached in my parameter search, yielded one flood per year. I did not extend the search to higher T_m, where more than one flood may occur per year. This was because, during simulations with $T_m > 26$ ^{o}C, floods are large enough for the lake to empty completely. The Nye equations cannot describe the different hydrological regime that occurs when a lake completely empties, but I tackle this problem in Chapter 6. Further work could extend my parameter search into $T_m > 26$ ^{o}C by including the additional physics discussed in that chapter.

Thirdly, meltwater input is not the only parameter that may change with climate. Other important climate-dependent parameters include the ice-dam height and the lake's area. Because both these parameters affect the lake's volume when full, changing them will affect the lake's resonant meltwater inputs. Further work could systematically vary these two parameters to investigate future changes to jökulhlaup systems in a warming climate more realistically.

Finally, another extension of this work could aim to investigate if resonance and the other complex behaviours exhibited by the model could operate in other glacio-hydrological situations, for example, in moulins. Moulins are roughly vertical conduits that can carry water from a glacier's surface to its bed. They may behave like jökulhlaup systems, filling and draining in response to meltwater input and discharge through a subglacial drainage system. Future work could investigate if resonance and chaotic dynamics could occur in these systems from some combination of moulin area, glacier height and surface meltwater input.

3.6   Conclusions

The findings I have presented in this chapter go beyond Fowler's (1999) to show that the Nye equations, with Fowler's modifications, can simulate stable periodic flood cycles, even when either the channel is not supplied with water along its length or no topographic seal exists. A water divide can form in the channel between floods whose

dynamics provide a mechanistic link between meltwater production and flood size. This link is system-specific because it depends on how meltwater is apportioned between the channel and the lake. When the model is forced with time-varying meltwater inputs, it can exhibit a number of complex behaviours that can be analysed using concepts borrowed from studies of forced non-linear oscillators.

Chapter 4   Quantifying the predictability of the timing of jökulhlaups from Merzbacher Lake, Kyrgyzstan

This chapter is based on a manuscript of the same title published in the Journal of Glaciology Volumes 59, Issue 217.

4.1   Introduction

Jökulhlaups pose significant hazards to downstream settlements and environments, a threat likely exacerbated by population growth and climatic warming (e.g. Barnett and others, 2005; Björnsson, 2004; Ng and others, 2007). While an ability to predict the timing and magnitude of these floods can enable mitigation of their consequences, this problem has remained largely untackled. Ng and Liu (2009) put forward a mathematical theory for understanding the long-term timing pattern of jökulhlaups. Their theory exposes key mechanisms behind irregular jökulhlaup timing and reproduces temporal structures in a sequence of floods recorded from Merzbacher Lake, a jökulhlaup system in Kyrgyzstan. If certain aspects of the timing of jökulhlaups can be explained, it may be possible to predict individual flood dates. I explore this in this chapter and take a first step towards the development of operational flood forecasting. Like Ng and Liu (2009), I focus on the timing of floods (which could inform predictions of flood size) and use the Merzbacher Lake system as an example (Fig. 4.1a). My aim is to establish how well simple models can predict the Merzbacher flood dates and develop measures of predictability that can be applied to other jökulhlaup lakes. The results can serve as a benchmark for future forecasting efforts.

Theory and observations have shown that the lake depth at which jökulhlaups initiate – the outburst threshold – varies from flood to flood (e.g. Chapter 3 of this thesis; Björnsson, 2003; Clague and Mathews, 1973; Ng and Liu, 2009; Walder and Costa, 1996). Because successful prediction requires accounting for such variability, I examine a hierarchy of assumptions for the outburst threshold, motivated by different hypotheses of how it depends on environmental factors. These 'threshold assumptions' range from the predominantly empirical to ones based more strongly on physical grounds, and are presented and studied in order of increasing complexity. Because of uncertainty in the geometry of the glacier that dams Merzbacher Lake attempts to predict floods using the full Nye-Fowler model (see Chapters 2 and 3) are not pursued here. This will have to await geophysical investigations of this glacier.

This chapter is organised as follows. In section 4.2, Ng and Liu's (2009) model of lake filling and draining is described and I explain how I use it to predict flood dates. Section

4.3 introduces Merzbacher Lake, its record of jökulhlaup dates, and a melt equation needed in the Ng-Liu model for estimating this lake's water supply. The flood dates are used with the melt equation to reconstruct flood volumes, whose distribution provides a probabilistic handle on the size and timing of future floods. In sections 4.4 and 4.5, I use the Ng-Liu model with different threshold assumptions to evaluate how well this model predicts the Merzbacher flood dates. After considering how to quantify mismatch between predicted and observed flood dates, I optimise each version of the model for prediction success. In this exercise, the choices of threshold behaviour, weather-data source, and assumptions of future weather lead to multiple prediction results, whose performances will be discussed.

4.2   Flood-date prediction with the threshold model

In Ng and Liu's (2009) model, the jökulhlaup lake, which has volume V and water depth h, fills in response to melt-water input at a rate Q_{in}, and it drains suddenly and completely in a flood when a threshold water depth, h_c, is reached (Figs. 1b & 1c). With t denoting time, their model equations are

$$\frac{dV}{dt} = Q_{in} \quad \text{when } h(V) < h_c,$$

4-1a

$$V = 0 \quad \text{when } h(V) = h_c,$$

4-1b

where the function $h(V)$ represents lake geometry. These equations generate sawtooth-shaped filling and draining cycles in the lake level that are irregular when Q_{in} depends on weather and h_c varies between floods. By assuming a constant h_c and estimating Q_{in} from daily air temperature with the sub-model described later (section 3.3), Ng and Liu (2009) simulated eqn. 4-1 for Merzbacher Lake through 1956 to 2005 to obtain model flood dates, which they compared with the observed flood dates in this period (listed in Table 4-1). Motivated by concepts from nonlinear dynamics, they analysed the simulated and observed date sequences with time-delay maps. They also integrated eqn. 4-1a for each period between successive floods to reconstruct the flood volumes and the long-term lake level history.

Table 4-1. Flood record of Merzbacher Lake for the period 1956 to 2008, showing the dates of peak discharge of 54 floods and the measured volumes of 19 floods. Of these 19 flood volumes, the 13 shown in bold are considered more reliable. Entries 1 to 51 come from Ng and Liu (2009), and entries 52 to 54 from S. Liu (personal communication). The reconstructed flood volumes are calculated from the two temperature forcings T_{NCEP} and T_{ERA} using the method described in section 4.3.4.

Flood Index	Date of Flood Peak	Measured Flood Volume [10^8 m^3]	Reconstructed Flood Volume T_{NCEP} [10^8 m^3]	Reconstructed Flood Volume T_{ERA} [10^8 m^3]	Flood Index	Date of Flood Peak	Measured Flood Volume [10^8 m^3]	Reconstructed Flood Volume T_{NCEP} [10^8 m^3]	Reconstructed Flood Volume T_{ERA} [10^8 m^3]
1	02/07/1956		-		28	21/08/1982	1.74 ± 0.14	1.95 ± 0.07	1.89 ± 0.08
2	03/09/1956		0.98 ± 0.14		29	22/08/1983		1.48 ± 0.06	1.35 ± 0.09
3	07/09/1957		1.75 ± 0.07		30	26/08/1984		1.71 ± 0.07	1.69 ± 0.07
4	24/11/1958	1.71 ± 0.09	2.07 ± 0.10	1.96 ± 0.08	31	15/08/1985		1.45 ± 0.06	1.44 ± 0.07
5	19/09/1959	**1.44 ± 0.19**	1.64 ± 0.06	1.59 ± 0.07	32	01/08/1986		1.36 ± 0.06	1.34 ± 0.07
6	16/07/1961		2.80 ± 0.12	2.94 ± 0.11	33	19/08/1987		1.77 ± 0.07	1.67 ± 0.08
7	06/06/1963	**2.99 ± 0.17**	3.01 ± 0.12	3.10 ± 0.10	34	12/12/1988	**2.10 ± 0.14**	2.03 ± 0.08	2.01 ± 0.08
8	18/09/1963	**0.95 ± 0.09**	1.14 ± 0.07	1.13 ± 0.06	35	31/08/1989	**1.28 ± 0.15**	1.20 ± 0.05	1.20 ± 0.06
9	28/09/1964	**1.40 ± 0.19**	1.71 ± 0.09	1.49 ± 0.09	36	10/08/1990		1.39 ± 0.06	1.39 ± 0.06
10	01/09/1965	**1.42 ± 0.13**	1.69 ± 0.06	1.70 ± 0.08	37	24/07/1991		1.31 ± 0.06	1.39 ± 0.07
11	03/08/1966		1.48 ± 0.06	1.44 ± 0.06	38	04/08/1992		1.65 ± 0.07	1.75 ± 0.07
12	13/12/1966		0.74 ± 0.04	0.66 ± 0.04	39	22/08/1993		1.53 ± 0.08	1.66 ± 0.08
13	13/09/1967	**1.82 ± 0.06**	1.54 ± 0.07	1.40 ± 0.06	40	24/07/1994		1.19 ± 0.05	1.48 ± 0.06
14	21/08/1968	**1.64 ± 0.22**	1.51 ± 0.06	1.34 ± 0.06	41	18/07/1995		1.42 ± 0.06	1.56 ± 0.07
15	20/08/1969		1.59 ± 0.07	1.49 ± 0.07	42	05/12/1996	2.84 ± 0.09	2.29 ± 0.09	2.33 ± 0.09
16	31/07/1970	0.86 ± 0.20	1.45 ± 0.07	1.25 ± 0.07	43	31/07/1997		1.26 ± 0.07	1.19 ± 0.06
17	17/08/1971	1.33 ± 0.19	1.64 ± 0.09	1.90 ± 0.07	44	27/07/1998		1.74 ± 0.07	1.77 ± 0.07
18	04/10/1972	**1.61 ± 0.10**	1.70 ± 0.11	1.93 ± 0.09	45	19/07/1999		1.72 ± 0.07	1.53 ± 0.07
19	02/09/1973		1.30 ± 0.06	1.45 ± 0.06	46	27/07/2000		2.04 ± 0.08	1.85 ± 0.07
20	08/08/1974		1.25 ± 0.06	1.37 ± 0.07	47	31/07/2001		1.88 ± 0.07	1.73 ± 0.07
21	12/09/1975		1.72 ± 0.07	1.80 ± 0.08	48	06/08/2002		1.83 ± 0.07	1.60 ± 0.07
22	24/08/1976	1.31 ± 0.27	1.25 ± 0.07	1.33 ± 0.07	49	26/07/2003		1.54 ± 0.07	
23	24/05/1978	**2.51 ± 0.35**	2.31 ± 0.15	2.38 ± 0.10	50	09/08/2004		1.95 ± 0.07	
24	09/08/1978		0.79 ± 0.05	0.91 ± 0.07	51	15/07/2005		1.52 ± 0.07	
25	27/05/1980	**2.36 ± 0.18**	2.33 ± 0.12	2.38 ± 0.12	52	30/07/2006		2.10 ± 0.08	
26	12/09/1980	**1.51 ± 0.06**	1.28 ± 0.10	1.17 ± 0.07	53	11/07/2007		1.89 ± 0.07	
27	15/07/1981		0.91 ± 0.09	1.01 ± 0.08	54	15/07/2008		2.07 ± 0.09	
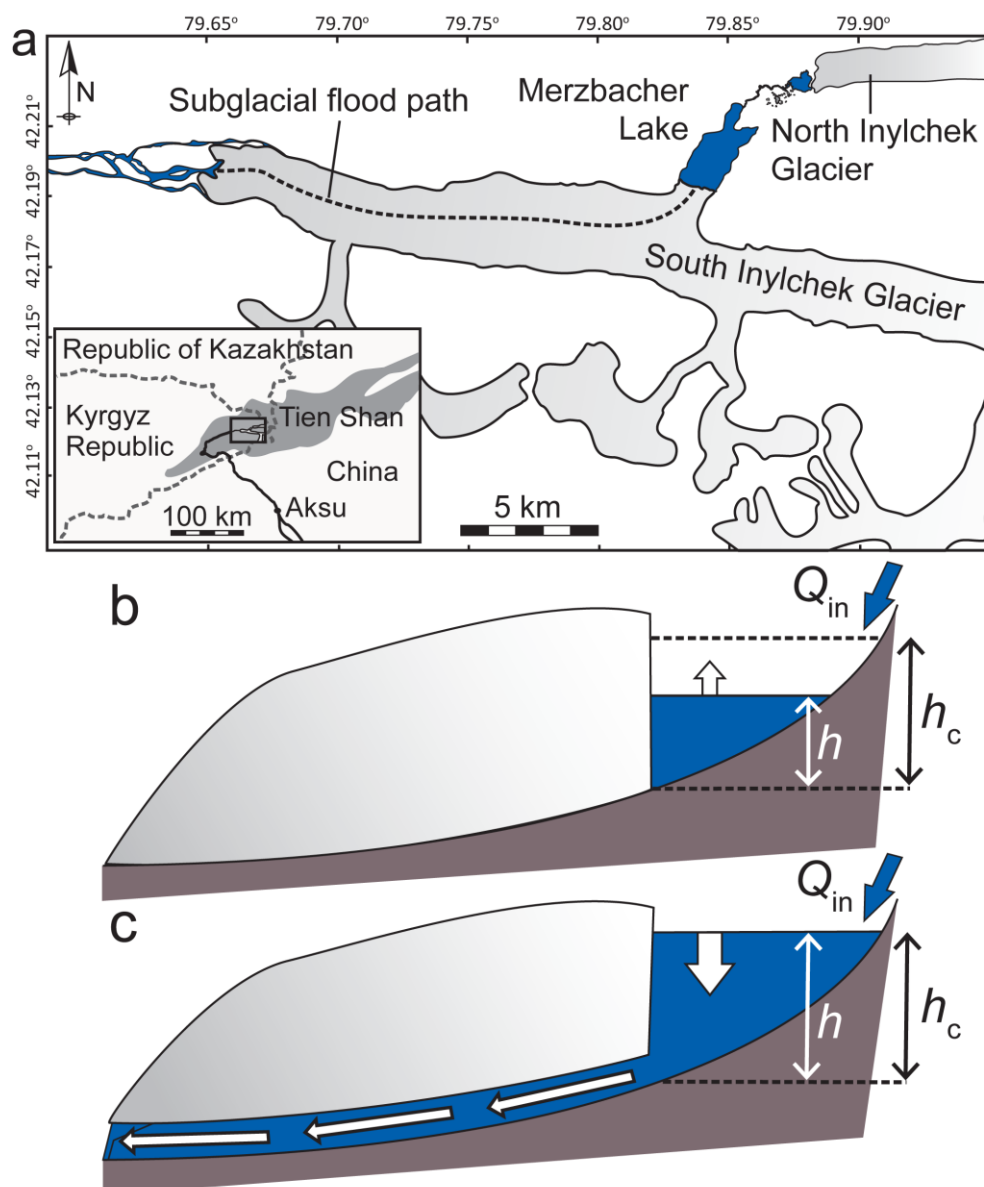
Fig. 4.1. The Merzbacher jökulhlaup system. (a) Map of Merzbacher Lake and North and South Inylchek Glaciers; inset shows the system's location in the Tien Shan. (b & c) Schematic lake and glacier cross-sections along a possible subglacial flood path (b) while the lake is filling and (c) after lake water depth *h* has reached the threshold *h*$_c$ and a flood has started.

In this chapter, I use this model for the purpose of predicting the next flood date from the date of the last (known) flood, and specifically for *hindcasting* the observed Merzbacher flood dates in Table 4-1. My study period spans the first and the last flood dates and has 19006 days on which one could ask when the next flood will be. I explore the effect of a variable outburst threshold on prediction success and seek the best assumption for h_c. Most of the simulations use eqn. 4-1, but one set of simulations use a modified model with a threshold different from h_c that mimics the moving subglacial water divide simulated in the previous chapter using the Nye-Fowler model. A detailed explanation of this threshold is given in section 4.3.
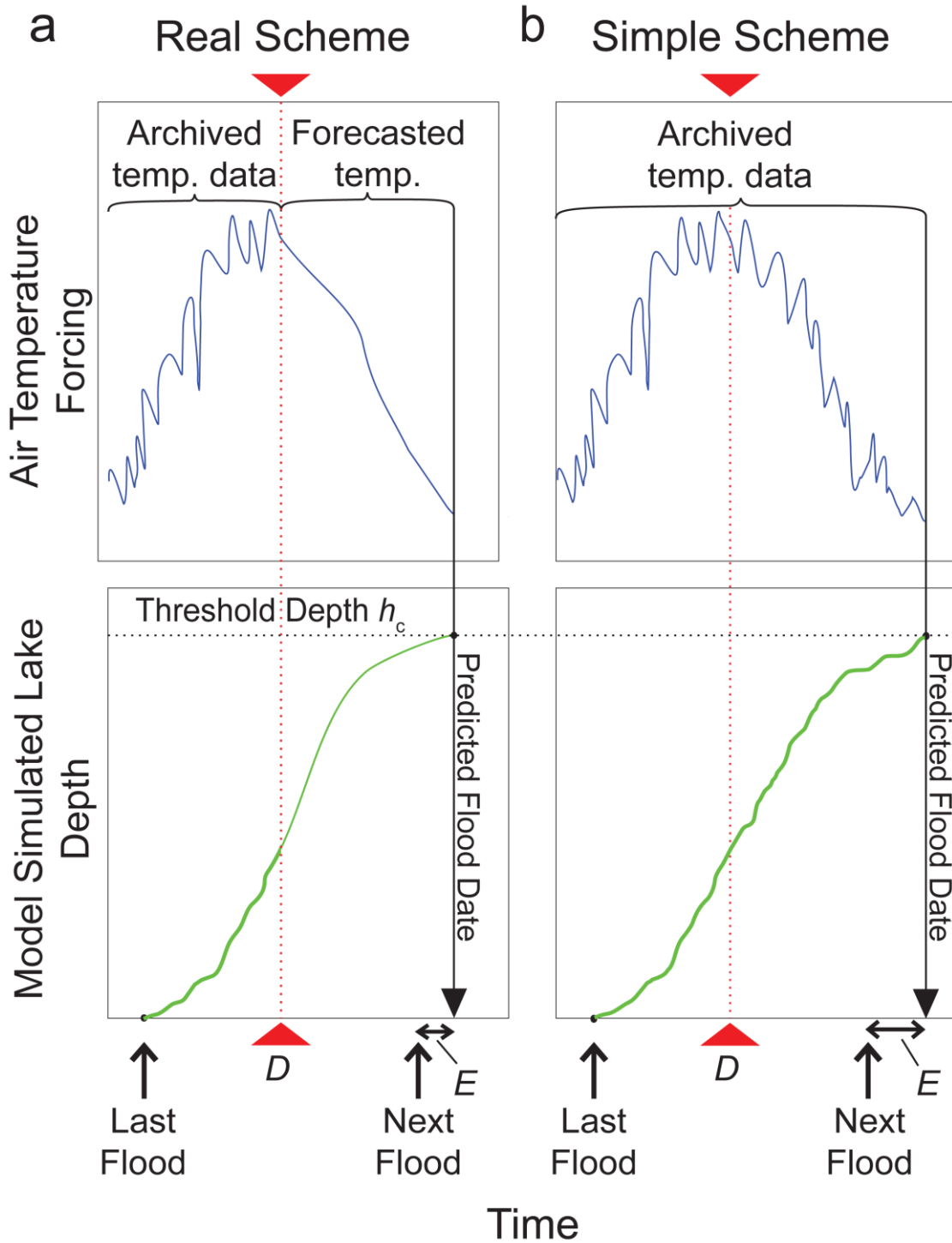
Fig. 4.2. (a) Real Scheme and (b) Simple Scheme of application of weather forcing in flood prediction models. In both (a) and (b), upper and lower plots show, respectively, the history of the temperature forcing used to calculate the lake water supply Q_{in} and the corresponding history of the simulated lake depth h. (a) The Real scheme calculates Q_{in} using archived daily temperature data on all days before the day on which the prediction is made, D, and using forecasted temperature on all days after D. (b) The Simple scheme calculates Q_{in} using archived daily temperature data throughout the prediction run. In both schemes, a flood is predicted when h reaches the outburst threshold h_c and E denotes the prediction error.

During prediction runs, for each day in the study period, D (Fig. 4.2), and starting with an empty lake on the day after the previous known flood (e.g. one of the floods in Table 4-1), eqn. 4-1a is integrated forward on a daily time step to fill the lake, until h, found from the lake volume via $h(V)$, reaches h_c. Thus the next flood date is predicted, and its mismatch in timing from the actual (observed) next flood forms a prediction error, E (Fig. 4.2). As D marches forward in time past a known flood date, the start date of the integration is renewed. In each set of prediction runs assuming specific threshold behaviour and specific temperature data source, this procedure is applied on every day in the study period to obtain the same number of predictions (and hence the same number of errors) as the length of the period. I summarise the errors into an overall measure of mismatch. Two measures considered later are the root-mean-square error and the fraction of predictions that are accurate to a fixed number of days.

4.2.1 'Real' and 'Simple' Schemes of weather forcing

When this exercise is performed for Lake Merzbacher to quantify its floods' predictability, past weather forcing – used for deriving Q_{in} in eqn. 4-1 – is known from archived daily temperature data. (These data will be outlined in section 4.3.3.) However, I put myself in the position of a forecaster in the past and assume that, on any day D on which a prediction is made, he or she knew the past weather but not the future weather, which must be estimated. I simulate this scenario by the procedure shown in Fig. 4.2a. For all days up to and including D, archived daily temperature data is used to find Q_{in}. But for all days after D (until the model lake reaches its outburst threshold), Q_{in} is found from a temperature *forecast*, taken to be the multi-year mean of the archived daily temperature on that calendar date (Fig. 4.2a). Although such a forecast could be made using sophisticated methods (e.g. regional climate models), this procedure is the easiest that incorporates weather uncertainty into flood predictions – it is called the 'Real' weather-forcing scheme. As D approaches the next flood, more of the lake-filling period is simulated with known weather forcing, so the predicted flood date or 'flood-date hindcast' varies with D. In section 4.5.3, this approach allows investigation of whether predictions improve as a forecaster approaches the next flood.

Later, in section 4.5.2, I consider a second scheme of weather forcing – called the 'Simple' scheme – to assess the impact of weather uncertainty on flood predictability. The previous procedure is followed, but it is assumed that the forecaster knew the future as well as the past weather; thus, archived daily temperature data are used to derive Q_{in} throughout each lake-filling period (Fig. 4.2b). In this case, flood-date hindcasts calculated on different days D that are bracketed by the same pair of observed floods are identical.

4.3   Study site and data sources

4.3.1 The Inylchek Glaciers and Merzbacher Lake

South Inylchek Glacier and North Inylchek Glacier together form the largest glacier system in the Tien Shan (Fig. 4.1a). The former glacier stretches for a distance of 50 km from its accumulation area by the ≈7000 m high peaks of Khan Tengri and Podeba to its debris-covered terminus at ≈2900 m a. s. l.. Although located in Kyrgyzstan, its runoff flows into China to feed this country's fifth largest river, the Tarim, which provides a vital water supply to oases around the Taklamakan Desert. Glacial meltwater contributes at least 35% of the Tarim's total runoff (Aizen and Aizen, 1998), and this figure is predicted to rise over the next few decades (Aizen and others, 2007).

Merzbacher Lake forms behind the ice dam made by South Inylchek Glacier across the valley occupied by North Inylchek Glacier (Fig. 4.1a). The lake fills typically to a depth of around 80 to 100 m before draining subglacially, producing jökulhlaups with a duration of about a week and peak discharges of up to 1500 $m^3 s^{-1}$ (Liu, 1992; Mavlyudov, 1997; Ng and Liu, 2009). Besides being a hazard, these floods represent a waste of valuable water resources (Shen and others, 2007). The Inylchek River is also a candidate for hydroelectric projects (Ng and others, 2007; Mamatkanov and Mingtszyan 2011). These reasons necessitate reliable forecasting of the floods.

4.3.2 Flood-date record

Merzbacher Lake is chosen for study because of its long and comprehensive jökulhlaup record and because its outbursts recur on a roughly regular basis (once every year on average, doubling or missing in some years; Ng and Liu, 2009), so that attempts to hindcast their dates may have some chance of success. Table 4-1 lists its 54 flood dates from 1956 to 2008. All but the last three dates are taken from Ng and Liu (2009), who compiled them from hydrological measurements at Xiehela gauging station near Aksu, China (Fig. 4.1a) and earlier publications. These authors also derived the volumes for 19 floods by subtracting an estimated baseflow component from the area of flood hydrographs (Ng and Liu, 2009; Ng and others, 2007). 13 of these flood volumes (in bold in Table 4-1) are considered more reliable than the remaining 6 (Ng and Liu, 2009) and are used to calibrate a melt sub-model described below. The last three dates in Table 4-1 come from Liu Shiyin (personal communication).

4.3.3 Lake water supply sub-model and temperature data

Following Ng and Liu (2009), I calculate the rate of meltwater input to the lake, Q_{in}, in eqn. 4-1a by using the temperature-index parameterisation

$$Q_{\text{in}} = k(T - T_0)_{0+} + c \,,$$

<div align="right">**4-2**</div>

where T [$^{\text{o}}$C] is air temperature near the lake, k [m^3 day^{-1} $^{\text{o}}$C^{-1}] quantifies the melt sensitivity to temperature, T_0 [$^{\text{o}}$C] is the temperature threshold above which melting occurs, and c [m^3 day^{-1}] denotes effective water input to the lake due to calving from the ice dam. k, T_0 and c are assumed constant. The subscript 0+ means that $T - T_0$ is set to zero whenever this difference is negative.

Ng and Liu (2009) prescribed data for T from the daily surface temperature provided by the US National Centers for Environmental Prediction (NCEP)/US National Center for Atmospheric Research (NCAR) Reanalysis Project (Kalnay and others, 1996; Kistler and others, 2001). Here, I also use the reanalysed daily surface temperature provided by the European Centre for Medium-Range Weather Forecasts, called ERA-40 (Uppala and others, 2005), in order to study the impact of different weather forcings on our predictions. These sources are called 'NCEP' and 'ERA' and T_{NCEP} and T_{ERA} are used to denote the respective temperature data after these have been interpolated to the coordinates of Merzbacher Lake. Both projects assimilate weather data from multiple sources (e.g. satellites, radiosondes, aircraft, ships, ocean buoys) into a global climate model to reconstruct the state of the atmosphere, but they have different temporal ranges. T_{NCEP} began before 1956 and continues to today and covers my entire study period. T_{ERA} is available from 01/09/1957 to 31/08/2002 so it can be used in the prediction of Floods 3 to 48 only. Like Ng and Liu (2009), I do not use the temperature data from Tien Shan Weather Station (41.92°N, 78.23°E) in Kyrgyzstan because gaps in this dataset make its application difficult.

Ng and Liu (2009) reported values of c estimated by other authors. They derived the other two sub-model parameters, k and T_0, by a nonlinear regression that fits eqn. 4-2 to the 13 reliable flood volumes in Table 4-1. The idea is that the daily melt volume predicted by eqn. 4-2, when summed over the known filling period in the run-up to each of these 13 jökulhlaups, should match each observed flood volume, because Merzbacher Lake is seen to drain completely during floods. The same method is used here to find k and T_0, assuming Ng and Liu's 'typical' value of c, $0.33 \ (\pm 0.06) \times 10^5$ m^3 s^{-1}. Table 4-2 lists the parameter values corresponding to the T_{NCEP} and T_{ERA} temperature forcings.

Table 4-2. Values of the parameters k and T_0 of the lake water supply sub-model, derived using a nonlinear multivariate regression that fits eqn. 4-2 to 13 measured lake volumes (Table 4-1). Parameters are derived separately for the two temperature forcings, T_{NCEP} and T_{ERA}.

Temperature Forcing	k [10^5 m^3 day^{-1} °C^{-1}]	T_0 [K]	r^2
T_{NCEP}	1.05	2.65	0.877
T_{ERA}	1.13	5.65	0.830

4.3.4 Probability distributions of flood volume and timing

Armed with eqns. 4-1a and 4-2, the flood dates in Table 4-1 can be used to derive an empirical probability distribution of historical flood volumes, which in turn helps gauge
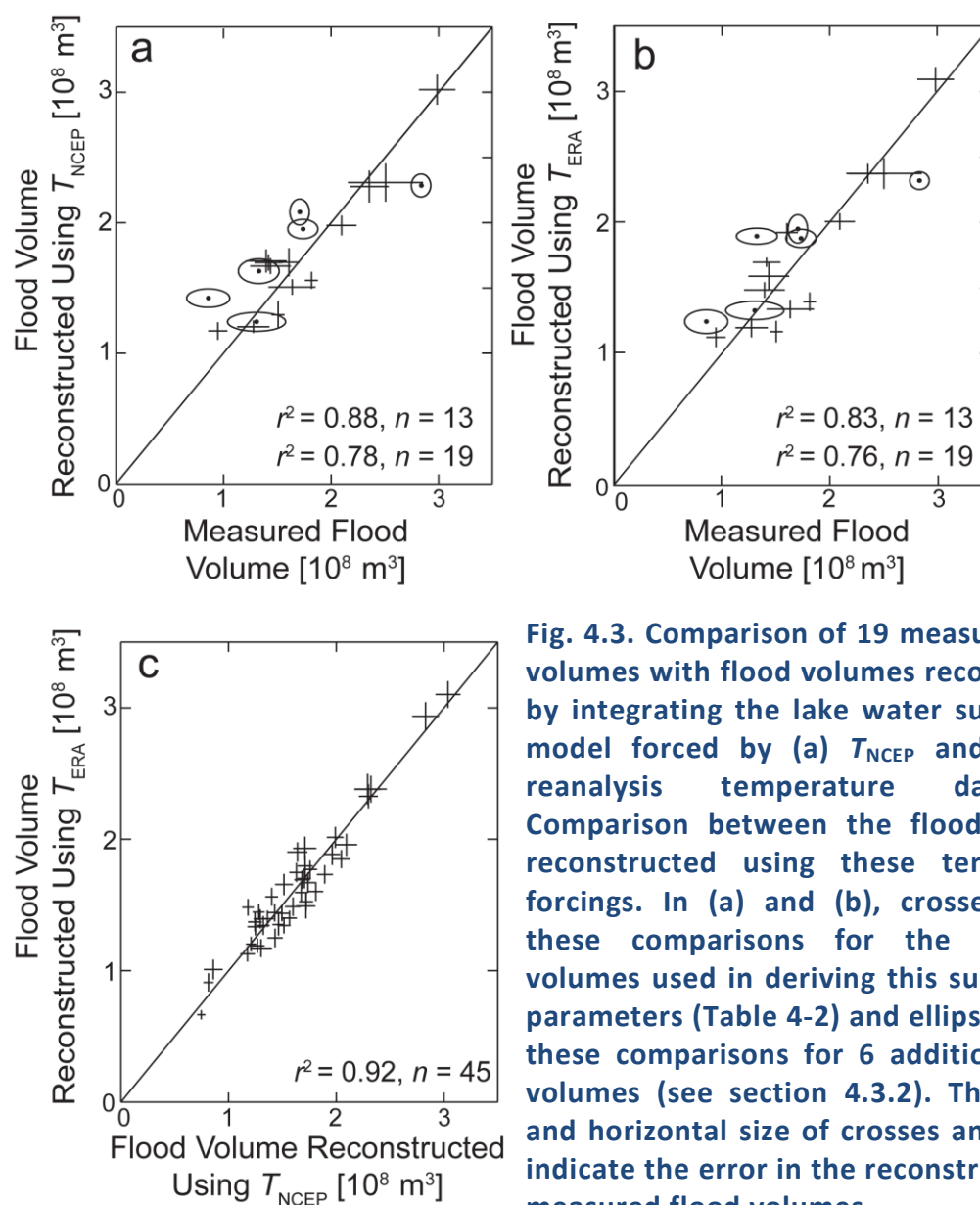
Fig. 4.3. Comparison of 19 measured flood volumes with flood volumes reconstructed by integrating the lake water supply sub-model forced by (a) T_{NCEP} and (b) T_{ERA} reanalysis temperature data. (c) Comparison between the flood volumes reconstructed using these temperature forcings. In (a) and (b), crosses display these comparisons for the 13 flood volumes used in deriving this sub-model's parameters (Table 4-2) and ellipses display these comparisons for 6 additional flood volumes (see section 4.3.2). The vertical and horizontal size of crosses and ellipses indicate the error in the reconstructed and measured flood volumes.

the size and timing of future floods. Here this is done in three steps. First the volumes of the floods in Table 4-1 are reconstructed by integrating eqn. 4-1a over the period between each pair of successive flood dates, filling the lake from empty. Two separate reconstructions are made with T_{NCEP} and T_{ERA} as forcings, with eqn. 4-2 taking the corresponding parameters in Table 4-2. With the NCEP and ERA forcings, this procedure reconstructs 53 and 45 flood volumes, respectively (Table 4-1). Fig. 4.3 compares these two sets of results with the 19 observed volumes in Table 4-1 and with each other. The uncertainties in the reconstructed flood volumes, quoted in Table 4-1 and denoted in Fig. 4.3 by the size of the error bars and the 'error ellipses', are estimated by conducting the reconstruction many times, each time introducing artificial errors to the reconstruction's inputs. The size of each uncertainty is the standard deviation of the distribution of volumes obtained for the corresponding flood. The good agreements shown by these plots support the use of both temperature data sources for flood-date prediction.

Next I form a cumulative probability distribution to represent the likelihood that a flood does not exceed a certain size, a volume V_F. This is done by putting the reconstructed flood volumes in Table 4-1 in ascending order, counting the number of floods with volumes ≤ V_F, and turning the number into a fraction of the total, to represent probability. Fig. 4.4a plots the resulting probability distribution against V_F. It shows that historically, the mean and the median flood volumes have been similar, $\approx 1.64 \times 10^8$ m^3. No floods had V_F exceeding 3.2×10^8 m^3, and 83% of them had 1.1×10^8 m^3 < V_F < 2.2×10^8 m^3 (the interval between guides A and C in Fig. 4.4a). This volumetric range, where the cumulative probability rises steeply, highlights the size of most floods.

Finally, I use the distribution in Fig. 4.4a to characterise flood timing. I assume that the probability of a flood having volume ≤ V_F is also the probability that the lake filled to this volume should have already outburst. Hence, by calculating how long the lake takes to fill to this volume (from empty), one can determine the probability of a flood having occurred by this time after the date of the last flood. By varying V_F in this calculation, I can also determine how this probability changes with time. Fig. 4.4b shows such an *outburst probability curve* calculated with Flood 3 (t = 1957.7 year) as the starting time reference. At any point on the curve with probability P, the time value has been found by integrating eqns. 4-1a from t = 1957.7 years until the lake reaches a volume that equals the V_F-value corresponding to the same probability P in Fig. 4.4a.
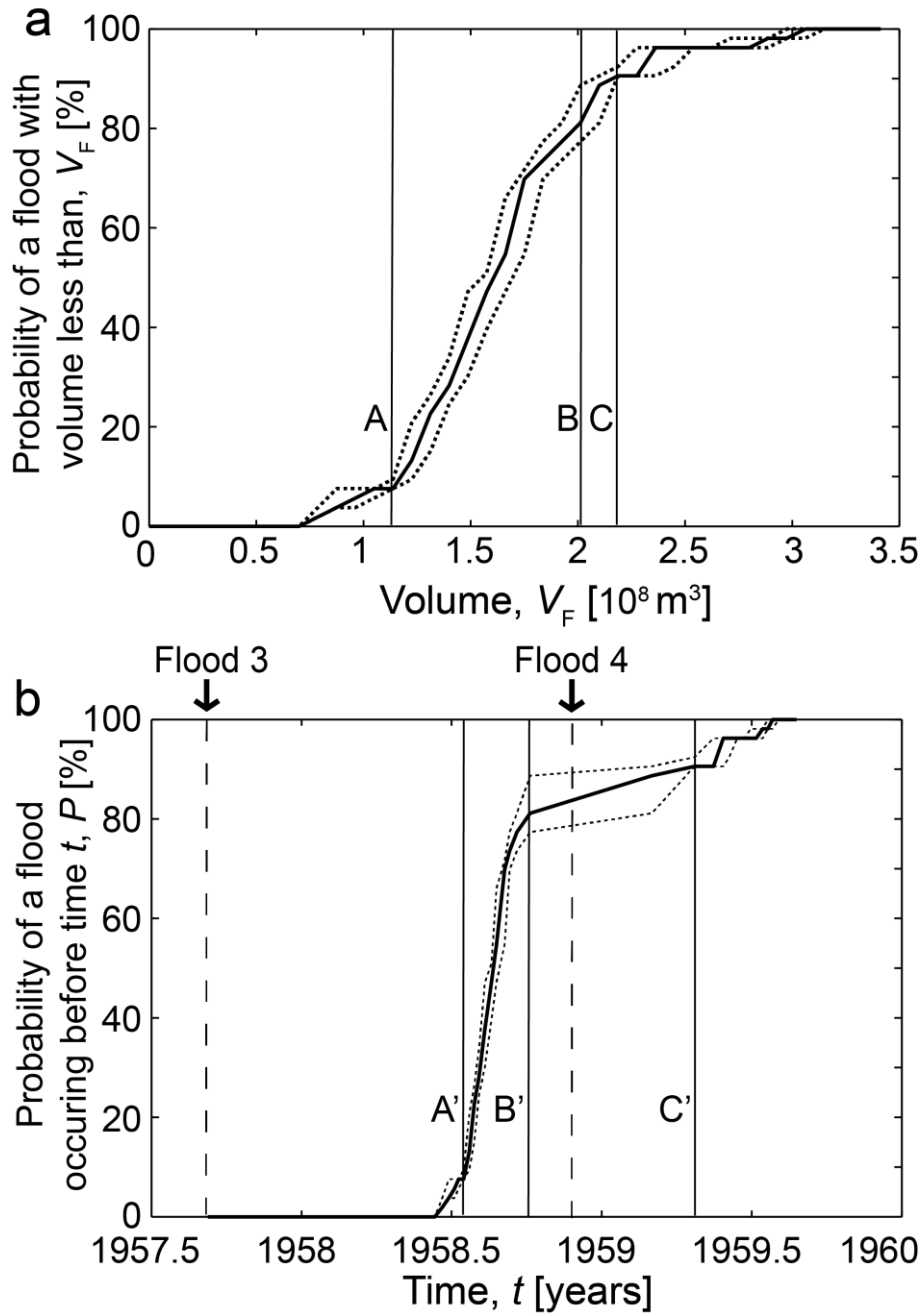
Fig. 4.4 Probability distributions of flood volumes and timing. (a) Percentage of jökulhlaups from Merzbacher Lake whose reconstructed volumes are less than V_F. (b) Probability of a flood having occurred before time t, given the modelled lake water supply between floods 3 and 4. The results derive from modelling where T_{NCEP} temperature data has been used to calculate the lake water supply. Dotted lines indicate upper and lower bounds on the volumes and probabilities based on the uncertainties in Fig. 4.3. The dates of Floods 3 and 4 (7th Sep 1957 and 24th Nov 1958) are marked by the vertical dashed lines. A, A', B, B', C and C' label the vertical guides described in Section 4.3.4.

Since the outburst probability curve combines information from the flood-volume distribution, the last flood date, and weather-dependent lake supply Q_{in} (which is seasonal, with peaks in summer and troughs in winter), probability curves constructed for other times using other floods in Table 4-1 (or future floods) as the starting reference will be different. However, Fig. 4.4b illustrates key features of such curves. Its shape derives from the curve in Fig. 4.4a, with the steep rise in outburst probability between A' and B' corresponding to the rise in cumulative probability between A and B in Fig. 4.4a. This rise occurs in 80 days (between 1958.53 and 1958.75 years). This is a manifestation of the 'focusing effect' discussed by Ng and Liu (2009; p.611 and Fig. 11), who showed that abundant meltwater supply during summer fills Merzbacher Lake rapidly and concentrates most of its outbursts in this period. In contrast, low supply towards the end of the melt season and through winter causes a slow increase in outburst probability with time. Fig. 4.4b shows that the interval B' to C' (corresponding to the interval B to C in Fig. 4.4a) is 200 days long but experiences only a 10% increase in outburst probability.

While useful, these results offer predictions whose validity relies wholly on past empirical data and that are probabilistic, unable to tell us each flood's size and timing. For instance, although Fig. 4.4b indicates a high probability of Flood 4 occurring by late August ($t \approx 1958.65$, $P = 50\%$) and a very high probability of this before early November (guide B', $P = 81\%$), the actual flood came later, on 24th November. Next I turn to the prediction of specific flood-dates.

4.4 Flood-date prediction models: threshold assumptions

This section details the four threshold assumptions to be used with eqns. 4-1 and 4-2 to hindcast the Merzbacher flood dates. Three of them concern the lake depth threshold h_c; the fourth invokes a mobile subglacial water divide. Each threshold assumption is labelled with an abbreviation (Table 4-3).

4.4.1 Constant Date (CD) model, and measures of prediction error

First I consider a naïve prediction model, called the Constant Date (CD) model, that does not implement an outburst threshold nor simulate filling of the lake, unlike the Ng-Liu model. The CD model postulates that the flood occurs on the same date each year, the motivation being that most Merzbacher flood dates cluster in the months of July to September (see histogram in Fig. 2 of Ng and Liu, 2009). Although this model neglects environmental influence on the system, it sets a benchmark for assessing other prediction models: those failing to match its performance are practically useless. In introducing it here, I also consider how to quantify prediction success.

Table 4-3. Summary of the five flood-date prediction models

No.	Model Name	Label	Equation	Tunable parameters [units]	Parameter Meaning
1	Constant Date	CD		Δ [day]	Calendar date on which flood occurs
2	Constant Threshold	CT	h_c = constant	h_c [m]	Constant threshold depth
3	Variable Threshold (lake rise rate)	VT$_h$	$h_c = h_{0\beta} + \beta \frac{dh}{dt}$	$h_{0\beta}$ [m]	Threshold depth if dh/dt = 0
				β [day^{-1}]	Sensitivity of threshold on the rate of lake-level rise
4	Variable Threshold (temperature)	VT$_T$	$h_c = h_{0\lambda} + \lambda(T - T_0)_{0+}$	$h_{0\lambda}$ [m]	Threshold depth if $T = T_0$
				λ [m °C^{-1}]	Sensitivity of threshold on temperature
5	Divide Model	DM	$\frac{dY}{dt} = -\alpha \left[Y - \left(\frac{h_{c\alpha} - h}{h_0} \right) \right]$	$h_{c\alpha}$ [m]	Threshold depth of the lake if there is no delay in the divide's arrival at the lake
				α [day^{-1}]	Rate constant of divide migration

The CD model assumes a fixed calendar date Δ (expressed in day of year) for all floods, where Δ is chosen by the forecaster to optimise prediction success. Using two trial values, Δ = 268 (25th September in non-leap years) and Δ = 216 (4th August in non-leap years), this model has been used to hindcast the next flood date on every day of the study period. Hence, each of these two sets of runs yields 19006 hindcasts (the total number of days in the study period: 3/07/1956 to 15/07/08). Fig. 4.5a shows their prediction errors, E, found by differencing each hindcast and the known date of the next flood (E is defined to be positive if the hindcast is early). Although the errors span a large range, most of them cluster within 100 days. The outlier errors are associated with floods that occurred after unusually long or short lake-filling periods.

A straightforward quantifier of the errors in Fig. 4.5a is their root-mean-square (RMS), and one can find the Δ that minimises the RMS error. But the RMS is not the only measure of prediction performance, nor necessarily the best measure, as it emphasises outliers. Other measures may be more desirable from a forecaster's viewpoint. For example, a good forecasting model may not be one with the lowest errors overall but one that gives the greatest number of 'successful' forecasts, i.e. forecasts near the actual flood dates. The histograms in Fig. 4.5b show the percentage frequency of the errors in the two trial runs. Their central bars, each 40 days wide, show that if one defines successful hindcasts as those having errors within ±20 days ($|E| \leq 20$), then the run assuming Δ = 216 yields five times more successful hindcasts (54.3%) than the run
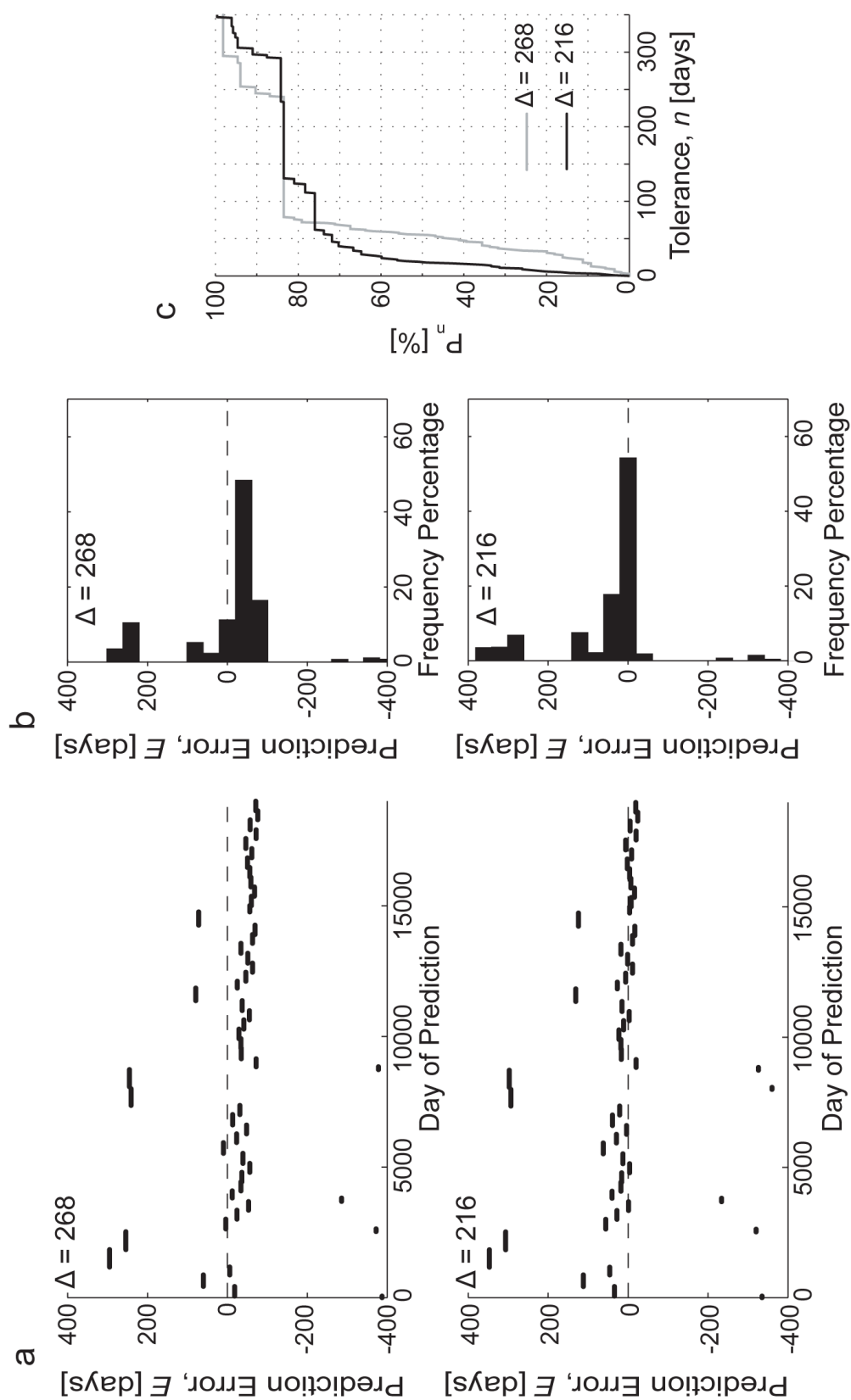
Fig. 4.5. Prediction errors obtained by running the Constant Date (CD) model with two different values of the model parameter, Δ = 268 days and Δ = 216 days. (a) Prediction errors for each day of the study period, (b) error frequency histograms and (c) the percentage of prediction errors within the tolerance n.

assuming Δ = 268 (11.2%). This percentage offers a measure of prediction success, and I call it 'P_{20}' (the subscript indicates the tolerance). In contrast to the RMS, P_{20} emphasises hindcasts that are relatively accurate over those that are out by a long way. It is a useful measure for the CD hindcasts because they miss some floods by over a year.

The CD model is optimised by making prediction runs with different Δ values and calculating the corresponding RMS and P_{20}. The results, in Fig. 4.6, show that the RMS is minimised at 121.9 days when Δ = 268 (then P_{20} = 11.2%), whereas P_{20} is maximised at 54.3% when Δ = 216 (then RMS = 133 days). These Δ choices are each optimal in their own right; each choice optimises one measure at the expense of the other, since RMS and P_{20} quantify different kinds of prediction success. In section 4.5, these measures and the approach described here are used to optimise all of the prediction models before their performance is evaluated.
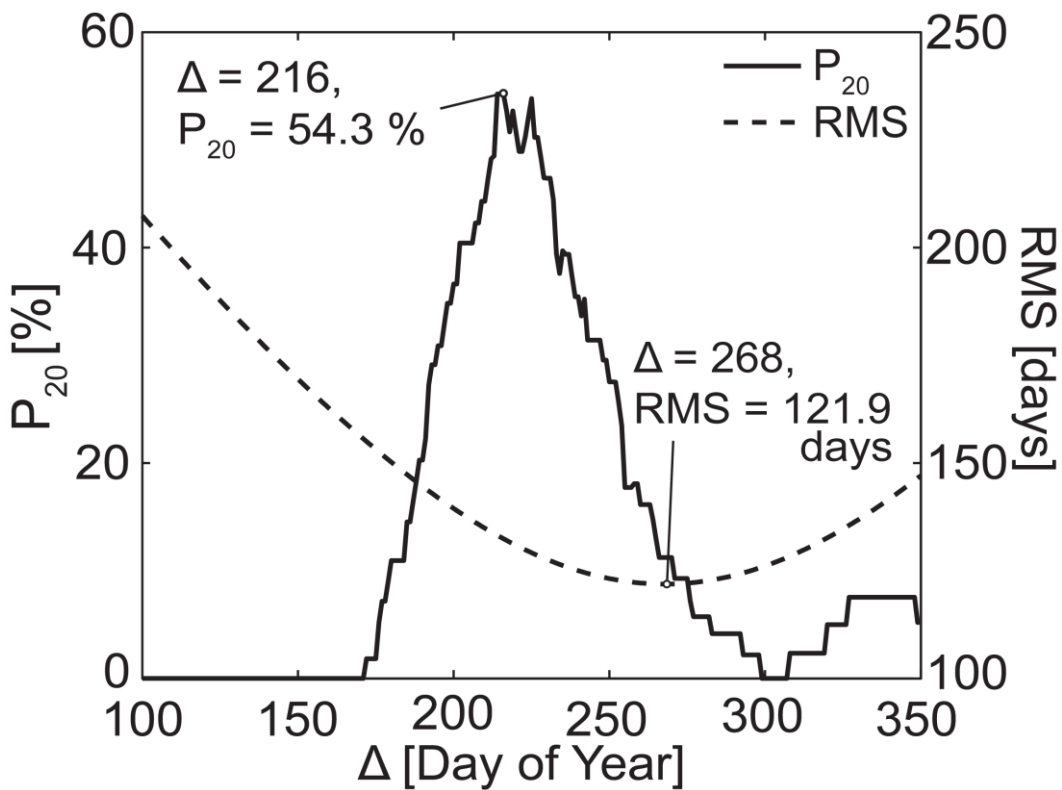
Fig. 4.6. Dependence of two measures of prediction success, P_{20} and RMS, on the parameter Δ in the Constant Date model. P_{20} is maximised with Δ = 216 and RMS minimised with Δ = 268. (The results in Fig. 4.5 are based on these parameter values.)

The tolerance of 20 days in the P_{20} measure is acceptable because jökulhlaup forecasts with such accuracy could be useful, but the tolerance choice depends on what one perceives as accurate. A general measure P_n considers a tolerance of $\pm n$ days, and this motivates another way of quantifying prediction errors. Fig. 4.5c plots the percentage

frequency of successful hindcasts for different tolerances; their window of admittance widens as n increases. The two curves relate the errors from the trial runs of Fig. 4.5a and rise monotonically. The perfect result would be zero errors for all hindcasts, plotting at 100% across the graph; in reality, one seeks a curve lying as close to the top-left corner of the graph as possible. Fig. 4.5c shows that the run that optimises P_{20} (Δ = 216; black curve) excels over the run that optimises RMS (Δ = 268; grey curve) for tolerances of tens of day. For $n > 72$ days, the latter run performs better on two occasions, but such tolerance is too large to be useful.

Other measures of prediction performance could be used. For instance, in order to facilitate flood mitigation and emergency evacuation, one might favour forecasts that are early as opposed to late and employ a one-sided definition of P_n based on $0 \le E \le n$. Generally, a suite of measures offer more complete characterisation of the prediction errors. The forecaster must decide which measures are more important in a given scenario and weigh their outcomes accordingly for decision making.
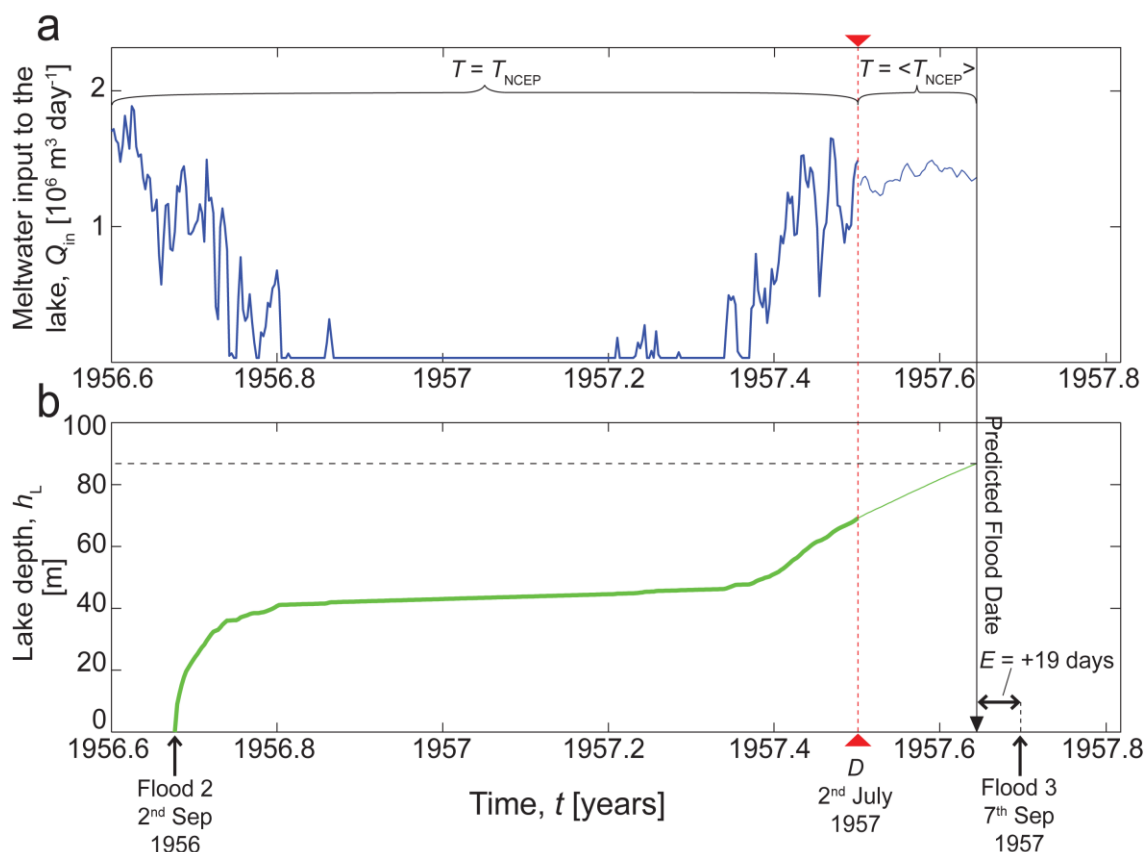
Fig. 4.7. Example of a Constant Threshold model prediction run made with the weather-forcing scheme. On day _D_ (2nd July 1957), the forecaster attempts to predict the date of Flood 3 (7th Sep 1957) by simulating histories of (a) lakewater supply rate and (b) lake depth. The lake water supply model is forced with T_{NCEP} daily temperature data on those days preceding _D_, and forced with the multi-year mean value of T_{NCEP} afterwards. With the outburst threshold h_c = 86 m, the flood-date hindcast is found to be 19th Aug 1957, and the corresponding prediction error is _E_ = +19 days.

4.4.2 Depth-threshold assumptions

In a real system, weather influences how fast the lake fills, and glaciohydrological factors govern the outburst condition of a flood, so prediction schemes incorporating environmental factors should excel over the Constant Date model. The Ng-Liu model is the simplest of such schemes: eqns. 4-1 has an adjustable outburst threshold h_c, and eqn. 4-2 captures the climatic dependence of lake filling. In the following I posit three alternative assumptions for the behaviour of h_c.

Constant Threshold (CT)

The simplest assumption, called Constant Threshold (CT), is that h_c is constant. Fig. 4.7 shows an example where it is used with the Ng-Liu model to hindcast Flood 3 in the Real Scheme (section 4.2). In this run, which assumes h_c = 86 m and that the forecaster made the prediction on 2 July 1957 (302 days after Flood 2), the flood hindcast is 19th August 1957, 19 days before the actual Flood 3. Many sets of prediction runs like this are made to hindcast the Merzbacher flood dates, while adopting different thresholds in the range 70 < h_c < 100 m and T_{NCEP} or T_{ERA} as weather forcing. Each set of runs uses a fixed combination of these inputs to produce next-flood hindcasts on every day of the study period and the prediction errors are compiled into the RMS and P_{20} as described in section 4.4.1. Fig. 4.8 shows how these error measures vary with h_c. For all values of h_c in the imposed range, prediction runs using the NCEP forcing yield lower RMS than runs using the ERA forcing, but the optimal values of h_c are similar: 87 m with NCEP and 86.5 m with ERA (Fig. 4.8a). P_{20} is maximised when h_c = 86.5 m with the NCEP forcing and
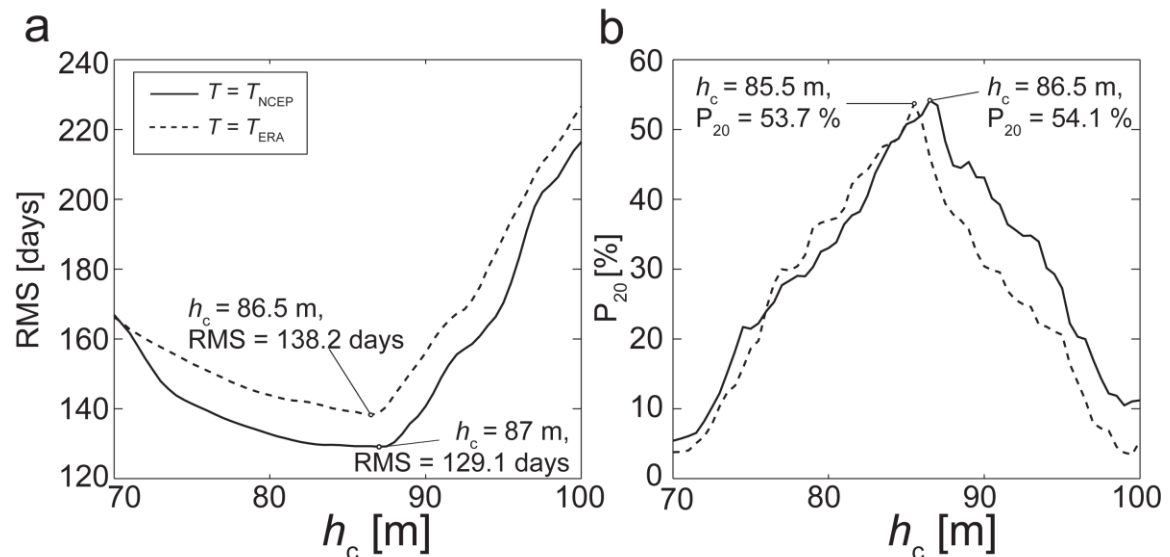
Fig. 4.8. Dependence of the prediction success of the Constant Threshold (CT) model, as quantified by (a) RMS error and (b) P_{20}, on the threshold value h_c. Solid and dashed lines correspond to results obtained using the T_{NCEP} and T_{ERA} weather-forcings respectively.

when h_c = 85.5 m with the ERA forcing (Fig. 4.8b). The value of h_c that optimises prediction performance thus falls within a narrow range (85.5 to 87 m). However, with the Constant Threshold assumption, the lowest achievable RMS is 129.1 days and the highest achievable P_{20} is 54.1%. This performance is worse than that of the Constant Date model (121.9 days, 54.3%). Thus, while using a threshold allows changing weather to be accounted by the model, a fixed threshold does not improve the flood-date predictions in the Real Scheme.

Variable Thresholds (VT$_h$ and VT$_T$)

The modelling explorations in the previous chapter and historical variability in h_c at Merzbacher Lake shown empirically in this chapter (see differences between the reconstructed flood volumes in section 4.3.4), suggest that one might improve the forecasts by using a threshold that responds to environmental conditions. This idea originates from Ng and Liu (2009), who reconstructed the lake-level history at Merzbacher Lake to extract h_c of each flood and the rate of lake-level rise (dh/dt) before it initiated. They found negative correlation between these two quantities (see their Fig. 15b) and interpreted it as being a result of pressure coupling between the lake and the subglacial hydraulics beneath the ice dam.

Motivated by this empirical finding, I explore two formulations of a variable threshold. The first formulation, labelled 'VT$_h$', is the linear model proposed by Ng and Liu (2009):

$$h_c = h_{0\beta} + \beta \frac{dh}{dt}$$

4-3

where $h_{0\beta}$ and β are constants. When using this with eqn. 4-1 to predict flood dates, h_c is calculated using the exponential moving average of dh/dt (with smoothing constant, S = 0.25; Brown, 1963). Ng and Liu (2009) determined $h_{0\beta}$ = 102 m and β = −58 day^{-1} for Merzbacher Lake from their correlation.

The second variable-threshold formulation, labelled 'VT$_T$', assumes control on h_c by surface temperature rather than the lake-level rise rate. The idea is that meltwater produced at the surface and penetrating to the glacier bed influences the subglacial outburst hydraulics. Hence, I suppose

$$h_c = h_{0\lambda} + \lambda(T - T_0)_{0+},$$

4-4

where $h_{0\lambda}$ and λ are constants. h_c is calculated using the exponential moving average of $(T - T_0)_{+0}$ (again with S = 0.25) and the same temperature data, weather-forcing scheme, and parameters as used in the lake water supply model in eqn. 4-2. Since dh/dt depends

on T via melt generation and lake filling, eqn. 4-4 is a more general threshold description than eqn. 4-3 in the sense that it encapsulates meltwater control on h_c via both the lake pressure and supraglacial water injection to the glacier bed.

When each formulation described here (VT_h or VT_T) is used with eqns. 4-1a and 4-2 to predict flood dates, I optimise the model in the same way as before, by minimising RMS and maximising P_{20}, but do so by searching over the corresponding two-parameter space (of $h_{0\beta}$ and β, or $h_{0\lambda}$ and λ).

4.4.3 Threshold based on subglacial water-divide migration (DM)

The final threshold assumption treats flood-initiation physics in more detail than any of the previous assumptions. It attempts to reproduce the dynamics of the subglacial water divide investigated in the last chapter that provided a mechanistic link between environmental conditions and flood size (see section 3-8). The full Nye-Fowler model is not used here because the basal topography of South Inylchek Glacier and the attendant hydraulic potential gradients are poorly known. Instead I attempt to capture key aspects of the full model's behaviour using the following expression for the time evolution of the divide's position;

$$\frac{dY}{dt} = -\alpha \left[Y - \left(\frac{h_{c\alpha} - h}{h_0} \right) \right].$$

<div align="right">4-5</div>

In this 'Divide Migration' (DM) model, h is the lake depth as before, Y measures the dimensionless distance of the divide from the lake, h_0 is the ice-dam flotation depth (estimated at 108 m by Ng and others (2007)), and $h_{c\alpha}$ and α are constants. The outburst condition $h = h_c$ in the Ng-Liu model is replaced by $Y = 0$, and eqn. 4-1 is modified to

$$\frac{dV}{dt} = Q_{\text{in}} \quad \text{when } Y > 0,$$

<div align="right">4-6a</div>

$$V = 0 \quad \text{when} \quad Y = 0.$$

<div align="right">4-6b</div>

During filling, this model describes the coupled evolution of lake volume and water divide position, with the divide migrating towards the target position $(h_{c\alpha} - h)/h_0$, which itself moves. The constant α controls the migration rate, and $h_{c\alpha}$ is the theoretical outburst depth of the lake if there were no delay in the divide's arrival at the lake. The water supply Q_{in} is calculated by eqn. 4-2 as before.

Equations 4-5 and 4-6a reproduce some aspects of the behaviour of the Nye-Fowler model. They can be solved analytically with constant and sinusoidally varying lake inputs to reveal how the divide's movement lags behind the forcing of the increasing lake

pressure during lake-filling. However, for use in the flood prediction model runs, with irregular weather forcing, the equations are integrated numerically using finite-difference, starting with $V = Y = 0$ on the day after the last flood. Low lake level initially locates the target downglacier from the lake, so the divide migrates into $Y > 0$. But filling of the lake relocates the target upglacier from the dam eventually (when $(h_{c\alpha} - h)/h_0 < 0$) attracting the divide back towards the lake after some delay. As with the models in section 4.4.2, the Divide Model is optimised by tuning α and $h_{c\alpha}$ over their parameter space.

4.5   Flood-date prediction experiments: results and discussion

Table 4-3 summarises my five prediction models. (For convenience the word 'model' is used to refer to the three versions of the Ng-Liu model with different thresholds, as well as to the Constant Date and Divide Migration models.) In this section I analyse their performance in prediction runs made to hindcast the Merzbacher flood dates. 18 sets of runs were made. The first 9 sets use the Real Scheme for weather forcing and consist of one set of runs for the CD model and two sets of runs each for the CT, VT_h, VT_T and DM models (one set with NCEP forcing, the other with ERA forcing). In each set of runs, model parameters were tuned to optimise prediction success separately in terms of RMS and P_{20}. Table 4-4 shows the results, listing in its columns the optimal model parameters and the RMS and P_{20} achieved when each of these is optimised. The other 9 sets of runs are structured identically but use the Simple Scheme for weather forcing. Table 4-5 shows the corresponding results.

Several matters guide the following analysis of these results: (1) model performance and the floods' predictability, (2) influences of model complexity and weather forcing on prediction success, and (3) the impact of weather uncertainty on the predictions. These matters are covered in sections 4.5.1 and 4.5.2. Section 4.5.3 looks at how the reliability of predictions varies with time, and this leads to the development of an ensemble prediction strategy that uses multiple prediction models to derive forecasts.

4.5.1 Prediction performance of the models

Since RMS and P_{20} are fundamentally different quantifiers of the prediction errors, a model optimised for RMS must yield lower RMS than the same model optimised for P_{20}, and a model optimised for P_{20} must yield higher P_{20} than the same model optimised for RMS. Table 4-4 confirms this expectation (compare the RMS's in column 4 with those in column 7, and the P_{20}'s in column 8 with those in column 5). Accordingly, further comparisons are now focused on columns 4 and 8. These show RMS around 120 days and P_{20} of 50–60%. The RMS values are not useful quantifiers of the models'

performances as they are disappointingly large and dominated by outlier errors (section 4.4.1). Thus, although Table 4 reports findings for both measures, forecasters of the Merzbacher floods might choose P_{20} as the main criteria for identifying the best model.

Considering the results in both columns 4 and 8 in Table 4-4, the overall pattern is that the Variable Threshold models (VT_h and VT_T) perform best, followed by the Divide Model (DM), then the Constant Threshold model (CT). This pattern is robust for each temperature forcing. Also, the CD model performs better than the CT model (as noted before), implying that a fixed threshold does not enhance prediction accuracy. Compared with the other models, the CD model performs nearly as well as the DM model but consistently worse than both Variable Threshold models. The latter models yield P_{20} = 57.3–57.5%, meaning they can hindcast the floods accurately to within 20 days about 57.4% of the time. Additional comparisons (not shown) with the generalised measure P_n (defined in section 4.4.1), show that the Variable Threshold models surpass all other models in the practical tolerance range $n \leq 20$. These results support the empirical finding of Ng and Liu (2009) and the theoretical finding from the previous chapter that dh/dt plays a role in flood-initiation physics. In the VT_h model used in the current chapter the optimal β-values are positive, not negative as found by Ng and Liu (2009); the threshold h_c found here needs to increase with dh/dt for successful prediction. The sign difference arises because the correlation analysis of Ng and Liu (section 4.4.2) and the fitting of flood hindcasts to observed flood dates do not amount to the same optimisation constraint for β.

Reassuringly, Table 4-4 shows that models incorporating environmental factors do better than the CD model. But does prediction success always improve with model complexity? A model with richer physics and more parameters ought to yield closer fit between hindcasts and observations, unless it is faulty. Hence model performance is expected to improve in the order: CD, CT, VT_h/VT_T, DM. The results upset this trend because the DM model performs worse than the VT models. The conclusion is that either the divide migration mechanism does not capture what happens at Merzbacher Lake, or it does but the DM model incorrectly mimics this mechanism.

Table 4-4 shows that the DM model improves upon the CT model in all cases. This is because these models are related. The CT model is the limit of the DM model as $\alpha \rightarrow \infty$: then the seal responds infinitely fast to lake-level changes to track the target, and the outburst condition $Y = 0$ in eqn. 4-5 becomes equivalent to $h = h_{c\alpha}$ (constant). Seen in this light, the DM model performs better because it has an extra degree of freedom over the CT model.

Table 4-4. Results from 9 sets of model runs using the Real weather-forcing scheme. For each of our five prediction models, listed in column 1, model parameters are optimised to minimise RMS and maximise P_{20}. The CT, VT_h, VT_T and DM models are optimised separately for each temperature forcing, T_{NCEP} and T_{ERA}. Displayed in columns 3 to 8 are the optimal model parameters and the RMS and P_{20} they yield.

Model	Temperature forcing	Optimised for RMS			Optimised for P_{20}		
		Optimal parameters	RMS	P_{20}	Optimal parameters	RMS	P_{20}
Constant Date (CD)	-	Δ = 268 days	121.9	11.2	Δ = 216 days	132.4	54.3
Constant Threshold (CT)	T_{NCEP}	h_c = 87.0 m	129.2	51.7	h_c = 86.5 m	129.3	53.3
	T_{ERA}	h_c = 86.5 m	138.3	45.9	h_c = 85.5 m	139.1	53.6
Variable Threshold (controlled by lake rise rate) (VT_h)	T_{NCEP}	$h_{0\beta}$ = 80.0 m, β = 90 days	112.6	15.3	$h_{0\beta}$ = 77.0 m, β = 30 days	123.0	57.4
	T_{ERA}	$h_{0\beta}$ = 78.0 m, β = 90 days	121.4	19.6	$h_{0\beta}$ = 75.5 m, β = 34 days	133.9	57.5
Variable Threshold (controlled by temperature) (VT_T)	T_{NCEP}	$h_{0\lambda}$ = 76.0 m, λ = 3.0 m $^{\circ}C^{-1}$	109.6	11.3	$h_{0\lambda}$ = 76.5 m, λ = 0.8 m $^{\circ}C^{-1}$	123.5	57.4
	T_{ERA}	$h_{0\lambda}$ = 76.0 m, λ = 4.0 m $^{\circ}C^{-1}$	118.0	11.6	$h_{0\lambda}$ = 76.5 m, λ = 0.9 m $^{\circ}C^{-1}$	133.6	57.3
Divide Model (DM)	T_{NCEP}	$h_{c\alpha}$ = 78.0 m α = 0.015 day^{-1}	117.2	27.1	$h_{c\alpha}$ = 84.5 m α = 0.170 day^{-1}	127.6	55.0
	T_{ERA}	$h_{c\alpha}$ = 78.0 m, α = 0.015 day^{-1}	127.9	22.2	$h_{c\alpha}$ = 82.5 m, α = 0.080 day^{-1}	136.6	54.5

4.5.2 Influence of weather forcing on prediction success

How does weather uncertainty influence the predictions? Such uncertainty features in the model runs implementing the Real Scheme in two ways: (i) via the difference between the NCEP and ERA temperature data, which themselves are estimates of a weather variable and (ii) via the fact that the forecaster does not know the future weather. The influence is assessed from both angles.

Considering the data sources first, Table 4-4 shows that the NCEP forcing yields consistently lower optimal RMS values than the ERA forcing, while the optimal P_{20} values are almost independent of the choice of forcing. Thus, NCEP temperature data seem to be only marginally better as a forcing for predicting the Merzbacher floods. As noted before, the choice of temperature forcing does not change the overall ordering of model performance (CT, DM, VT_h/VT_T) in Table 4-4.

Table 4-5. Results from 9 set of model runs using the Simple weather-forcing scheme, where archived weather is used throughout each prediction (see section 4.2). The layout is identical to that of Table 4-4.

Model	Temperature forcing	Optimised for RMS			Optimised for P_{20}		
		Optimal parameters	RMS	P_{20}	Optimal parameters	RMS	P_{20}
Constant Date (CD)	-	$\Delta = 268$ days	121.9	11.2	$\Delta = 216$ days	132.4	54.3
Constant Threshold (CT)	T_{NCEP}	$h_c = 83.0$ m	129.8	43.5	$h_c = 87.5$ m	137.7	50.6
	T_{ERA}	$h_c = 84.0$ m	139.4	52.6	$h_c = 84.0$ m	139.4	52.6
Variable Threshold (controlled by lake rise rate) (VT$_h$)	T_{NCEP}	$h_{0\beta} = 76.0$ m, $\beta = 99$ days	108.9	21.1	$h_{0\beta} = 76.5$ m, $\beta = 24$ days	126.1	55.6
	T_{ERA}	$h_{0\beta} = 78.5$ m, $\beta = 118$ days	120.3	11.6	$h_{0\beta} = 74.0$ m, $\beta = 52$ days	131.0	62.2
Variable Threshold (controlled by temperature) (VT$_T$)	T_{NCEP}	$h_{0\lambda} = 74.5$ m, $\lambda = 3.6$ m $^{\circ}$C^{-1}	108.1	12.2	$h_{0\lambda} = 75.0$ m, $\lambda = 1.0$ m $^{\circ}$C^{-1}	123.1	56.7
	T_{ERA}	$h_{0\lambda} = 70.5$ m, $\lambda = 5.0$ m $^{\circ}$C^{-1}	117.5	12.3	$h_{0\lambda} = 79.5$ m, $\lambda = 0.8$ m $^{\circ}$C^{-1}	131.8	58.4
Divide Model (DM)	T_{NCEP}	$h_{c\alpha} = 79.0$ m $\alpha = 0.02$ day^{-1}	116.0	25.7	$h_{c\alpha} = 85.5$ m $\alpha = 0.15$ day^{-1}	127.9	51.3
	T_{ERA}	$h_{c\alpha} = 80.0$ m, $\alpha = 0.02$ day^{-1}	126.4	21.1	$h_{c\alpha} = 79.0$ m, $\alpha = 0.06$ day^{-1}	134.5	53.5

And what of the need to forecast future weather in the Real Scheme? The impact of this on prediction performance is assessed by comparing Table 4 with Table 5, focusing again on the optimal RMS and P_{20} results in columns 4 and 8. The Simple scheme ought to perform better than the Real scheme because it uses reanalysis data rather than forecasts of future daily temperature to derive the lake water supply, and this eliminates a source of uncertainty. Tables 4-4 and 4-5 show that only the Variable Threshold models that use the ERA forcing fulfil this expectation. In contrast, the Variable Threshold models that use the NCEP forcing perform worse in the Simple scheme than in the Real scheme. The same is true of the CT and DM models, but the poorer performance of these models suggests that they are limited more by other deficiencies (notably in their threshold assumptions) than by weather uncertainty. However, it is less clear why the Variable Threshold models with NCEP forcing do not perform better in the Simple Scheme. A possible explanation is that short-term weather fluctuations are more accurately represented by T_{ERA} than by T_{NCEP}, even though these temperature forcings produce similar melt-water volumes on seasonal and annual timescales (e.g. Fig. 3a) and

have similar multi-year means so that their flood-prediction performances in the Real Scheme are similar (Table 4-4).

4.5.3 The forecaster's time frame and ensemble prediction

Having used the statistical measure RMS and P_{20} to evaluate performance of the models, I now turn to a different aspect of the forecasting problem. As each prediction is made, the forecaster may wish to know whether its reliability depends on how far the next flood lies in the future. Given the impact of weather uncertainty examined above, a reasonable hypothesis is that predictions close to the flood are more successful than those made far in advance. This time dependence is studied using the hindcast results produced during optimised model runs using the two best models in Table 4-4: VT_h with T_{ERA} temperature forcing, and VT_T with T_{NCEP} temperature forcing.

On the day when each prediction is made, D, the forecaster cannot in fact determine the difference between D and the next flood because the flood has not occurred. However, they know the time difference between D and the predicted flood date. I denote by N this 'predicted time before the next flood'. N is easily calculable for the two sets of hindcast results.
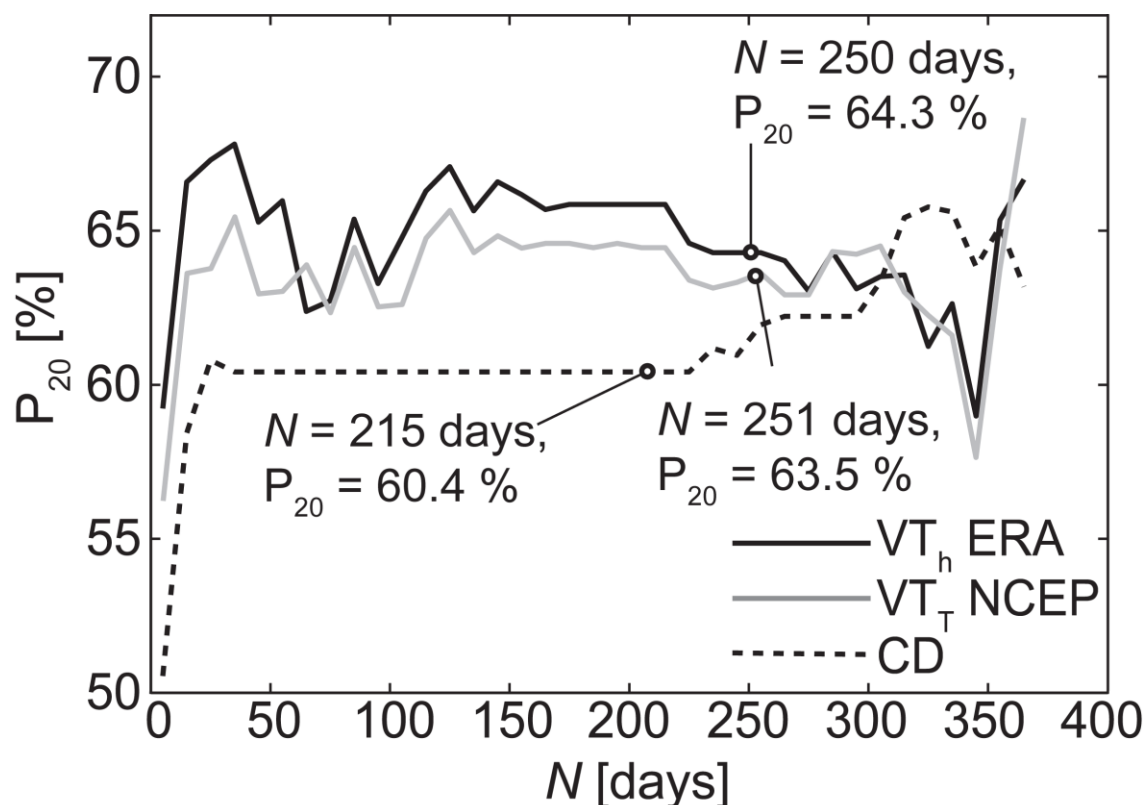

Fig. 4.9. The variation of prediction success (as quantified by P_{20}) with the predicted time before the next flood, N, for three models: the Constant Date model (CD), the Variable Threshold model VT_h with T_{ERA} temperature forcing, and the Variable Threshold model VT_T with T_{NCEP} temperature forcing.

Fig. 4.9 shows how the success of hindcasts (measured with P_{20}) varies with N in the two Variable Threshold models, with the data for N arranged in 10-day bins to suppress noise on the distributions. Results of the Constant Date model are included for comparison. In practice, after predicting a flood date with a given model, the forecaster can look up the corresponding distribution on this plot to learn the probability that the forecast is accurate to within 20 days. Both Variable Threshold models excel over the CD benchmark for most of the range in N, and the VT_h model with the ERA temperature forcing performs best overall. The distributions of both Variable Threshold models seem to be consistent with the hypothesised increase in prediction success as the next flood approaches, as they show a negative (albeit weak) trend. In the Real Scheme, prediction runs that forecast an imminent flood (with a small value of N) would have used more archived temperature data and fewer forecasts of future weather for deriving the lake-water supply and hence be more likely to be accurate. The CD model shows no such trend as it does not incorporate weather forcing.

The empirical probabilities in Fig. 4.9 motivate an *ensemble prediction strategy*. The forecaster predicts the next flood date using each of the models (VT_h, VT_T and CD), then calculates the values of N for these predictions, and reads the corresponding probabilities of prediction success from Fig. 4.9. In the simplest strategy, the forecast having the highest P_{20} is taken as the best guess of the flood date. Consider using this ensemble method on 1st Jan 1959 (this is 38 days after the date of Flood 4, 24th Nov 1958) to forecast Flood 5 (19th Sep 1959). The CD model predicts the next flood on 4th Aug 1959, whereas the VT_h and VT_T models predict it will occur on 8th Sep 1959 and 9th Sep 1959, respectively. The circles in Fig. 4.9 mark the corresponding values of N (215 days, 250 days, 251 days) and P_{20} (60.4 %, 64.3 %, 63.5 %). In this example, the forecaster learns that the best forecast is the one made by the VT_h model, 8th Sep 1959. The P_{20} of this forecast (64.3 %) is much higher than the mean P_{20} of this model in Table 4-4 (57.5 %). In fact, this forecast is successful (accurate to within 20 days) and has a true error of $E = 11$ days, while the true errors of the other two forecasts by the VT_T and CD models are 10 days and 46 days, respectively. This ensemble strategy allows the forecaster to choose between models based on empirical experience.

4.6   Conclusions and outlook

Low-order models that implement an outburst threshold based on the lake-water depth can give useful predictions of the date of jökulhlaups from Merzbacher Lake. The best models studied here (VT_h and VT_T) assume a variable threshold depth governed by weather. They hindcast observed flood dates successfully to within ±20 days 57.4 % of the time, excelling over a benchmark model that assumes a constant flood date each

year. For the Merzbacher Lake – Inylchek Glacier system, these models can be readily incorporated into practical flood-forecasting schemes, and may aid decisions regarding the development of hydropower down-valley and management of the corresponding reservoirs (Mamatkanov and Mingtszyan, 2011). The present work complements the theory by Ng and Liu (2009) that addressed mechanisms underlying the long-term timing pattern of multiple floods.

Although one can understand why predictions made far in advance of flood events are generally less reliable (sections 4.5.3), it is less clear why weather uncertainty impacts differently on the success of model predictions made with NCEP and ERA temperature forcings (section 4.5.2). A limitation of the current work is the use of these reanalysis data, which are themselves uncertain estimates of the past weather. By comparing them to meteorological measurements at the lake, future work could evaluate how severely such uncertainty affects jökulhlaup predictability. For example, reanalysis data may prove completely incapable of reproducing short-term (e.g. daily) weather variations, limiting the prediction ability of models that use such data.

An ability to forecast flood dates to within ±20 days a little more than half of the time is not overwhelmingly successful, and reflects how, despite attempts at physical modelling such as that in the previous chapter, the physics of flood initiation in real systems are still understood only poorly. The threshold assumptions in our best models (h_c = f(dh/dt) and h_c = f(T - T_0)) support an earlier inference by Ng and Liu (2009) that, at Merzbacher Lake, dh/dt influences the outburst threshold through the dynamics of a subglacial water divide. Further consideration of how this behaviour arises could illuminate the flood initiation process. Notably, although the Divide Migration (DM) model was designed to mimic the divide's dynamics, it does not yield the most successful flood-date predictions. In that model a parameter that controls the divide migration rate was kept constant during model runs and tuned to optimise the model. The findings of the investigation of the Nye-Fowler model presented in the last chapter suggests that the migration rate may not be constant and instead may be controlled by the supply of water to the channel along its length beneath the ice-dam. Further work could incorporate this control in a modified Divide Migration model by allowed the migration rate constant to vary with weather conditions. Also, in future work it will be worthwhile applying the full Nye-Fowler model to the Merzbacher Lake system, optimising it and quantifying its prediction ability. Problems associated with the uncertain geometry of the South Inylchek Glacier could be avoided by conducting the optimisation with a number of plausible bed geometries. Aside from illuminating flood initiation physics, applying the full model to Merzbacher Lake may allow our ability to predict flood size and duration to be quantified.

Future work could explore several other extensions. First, observations show that after a lake empties in a jökulhlaup, water entering the lake basin may flow directly into the glacier dam as an open subglacial stream for some time before the lake reforms (e.g. Bartholomaus and others, 2011). In Chapter 6 I develop and analyse a model capable of simulating flood cycles that include such periods of open-channel flow. I derive an expression for the duration of periods of open-channel flow and show how it depends on ice thickness, lake input and the size of the preceding flood. This could be incorporated into improved prediction models in the future. Second, the rate of calving from the ice dam, c, which affects lake-water balance (see Eqn. 4-2), may vary in time and depend on factors like the lake water depth. This variability could be accounted for in prediction models using some form of 'calving law' (e.g. Benn and others, 2007). Third, the ensemble prediction strategy in section 4.5.3 could be developed to exploit weighted averages of the predictions from different models.

Chapter 5   The coupling of flood discharge with glacier flow during jökulhlaups

This chapter is based on a manuscript entitled "Modelling the coupling of flood discharge with glacier flow during jökulhlaups" accepted for publication in the Annals of Glaciology on the 29th August 2012 and published online in December 2012.

5.1   Introduction

In Chapter 3 I simulated jökulhlaup cycles using the Nye-Fowler model and showed how their size is controlled by the time evolution of a subglacial channel. In simulations, this evolution depends on, among other things, the input of water to the channel along its length. This input was presumed to originate from an adjacent higher-pressure drainage system but, for simplicity, in simulations I assumed it remained uniform in time and constant in space. This ignores potential variations in the input due to changes in water pressure in the channel and in the adjacent drainage system. Such variations could affect jökulhlaup dynamics and the motion of the glacier. In this chapter I replace the uniform, constant channel water input with a temporally- and spatially-varying water transfer from an adjacent, distributed linked-cavity system (see section 2.3). This allows me to investigate how this variable input affects floods and, because cavities are maintained by ice flow of glacier ice over its bed, how flood discharge and glacier flow are coupled during jökulhlaups.

Such coupling has been observed in alpine jökulhlaup systems as 'ice-motion' events, such as speed-up (Anderson et al., 2005; Bartholomaus et al., 2011; Mayer et al., 2008; Riesen et al., 2010; Sugiyama et al., 2010) and uplift (e.g. Anderson et al., 2005; Magnusson et al., 2011 Sugiyama et al., 2008) during flood growth followed by deceleration or reversal in ice flow during flood recession (Anderson et al., 2005; Magnusson et al., 2011; Sugiyama et al., 2008). This coupling also occurs in ice sheets. Studies in Greenland show that surface meltwater routed via supraglacial lakes and moulins to the bed can cause short-term changes in surface velocity (Das et al., 2008; Zwally et al., 2002) and seasonal ice speed-up (Bartholomew et al., 2011). These observations raise the question of whether and how much climate-warming induced changes will increase the long-term ice flux (e.g. Schoof, 2010; Sundal et al., 2011).

In this chapter, studying alpine jökulhlaups only, I build on previous work and present a consistent model of this coupling. Recent numerical studies have highlighted the rich hydrological and glacier-dynamical behaviour that can arise when the Nye-Fowler model's evolving channel coexists with a distributed drainage system. Flowers et al.

(2004) showed that lake water injected into a subglacial water sheet, that in turn feeds and rapidly enlarges a channel, can explain the fast-rising discharge seen at the start of the 1996 Grímsvötn flood hydrograph (Björnsson, 2002), not reproducible using Nye's equations (Jóhannesson, 2002). Pimentel and Flowers (2011) added other processes to this description – high-order glacier dynamics, basal sliding, ice hydraulic fracture and ice uplift – to explore several glacio-hydraulic scenarios, including the drainage of marginal and surface lakes. Since these studies did not focus on flood dynamics, they prescribed a known discharge at the top end of the drainage system and did not couple its pressure to the lake's pressure. This precluded investigation of the controls on floods and the simulated pressure in the drainage system was generally inconsistent with the lake's pressure. In the present work, using the Nye-Fowler model avoids these limitations; a channel is coupled to a lake both in terms of discharge and pressure.

Hewitt and Fowler (2008), who proposed a theory to explain seasonal waves on glaciers, provide a model of distributed drainage and sliding. By linking channelised subglacial drainage to cavity drainage with sliding, they showed that periodic meltwater input to this system can cause oscillations in ice flow resembling observations. I adopt some of their equations below to describe a distributed linked-cavity system.

This chapter is organised as follows. My model of lake drainage through a coupled channel-cavity system is described in section 5.2. Section 5.3 reports the results of numerical simulations using the same idealised lake and glacier geometries used in Chapter 3. I show that the coupled model can simulate repeating floods when the cavities transfer water to the channel at a sufficient rate and investigate the spatial and temporal evolution of cavity water pressure and the associated motion of the glacier. I also investigate how varying the background meltwater input to the cavities affects lake drainage and the glacier dynamics response to it. I discuss these findings alongside field observations from several jökulhlaup lakes in section 5.4.

5.2   Channel-cavity drainage model

Fig. 5.1 shows my model system. A lake feeds a subglacial channel of length s_0, which exchanges water with a distributed system of linked cavities outside it; the cavities influence and are influenced by sliding. As in previous chapters, I denote distance downglacier from the lake by s and time by t. Here I introduce the subscripts R and C to label channel ('R' for Röthlisberger) and cavity variables, respectively. While I aim to couple flood and ice-flow dynamics, three specific 'couplings' occur in the model: between lake and subglacial drainage, between the channel and cavities, and between cavities and sliding.

a

Marginal Lake

Q_{in}

Outlet

Glacier

h_L

S

u_b

Cavity-channel drainage system

H

b

Cavities

Channel

⇧ Transfer between cavities and channel, T

➡ Cavity discharge, Q_C

⇨ Channel discharge, Q_R
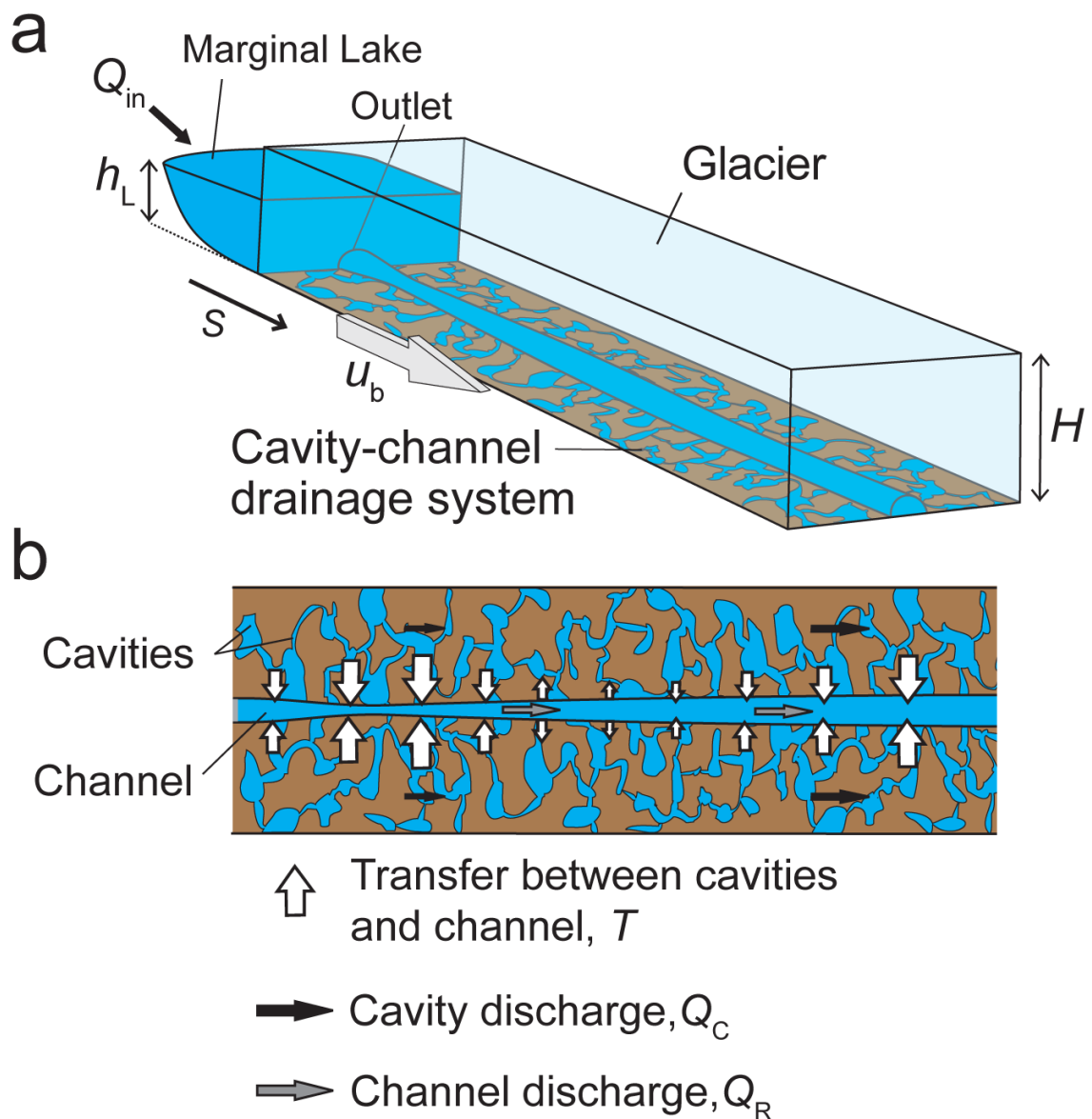
Fig. 5.1. Cartoon of my model jökulhlaup lake that drains through a cavity-channel system.

5.2.1 Channelised drainage

As in Chapter 3, the channel's cross-sectional area, S^*, evolves with time, t^*, according to eqn. 2-59:

$$\frac{\partial S_R^{\,*}}{\partial t^*} = \frac{|Q_R^{\,*}|^3}{S_R^{\,*\frac{8}{3}}} - S_R^{\,*} N_R^{\,*3}$$

<div align="right">**5-1**</div>

where Q^* is the discharge, N^* is the effective pressure and asterisks denote variables that have been nondimensionalised as described in section 2.2.4. In the channel the gradients in the discharge and the effective pressure are given by

$$\frac{\partial Q_R^*}{\partial s^*} = \epsilon_R (r-1) \frac{|Q_R^*|^3}{S_R^{*\frac{8}{3}}} + \epsilon_R S_R^* N_R^{*3} + T^*(N_R^*, N_C^*),$$

<div align="right">**5-2**</div>

$$\frac{\partial N_R^*}{\partial s^*} = \frac{1}{\delta}\left(\frac{Q_R^*|Q_R^*|}{S_R^{*\frac{8}{3}}} - \psi^*\right).$$

<div align="right">**5-3**</div>

The above three equations form the channelised component of the coupled model. They are identical to the original Nye-Fowler model (eqns. 2-60 and 2-61) except the source term in the original mass conservation equation, M^*, has been replaced by a transfer term T^*. This represents the rate of water transfer into the channel from the cavities (as a volume flux per unit distance). Following Hewitt and Fowler (2008) I model this transfer of water as proportional to the pressure difference between these drainage components. Dimensionally this is

$$T = R_k k(N_R - N_C),$$

<div align="right">**5-4**</div>

where N_C is the cavity effective pressure and k is a connectivity constant (I use Hewitt and Fowler's value, 10^{-9} m^2 s^{-1} Pa^{-1}). R_κ is a dimensionless factor used in experiments (section 5.3) for varying the transfer rate $R_\kappa k$ that saves me from writing out its units each time. In non-dimensional form, the channel water continuity equation is therefore

$$\frac{\partial Q_R^*}{\partial s^*} = \epsilon_R (r-1) \frac{|Q_R^*|^3}{S_R^{*\frac{8}{3}}} + \epsilon_R S_R^* N_R^{*3} + R_k \kappa_R (N_R^* - N_C^*),$$

<div align="right">**5-5**</div>

where

$$\kappa_R = \frac{N_{R0} s_0}{Q_{R0}} k.$$

<div align="right">**5-6**</div>

As in previous chapters, the lake depth h_L (Fig. 5.1) evolves with water input, Q_{in}, and outflow, Q_R at the lake outlet, following the lake continuity equation,

$$\frac{dh_L^*}{dt^*} = \frac{\lambda_L}{h_L^{*p_L-1}}[Q_{in}^* - Q_R^*(0, t^*)].$$

<div align="right">**5-7**</div>

The lake's depth defines the effective pressure in the channel at the lake outlet (Fig. 5.1) to be

$$N^*(0, t^*) = \beta_R[1 - h_L{}^*]$$

<div align="right">**5-8**</div>

at all times, and this provides a boundary condition for N_R in eqn. 5-3. The nondimensional parameters δ, ϵ_R, r, λ_L and β_L, and the scales of the channel variables were defined in Chapter 2, and summarised in Box 2-1.

5.2.2 Linked-cavity drainage and basal sliding

I follow Hewitt and Fowler (2008) in using a pseudo-steady description for the geometry of the cavities, with a conservation equation for the water flux through them and a sliding law. For sliding at velocity u_b over bed obstacles of height R, Walder (1986) showed that the typical cavity cross-sectional area is given by eqn. 2-112,

$$S_C = \frac{\pi}{4}\left[Ru_b + (1 - \gamma)\frac{Q_C}{Lk_1\rho_i}G\right]\frac{1}{K_0}\left(\frac{n}{N_c}\right)^n,$$

<div align="right">**5-9**</div>

where $\gamma \approx 0.32$ and $k_1 \approx 1.1$ are constants, L is water's latent heat of fusion, ρ_i is the density of ice, K_0 is an ice flow parameter (= 10^{-24} Pa^{-3} s^{-1}), Q_C is the water discharge through the cavity system and G is the total hydraulic potential gradient. In the above expression the first term in the square brackets represents enlargement of the cavities due to the sliding of ice past bed obstacles and the second term represents enlargement through melt due to heat dissipation in water as it flows through the potential gradient G. In the channelised model, G is given by eqn. 2-22; substituting this into the expression yields the cavity-geometry equation,

$$S_C = \frac{\pi}{4}\left(Ru_b + (1 - \gamma)\frac{Q_C}{Lk_1\rho_i}\left(\frac{\partial N_C}{\partial s} + \psi\right)\right)\frac{1}{K_0}\left[\frac{n}{N_c}\right]^n.$$

<div align="right">**5-10**</div>

Walder (1986) related the cavity cross-sectional area to the discharge and the total along-glacier hydraulic gradient using Manning's equation (eqn. 2-4),

$$\frac{Q_C}{S_C} = \frac{R_H{}^{\frac{2}{3}}}{n'}\left[\frac{1}{\rho_w g}\left(\frac{\partial N_C}{\partial s} + \psi\right)\right]^{\frac{1}{2}},$$

<div align="right">**5-11**</div>

and assumed the cavity roof is elliptical in cross-section

$$R_H \approx \frac{\pi R}{4k}.$$

<div align="right">5-12</div>

Substituting eqn. 5-12 into eqn. 5-11, and the result into eqn. 5-10, yields the following relationship between S_C and Q_C:

$$S_C = \left(\frac{\pi R}{4k_1}\right)^{-\frac{2}{3}} (\rho_w g)^{\frac{1}{2}} n' Q_C \left(\frac{\partial N_C}{\partial s} + \psi\right)^{-\frac{1}{2}}.$$

<div align="right">5-13</div>

I adopt a power law, discussed in section 2.3.2, to describe sliding,

$$u_b = c_s \frac{\tau_b^{p_b}}{N_C^q}$$

<div align="right">5-14</div>

(e.g. Bindschadler, 1983), where p_b = 4, q = 1, c_s is a constant dependent on bed roughness ($\approx 2 \times 10^{-20}$ m s^{-1} Pa^{-3}; Hewitt and Fowler, 2008), τ_b is the basal shear stress assumed to balance local driving stress $\rho_i g H \sin\phi_s$ where ϕ_s is glacier surface slope (Cuffey and Paterson, 2010). Out of several theories discussed in section 2.3.2 I use this power law because it is the simplest that includes the effect of water pressure on sliding (Hewitt and Fowler, 2008) and has been verified experimentally (Budd et al., 1979). Substituting this sliding law into the cavity geometry equation (eqn. 5-10) yields

$$S_C = \frac{\pi}{4}\left(R\frac{c_s\tau_b^{p_b}}{N_C^q} + (1-\gamma)\frac{Q_C}{Lk_1\rho_i}\left(\frac{\partial N_C}{\partial s} + \psi\right)\right)\frac{1}{K_0}\left[\frac{n}{N_c}\right]^n.$$

<div align="right">5-15</div>

A final equation describes water conservation in the cavities:

$$\frac{\partial S_C}{\partial t} = M_C - \frac{\partial Q_C}{\partial s} - T,$$

<div align="right">5-16</div>

where M_C is the background water supply to the cavities from basal- and surface-derived melt. I assume that the channel receives meltwater only via the cavities (through T) and none directly via moulins or other englacial routes.

5.2.3 Nondimensionalisation

Scales for s, t and ψ are the same as those used in the Nye-Fowler model (see Box 2-1). Similarly, the scale for the channel effective pressure defines the cavity effective pressure scale. Scales for the other cavity variables are defined as follows:

$$S_C{}^* = \frac{S_C}{S_{C0}}, \qquad Q_C{}^* = \frac{Q_C}{Q_{C0}}, \qquad M_C{}^* = \frac{M_C}{M_{C0}}, \qquad \tau_b{}^* = \frac{\tau_b}{\tau_{b0}}.$$

<div align="right">**5-17**</div>

Substituting the appropriate scales into eqn. 5-13 and equating terms defines S_{C0} with respect to Q_{C0} and ψ_0:

$$S_{C0} = \frac{Q_{C0}}{c_m \psi_0^{\frac{1}{2}}},$$

<div align="right">**5-18**</div>

where

$$c_m = \left(\frac{\pi R}{4k_1}\right)^{\frac{2}{3}} (\rho_w g)^{-\frac{1}{2}} \frac{1}{n'}.$$

<div align="right">**5-19**</div>

This leaves

$$S_C{}^* = Q_C{}^* \left(\delta \frac{\partial N_C{}^*}{\partial s^*} + \psi^*\right)^{-\frac{1}{2}},$$

<div align="right">**5-20**</div>

where δ is the same as in the channelised model,

$$\delta = \frac{N_0}{s_0 \psi_0}.$$

<div align="right">**5-21**</div>

Substituting scales into the cavity water continuity equation (eqn. 5-16) and using the definitions of T and S_{C0} (eqns. 5-4 and 5-18) yields

$$\frac{Q_{C0}}{c_m \psi_0^{\frac{1}{2}} t_0} \frac{\partial S_C{}^*}{\partial t^*} + \frac{Q_{C0}}{s_0} \frac{\partial Q_C{}^*}{\partial s^*} = M_C{}^* M_{C0} - R_k k N_0 (N_R{}^* - N_C{}^*).$$

<div align="right">**5-22**</div>

Rearranging this, defining

$$M_{C0} = \frac{Q_{C0}}{s_0},$$

<div align="right">**5-23**</div>

and dropping the asterisks gives

$$\alpha_C \frac{\partial S_C}{\partial t} + \frac{\partial Q_C}{\partial s} = M_C - R_k \kappa_C (N_R - N_C),$$

<div align="right">**5-24**</div>

where α_C and κ_C are defined by

<div align="right">115</div>

$$\alpha_C = \frac{s_0}{c_m \psi_0^{\frac{1}{2}} t_0}, \qquad \kappa_C = k \frac{N_0}{M_{C0}}.$$

5-25

Finally, substituting scales into eqn. 5-15 yields the scaled model equation for the cavity geometry

$$S_C{}^* = \epsilon_s \frac{\tau_b{}^{*p_b}}{N_C{}^{*n+q}} + \epsilon_m \frac{Q_c{}^*}{N_C{}^{*n}} \left(\delta \frac{\partial N_C{}^*}{\partial s^*} + \psi^* \right),$$

5-26

where

$$\epsilon_s = \frac{\pi}{4} \frac{R c_s \tau_{b0}^{p_c} n^n}{K_0 S_{C0} N_{C0}^{n+q}}$$

5-27

and

$$\epsilon_m = \frac{\pi}{4} (1 - \gamma) \frac{Q_{C0} \psi_0}{S_{C0} L k_1 \rho_i K_0} \left[\frac{n}{N_{C0}} \right]^n.$$

5-28

Equations 5-1, 5-3, 5-5, 5-7, 5-8, 5-20, 5-24 and 5-26 complete the model. In essence it describes the coupled evolution of channel size, cavity size, and lake level. S_R, Q_R, N_R, S_C, Q_C, N_C, u_b are functions of t and s, while h_L is a function of t only. This model differs from Hewitt and Fowler's not just in its inclusion of the lake and a channel that evolves at a rate dictated by melt and ice creep, but also in using the total hydraulic gradients $\psi + \partial N_R/\partial s$ and $\psi + \partial N_C/\partial s$ to drive channel and cavity flow (rather than ψ alone).

Four boundary conditions are needed in eqns. 5-3, 5-20 and 5-24 for determining the discharge and pressure in both drainage systems. As in previous chapters, for the channel I impose the condition in eqn. 5-8 and $N_R = 0$ at the terminus ($s = s_0$). For the cavities, an equation like eqn. 5-8 could be used to couple the cavities and the lake hydraulically. Preliminary investigations indicate interesting dynamics result from this coupling, but a full exploration of its consequences is beyond the scope of this chapter. Instead, for simplicity I isolate the cavities from the lake, by assuming that $N_C{}^*$ at the lake ($s = 0$) and at the terminus ($s = s_0$) are both constant, $=0.1$. Although this value may seem arbitrary, the qualitative features of the results reported below are not sensitive to its size.

The assumption of pseudo-steady cavity geometry is motivated by the supposition that, unlike in channels, the cavity system's effective pressure-discharge relationship will be negative whether the system is steady or not, and motivated by the lack of unsteady cavity drainage models that are strongly verified by subglacial observations. However,

the potential limitations of the model need to be recognised. Since, in reality, cavity size will not react instantaneously to pressure changes, the model overestimates the role of water storage in cavities when water transfer changes rapidly and neglects the lag of peak cavity size behind peak cavity water pressure. In such situations, the model will underestimate actual N_C and u_b variations. Also, the model precludes investigation of a possible negative feedback between cavity size and pressure suggested by Bartholomaus and others (2011). In a recent theory, Hewitt and others (2012) have tried to overcome these limitations by modelling the cavity system dynamically as a sheet with a cavity evolution equation analogous to eqn. 5-1.

5.2.4 The size of parameters and scales

I use the same glacier and lake geometry as I used in Chapter 3. This is illustrated in Fig. 3.1. The glacier is described by s_0 = 10 km, H = 100 m and $\sin\phi_s$ = $\sin\phi_b$ = 0.01, and slides over bedrock obstacles R = 0.1 m in height. These parameters lead to $\psi \approx$ 100 Pa m^{-1} and $\tau_b \approx$ 9 kPa. The lake has hypsometry defined by V_{Li} = 0.5 km^3, h_{Li} = 100 m and p_L = 1. A typical peak flood discharge defines the channel discharge scale, Q_{R0} = 1500 m^{3}s^{-1}, and a typical terminus cavity discharge defines the cavity discharge scale, Q_{C0} = 1 m^3 s^{-1}. Equations 6-63, 5-18 and 5-23 are used to calculate the following scales:

$$S_{R0} \approx 490 \text{ m}^2, \ N_{C0} = N_{R0} \approx 10^6 \text{ Pa}, \ t_0 \approx 10^6 \text{ s}$$

$$S_{C0} \approx 6 \text{ m}^2, \quad Q_{C0} = 1 \text{ m}^3\text{s}^{-1}, M_{C0} = 0.0001 \text{ m}^2\text{s}^{-1}.$$

5-29

And eqns. 2-65, 5-25, 5-27 and 5-28 are used to calculate the following model parameters:

$$\epsilon_R \approx 0.0034, \ \beta_L = 0.9, \ r = 0.9, \ \delta \approx 1, \ \lambda_L \approx 3.2, \ \kappa_R \approx 0.0067,$$

$$\alpha_C \approx 0.06, \ \kappa_C = 10, \ \epsilon_s \approx 0.11, \ \epsilon_m \approx 0.11.$$

5-30

Interestingly, ϵ_s and ϵ_m are roughly equal. This suggests that the contributions to cavity enlargement from frictional heating from the flowing water (the first term on the right of eqn. 5-26) and from basal sliding (the second term) are roughly equal. This is contrary to previous work (Walder, 1986; Kamb, 1987) that has concluded that the sliding control on cavity size dominates frictional heating. This is discussed later, but for now, in the interest of simplifying the numerical solution of the model in the next section, the frictional heating term is neglected, allowing eqn. 5-26 to be rearranged to give N_C in terms of S_C:

$$N_C{}^* = \left(\epsilon_s \frac{\tau_b{}^{*p_b}}{S_C{}^*} \right)^{\frac{1}{n+q}}.$$

5-31

5.2.5 Numerics

Space and time domains are discretised as described in section 2.2.5 with non-dimensional time steps of 0.005 and a grid spacing of 0.01. At each time step, using the forward Euler method, I integrate eqns. 5-1, 5-7 and 5-24 to find the next time-step's S_R, h_L and S_C. From the latter, the cavity discharge Q_C and pressure N_C can be calculated from eqns. 5-20 and 5-31 respectively. The dimensional sliding velocity u_b can be calculated from eqn. 5-14. I use the relaxation method, described in 2.2.5, to solve the channel mass and momentum conservation equations, eqns. 5-3 and 5-5. The only modification is the addition of the transfer term $R_\kappa \kappa_R (N_R - N_C)$ to the right-hand-side of eqn. 2-74.

5.3   Results of numerical simulations

Here I report the results of numerical experiments made with the model to study (i) the model's ability to simulate repeating flood cycles, (ii) variations in ice flow during each jökulhlaup cycle, and (iii) sensitivity of these variations to the cavity meltwater input, M_C.

5.3.1 Flood cycles

As discussed in Chapter 3, the size of floods simulated using Nye's jökulhlaup model formulated with only time dependence, increases unstably. In that chapter I showed that the spatially-dependent Nye-Fowler model exhibited similar behaviour when no 'topographic seal' existed and the channel was hydraulically isolated from its surroundings. Only when either the basic hydraulic gradient (ψ) was negative near the lake (a topographic seal exists) or the channel was supplied with an input of water along its length, could the model simulate floods that remained bounded in size. As the coupled model developed in the current chapter treats how the channel captures subglacial water in more detail than the Nye-Fowler model, I begin by asking whether the new model can simulate stable flood cycles.

Fig. 5.2 shows the simulated timeseries from a set of model runs, each spanning 15 model years and conducted with an initial lake depth of 30 m (h_L at $t = 0$), a constant lake-water input $Q_{in} = 10$ m^3 s^{-1}, a constant background water supply to cavities $M_C = 1 \times 10^{-3}$ m^2 s^{-1}, and several values of the parameter R_κ between 0 and 1. $R_\kappa = 0$ and $R_\kappa = 1$ refer to total hydraulic isolation and the hydraulic coupling used by Hewitt and

Fowler (2008), respectively. The coupled lake–channel–cavity system oscillates in time, yielding asymmetric filling and draining cycles of lake depth (Figs. 5.2a, 5.2c, 5.2e & 5.2g) and corresponding floods in the channel discharge depth (Figs. 5.2b, 5.2d, 5.2f & 5.2h). In all runs, initially, the peak discharge and volume of successive floods increase with time in a transient response to initial conditions. When $R_\kappa \leq 0.3$, the lake's post-flood lowstand level decreases until the lake empties completely, interrupting the simulation (Figs. 5.2a–5.2d). In contrast, when $R_\kappa \geq 0.6$, the cycles become periodic and stable without emptying the lake (Figs. 5.2e–5.2h). Runs using $0.3 < R_\kappa < 0.6$ (not shown) show increasing R_κ delays the emptying of the lake as peak discharge is suppressed by increased cavity-to-channel water transfer.
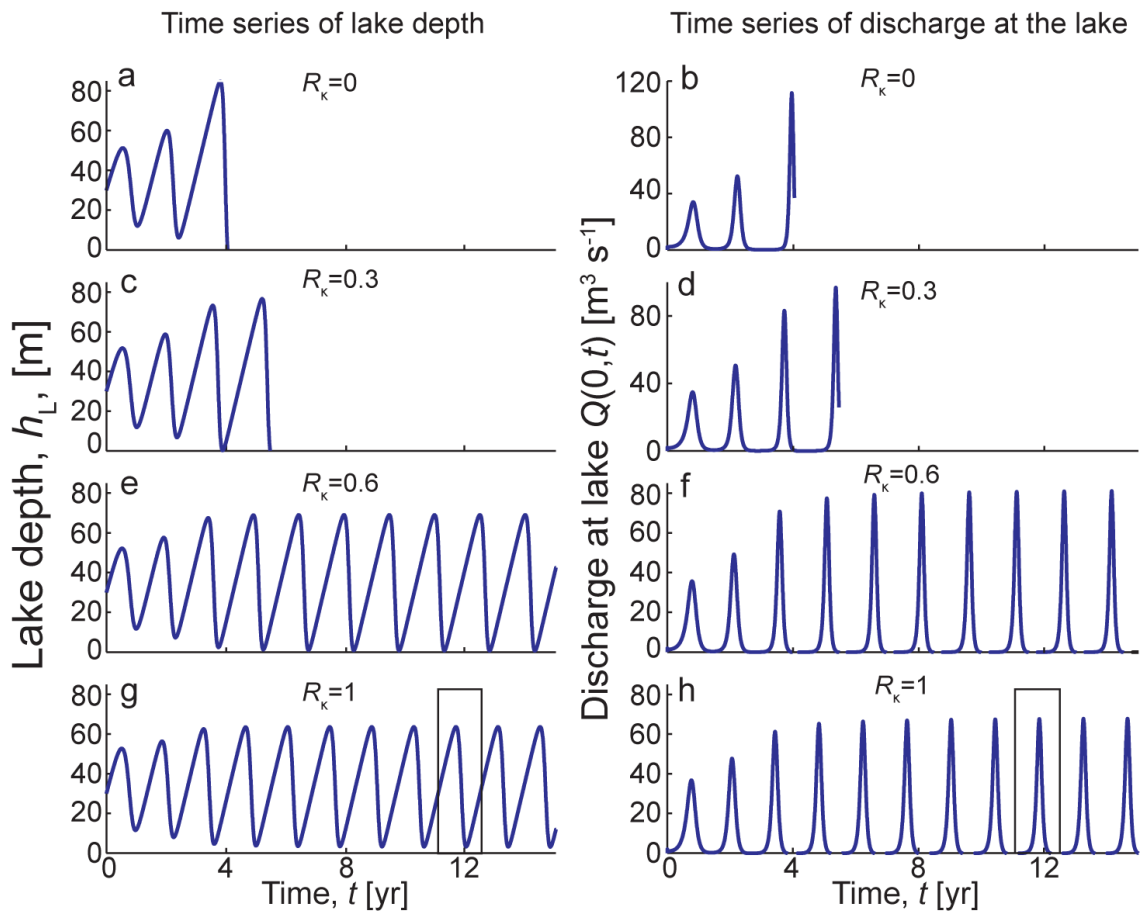

Fig. 5.2. Time series of modeled lake level, $h_L(t)$, (left) and channel discharge at the lake, $Q_R(0,t)$, (right) for R_κ = 0, 0.3, 0.6 and 1. Cavity water supply, M_C = 10^{-3} m^2 s^{-1}.

These results go beyond those presented in Chapter 3 (section 3.2) to show that stable limit cycles occur when high T values allow the channel to capture water efficiently from the cavities and a water divide (or seal) to form between floods. The stabilising effect of this transfer is evidenced also by the impact of R_κ on the cycles: the higher is R_κ, the shorter is their period and the smaller the flood volumes. Also, as was shown first in

Chapter 3, a divide forms even when the basic hydraulic gradient is positive everywhere
– a topographic seal is not a necessary condition for water divide formation.

5.3.2 Spatial-temporal evolution of sliding and drainage

Here, I analyse the spatio-temporal behaviour of subglacial drainage and ice flow in the
(≈1.5-year long) flood cycle highlighted by the boxes in Figs. 5.2g & 5.2h.
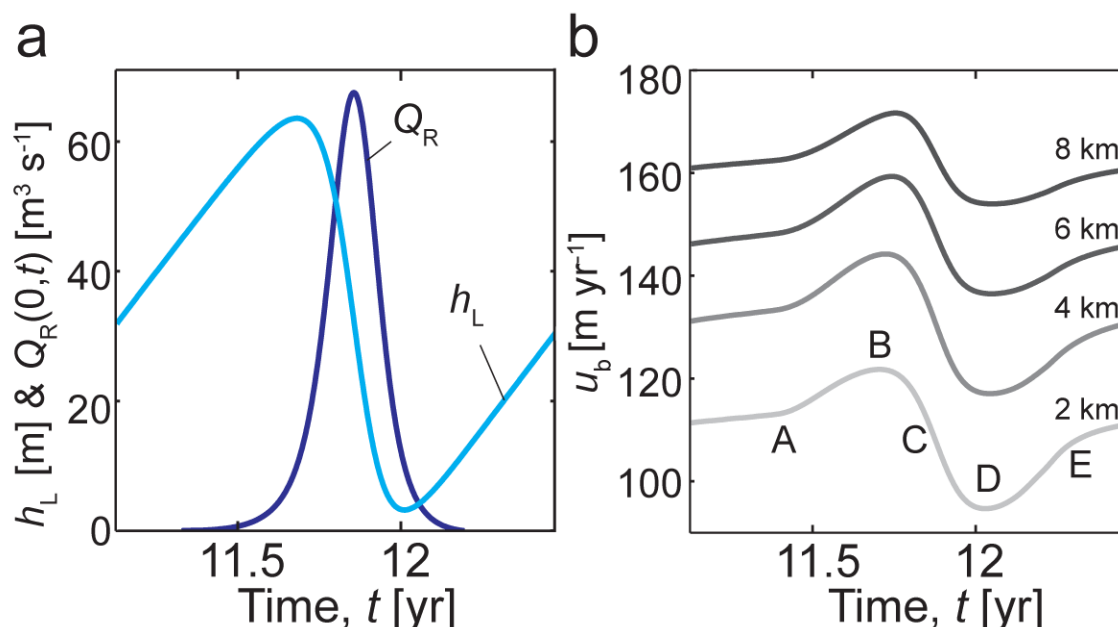
Fig. 5.3. Time series of (a) lake level, $h_L(t)$, and channel discharge at the lake and (b) sliding velocity at four locations along the glacier, $u_b(s = \{2, 4, 6, 8\}$ km, $t)$, in the limit cycle indicated by the boxes in Fig. 5.2g & 5.2h. $M_C = 10^{-3}$ m^2 s^{-1}, $R_\kappa = 1$.

Fig. 5.3 shows time series of the simulated lake depth $h_L(t)$ and lake outflow $Q_R(s=0,t)$
(Fig. 5.3a) and basal sliding velocity, $u_b(s,t)$, at four locations along the glacier, $s = \{2, 4, 6, 8\}$ km (Fig. 5.3b) during the cycle. Fig. 5.4 shows filled contour maps of the basal sliding
velocity $u_b(s,t)$ (Fig. 5.4a) and the rate of cavity-to-channel water transfer $T(s,t)$ (Fig. 3c).
Figs. 5.4a & 5.4b are maps over time and distance. The hydrographic sequence here was
discussed in Chapter 3. In Fig. 5.3b, the time before point A (and after point E of the last
cycle) is the lake-refilling phase between successive floods. At point A, high lake level
moves the subglacial water divide back to the lake, initiating the flood and allowing
Nye's positive feedback to enlarge the channel. B marks the time of the lake-level
highstand when the flood's growing discharge instantaneously matches the lake-water
input. C and D mark the flood peak and the post-flood lake lowstand, respectively.
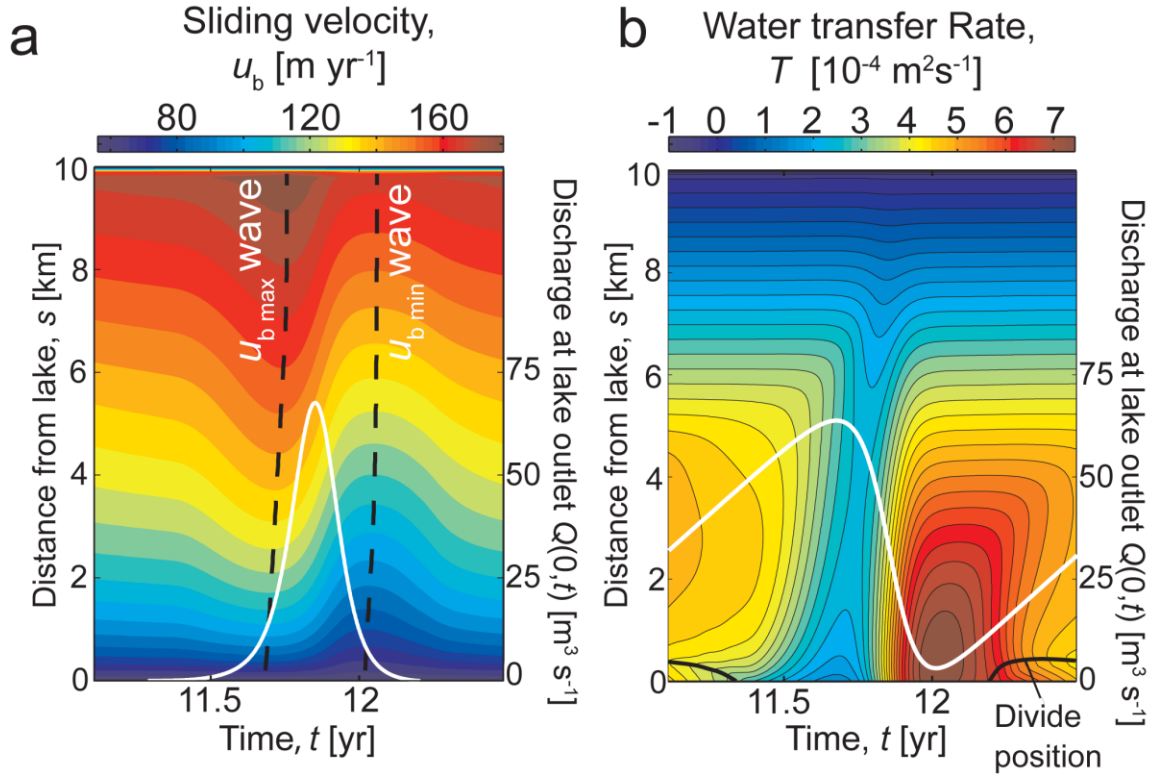
Fig. 5.4. Spatio-temporal evolution during the limit cycle indicated by the boxes in Fig. 5.2g and 5.2h. (a) Sliding velocity $u_b(s,t)$ (filled contour map and left-hand vertical axis) and discharge at the lake, $Q_R(s,t)$, (white line and right-hand vertical axis) and (b) cavity-channel transfer rate, $T(s,t)$, (filled contour map and left-hand vertical axis) and lake depth, $h_L(t)$, (white line and right-hand vertical axis. $M_C = 10^{-3}$ m^2 s^{-1}, $R_K = 1$.

Regarding ice motion, Fig. 5.3b and Fig. 5.4a show similar responses in u_b at different positions on the glacier. u_b rises gradually as the lake fills, but accelerates rapidly after flood initiation (A) to peak soon after the time of the lake highstand (B). u_b drops during the main flood (B to D) to a much lower velocity than during lake refilling, then increases again after flood termination (D to E). The durations of elevated and depressed u_b are comparable. Spatially, u_b rises monotonically with distance down-glacier, but its time-variations at different positions are not precisely synchronous. Fig. 5.3b shows that the peak and minimum in u_b propagate down-glacier at ≈250 m d^{-1} and ≈450 m d^{-1}, respectively (see the dashed lines in Fig. 5.4a).

This sliding response can be explained by considering the model's physics and is the direct result of the pressure-coupling between the lake and the drainage system. Eqn. 5-31 shows that cavity effective pressure N_c decreases with cavity size, S_C. Hence, because u_b decreases with N_C (eqn. 5-14), u_b varies directly with cavity size, S_C. In turn, S_C depends on how much water the cavities gain from the background meltwater input M_C and lose to the channel via water transfer, whose rate T increases with channel effective

pressure, N_R, via $T = R_\kappa \kappa_C(N_C^* - N_R^*)$. The sliding response thus stems ultimately from changes in lake level, which – through its effect on the channel pressure – governs how fast the channel draws water from the cavities. The timing associations in Fig. 5.4 between h_L, T and u_b confirm this explanation. When the lake fills between floods (E to A), reducing N_R at the channel inlet, its hydrostatic pressure is not transmitted past the divide (located in Fig. 5.4b by the black line) to modulate T and u_b directly far down-glacier (further simulations show that this effect would be diminished if the cavities and lake were coupled hydraulically); there is a slight increase in u_b only because the lake level weakly affects the distributions of N_R and T in the channel through its control on the migrating divide position. However, after the flood starts at $t \approx 11.4$ yr, the divide's absence means that the pressure transmission is unimpeded and able to reduce N_R and T markedly down most of the channel (Fig. 5.4); this causes the cavities to expand and sliding to accelerate (A to B; $11.4 < t < 11.7$ yr). Later, as flood discharge grows, peaks, and recedes under Nye's mechanisms (B to D, $11.7 < t < 12$ yr), the lake level drops rapidly, raising N_R along the channel so that enhanced water transfer out of the cavities shrinks their size and decelerates sliding. After the divide reforms at flood termination (E, $t \approx 12.2$ yr) the system enters a new cycle. During the flood when the lake strongly modulates the cavity-to-channel water transfer, the nonlinear wave properties of eqns. 5-1, 5-3 and 5-5 determine the propagation of changes in T and u_b down the channel.

5.3.3 Sensitivity to the cavity background supply, M_C

Finally, I study how the ice-flow and flood evolution depends on the meltwater input M_C, which is the other control on cavity drainage beside T. For temperate glaciers, M_C likely encompasses water reaching the bed from the surface, so it can be viewed as a proxy for weather conditions.

Figs. 5.5a–5.5d plot the maps of $u_b(s,t)$ and timeseries of lake outflow from four model runs that assumed different values of M_C between 2×10^{-4} and 2×10^{-3} m^2 s^{-1}. Each plot's duration is one flood cycle. The third panel (Fig. 5.5c), identical to Fig. 5.4a, serves as the control. An enduring pattern in these runs is that the ice flow speeds up after flood initiation and begins to decelerate before the flood peaks. In the run with the lowest M_C (Fig. 5.5a), the speed-up is very sudden and a strong compression wave ($\partial u_b/\partial s < 0$) propagates down-glacier some 70 days prior to the flood peak (around $12.5 < t < 12.7$ yr).

Physically, decreasing M_C is expected to reduce cavity size and discharge via mass conservation (eqn. 5-21) and hence reduce the sliding velocity u_b. This trend is seen in Figs. 5.5a–5.5d (note their different scales); however, the percentage variation in u_b in

the cycles increases. Fig. 5.6 quantifies both trends by plotting the mean,
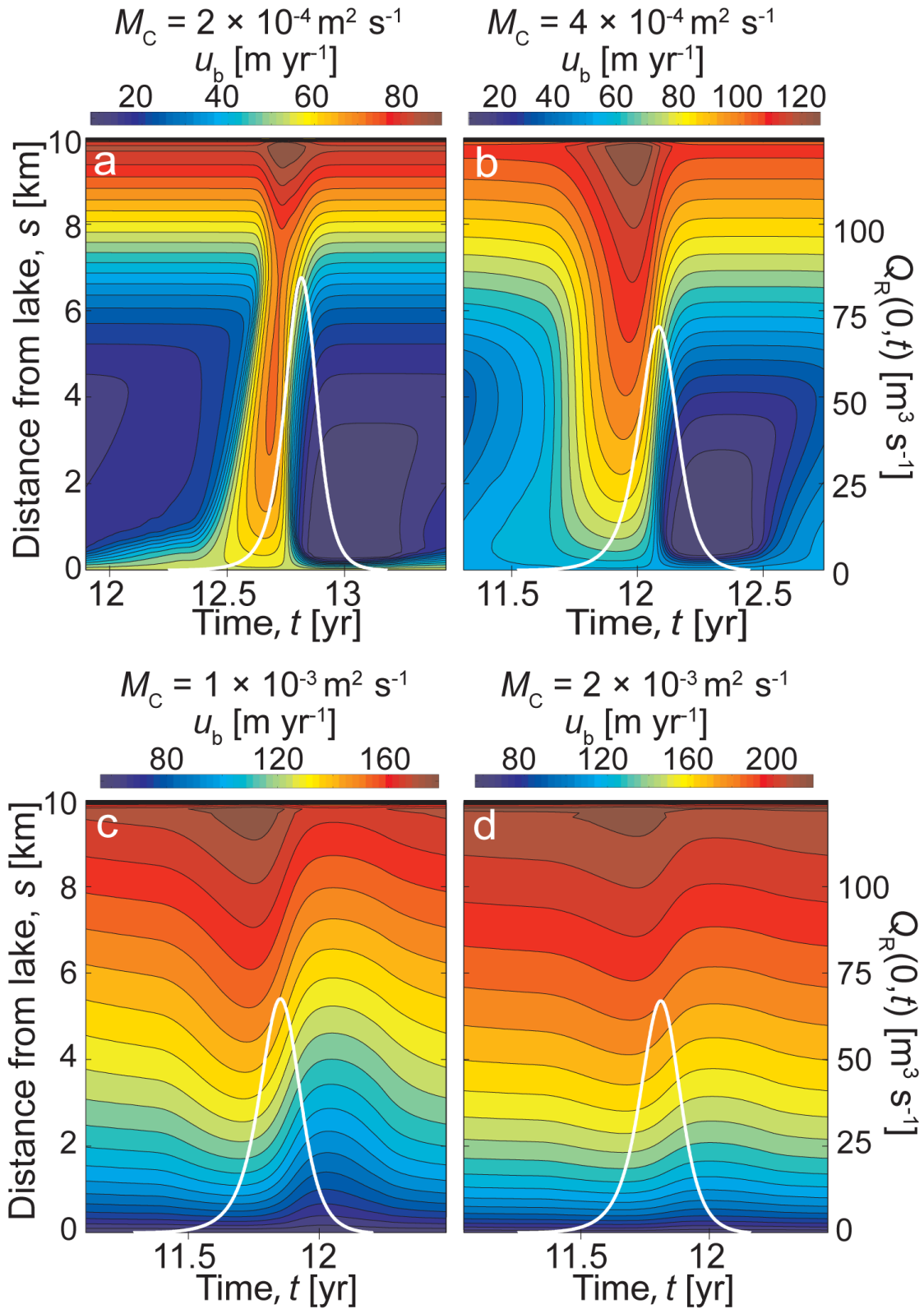

Fig. 5.5. Sliding velocity, $u_b(s,t)$, (filled contour maps) and channel discharge at the lake $Q_R(0,t)$ (white dashed lines and right-hand vertical axis) in one limit cycle for (a) $M_C = 2 \times 10^{-4}$ m^2 s^{-1}, (b) $M_C = 4 \times 10^{-4}$ m^2 s^{-1}, (c) $M_C = 1 \times 10^{-3}$ m^2 s^{-1} and (d) $M_C = 2 \times 10^{-3}$ m^2 s^{-1}.

maximum and minimum values of u_b at 4 km from the lake in each cycle, including results from extra runs where M_C is varied within the same range. As M_C is raised, the mean value of u_b increases but its maximum-to-mean ratio decreases.

Two outcomes of decreased M_C are expected on cavity-channel interaction. One is increased dominance of the transfer term in the cavity mass conservation equation (eqn. 5-21). This explains the variable maximum-to-mean u_b ratio; when M_C is large, the remaining, time-varying terms in eqn. 5-21, $\partial Q_C/\partial s$ and T, are comparatively small and S_C and u_b vary less than when M_C is small; then, S_C and u_b are modulated strongly because T dominates the mass balance. In addition, when $M_C \leq 4 \times 10^{-4}$ m^2 s^{-1}, the cavities collapse after the lake reaches its highstand due to high effective pressure in the channel, preventing significant reduction of u_b below its mean value (Fig. 5.6); then, most of the background water supply to the cavities reaches the channel, and the cavity area is controlled by $M_C = k(N_R - N_C)$ and eqn. 5-31. In the case where $M_C = 2 \times 10^{-4}$ m^2 s^{-1}, the cavity system does not recover until after the divide reaches the lake (Fig. 5.5a, $t \approx 12.3$ yr). These model results imply that under cold weather conditions when subglacial water is less abundant, glacier flow velocities would be lower during quiescence but respond more strongly in absolute and relative magnitudes to subglacial floods.
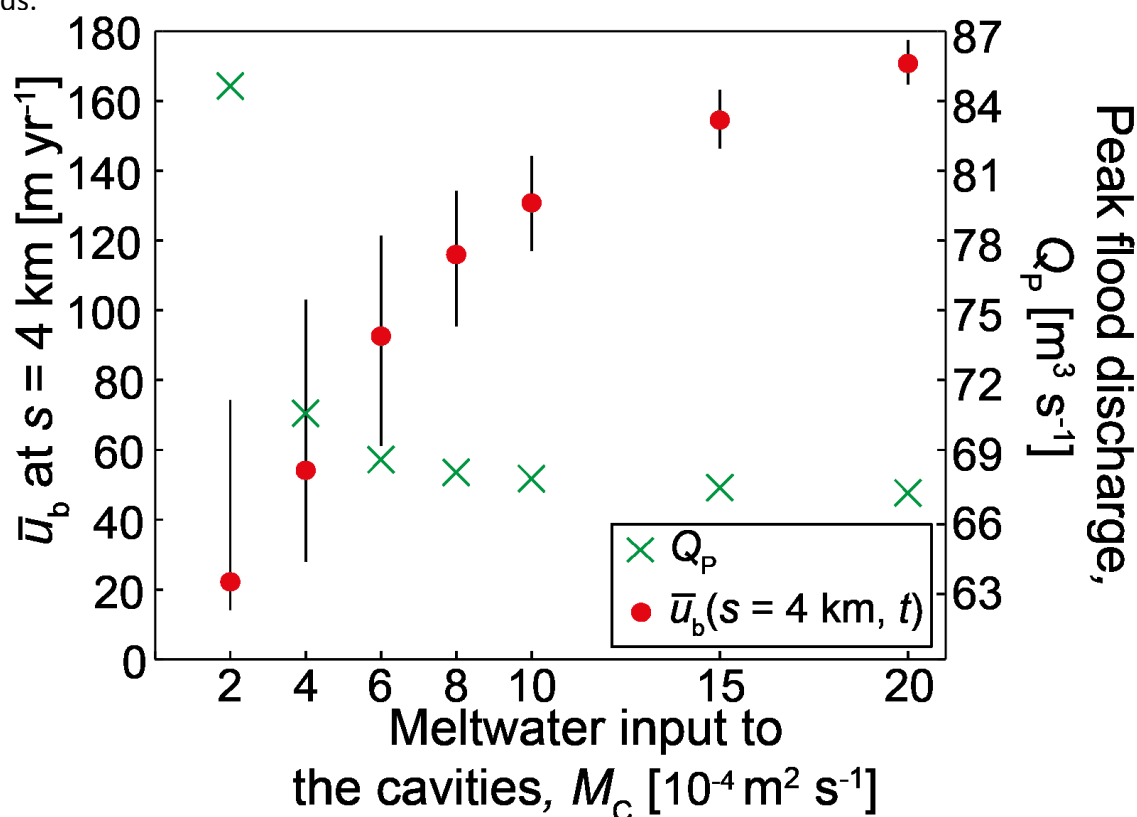

Fig. 5.6. Mean sliding velocity at 4 km from the lake, u_b (red circles and left-hand axis) and peak lake discharge, Q_P (green crosses and right-hand axis) for $M_C = 2 \times 10^{-4}$ m^2 s$^{-1} \rightarrow 2 \times 10^{-3}$ m^2 s^{-1}. The top and bottom ends of the vertical lines indicate the maximum and minimum u_b at 4 km from the lake reached during each limit cycle.

The other expected outcome of decreasing M_C is that the cavity effective pressure N_C increases (eqn. 5-31) reducing water transfer T to the channel (eqns. 5-2 & 5-4). The analysis of the channel-only model in Chapter 3 showed that, when the channel receives less water, the divide migrates more slowly towards the lake as it refills; this delays flood initiation, so the lake reaches a higher highstand to cause a higher flood peak discharge, Q_P. The same mechanism is operating here; reducing the water transfer to the channel impedes divide migration and increases highstand and Q_P. Figs. 5.5 and 5.6 show that the negative dependence of Q_P on M_C is nonlinear and becomes significant only for $M_C <$ $6 \times 10^{-4} \, \mathrm{m^2 \, s^{-1}}$.

5.4   Discussion and conclusions

I have presented the first fully coupled and consistent jökulhlaup model capable of explaining the broad pattern of observed sliding velocity changes during jökulhlaups. At Gornergletscher, Switzerland, and the Grimsvötn and Skaftá subglacial cauldrons, Iceland, sliding velocity increases during flood growth and, at Gornerglestcher and Skaftá, it decreases during flood recession (Sugiyama et al., 2010; Magnússon et al., 2007). At Gornergletscher, ice surface motion has been observed to reverse following the slow-down (Sugiyama and others, 2007), with maximum sliding velocity occurring before peak flood discharge. My model reproduces this timing and the marked post-flood sliding deceleration (e.g. in Figs. 5.3a–5.3b). In contrast, at Hidden Creek Lake, Alaska, maximum sliding velocity peak occurs after peak discharge (Anderson et al., 2005; Bartholomaus et al., 2011).

These observations reveal variability in the hydro-dynamic behaviour of jökulhlaup systems that stems from their glaciological and environmental factors – factors which may be difficult to constrain with field data. However, future work can use my model to investigate if differences in drainage system connectivity, lake and glacier geometry, background cavity water input, lake input, sliding parameterisation or a combination of these can account for observed variability. For example, my assumed basal shear stress, τ_b, is relatively low ($\tau_b \approx 9$ kPa; based on the thin ice dam at Merzbacher Lake). Preliminary study shows that increasing τ_b results in a monotonic increase in u_b and decrease in maximum-to-mean u_b ratio. Also, the duration of my simulated floods are unrealistically large, lasting months rather than weeks. This is due to the assumed model parameters; model runs using lake and glacier geometries, and lake and cavity water supplies, derived from observations at Gornergletscher (Sugiyama and others, 2010) and Hidden Creek Lake (Bartholomaus and others, 2011), simulate more realistic, shorter duration floods. These modelling explorations will be reported elsewhere.

Like previous work (e.g. Hewitt and Fowler, 2008; Hewitt et al., 2012; Pimentel and Flowers, 2011), I have modelled drainage one-dimensionally. This ignores lateral propagation of variations in N_C within the cavity system, the velocity of which may be comparable to their downglacier propagation velocities. Including lateral variation in N_C would be vital in a study of the lateral extent of the dynamic response of glaciers to jökulhlaups. Hewitt (2011) recently used a two-dimensional channel-distributed system model to investigate the steady-state spacing of channels beneath ice sheets. It may possible to extend my present model with his formulation to study lateral processes in distributed drainage during subglacial floods.

Unlike previous work (e.g. Walder, 1986; Kamb, 1987), my scaling analysis of the cavity steady-state geometry equation (eqn. 5-15) suggested that the contribution to cavity enlargement from sliding and frictional melting are roughly equal. This is due to the large values I used for the scales of the cavity discharge (Q_{C0} = 1 m^3 s^{-1}) and the basic hydraulic gradient that drives cavity water flow (ψ_0 = 100 Pa m^{-1}). Both values are at the largest extremes of those considered in Walder's (1986) analysis of the relative contributions of sliding and frictional melt to cavity enlargement (see his Table 1). I followed Hewitt and Fowler (2008) in assuming that the basic hydraulic gradient that drives cavity flow is the same as that which drives channel water flow – i.e. that which is due to the glacier's longitudinal surface and bed slopes. Walder (1986) points out that, because cavity flow is tortuous, the basic hydraulic gradient 'seen' by the cavities may be only a small fraction of the longitudinal hydraulic gradient. This is the cause of my finding that melting plays a significant role in cavity enlargement and suggests that I was right to ignore the melting term despite this finding and that further exploration of the model should look at modifying the longitudinal hydraulic gradient when it is used to drive water flow in cavities.

What are the implications of this model for the coupling between subglacial drainage and ice motion in an ice sheet setting? The results introduce the possibility that supraglacial lake drainage in Greenland could, depending on basal conditions, cause both ice speed-up and slow-down. This awaits further exploration, using parameters associated with the thicker ice, reduced basic hydraulic gradients, and lower basal shear stress typical of ice sheets whilst treating Greenland supraglacial lake and moulin drainage as analogues of alpine jökulhlaup systems.

Chapter 6   Subglacial open-channel flow after jökulhlaups

6.1   Introduction

In previous chapters I have assumed that subglacial drainage occurs exclusively through channels and cavities that are completely full and pressurised. I have ignored the fact that these drainage pathways can sometimes be only partially-filled, with a head-space of air above the flowing water. Such open-channel flow occurs when a drainage system's capacity exceeds the input it receives. This can happen beneath glaciers late in the melt season when a drainage system, enlarged by months of melt, receives low surface melt input (e.g. Fountain, 1993; Hooke, 1984; Sharp, 2005; Smart, 1986), year-round near the terminus where thin ice prevents channel closure through creep (Evatt, 2006), or after jökulhlaups, when drainage leads to the lake's surface dropping below the height of the channel's roof (e.g. Aitkenhead, 1960; Bartholomaus et al., 2011, Collins and Clarke, 1977; Glen, 1953).

Post-jökulhlaup open-channel drainage was not considered in the reconstruction of flood volumes from Merzbacher Lake, Kyrgyzstan in Chapter 4. Following floods, the delay in the onset of lake re-filling associated with a period of open-channel flow will vary between events and between systems. Including this process in flood volume reconstructions could improve their reliability.

In addition, the hydraulics of open-flow cannot be described by the Nye-Fowler model, used in Chapters 3 and 5 to investigate jökulhlaup physics. In those chapters, jökulhlaup simulation had to be terminated if the lake depth reached zero. Hence, as it stands, attempts to realistically simulate repeating flood cycles from real systems are restricted to the minority of cases where lake lowstand is higher than the roof of the drainage channel and full-pipe, pressurised flow continues uninterrupted after floods (e.g. Grimsvötn and lakes beneath Antarctica).

To address these issues, the aims of this chapter are: (i) to develop a physical model of this phenomenon, (ii) to analyse the model to understand what controls whether open-channel flow occurs and how long it lasts when it does, (iii) to simulate complete flood cycles allowing the lake to reach the height of the roof of the channel, inducing open-channel flow, and (iv) to investigate the effect this has on jökulhlaup characteristics.

When modelling full pipe flow the challenge is to determine the discharge and the water pressure. In open-channel flow, unlike in full-pipe flow, water pressure is atmospheric, the aim for a modeller is to determine the flow depth. Subglacially, during and

immediately following jökulhlaups, water flow is through an enclosed pipe (one that is enclosed by a 'roof' not open like a subaerial stream). Because flow depth almost always increases with discharge, open-channel flow is associated with periods of low discharge and fluctuations in meltwater flux can produce spatial and temporal transitions between open and full flow conditions (Schuler et al. 2004; Kohler, 1995).

Few modelling studies have tackled open-channel subglacial drainage. Two that have are Hewitt et al. (2012) and Schuler and Fischer (2009). Hewitt et al. (2012) modelled open-channel flow by constraining the total hydraulic potential (the spatial derivative of which is equal to the total hydraulic potential gradient used in previous chapters; ($\partial N/\partial s + \psi$)) to remain above a minimum value corresponding to open-channel flow. In areas of the glacier bed where the total hydraulic potential reaches this value, channels and a macro-porous sheet that emulates a linked-cavity system become partially-filled. They ignore differences in the physics of frictional flow resistance and heat dissipation between full- and open-flow regimes. Numerical solution of their model suggests that open-channel flow is more common when discharge is low and where ice is steep and thin. Schuler and Fischer (2009) supposed that open-channel flow occurs when the discharge through a subglacial channel goes below the maximum discharge the channel could transfer without filling. They vary the heat dissipation in the flow in proportion to the fraction of the channel's perimeter that is wetted and ignore the fact that in an enclosed channel of uniform roughness the maximum discharge does not occur when the flow depth is equal to the channel height (Chow, 1959).

In this chapter I model the open-channel flow that occurs immediately following jökulhlaups by assuming it begins at the moment the height of the roof of the channel at the lake exceeds the lake's depth. The depth of flow in a semi-circular rock-floored and ice-walled channel during the subsequent period of open-channel flow is modelled using Manning's equation while taking into account the effect on the momentum balance of differing hydraulic roughnesses between the channel's rock floor and ice walls. I ignore melt enlargement of the channel during periods of open-channel flow.

This chapter is arranged as follows. In section 6.2 I describe the complete glaciohydrological cycle I assume begins when the lake empties, the equations I use to describe each stage of this cycle and a scaling analysis of these equations. In sections 6.3 and 6.4 I simplify the model to investigate how open-channel flow begins and ends, and how long it lasts. In section 6.5 results of numerical simulations of the model are shown to agree closely with the analytical results of the preceding two sections. Findings are discussed in section 6.6.

6.2   Model formulation

6.2.1 The glacio-hydrological cycle

Fig. 6.1 illustrates four stages of the glacio-hydrological cycle assumed by the model to occur when lake depth reaches the elevation of the roof of the semi-circular channel at the base of the ice dam (Fig. 6.1a). At this moment air enters the channel and open-channel flow begins at the lake (labelled the lake outlet in Fig. 6.1a). Progressively more of the channel becomes open as the upper limit of full-pipe flow moves down glacier (Fig. 6.1b). This limit, or transition between open and full flow, moves down glacier, reaching the terminus. Flow is now completely open (Fig. 6.1c). This persists until the channel closes through creep sufficiently that it can no longer transfer the discharge required of it (the sum of the lake input and all the water supplied to the channel along its length). At this moment the transition migrates back up glacier (Fig. 6.1d). When the transition reaches the lake the channel is entirely full and the lake's depth is equal to the
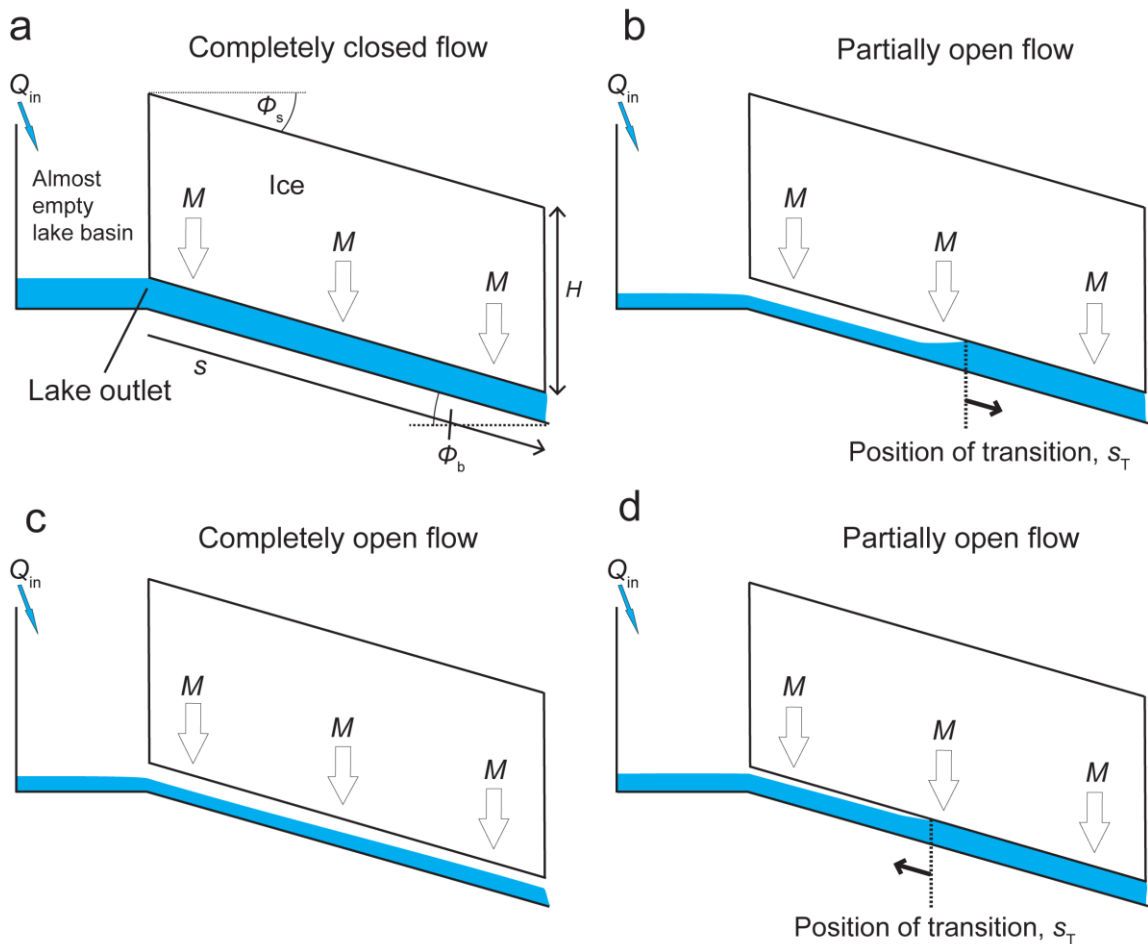

Fig. 6.1. The glacio-hydrological cycle assumed in the model. Flow is initially (a) entirely full pipe, then (b) partially full pipe and partially open channel while the transition travels down glacier, then (c) entirely open channel until the channel closes sufficiently that (d) the transition reforms and travels upglacier.

129

height of the channel roof. The lake level now rises or falls, depending on the rate at which the newly-established full pipe-flow removes water from the lake. If the lake level rises (or drops slower than the channel roof lowers through creep closure) full-pipe flow continues and the next flood cycle begins. I now describe the equations I use to describe these mechanisms in the model.

6.2.2 Equations

Full-pipe flow

As in earlier chapters (see Box 2-1), evolution of the channel's (dimensionless) cross-sectional area, S^*, with (dimensionless) time, t^*, is described by

$$\frac{\partial S^*}{\partial t^*} = \frac{|Q^*|^3}{S^{*\frac{8}{3}}} - S^* N^{*3},$$

6-1

where Q^* is the dimensionless discharge and N^* is the dimensionless effective pressure. The R-subscripts from the previous chapter have been dropped as all variables refer to a channel. Down glacier of the transition (Fig. 6.1b) and along the entire channel during periods when no open-channel flow occurs, full-pipe flow is described by the dimensionless mass and momentum equations from earlier chapters:

$$\frac{\partial Q^*}{\partial s^*} = \epsilon_R(r-1)\frac{|Q^*|^3}{S^{*\frac{8}{3}}} + \epsilon_R S^* N^{*3} + M^*,$$

6-2

$$\frac{\partial N^*}{\partial s^*} = \frac{1}{\delta}\left(\frac{Q^*|Q^*|}{S^{*\frac{8}{3}}} - \psi^*\right).$$

6-3

As before, s^* denotes distance along the channel, ψ^* is the basic hydraulic gradient and M^* is the supply of water to the channel along its length (all dimensionless). The dimensionless parameters ϵ_R, r and δ were derived in the scaling analysis in section 2.2.4. The dimensionless lake depth, h_L^*, evolves due to discharge into or out of the channel, $Q^*(0,t)$, and lake input, Q_{in}^*. The rate of change of lake level is therefore given by

$$\frac{dh_L^*}{dt^*} = \frac{\lambda_L}{h_L^{*\,p_L-1}}[Q_{in}^* - Q^*(0,t)].$$

6-4

Because I am interested in processes that happen when lake level is low, I modify the equation I previously used to convert lake level to channel effective pressure at the lake (eqn. 6-59) to take account of the time-varying channel height, h_r^*, in this conversion

(see Fig. 6.2a):

$$N^*(0, t^*) = N_L = \beta[1 - (h_L^* - \epsilon_h h_r^*)],$$

6-5

where β is a dimensionless parameter derived in section 2.2.4 and ϵ_h is given by

$$\epsilon_h = \frac{4}{3\pi} \frac{h_{r0}}{h_{L0}}.$$

6-6

In this expression h_{L0} is the lake depth scale and h_{r0} is the channel height scale (see section 2.2.4 and eqn. 2-24). The mean height of the channel mouth above the lake bed is $4/(3\pi)h_r h_{r0}$, so I am assuming that the lake water pressure head in the channel at the lake outlet is the difference between this mean channel height and the lake level h_L (Fig. 6.1a). This small correction only becomes important when the lake's depth approaches the height of the roof of the channel mouth $h_r^*(0,t)$, for example, immediately before and after periods of open-channel flow.

Equation 6-5 provides one boundary condition on the effective pressure in the channel. As before, at the terminus I assume a constant effective pressure, N_T, during full-pipe flow. Here I use the value corresponding to zero water pressure and a finite ice-overburden pressure due to an ice thickness at the terminus of H:

$$N_T = N_a = \rho_i g H.$$

6-7
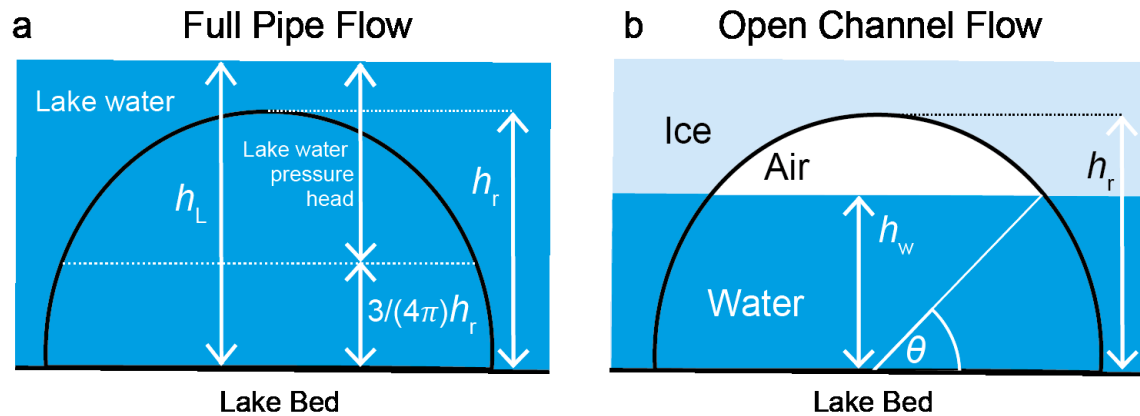
Fig. 6.2. The lake outlet mouth during (a) full-pipe flow and (b) open-channel flow.

Open-channel flow

Upglacier of the transition (Fig. 6.1b) and along the entire length of the channel when no full-pipe flow occurs (Fig. 6.1c), flow is open-channel. Fig. 6.2b shows the lake outlet (labelled the lake outlet in Fig. 6.1). Momentum balance between this flowing water and

the channel is modelled using Manning's equation, introduced in section 2.2.1. Substituting eqns. 2-6 and 2-5 into eqn. 2-4 yields

$$v = \frac{S_w^{\frac{2}{3}}}{P_w^{\frac{2}{3}} n_a'} \left[\left(\sin \phi_b - \frac{1}{\rho_w g} \frac{\partial p_w}{\partial s} \right) \right]^{\frac{1}{2}},$$

6-8

where v is the flow velocity, S_w is the cross-sectional area of the flow (which, during open-channel flow, is less than the channel's cross-sectional area S), P_w is the wetted perimeter, n_a' is perimeter-averaged Manning's roughness coefficient, ϕ_b is the bed slope, ρ_w is the density of water, g is acceleration due to gravity and p_w is water pressure. Using $Q = vS_w$, taking the pressure p_w along the water's surface, so $\partial p_w/\partial s = 0$, and taking $\sin(\phi_b) \approx \phi_b$ yields

$$Q = \frac{S_w^{\frac{5}{3}} \sqrt{\phi_b}}{P_w^{\frac{2}{3}} n_a'}.$$

6-9

The cross-sectional area of the flow S_w and the wetted perimeter P_w are functions of the depth of flow, h_w, and the height of the channel, h_r, (Fig. 6.2b):

$$S_w = h_r^2 \left(\frac{\pi}{2} - \cos^{-1} \frac{h_w}{h_r} \right) + h_w \sqrt{h_r^2 - h_w^2},$$

6-10

$$P_w = 2h_r \left(\frac{\pi}{2} - \cos^{-1} \frac{h_w}{h_r} + 1 \right).$$

6-11

The wetted perimeter of the channel is partially ice and partially bedrock (Fig. 6.2b). If the roughnesses of bedrock n_b' and ice n_i' are different, the perimeter-averaged Manning's roughness n_a' is a function of flow depth:

$$n_a' = \beta_i n_i' + (1 - \beta_i) n_b',$$

6-12

where β_i is the fraction of the wetted perimeter that consists of the ice:

$$\beta_i = \frac{\left(\frac{\pi}{2} - \cos^{-1} \frac{h_w}{h_r} \right)}{\left(\frac{\pi}{2} - \cos^{-1} \frac{h_w}{h_r} + 1 \right)}.$$

6-13
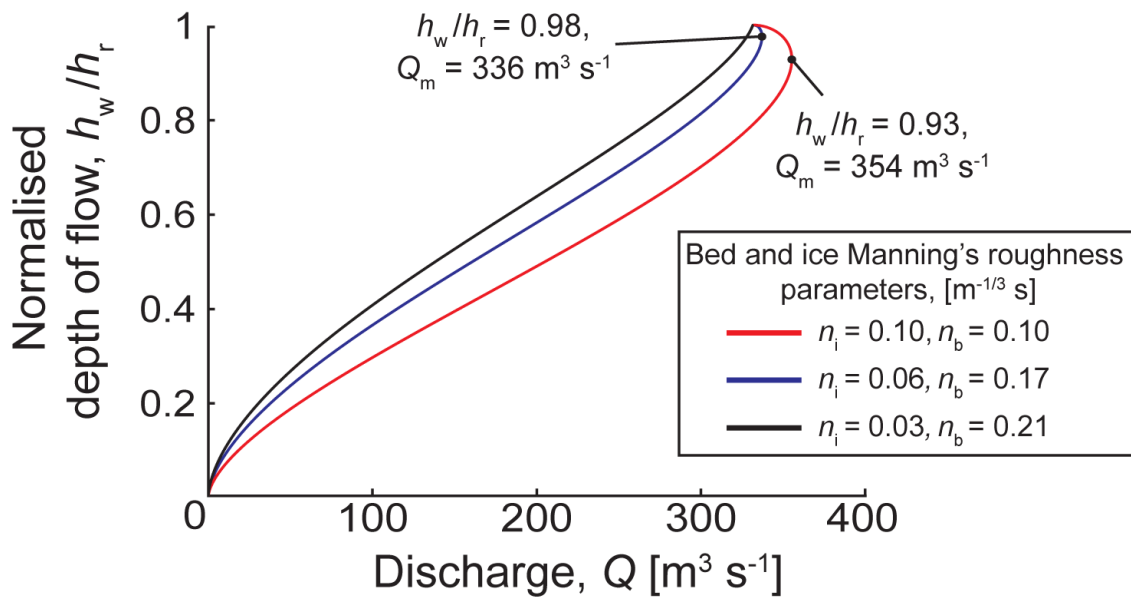
Fig. 6.3. Discharge as a function of flow depth in a 10 m high semi-circular channel with an along-glacier slope of 0.01.

Fig. 6.3 plots the variation of discharge Q with normalised flow depth h_w/h_r, defined by eqns. 6-9–6-13, for three pairs of values for the Manning's roughness parameters of the bed and the ice. Each pair corresponds to $n_a' = 0.1$ when the channel is full – the value used in simulations presented in earlier chapters. It can be shown analytically that according to Manning's equation, in a semi-circular channel with $n_b'/n_i' < (\pi + 3)$, maximum discharge Q_{max}, occurs when the channel is not full. Examples where this is the case are given by the red and blue curves in Fig. 6.3. As the ratio n_b'/n_i' increases the depth corresponding to maximum discharge, labelled in the plots, also increases (compare the blue and red curves in Fig. 6.3). The black curve in Fig. 6.3 corresponds to a channel with $n_b'/n_i' > (\pi + 3)$ in which maximum discharge occurs when the channel flow is full, $h_w/h_r = 1$.

For simplicity, during open-channel flow I assume discharge into the channel from the lake equals the lake input, Q_{in}, so the lake level equals the depth of flow in the channel mouth. Also I assume the discharge gradient is given by

$$\frac{dQ}{ds} = M.$$

6-14

This assumes pseudo-steady flow; Q and S_w respond instantaneously to change in discharge into the channel from the lake. Rapidly time-varying lake input and channel cross-sectional area could invalidate this assumption, but I assume that channel area changes relatively slowly compared to the velocity at which water flows through the channel and restrict application of the model to situations when lake input is constant.

133

During open-channel flow I ignore melt enlargement of the channel, assuming that the channel only closes through creep:

$$\frac{\partial S}{\partial t} = -K_0 S N_a{}^3 \ ,$$

<div align="right">**6-15**</div>

where K_0 is an ice rheology constant (= 10^{-24} Pa^{-3} s^{-1}) and N_a is the effective pressure when the water pressure is zero ($N_a = \rho_i g H$). In reality, preferential melting at the ice-water interface would change the channel's shape which would affect closure rates (Hooke 1990; Ng, 1998), but I ignore this effect here.

The transition

Immediately following the moment the lake level reaches the height of the channel, $h_L(t)$ = $h_r(s{=}0,t)$, a transition between open flow and full-pipe flow moves down glacier towards the terminus. Similarly, after discharge exceeds the maximum discharge the channel can transfer through open-channel flow at some point along it, the transition moves upglacier from this point towards the lake. I assume this occurs at the terminus because discharge increases downglacier (eqn. 6-14). The depth of flow corresponding to maximum discharge, $h_{w\,m}$, can be found by solving

$$0 = \frac{5}{3}\frac{1 + \cos 2\theta_m}{\theta_m + \frac{1}{2}\sin 2\theta_m}(\theta_m + 1) - \frac{2}{3} + \frac{n_b - n_i}{\theta_m n_i + n_b}$$

<div align="right">**6-16**</div>

for θ_m and using

$$h_{w\,m} = h_r \sin(\theta_m).$$

<div align="right">**6-17**</div>

This depth of flow can then be used in Manning's equation (eqns. 6-9 through 6-13) with the channel cross-sectional area at the terminus, to find the maximum discharge the channel can transfer there, Q_m ($s = s_0$).

I use the continuity of mass at the transition to calculate how the transition moves. In the spatial reference frame of the glacier the transition moves at a rate of $\dot{s}_T$ (in my coordinate system $\dot{s}_T > 0$ means downglacier movement of the transition). Still in the glacier's reference frame, water flows into the transition at a velocity of v_1 from its upglacier side and out of the transition at a velocity of v_2 on its downglacier side (Fig. 6.4a). Ignoring the details of the flow near the transition, I assume that, for the purposes of water continuity, I can approximate the cross-sectional area of the flowing water on the upglacier side of the transition by inverting Manning's equation, $S_w(s = s_T)$. On the downglacier side of the transition flow the cross-sectional area of the flow is equal to the channel's area $S(s = s_T)$.

Relative to the reference frame that moves with the transition (see Fig. 6.4b) water flows into the transition from upglacier at a velocity of $v_1 - \dot{s}_T$ and out of it at a velocity of $v_2 - \dot{s}_T$. Mass conservation in the transition's reference frame leads to

$$[v_1 - \dot{s}_T]S_w(s = s_T) = [v_2 - \dot{s}_T]S(s = s_T).$$

6-18

I define $Q_{oc} = v_1 S_w$ and $Q_F = v_2 S$, as the discharge into the transition from its upglacier side and the discharge moving out of the transition in a downglacier direction. Q_F and Q_{oc} are relative to the glacier reference frame. I rearrange eqn. 6-18 to give $\dot{s}_T$ in terms of Q_F, Q_{oc}, S and S_w:

$$\dot{s}_T = \frac{Q_F - Q_{oc}}{S - S_w}.$$

6-19

The four quantities on the right of this expression are known from elsewhere in the model so eqn. 6-19 allows me to calculate the velocity of the transition's movement.

a   In the glacier's reference frame

Q_{oc}, v_1, S_w ┊ Q_F, v_2, S

$\dot{s}_T$

b   In the transition's reference frame

$(v_1 - \dot{s}_T), S_w$ ┊ $(v_2 - \dot{s}_T), S$

$\dot{s}_T$
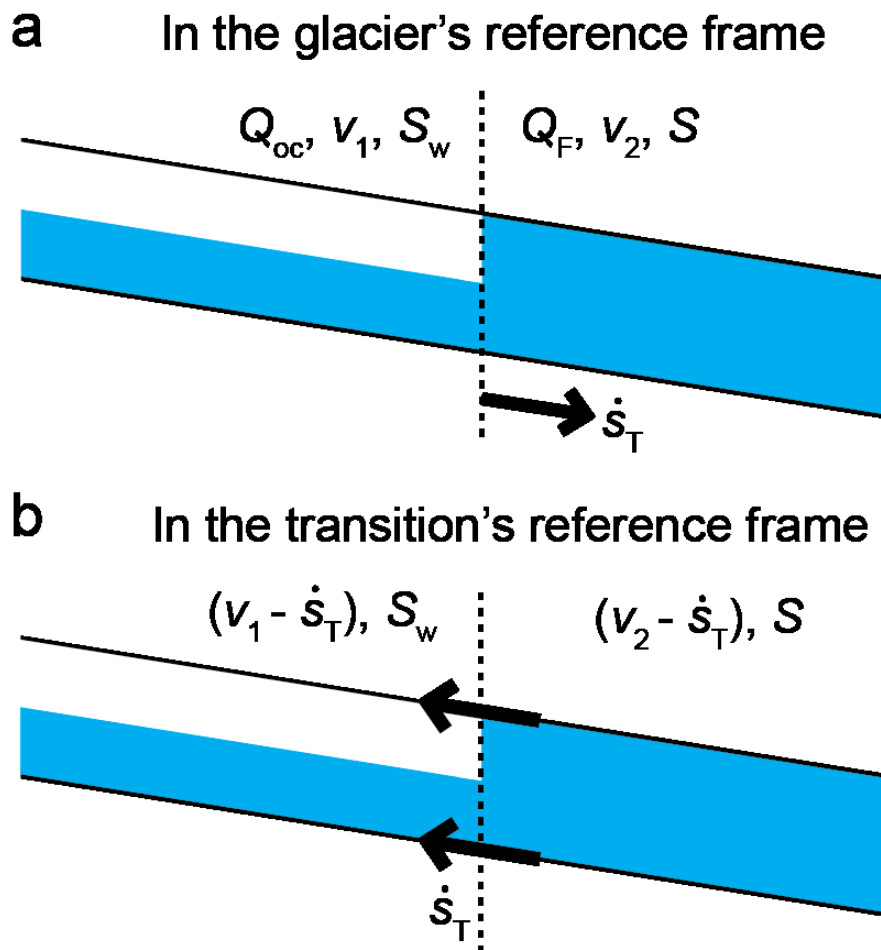
Fig. 6.4. The movement of the transition. (a) In the glacier reference frame, the transition moves downglacier at velocity $\dot{s}_T$, (b) in the transition reference frame the channel moves upglacier at velocity $\dot{s}_T$.

135

6.2.3 Non-dimensionalisation

Equations 6-9 to 6-17, and 6-19 define the (dimensional) open-channel component of the model. Non-dimensionalisation of these equations starts by defining the same scales for, S, N, Q, M, ψ, t and s as were derived in the scaling analysis of the full-pipe equations in section 2.2.4:

$$S = S_0 S^*, \qquad N = N_0 N^*, \qquad Q = Q_0 Q^*,$$
$$M = M_0 M^*, \qquad t = t_0 t^*, \qquad s = s_0 s^*.$$

6-20

I define scales and non-dimensional variables corresponding to the new variables introduced in the previous section:

$$s_{\mathrm{T}} = s_{\mathrm{T}0} s_{\mathrm{T}}^*, \qquad S_{\mathrm{w}} = S_{\mathrm{w}0} S_{\mathrm{w}}^*, \qquad h_{\mathrm{w}} = h_{0\mathrm{w}} h_{\mathrm{w}}^*, \qquad h_{\mathrm{r}} = h_{0\mathrm{r}} h_{\mathrm{r}}^*, \qquad P_{\mathrm{w}} = P_{\mathrm{w}0} P_{\mathrm{w}}^*,$$
$$S_{\mathrm{w}} = S_{\mathrm{w}0} S_{\mathrm{w}}^*, \qquad n_{\mathrm{a}}' = n_{\mathrm{a}0}' n_{\mathrm{a}}'^*.$$

6-21

The non-dimensional equations for the discharge gradient and channel creep closure during open-channel flow, eqns. 6-14 and 6-15, are simply

$$\frac{dQ^*}{ds^*} = M^* \quad \text{and} \quad \frac{\partial S^*}{\partial t^*} = -S^* N^{*3}.$$

6-22

It is logical to define

$$s_{\mathrm{T}0} = s_0, \qquad S_{\mathrm{w}0} = S_0,$$

6-23

and, as $S = \pi h_{\mathrm{r}}^2/2$,

$$h_{\mathrm{w}0} = h_{\mathrm{r}0} = \left(\frac{2S_0}{\pi}\right)^{\frac{1}{2}}.$$

6-24

Substituting this into eqn. 6-10 yields

$$S_{\mathrm{w}}^* = h_{\mathrm{r}}^{*2}\left(1 - \frac{2}{\pi}\cos^{-1}\frac{h_{\mathrm{w}}^*}{h_{\mathrm{r}}^*}\right) + \frac{2}{\pi} h_{\mathrm{w}}^* \sqrt{h_{\mathrm{r}}^{*2} - h_{\mathrm{w}}^{*2}}.$$

6-25

Defining

$$P_{\mathrm{w}0} = h_{\mathrm{r}0}(\pi + 2)$$

6-26

ensures $P_{\mathrm{w}}^* = S_{\mathrm{w}}^* = 1$ when $h_{\mathrm{r}}^* = h_{\mathrm{w}}^* = 1$, and substituting this into eqn. 6-11 yields

$$P_{\mathrm{w}}^* = \frac{1}{\frac{\pi}{2} + 1} h_{\mathrm{r}}^*\left(\frac{\pi}{2} - \cos^{-1}\frac{h_{\mathrm{w}}^*}{h_{\mathrm{r}}^*} + 1\right).$$

The perimeter-averaged Manning's roughness equation is

$$n_a'^* = \beta_i n_i'^* + (1 - \beta_i)n_b'^*; \quad \beta_i = \frac{\left(\frac{\pi}{2} - \cos^{-1}\frac{h_w{}^*}{h_r{}^*}\right)}{\left(\frac{\pi}{2} - \cos^{-1}\frac{h_w{}^*}{h_r{}^*} + 1\right)},$$

where $n_i'^* = n_i'/n_{a0}'$ Substituting appropriate scales into eqns. 6-9 yields the non-dimensional Manning's equation,

$$Q^* = \mu \frac{S_w^{*\frac{5}{3}}}{P_w^{*\frac{2}{3}} n_a'},$$

where

$$\mu = \frac{S_{w0}^{\frac{5}{3}} \sqrt{\phi_b}}{P_{w0}^{\frac{2}{3}} Q_0 n_{a0}'}.$$

Substituting scales into eqn. 6-19 yields the non-dimensional transition migration equation:

$$\dot{s}_T = \eta \frac{Q_F^* - Q_{oc}^*}{S^* - S_w^*},$$

where

$$\eta = \frac{t_0 Q_0}{s_0 S_0}.$$

Some model scales and parameters are the same as those used in previous chapters (e.g. section 3.2):

$$S_0 \approx 490 \text{ m}^2, \quad N_0 \approx 1 \times 10^6 \text{ Pa}, \quad Q_0 = 1500 \text{ m}^3 \text{ s}^{-1},$$

$$M_0 \approx 0.15 \text{ m}^2 \text{ s}^{-1}, \quad t_0 \approx 1 \times 10^6 \text{ s}, \quad s_0 = 10 \text{ km},$$

$$\epsilon_R \sim 0.0034, \quad r = 0.9, \quad \delta \sim 1,$$
$$\beta_R \sim 0.9, \quad \lambda_L \sim 3.2 .$$

Eqns. 6-23, 6-24 and 6-26 are used to calculate the scales of new variables introduced here:

$$s_{T0} = 10 \text{ km}, \qquad S_{w0} \approx 490 \text{ m}^2, \qquad P_{w0} \approx 90 \text{ m},$$

$$h_{w0} = h_{r0} \approx 17.6 \text{ m}, \qquad n'_{a0} = 0.016 \text{ m}^{-\frac{1}{3}} \text{ s}.$$

6-34

Eqns. 6-6, 6-30 and 6-32 are used to calculate new parameters,

$$\epsilon_h \approx 0.08, \qquad \mu \approx 6.1, \qquad \eta = 297.$$

6-35

The value of n'_{a0} does not depend on the other scales and does not affect my analysis. It is chosen arbitrarily.

6.2.4 Summary

Box 6-1. The full-pipe and open-channel model equations and boundary conditions.

Full-pipe	Open-channel
Model equations	Model equations
$$\frac{\partial S^*}{\partial t^*} = \frac{|Q^*|^3}{S^{*\frac{8}{3}}} - S^* N^{*3}$$ **6-36**	$$\frac{\partial S^*}{\partial t^*} = -S^* N_a^{*3}$$ **6-41**
$$\frac{\partial Q^*}{\partial s^*} = \epsilon_R(r-1)\frac{|Q^*|^3}{S^{*\frac{8}{3}}} + \epsilon_R S^* N^{*3} + M^*$$ **6-37**	$$\frac{dQ^*}{ds^*} = M^*$$ **6-42**
$$\frac{\partial N^*}{\partial s^*} = \frac{1}{\delta}\left(\frac{Q^*|Q^*|}{S^{*\frac{8}{3}}} - \psi^*\right)$$ **6-38**	$$Q^* = \mu \frac{S_w^{*\frac{5}{3}}}{P_w^{*\frac{2}{3}} n'_a}$$ **6-43**
Boundary condition at the lake $$N^*(s_T, t) = N_a = \beta_R[1 - (h_L^* - \epsilon_h h_r^*)]$$ **6-39**	Boundary condition at the lake $$Q^*(0,t) = Q_{in}^*$$ **6-44**
Lake level evolution $$\frac{dh_L^*}{dt^*} = \frac{\lambda_L}{h_L^{*P_L-1}}[Q_{in}^* - Q^*(0,t)]$$ **6-40**	Lake level evolution $$h_L^* = h_w^* \frac{h_{w0}}{h_{L0}}$$ **6-45**

Movement of the transition
$$\dot{s}_T = \eta \frac{Q_F^* - Q_{oc}^*}{S^* - S_w^*}$$ **6-46**

Box 6-1 summarises the full-pipe and open-channel model equations. When flow is entirely full-pipe, eqns. 6-36 to 6-40 describe the evolution of the channel and lake's

depth. If lake level drops below the height of the channel roof at the lake, a transition between open and full-pipe flow forms.

Above the transition, channel closure is described by eqn. 6-41 and integration of eqn. 6-42 from the lake, where the discharge is given by eqn. 6-44, to the upglacier side of the transition provides the discharge here, Q_{oc}. The area of flow, $S_w(s=s_T)$ is found by inverting Manning's equation (eqn. 6-43 with area of flow, wetted-perimeter and perimeter-averaged Manning's roughness coefficient given by eqns. 6-25, 6-27 and 6-28, respectively).

Below the transition, eqns. 6-36 to 6-38 model full-pipe flow and channel evolution with effective pressure boundary conditions of $N(s,t) = N_a = \rho_i gH$ at the transition, $s = s_T$, and the terminus, $s = s_0$. This provides the discharge on the downglacier side of the transition, Q_F. The transition moves according to eqn. 6-46 and if it reaches the terminus flow remains completely open until discharge at the terminus exceeds the maximum discharge the channel can transfer via open-channel flow, Q_m. This maximum discharge is found by inverting eqn. 6-16 for θ_m, using eqn. 6-17 to find h_w and substituting this into Manning's equation.

6.3   The beginning and end of open-channel flow

Before studying periods of open-channel flow in detail (in section 6.4) and solving the full model numerically (in section 6.5) it is worth considering how the system moves into and out of periods of open-channel flow

Open-channel flow starts when the lake depth, h_L, falls below the height of the channel's roof at the lake, $h_r(s = 0)$; for simplicity, in this analysis I refer to the latter as h_r. Fig. 6.4 shows the channel mouth when lake depth and channel height are momentarily equal (see Fig. 6.1a for a side view of the system at this stage of the flood cycle). At this moment, a period of open-channel flow will begin if the lake depth decreases faster than the channel roof drops due to creep closure of the channel. Conversely, if the channel closes faster than the lake depth decreases, full-pipe flow will continue uninterrupted.

In the following I consider the competition between the rate at which the lake depth changes and the rate at which the channel roof drops to show that there exists a critical value for the channel height at this stage of the flood cycle. While the channel height is lower than this critical height, a period of open-channel flow cannot begin because the lake level cannot fall sufficiently to reach the channel roof and start open-channel flow. Open-channel flow can only begin when the channel is larger than the critical height and the lake level falls to the height of the channel.

The same critical channel height also determines the system's evolution immediately after the transition has reached the lake following a period of completely open-channel flow. At this stage in the flood cycle full-pipe can only persist if the channel has shrunk to a size corresponding to a height less than the critical channel height.

Here I consider in detail the special case of a vertically-walled lake ($p_L = 1$) and only mention briefly the effect that a lake area that increases with lake depth ($p_L > 1$) has on the critical channel height.
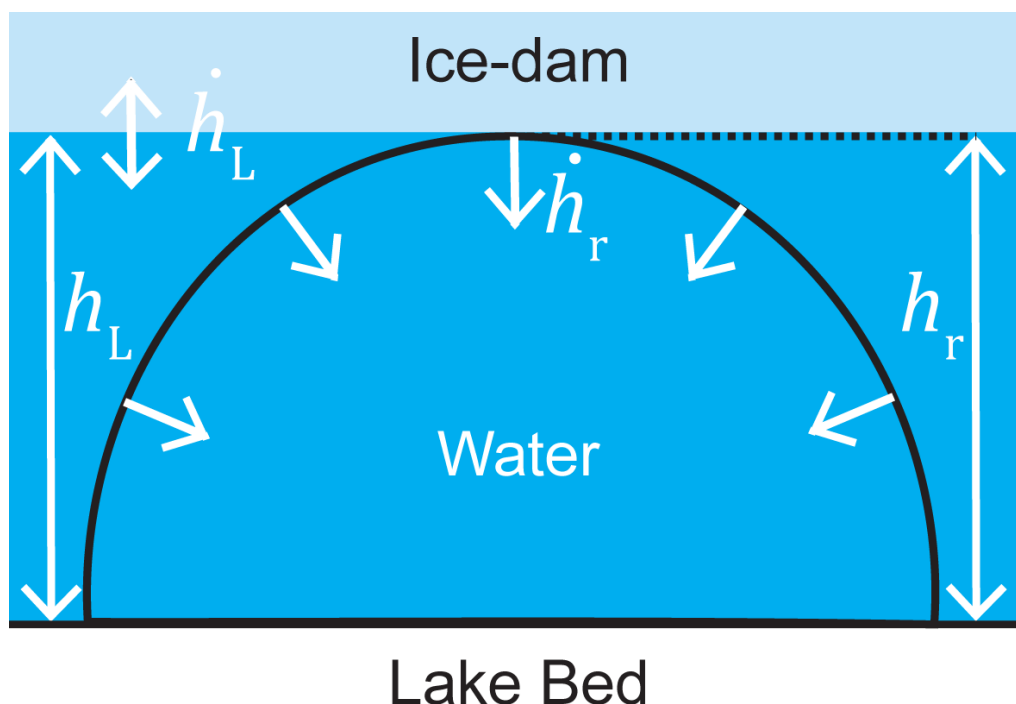

Fig. 6.5. Conditions at the lake outlet at two critical stages of the flood cycle: the moment the lake depth reaches the channel height immediately after a flood, and the moment the transition arrives at the lake after a period of open-channel flow.

I aim to compare how the lake level and the height of the channel roof evolve with time when lake depth is low compared to the height of the ice dam. I start by examining channel evolution.

Ignoring channel enlargement through frictional melt, a positive (non-dimensional) effective pressure in the channel adjacent to the lake, N_L^*, causes the channel to close through ice creep. The non-dimensional rate of change of channel height $\dot{h_r}^*$ is given by:

$$\dot{h_r}^* = -\frac{N_L^{*3}}{2} h_r^*,$$

6-47

where the dot above the h_r^* denotes a time derivative. Defining

$$\xi = \frac{h_{L0}}{h_{r0}}$$

6-48

and substituting this and eqn. 6-5 into eqn. 6-47 yields

$$\dot{h_r}^* = -\frac{\beta^3 [1 - \varsigma h_r^*]^3}{2} h_r^* \, ,$$

6-49

where

$$\varsigma = (\xi - \epsilon_h) \approx 0.11.$$

6-50

Multiplying out the expression in the square brackets in eqn. 6-49 gives

$$\dot{h_r}^* = -\frac{\beta^3 [h_r^* - 3\varsigma^2 h_r^{*2} + 3\varsigma^3 h_r^{*3} - \varsigma^4 h_r^{*4}]}{2}.$$

6-51

At both stages of the flood cycle I am considering here $h_r^* \leq 1$. Hence, the first term in the square brackets above is at least a factor of $1/(3\varsigma^2) \approx 27$ larger than the second. The third and fourth terms are smaller still. Neglecting the small terms, which is equivalent to neglecting the pressure of the water in the channel mouth acting to impede channel creep closure, leaves the following expression for the rate of change of channel height when the lake level is low:

$$\dot{h_r}^* = -\frac{\beta^3 h_r^*}{2}.$$

6-52

The rate of change of lake level, $\dot{h_L}^*$, is given by eqn. 6-4 with $p_L = 1$:

$$\dot{h_L}^* = \lambda_L [Q_{in}^* - Q^*] \, .$$

6-53

To determine the discharge Q^* I assume the along-channel gradient in the effective pressure, $\partial N^*/\partial s^*$, is small compared to the basic potential gradient, ψ^*. Hence, Q^* is given by eqn. 6-3 with $\partial N^*/\partial s^* = 0$:

$$\psi^* = \frac{Q^*|Q^*|}{S^{*\frac{8}{3}}}.$$

6-54

Eliminating Q^* between this expression and eqn. 6-53 gives:

$$\dot{h}_{\mathrm{L}}^{*} = \lambda_{\mathrm{L}} \left[Q_{\mathrm{in}}^{*} - \sqrt{\psi^{*} S^{*\frac{8}{3}}} \right].$$

6-55

The cross-sectional area S^* is related to channel height by eqn. 6-24, so

$$\dot{h}_{\mathrm{L}}^{*} = \lambda_{\mathrm{L}} \left[Q_{\mathrm{in}}^{*} - \sqrt{\psi^{*}} h_{\mathrm{r}}^{*\frac{8}{3}} \right].$$

6-56

Equations 6-52 and 6-56 form a pair of ordinary differential equations for h_{r} and h_{L}. Fig. 6.6 plots the system's trajectories on the h_{r}-h_{L} phase-plane in the region where $h_{\mathrm{L}} \geq h_{\mathrm{r}}$ and the channel flow is full. I determined the trajectories by noting that neither variable's rate of change depends on h_{L} and then by determining their incline on three lines of constant h_{r}. Firstly, when $h_{\mathrm{r}} = 0$; $\dot{h}_{\mathrm{r}}^{*} = 0$ and $\dot{h}_{\mathrm{L}}^{*} > 0$. So, trajectories are orientated along the h_{L}-axis in the direction of increasing h_{L}. Secondly, when $h_{\mathrm{r}}^* < Q_{\mathrm{in}}^{*3/8}\psi^{*-3/16}$; $\dot{h}_{\mathrm{L}}^{*} = 0$. Trajectories cross this line parallel to the h_{r}^*-axis. Thirdly, equating eqns. 6-52 and 6-56 yields an expression for the channel height that results in the lake level and channel height changing at the same rate, $\tilde{h}_{\mathrm{r}}^{*}$

$$-\frac{\beta^3}{2} \tilde{h}_{\mathrm{r}}^{*} = \xi \lambda_{\mathrm{L}} \left[Q_{\mathrm{in}}^{*} - \sqrt{\psi^{*}} \tilde{h}_{\mathrm{r}}^{*\frac{8}{3}} \right].$$

6-57
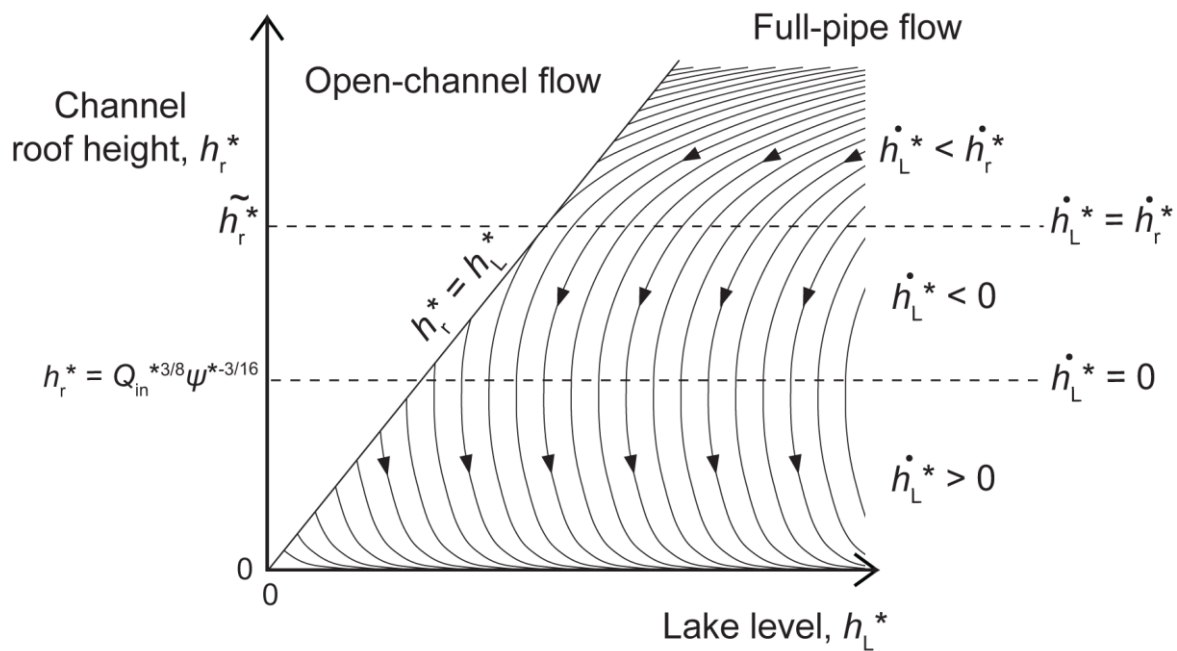
Fig. 6.6. The trajectories of the model consisting of differential equations for channel height, h_{r}, and lake level, h_{L}, (eqns. 6-52 and 6-56) in h_{r}-h_{L} phase-phase, in the region $h_{\mathrm{L}} \geq h_{\mathrm{r}}$.

Trajectories pass through $h_r = \tilde{h}_r^{\,*}$, with an incline of 45°. Between these three lines the inclines of the trajectories vary smoothly and non-linearly.

Indicated in Fig. 6.6 is the line $h_r^* = h_L^*$. When the system crosses this line from the lower-right half of the plot into the upper-left half, open-channel flow begins. The trajectories in Fig. 6.6 show this is only possible when $h_r^* > \tilde{h}_r^{\,*}$. If this is not the case the system will not reach $h_r^* = h_L^*$ and full-pipe flow will continue uninterrupted. A channel height larger than the critical value is a necessary but not sufficient requirement for open-channel flow. The trajectory also needs to meet the $h_r^* = h_L^*$ line. Where a trajectory enters this region of phase space determines whether it does so and this is determined by the history of the flood's development.

When the system crosses the line $h_r^* = h_L^*$ from the upper-left to the lower-right of the plot, open-channel flow ends. This occurs after the spatial transition between open-channel and full-pipe flow has travelled upglacier to the lake. The trajectories in Fig. 6.6 show that full-pipe flow can only continue if the system emerges from the upper-left part of the plot in the region where $h_r^* < \tilde{h}_r^{\,*}$. If the system emerges where $h_r < Q_{in}^{*3/8} \psi^{*-3/16}$, the lake level increases, in the region $Q_{in}^{*3/8} \psi^{*-3/16} \le h_r \le \tilde{h}_r^{\,*}$ the lake
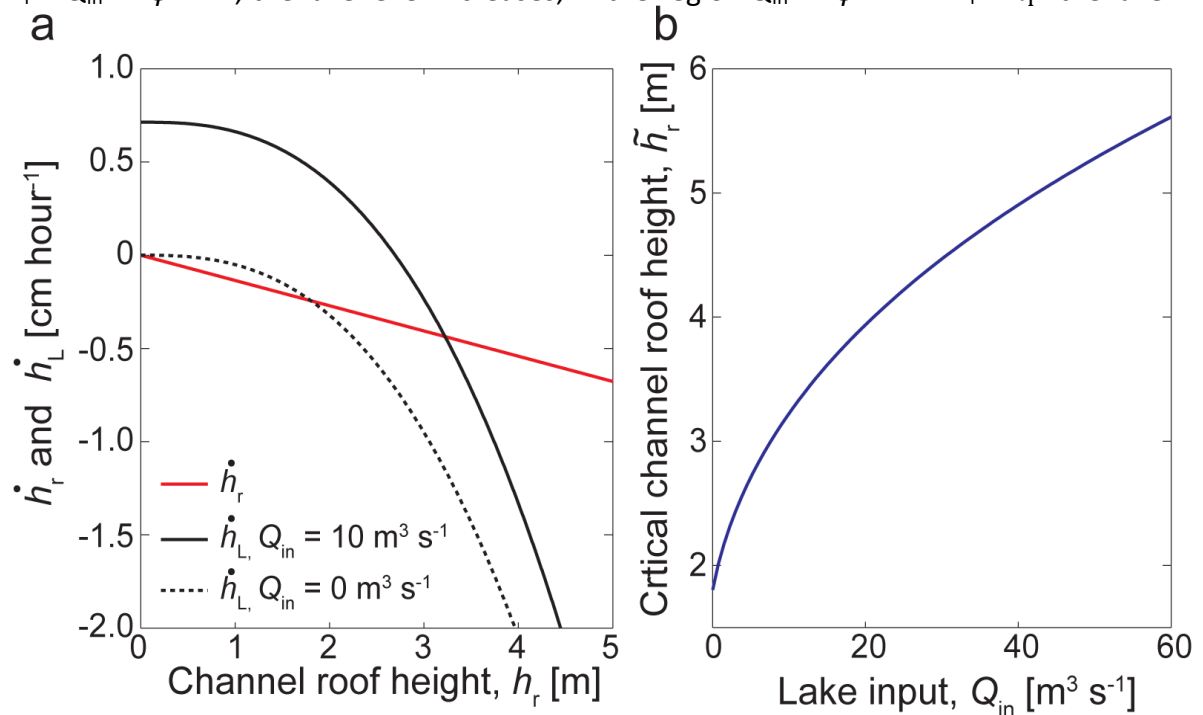

Fig. 6.7. (a) The rate of change of lake level, $\dot{h}_L$ (black curves) and channel roof height, $\dot{h}_r$ (red curve) as a function of the channel roof height. The dashed and solid black lines show $\dot{h}_L$ when lake input $Q_{in} = 0$ m³ s⁻¹ and $Q_{in} = 10$ m³ s⁻¹ respectively. The position along the horizontal hr-axis of the intercept between the black and red lines corresponds to the critical channel height discussed in the text. The critical height depends on the lake input and (b) plots this non-linear dependence. All calculations consider a vertically-walled lake ($p_L = 1$).

level drops more slowly than the channel roof, and in the region $h_r^* > \widetilde{h}_r^{\,*}$, lake level falls faster than the channel roof drops and open-channel flow would immediately be re-established.

Equation 6-57 can be used to calculate the critical channel height. In the special case when $Q_{in}^* = 0$,

$$\widetilde{h}_r^{\,*} = \left(\frac{\beta^3}{2\lambda_L \xi \sqrt{\psi^*}} \right)^{\frac{3}{5}}.$$

<div align="right">

6-58

</div>

With $\beta = 0.9$, $\lambda_L \approx 3.2$, $\xi \approx 0.2$ and $\psi^* = 1$, this gives $\widetilde{h}_r^{\,*} \approx 0.102$ or, dimensionally, ≈ 1.8 m.

Fig. 6.7a shows the solution of eqn. 6-57 graphically (and dimensionally). The black dashed curve is the dimensional rate of change of lake depth, $\dot{h}_L$, as a function of the channel roof height, h_r, given by eqn. 6-56 with $Q_{in} = 0$ m^3 s^{-1}. It is negative for all h_r, because the lake is not being filled, and its magnitude increases nonlinearly with the channel roof height, because the lake drains faster through a larger channel according to the (nonlinear) Manning's equation. A second curve, in red, shows the rate of change of channel height, $\dot{h}_r$, as a linear function of h_r as given by eqn. 6-52. The two lines intersect at the point predicted by eqn. 6-58, ($h_r \approx 1.8$ m, $\dot{h}_L \approx -0.24$ cm hour^{-1}). The solid black curve in Fig. 6.7a shows the same as the dashed black curve, but is calculated numerically from eqn. 6-57 with $Q_{in} = 10$ m^3 s^{-1}. The lake input increases the rate of change of lake level and when $h_r < h_{r0}Q_{in}^{*3/8}\psi^{*-3/16} \approx 2.7$ m this rate is positive. This increases the critical channel height to 3.2 m. The nonlinear relationship between lake input and the critical channel height is shown in Fig. 6.7b where the critical channel height is plotted as a function of the lake input by repeatedly solving eqn. 6-57 numerical for $\widetilde{h}_r$ using Newton-Raphson while varying h_r.

The critical channel height also depends on other glacio-hydraulic parameters. Substituting expressions for β, ξ, h_{L0}, h_{r0} and S_0 into eqn. 6-58 from eqns. 2-55, 6-48, 2-53, 6-24 and 2-47 respectively, shows how $\widetilde{h}_r^{\,*}$ is related to the ice-flow constant, K_0, the ice-dam height, H_D, the area of the lake, A_{Li}, and the basic hydraulic gradient scale, ψ_0:

$$\widetilde{h}_r^{\,*} \propto \left(\frac{K_0 H_D{}^3 A_{Li}}{\psi_0^{\frac{3}{16}}} \right)^{\frac{3}{5}}.$$

<div align="right">

6-59

</div>

Higher H_D and K_0 correspond to a thicker, more deformable ice-dam which speeds-up channel closure, hence $\widetilde{h}_r^{\,*}$ increases with both parameters. The surface of a lake with a

larger surface area is drawn down more slowly than that of a smaller lake, hence the increase in $\widetilde{h}_r^*$ with A_{Li}. Finally, the larger the basic hydraulic gradient, ψ_0, the larger the discharge through a channel of a particular size. Hence, increasing ψ_0 decreases $\widetilde{h}_r^*$. The strongest control on $\widetilde{h}_r^*$ is the ice-dam thickness.

I have assumed a lake with vertical walls ($p_L = 1$) whereas in reality when lake level is low the area is likely to be smaller than at other times (due to a non-uniform lake bed or icebergs deposited on the bed during the flood). In the model this can be represented using $p_L > 1$. The decreased area increases the rate at which the lake level changes (see eqn. 6-4 with $p_L > 1$ and $h_L^* \ll 1$), which will increase the critical channel roof height $\widetilde{h}_r^*$.

6.4   The duration of open-channel flow

One result of the scaling analysis in section 6.2.3 motivates the derivation of a simple expression for the duration of periods of open-channel flow. This expression could be used in future extensions to the flood prediction work presented in Chapter 4 to include post-flood open-channel flow in reconstructions of past flood volumes (see Fig. 1.3b and section 4.3.4).

In the non-dimensional transition equation (eqn. 6-46), the parameter η is the ratio of two timescales: the flood evolution time scale, t_0, and the time it takes a channel of typical peak total volume $s_0 S_0$ to empty of water if the discharge out of it is a typical peak discharge Q_0. Because $\eta \gg 1$, if the lake depth goes below the channel height while discharge at the lake outlet is much higher than the input to the lake, as in previous numerical simulations (e.g. Fig. 3.2b), the transition's downglacier movement will be rapid. Supposing that its upglacier movement after the end of the period of completely open flow is also rapid, which is favoured by a small total air-filled headspace in the channel, the duration of open flow is largely controlled by the time the channel takes to close. In what follows I make the assumption that the transition's migration from the lake to the terminus and its later migration back to the lake happen instantaneously. Hence, I derive an analytical expression for the duration of open-channel flow in terms of the ice thickness at the terminus and the ratio between the discharge at the lake outlet when open-channel flow starts and the discharge at the terminus.

Reverting temporarily to dimensional equations; using $h_w = h_r \sin(\theta_w)$, Manning's equation in a semi-circular channel is written as

$$Q = \gamma h_r^{\frac{8}{3}}$$

6-60

where

$$\gamma = \frac{\left[\theta + \frac{1}{2}\sin 2\theta\right]^{\frac{5}{3}}\sqrt{\phi_b}}{[2(\theta + 1)]^{\frac{2}{3}}\left[\left(\frac{\theta}{1+\theta}\right)n_i + \left(1 - \frac{\theta}{1+\theta}\right)n_b\right]} .$$

<div align="right">6-61</div>

The maximum discharge the channel can transfer via open-channel flow, Q_m, is given by

$$Q_m = \gamma(\theta = \theta_m)h_r^{\frac{8}{3}} = \gamma_m h_r^{\frac{8}{3}},$$

<div align="right">6-62</div>

where the depth-angle corresponding to maximum discharge, θ_m, can be found by solving 6-16. Using eqn. 6-41, $S = (\pi h_r^2)/2$ and the chain rule, channel closure can be expresses in terms of h_r:

$$\frac{dh_r}{dt} = -\frac{K_0 N_a^3}{2}h_r .$$

<div align="right">6-63</div>

Using eqn. 6-60, eqn. 6-63 and the chain rule, solving the resulting Q_{max} time-evolution equation shows that Q_m decays exponentially with time as the channel closes according to the following expression:

$$Q_m = Q_{m0}e^{-\frac{t}{\tau_0}} ,$$

<div align="right">6-64</div>

where τ_0 is the time constant of the decay

$$\tau_0 = \frac{3}{4K_0(\rho_i gH)^3} .$$

<div align="right">6-65</div>

The decay is quicker beneath thicker and more deformable ice (larger H and K_0). Q_{m0} is the maximum discharge at the moment the flow becomes completely open and the transition forms. I ignore the time the transition takes to travel from the lake to the terminus and assume Q_{m0} corresponds to the moment the lake level reaches the channel height at the lake. I also assume the effective-pressure gradient in the channel is small and the channel's cross-sectional area is given by eqn. 2-31 (the dimensional form of eqn. 6-3) with $\partial N/\partial s = 0$:

$$S = Q_{F0}^{\frac{3}{4}}\left(\frac{6.6\rho_w gn_a'^2}{\psi}\right)^{\frac{3}{8}},$$

<div align="right">6-66</div>

where Q_{F0} is the channel discharge at the lake at the moment the transition forms and ρ_i is the density of ice. Substituting $S = (\pi h_r^2)/2$ into eqn. 6-66 and eliminating h_r between the resulting expression and eqn. 6-62 yields an expression for Q_{m0} in terms of Q_{F0}:

$$Q_{m0} = \gamma_m \left(\frac{2}{\pi}\right)^{\frac{4}{3}} \sqrt{\frac{6.6\rho_w g n_a'^2}{\psi}} Q_{F0} .$$

6-67
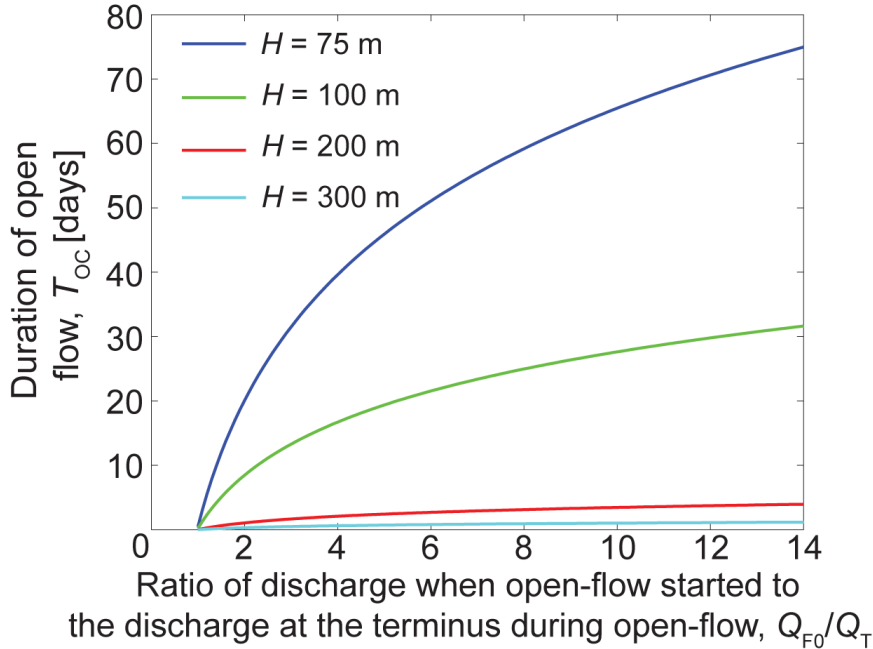
Fig. 6.8. The dependence of the duration of open flow on the ratio between the discharge when open-flow started to the discharge at the terminus, Q_{F0}/Q_T, predicted by eqn. 6-69 using four different ice thicknesses.

Assuming open-channel flow continues until the discharge at the terminus, Q_T, exceeds Q_m, substituting eqns. 6-65 and 6-67 into eqn. 6-64 and rearranging approximates the duration of open-channel flow, T_{oc}:

$$T_{OC} = \frac{3}{4K_0(\rho_i g)^3 H^3} \ln \left[\gamma_m \left(\frac{2}{\pi}\right)^{\frac{4}{3}} \sqrt{\frac{6.6 \rho_w g n_a'^2}{\psi}} \frac{Q_{F0}}{Q_T} \right] ,$$

6-68

or

$$T_{OC} = C_1 H^{-3} \ln \left(C_2 \frac{Q_{F0}}{Q_T} \right)$$

6-69

where C_1 and C_2 are constants ($C_1 \approx 10^{12}$ s m^3 and $C_2 \approx 1$, when $\gamma \approx 0.72$ m$^{1/3}$ s^{-1}, $n_i' = 0.06$ m$^{-1/3}$ s, $n_b' = 0.17$ m$^{-1/3}$ s and $\psi = 100$ Pa m^{-1}). The duration of open flow, T_{OC}, is more strongly dependent on ice thickness than on the discharge at the lake when open flow begins, Q_{F0}, and the discharge at the terminus during open-flow, Q_T. Fig. 6.3 shows this graphically. The dependence of T_{OC} on the ratio Q_{F0}/Q_T predicted by 6-69 is plotted for several different ice thicknesses, $H = \{75, 100, 200, 300\}$ m. In section 6.5.4   the

predictions of this expression are shown to agree closely with results from numerical simulations of the full open-channel flow model.

6.5   Numerical simulations

Here I present results from numerical model simulations of full flood cycles including periods of open-channel flow. I use the same model geometry as I did in previous chapters: a rectangular lake drains beneath a uniform slab glacier, $p_L = 1$, $V_{Li} = 5 \times 10^8$ m³, $h_{Li} = 100$ m, $a = 0$, $\psi_0 = 100$ Pa m^{-1}, $s_0 = 10$ km, $H = 100$ m (see Fig. 3.1). The discharge scale is chosen as $Q_0 = 1500$ m³ s^{-1}. The results of the model simulations are used to validate assumptions made during the analyses above and shown to be consistent with the findings of those analyses. Multiple simulations are conducted to investigate the controls on the size of flood cycles that include periods of open-channel flow.

6.5.1 Numerics

Time and space domains are discretised in the manner described in section 2.2.5 using non-dimensional time steps of 0.02 and a grid spacing of 0.01. When flow is entirely full-pipe eqns. 6-36 to 6-40 are solved by stepping lake level and channel area forward in time using the Euler method and the previous time-step's discharge and effective pressure profiles computed with the relaxation method (2.2.5).

When flow is partially open (Fig. 6.1b), the transition's movement is simulated by eqn. 6-46. As indicated by the scaling analysis above, this is found to be very rapid. Hence, this part of the simulation must be implemented in an inner loop that effectively reduces the time step by a factor of 10 during periods of partially-open flow. During each iteration of the inner loop, five steps are taken: (i) eqn. 6-42 is numerically integrated from the lake to the transition with a discharge boundary condition at the lake given by the lake input (eqn. 6-44); (ii) at each grid-point between the lake and the transition and at the transition (which can be between grid-points), Manning's equation (eqn. 6-43, with eqns. 6-25, 6-27 and 6-28) is inverted for flow depth using the Newton-Raphson method; (iii) discharge and effective pressure profiles are computed from eqns. 6-37 and 6-38 using Newton's method (see section 2.2.5); (iv) the channel area is evolved forward in time with eqn. 6-41 above the transition and eqn. 6-36 below, using Forward-Euler time-stepping; and (v) the transition's movement is simulated using Forward-Euler time-stepping with eqn. 6-46.

When flow is entirely open, discharge, channel closure and flow depth are calculated as described above for the above-transition region. At the terminus the maximum discharge is calculated from Manning's equation using the channel height here and the depth-angle corresponding to maximum discharge for the channel. The latter is

pre-calculated from eqn. 6-16 using Newton-Raphson. The initial lake level is 30 m and the uniform initial channel cross-sectional area is $0.01S_0 \approx 5$ m^2.
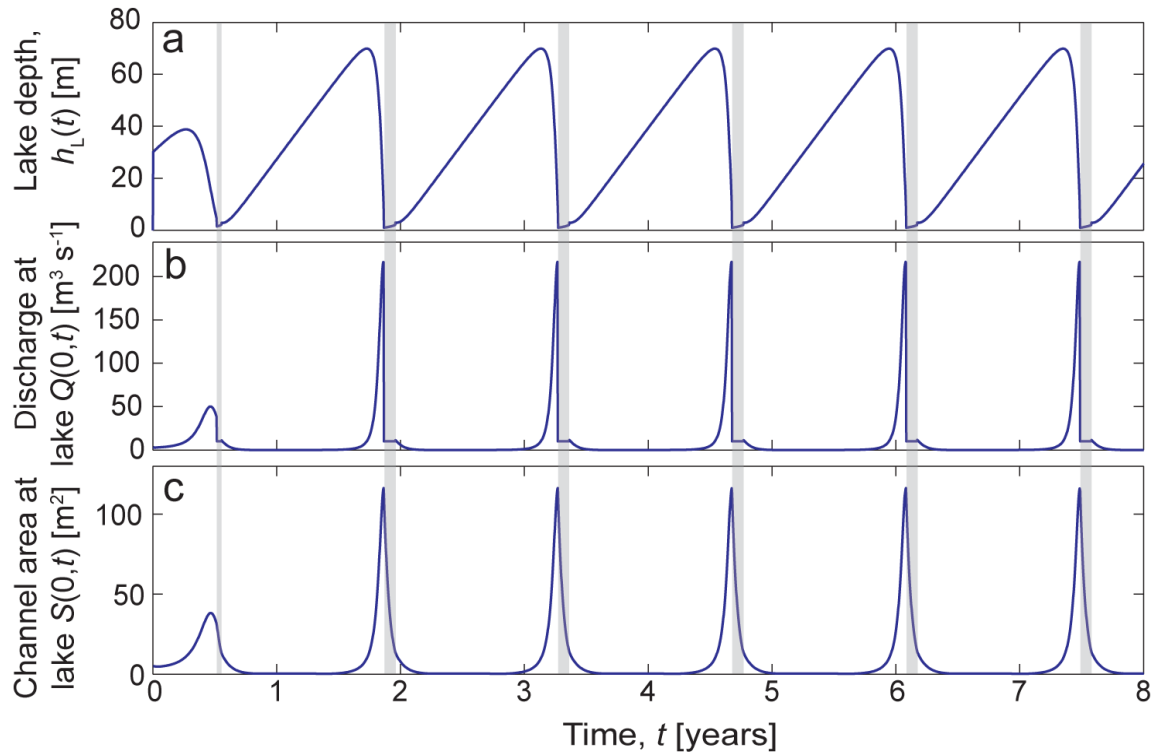

Fig. 6.9. Simulated flood cycles including open-channel flow. Timeseries of (a) lake level, $h_L(t)$, (b) discharge at the lake, $Q(0,t)$, and (c) channel area at the lake, $S(0,t)$. Shading indicates periods of open-channel flow. Lake input, Q_{in} = 10 m^3 s^{-1}, channel water supply, $M \approx 0.0002$ m^2 s^{-1} and basic hydraulic gradient parameter, a = 0 (see eqn. 3-9).

6.5.2 Flood cycles

Fig. 6.9 shows results from a model run with lake input Q_{in} = 10 m^3 s^{-1} and channel water supply $M \approx 0.0002$ m^2 s^{-1}. This model run acts as a control. The time series of the lake level, the discharge at the lake outlet and the channel cross-sectional area at the lake show how the model simulates periods of lake filling followed by floods with peak discharges of 50-200 m^3 s^{-1}. During each flood the lake level drops below the height of the channel at the lake, which results in periods of open-channel flow (indicated by the shaded time-periods in Fig. 6.9). The system reaches a limit cycle after several floods.

Fig. 6.10 shows the last flood cycle displayed in Fig. 6.9 in more temporal detail with the addition of the channel-height time series. The flood's early stages are similar to those of floods simulated in Chapters 3; discharge and channel size increase (Fig. 6.10a & b) through Nye's (1976) melt-discharge feedback and the lake level begins to drop when discharge exceeds lake input (Fig. 6.10a). In this simulation, the lake level reaches the
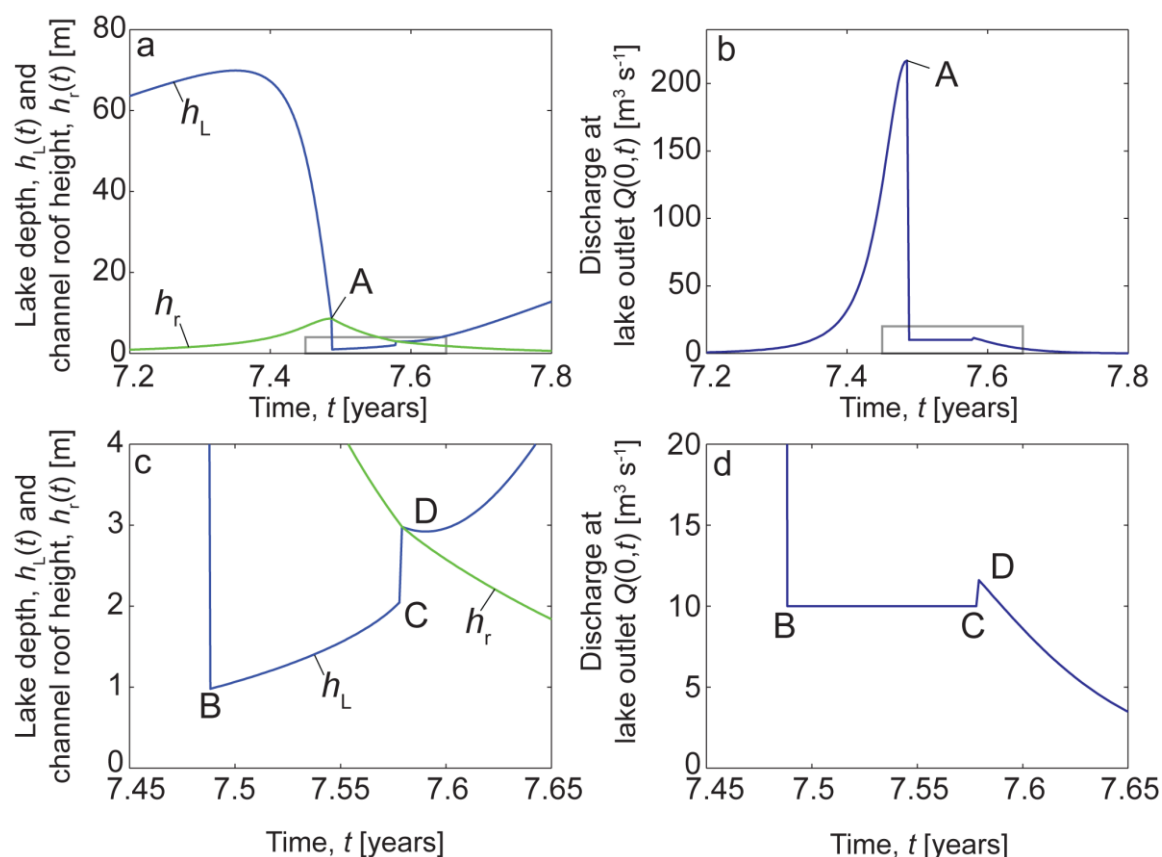
Fig. 6.10. A simulated flood that resulted in a period of open-channel flow. (a and b) show the entire flood and (c and d) show the period of open-channel flow in more detail, their vertical and horizontal extents are indicated in (a) and (b) by black boxes. In both cases, the left plots show timeseries of lake depth (blue) and channel roof height (green) and the right plots show timeseries of discharge through the channel at the lake.

height of the channel roof at the lake when it is 8.6 m (labelled A in Fig. 6.10a & b). This is larger than the critical channel height of 3.2 m and after the lake level falls below the channel roof height a transition between open-channel and full-pipe flow forms and rapidly travels downglacier to the terminus. This is the beginning of the period of completely open flow (see Fig. 6.1c). During this period (between B and C, Fig. 6.10c & d) the lake depth equals the depth of flow in the channel at the lake, which slowly increases as the channel closes through creep, and the discharge at the lake equals the lake input. After ~30 days the channel has closed sufficiently that the discharge at the terminus exceeds the channel's maximum open-channel capacity and the transition re-forms and rapidly travels upglacier to the lake (C, Fig. 6.10c & d). At this stage the channel height at the lake is 3.0 m. This value is below the critical channel height of 3.2 m calculated in section 6.3, and, as predicted during that analysis, initially the discharge at the lake is larger than the lake input (D, Fig. 6.10d) and lake level drops (D, Fig. 6.10c).

150

However, the channel height drops more quickly than the lake level drops and full-pipe flow persists.

Before and after periods of completely open-channel flow (between A and B, and between C and D, in Fig. 6.10, respectively) the transition's movement is very rapid. In both cases it completes the journey between the lake and the terminus in less than one time step (< 5.4 hours). This suggests that it was appropriate to ignore the transition's journey time in comparison to the total duration of open-channel flow. To help explain the transition's rapid movement, Fig. 6.11a plots along-glacier profiles of the channel height from stages in the flood cycle corresponding to A and B in Fig. 6.10. The solid green line is the channel height profile at stage A, when the transition first forms at the lake. The channel is large, with a mean height of 8.6 m. Downglacier of the transition it can transfer a much larger water discharge, Q_F, than reaches the transition from its upglacier side – the lake input plus a contribution from the channel water supply M. A first order estimate of Q_F is given by eqn. 6-3 with $\partial N^*/\partial s^* = 0$: $Q_F \approx 200$ m^3 s^{-1}. Lake
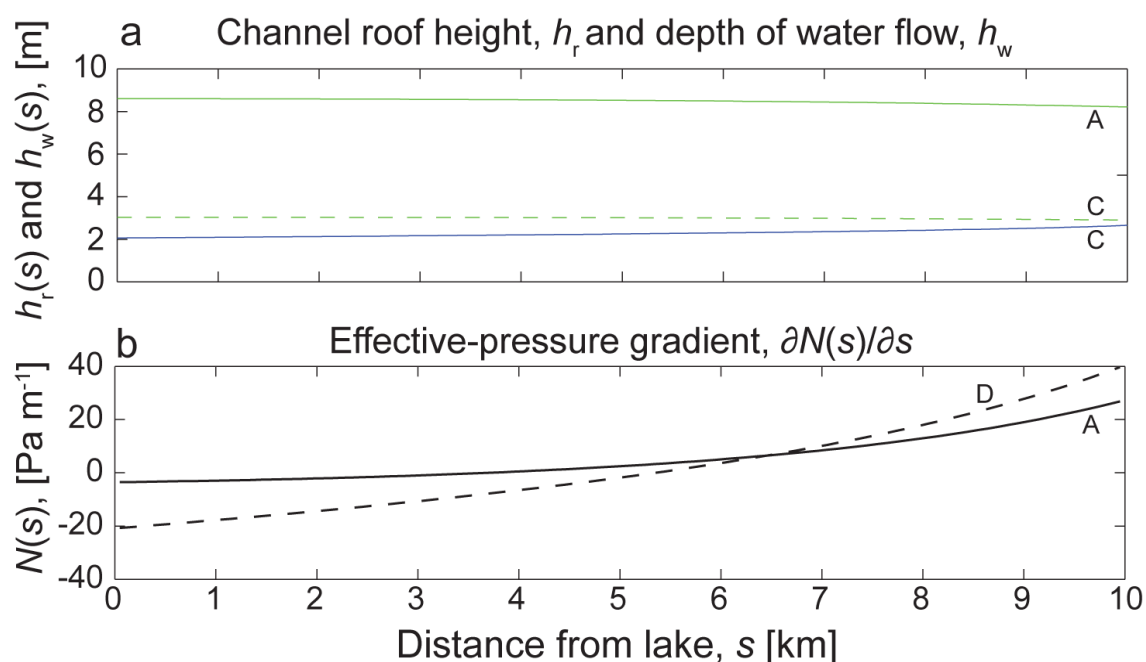

Fig. 6.11. Along-glacier profiles of (a) channel height (green) and depth of water flow (blue) and (b) effective-pressure gradient. Each profile is labelled A, C or D, indicating the stage in the flood cycle shown in Fig. 6.10 it corresponds to.

input is only 10 m^3 s^{-1}, hence the transition moves downglacier rapidly. After the subsequent period of open-channel flow, the transition moves upglacier similarly rapidly to the lake. The dashed green line in Fig. 6.11a shows the channel height profile at stage C of the flood cycle and the solid blue line is the corresponding profile of the water's depth of flow. The air-filled head-space between the water's surface and the channel roof is small; the total air-filled volume in the channel is only ~18000 m^3. In this case it is this small head-space that causes the transitions rapid movement.

In sections 6.3 and 6.4 I assumed the effective pressure gradient was small compared to the basic hydraulic gradient at the beginning and end of periods of open-channel drainage. Profiles of effective-pressure gradient, corresponding to stages A and D of the flood cycle (see Fig. 6.10) and plotted in Fig. 6.11c suggest that this was appropriate.

6.5.3 Controls on flood size

Fig. 6.12 plots results extracted from 19 nine-year-long model simulations, with different channel water supplies (Fig. 6.12a) and lake meltwater inputs (Fig. 6.12b). Each pair of points (one green, one blue) corresponds to one simulation. The results corresponding to the simulation described in detail above are labelled in the figure. During most simulations the system approaches limit cycles. Three exceptions, indicated in the figure, are simulations during which the lake filled too slowly to flood more than a few times. The highest level the lake reached – the highstand – and the peak discharge during the final flood cycle in each simulation are plotted.

Fig. 6.12a shows that highstand and peak discharge decrease with the channel water supply. In Chapter 3 and Chapter 5 a similar result, found while simulating flood cycles with no periods of open-channel flow, was explained by considering the dynamics of a subglacial water divide that forms between floods. Further analysis of the results of these new simulations reveals that a divide forms between each simulated flood. I conclude that, like in situations when no open-channel flow occurs, the dynamics of a subglacial water divide cause the channel supply's control on highstand and peak discharge.

Fig. 6.12b shows how peak discharge and highstand varied between different simulations using different lake meltwater inputs, Q_{in}. The relationship is not monotonic. When $Q_{in} < 12$ m^3 s^{-1}, peak discharge and highstand increase with Q_{in} and when $Q_{in} > 12$ m^3 s^{-1} they decrease with Q_{in}. In Chapter 3 these measures of flood size were found to increase with Q_{in}. As with their relationship to channel water supply, this relationship was explained by considering the dynamics of a subglacial water divide.

Of the 11 simulations that produced the results shown in Fig. 6.12b, no divide formed between floods during the four that used the highest Q_{in} (= 14, 16, 18, 20 m^3 s^{-1}). Despite this, all four reached limit cycles. Note that these are the same model runs that display the negative relationship between lake input and flood size. In Chapter 3 I found that simulations could only reach limit cycles if a divide formed between floods or there was a topographic divide, i.e. the basic hydraulic gradient near the lake was negative. Neither is the case for these four simulations.

The contrast between the previous chapter's results and those presented here points to
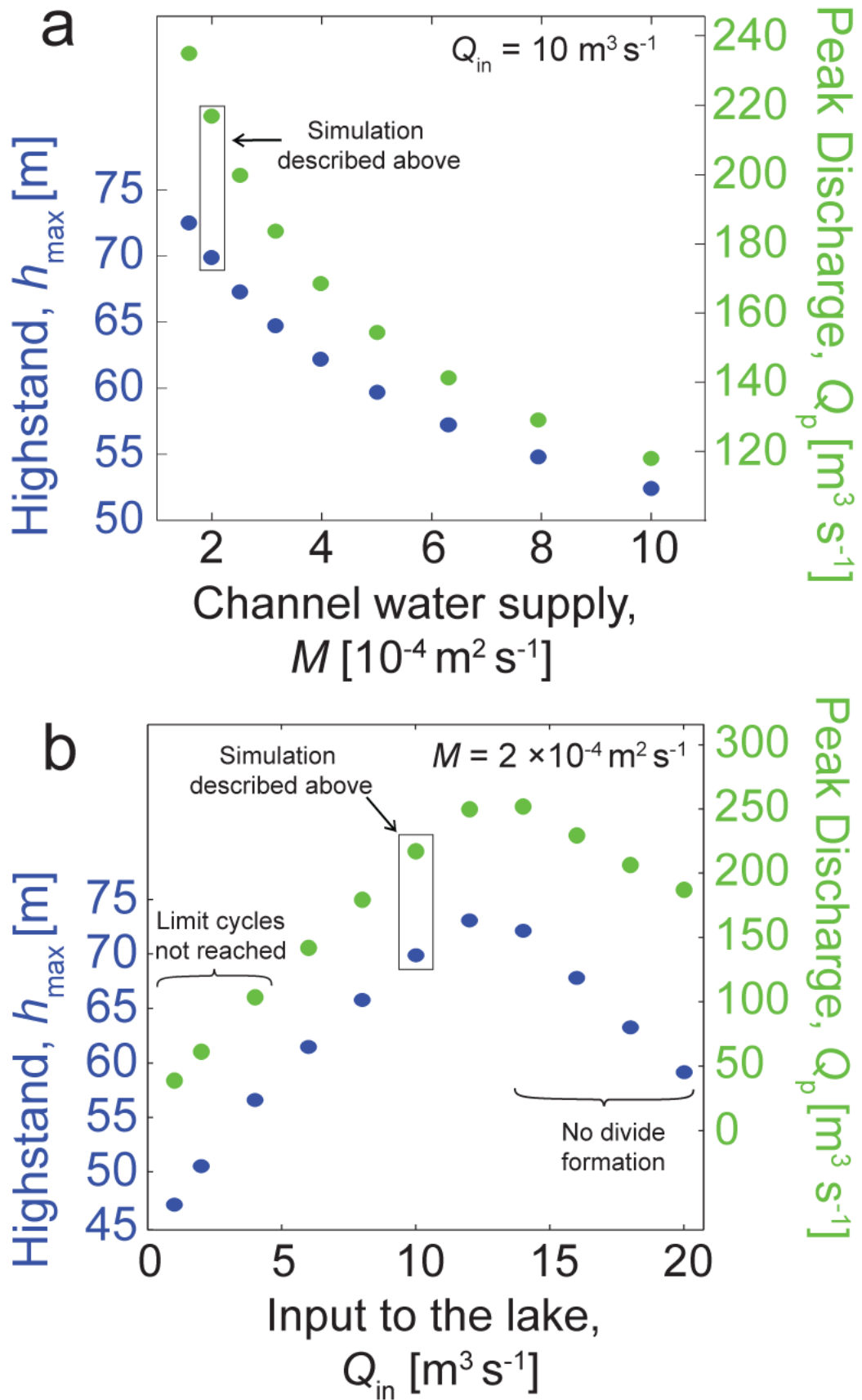
**Fig. 6.12. Peak discharge and highstand as a function of (a)** M**, with** Q_{in} **= 10 m^3 s^{-1}, and (b)** Q_{in}**, with** $M \approx$ **0.0002 m^2 s^{-1}. During all simulations, except were indicated, a water divide forms between floods**

a new mechanism linking lake input and flood size that is exclusive to cycles that include periods of open channel flow. Such periods end when the discharge at the terminus, consisting of the lake input, Q_{in}, plus the total water supply to the channel along its length, Ms_0, exceeds the maximum discharge the channel can transfer, Q_m. The latter is related to the channel's height, h_r, by eqn. 6-62,

$$Q_{m} = \gamma_{m} h_{r}^{\frac{8}{3}},$$

<div align="right">**6-70**</div>

where γ_m is a constant. Therefore, assuming the channel remains spatially uniform (see Fig. 6.11a) and ignoring the transition's journey time between the terminus and the lake (see discussion in section 6.5.2), the size of the channel after a period of open-channel flow increases with the lake input and the channel water supply:

$$h_{r} = \left(\frac{Q_{in} + Ms_0}{\gamma_{m}} \right)^{\frac{3}{8}}.$$

<div align="right">**6-71**</div>

The conditions after a period of open-channel flow act as the next flood's initial conditions. For a given initial lake height ($h_L \sim 0$ m), a larger initial channel size will tend to expedite flood development and decrease the size of the next flood. But, during most simulations the formation of a water divide and a long period of low discharge between floods shrinks the channel significantly and prevents this 'memory effect'. However, during the four simulations that used the highest lake input, the initial channel was larger enough to prevent a divide forming. With no divide formation, the mechanisms described in Chapter 3 that link lake input and flood size based on divide dynamics do not operate and the channel's initial conditions can affect flood development. Hence, flood size decreases with lake input for these four simulations.

6.5.4 Numerically simulated duration of open-channel flow

I now compare the predictions of the analytical model of the duration of periods of open-channel flow with the results of the numerical simulations that produced the results discussed in the section above. Between them, the 19 model simulations produced 112 complete flood cycles. Every cycle included a period of open-channel flow whose duration, T_{oc}, has been extract from the results. Fig. 6.13 plots, as blue crosses, each period's duration against the ratio of the discharge just before open-channel flow began, Q_{F0}, to the discharge at the terminus during open-channel flow, Q_T. The green line plots T_{oc} as predicted by eqn. 6-69 with $H = 100$ m. The numerically-derived results

lie close to the analytically-derived line with small discrepancies due to the assumptions of spatially uniform effective-pressure and channel height before and after periods of open-channel flow. This finding increases confidence in the assumptions that underlie the simplified analytical model.
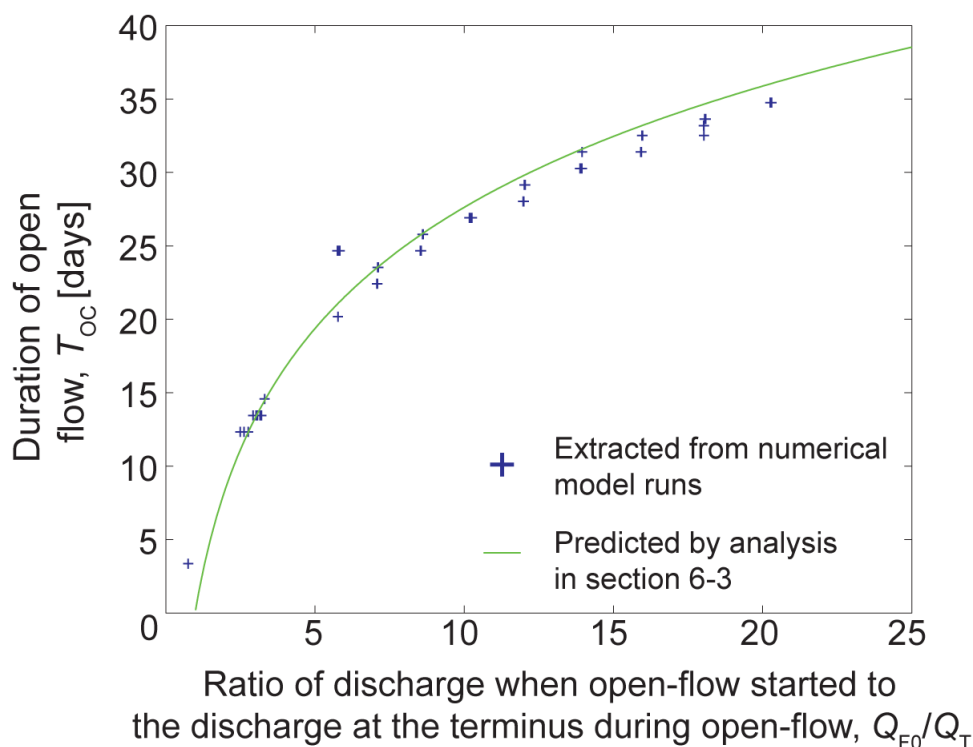

Fig. 6.13. Comparison of the duration of open channel flow extracted from many numerical model simulations to the predictions of eqn. 6-68.

6.6   Discussion and conclusions

The simplified model of full-pipe flow at low lake levels analysed in section 6.3 shows that model behaviour when the system switches between open and full-pipe conditions depends on the channel's height relative to a critical channel height. This critical height increases with the lake meltwater input, the ice-dam thickness, the deformability of the ice and the area of the lake. It decreases with the magnitude of the basic hydraulic gradient driving water flow away from the lake. The system cannot switch to open-channel conditions without the channel reaching this critical height. Conversely, the system cannot switch back to full-pipe flow unless the channel shrinks to below this critical height during a period of open-channel flow. The simplified model highlights one set of controls on whether a flood results in open-channel flow – the glacio-hydraulic controls on critical channel height – but it does not address whether the lake level will reach this critical height. Asking whether it does or not amounts to asking what trajectory in the phase space depicted in Fig. 6.6 the system is on as it enters this region

of phase space (the region of low lake level). As shown in Chapter 3 such trajectories depend on environmental factors, for example, lowstand decreases with lake input and increases with channel water supply. I stop short of a combined analysis of the controls on flood size and the critical channel height, as the aim of this chapter is to present the first attempt at modelling open-channel flow after jökulhlaups. Future work could take on such a combined analysis.

In section 6.4, motivated by its potential future use in improved reconstruction of jökulhlaup lake level, I derived an expression for the duration of periods of open-channel flow. The analysis showed that their duration is more sensitive to ice thickness than the hydrological conditions before or during open-channel flow. It is sensitive to ice thickness because this controls the ice overburden pressure and hence the rate of channel closure. Hence, open-flow duration may vary more between systems than between floods from the same system. For simplicity I have assumed that ice thickness is uniform and the first position at which the channel closes sufficiently to end open-channel flow locally is the terminus. In a real, non-uniform glacier, thicker areas will close most rapidly and, when applying the model to such a glacier, it may be appropriate to replace the ice thickness H in eqn. 6-68 with the glacier's maximum thickness along its centre line.

For the purpose of reconstructing past flood volumes one wants to know the length of the delay between a flood terminating and the lake resuming the impoundment of meltwater. This delay may be longer than the duration of open-channel flow predicted by the simple model. Numerical solution of the full model shows that when full-pipe flow resumes, discharge remains positive for tens of days after open-channel flow ceases. This slow recession is controlled by the closure of the channel at the lake and it will be possible in future work to derive an expression, equivalent to eqn. 6-68, that approximates its duration.

Numerical solution of model equations can simulate the full glacio-hydraulic cycle introduced in section 6.2.1. Detailed analysis of the hydrological state of the system at key points in this cycle suggest assumptions regarding the spatial uniformity of the effective pressure and channel size, made during earlier analyses were appropriate. Comparing the results of multiple model simulations has shown that, in some parts of parameter space, the dynamics of a water divide dominate the relationship between environmental parameters and flood size – this was also seen in Chapter 3. However, when lake input is high, a divide does not form and instead the size of the channel after one flood significantly affects the next. This results in the size of floods decreasing with lake input – the opposite relationship to that found in earlier chapters when cycles with no open-channel flow were investigated. Crucially, this new mechanism allows the

environmental conditions immediately following a flood to affect the size of the next flood. This memory effect only occurs when meltwater input to the lake is large enough. It has implications for real jökulhlaup systems where floods habitually result in open-channel flow and lake input varies inter-annually. In these systems, an isolated warm year would result in a large flood, because the previous flood, having occurred in a year of 'average weather', was not abnormally large, so the memory effect does not operate. Because the weather is warm when this large flood ends, the channel at the end of the period of open-channel flow is large. Hence, the next flood cycle starts with a large initial channel size. This prevents a divide forming and the next flood will consequently be small. Such a pattern is in fact observed in the reconstructed lake level history from Merzbacher Lake; several anomalously large floods are followed by short filling periods and small floods (see Fig. 1.3a). Future work will investigate this idea further.

Chapter 7   Supraglacial lake drainage

7.1   Introduction

In previous chapters I have focused on subglacial processes. Here I turn my attention to the surface analogue of subglacial jökulhlaups: surface drainage of supraglacial lakes through melt enlargement of a surface channel. Water from rain or melt can flow over ice surfaces and collect in topographic depressions to form lakes (e.g. Echelmeyer et al., 1991; Lüthje et al., 2006; Sundal et al., 2009; Selmes et al., 2011; Reynolds, 1981). Lakes are important because they lower the glacier's surface albedo, thereby increasing the absorption of incoming radiation (Lüthje et al., 2006; Tedesco et al., 2012); they can rapidly drain to the bed of an ice sheet, affecting ice dynamics (e.g. Das et al., 2008); and they are thought to play a role in ice-shelf disintegration (e.g. Scambos et al., 2009). Surface drainage of lakes relocates water down glacier, affecting where these processes operate. In the following I consider examples of such water relocation from the
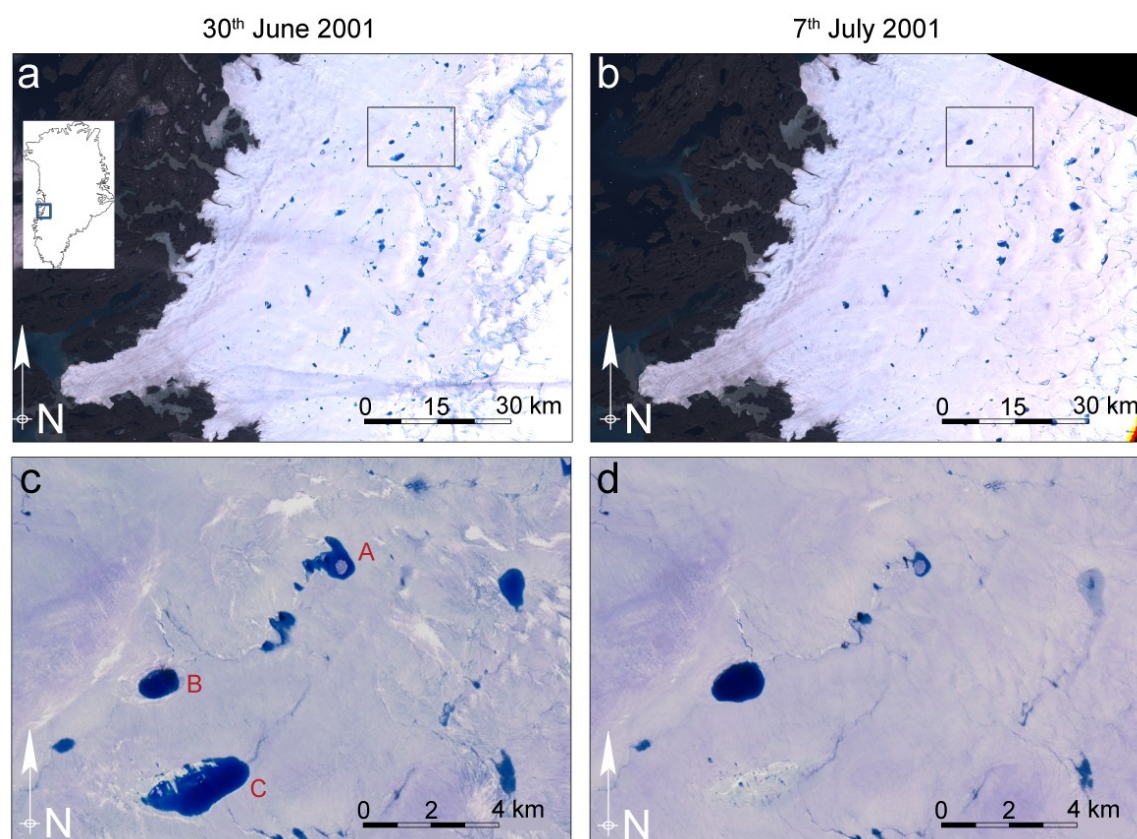
**Fig. 7.1. Supraglacial lake drainage in Greenland. (a) and (b) two LANDSAT 7 images acquired 7 days apart on 30ᵗʰ June 2001 and 7ᵗʰ July 2001. Inset in (a) shows the location this part of the ice sheet in Greenland. Boxes in (a) and (b) indicate the region shown in more detail in (c) and (d), where the supraglacial drainage of one lake (A) to another (B) and the rapid drainage of a third lake (C) are visible.**

Greenland and East Antarctic Ice Sheets to motivate this chapter's modelling investigation of supraglacial lake drainage.

Fig. 7.1 displays two LANDSAT 7 satellite images acquired on 30th June 2001 and 7th July 2001 of a land-terminating section of the Greenland Ice Sheet south of Jakobshaven Isbræ. Figs. 7.1c & 7.1d are enlarged images of the area outlined by the boxes in Figs. 7.1a & 7.1b. Several blue supraglacial lakes can be seen clearly against the white ice sheet surface. During the 7 days that separate the images, the upglacier limit of the region of the ice sheet populated by lakes moved upglacier and individual lakes shrunk, grew and drained completely (examples are labelled in Fig. 7.1 as A, B and C respectively). Water from a lake that drains completely can reach the bed (e.g. Das et al., 2008). Because such lake-to-bed drainage can affect ice dynamics through the subglacial coupling considered in Chapter 5 and through its effect on seasonal subglacial drainage-system evolution (Bartholomew et al., 2011b; Das et al., 2008), the location and evolution of supraglacial lakes has implications for the future dynamic response of the ice sheet to atmospheric warming. However, water from a supraglacial lake can also breach surface topographic divides to flow supraglacially into another lake, thus redistributing potential points of basal melt water injection. An example of such supraglacial drainage is visible in Fig. 7.1 between lakes A and B. Modelling and understanding such drainage is the focus of this chapter.

The present study is also motivated by new observations of surface drainage in Antarctica, where surface melt and lake formation have been implicated as the cause of ice-shelf collapse in the warmest parts of Antarctica (the Antarctic Peninsula) (e.g. Fahnestock and Abdalati, 2002; Scambos et al., 2000; Scambos et al., 2003; Scambos et al., 2009; Sergienko and Macayeal, 2005; van den Broeke, 2005). As Fig. 7.2 shows, surface melt and lake formation also occur in East Antarctica along with large-scale relocation of water from the ice sheet flank to an adjacent ice shelf.

The MODIS and LANDSAT satellite imagery show multiple images of Nivlisen Ice Shelf, Dronning Maud Land (70°68'S, 12°09'E) and were acquired at different stages of one melt season. Lakes form on the ice-sheet's flank (source lakes, Fig. 7.2a) before rapidly draining, spreading meltwater across the ice shelf. Fig. 7.2a was acquired on 5th Jan 2008 after several weeks of melt and drainage. The temporal evolution of this drainage is shown in detail in Figs. 7.2b–7.2g. The meltwater wave front (red arrows) propagates across the shelf, at average velocities of 1.7-6.8 m min^{-1}, along paths created by the previous year's refrozen flood water, travelling up to 70 km and flooding an area of ~260 km^2 (~3.3% of the ice-shelf's area). More images (acquired between 2002 and 2009; not shown) show that this previously unreported phenomenon occurs nearly every year. The
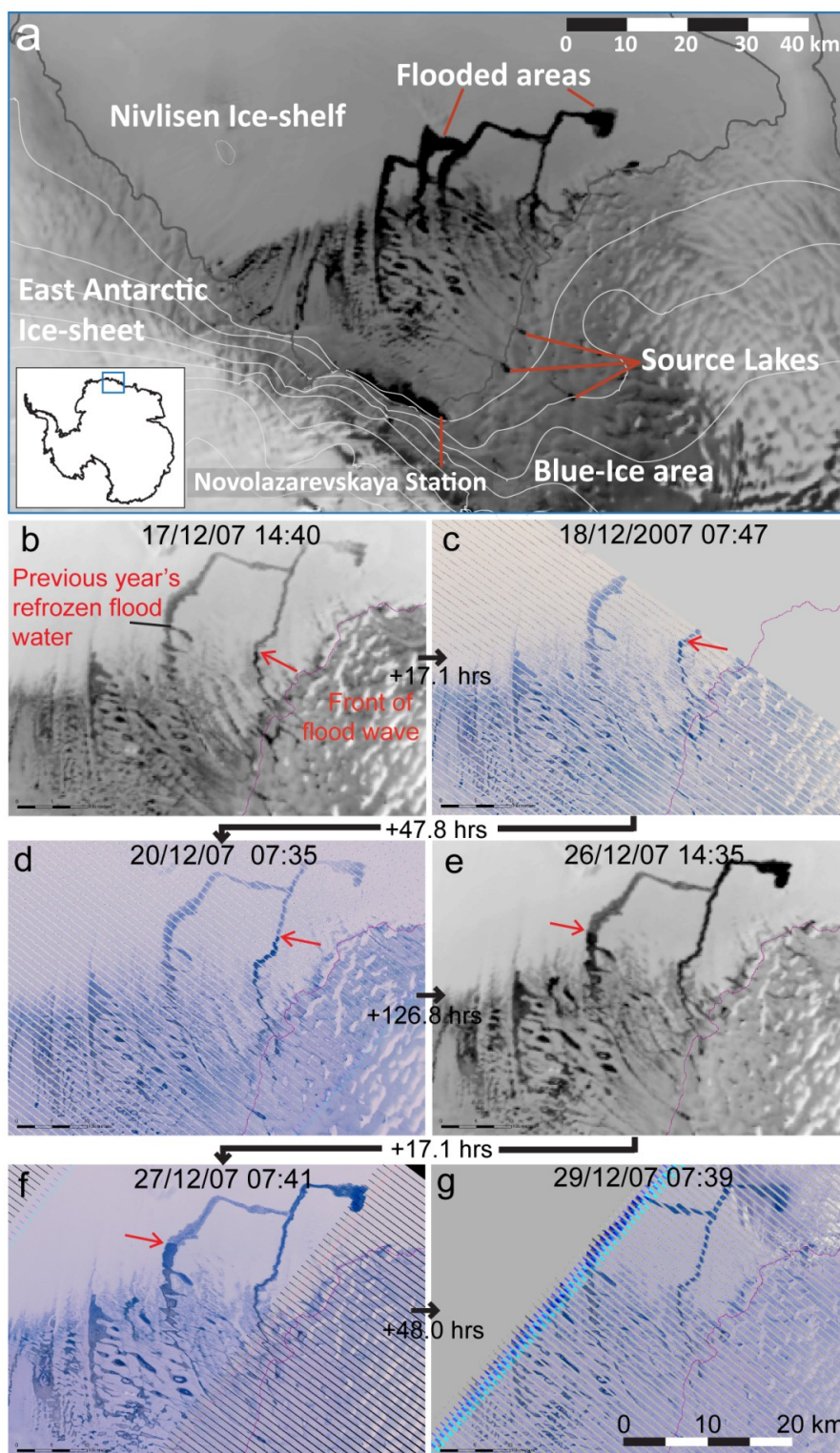
Fig. 7.2. Surface Drainage in East Antarctica. (a) MODIS optical satellite image acquired on 5th Jan 2008, showing: Nivlisen Ice shelf inundated with melt water, source lakes, 100 m surface contours (in white) and the grounding line (in grey). **(b)** Six MODIS and LANDSAT images showing the time evolution of the 2007-08 flood. Red arrows indicate the flood wave front and the time separating image acquisition is shown beneath the black arrows. In **(f)** flood water completely covers the previous year's refrozen flood path. See Scambos et al. (1996) for more details on how the images are acquired.

images also reveal large inter-annual variability in drainage. This, coupled with an analysis of weather station data from a nearby Russian research station Novolazarevskaya (Fig. 7.2a), suggests that the extent of lake formation and drainage is highly sensitive to air temperature. The effect of melt water on ice shelf stability has been demonstrated by disintegration events in the Antarctic Peninsula and these new observations from East Antarctica further motivate my efforts to understand surface drainage of supraglacial lakes.

In this chapter I develop a model of lake drainage through an ice-walled surface channel, incised in ice by melting caused by the turbulent dissipation of heat in the flowing water. Previous work has taken a similar approach (Walder and Costa, 1996; Raymond and Nolan, 2000, Vincent et al., 2010; Mayer and Schuler, 2005). The novelty here is the more generally applicable model of hydrology in the channel and my application of the model to supraglacial lakes in ice sheets.

Raymond and Nolan (2000) adapted Walder and Costa's (1996) model of lake drainage through an ice-rock breach to describe surface lake drainage in the alpine, debris-covered glacier setting. They introduced a criterion for unstable drainage: initial channel incision rate exceeding the initial rate of lake surface lowering. Using this, they showed that a critical lake area exists above which drainage, initiated by the lake overtopping its bank, is unstable. Using the same criterion Mayer and Schuler (2005) found a critical lake temperature above which lake drainage is unstable.

Both studies assumed a constant channel width much larger than the water's depth of flow in the channel, whereas Vincent et al. (2010) followed Walder and Costa (1996) and assumed critical flow to simplify the determination of the channel water depth.

In my model water depth is instead determined by Bernoulli's equation and momentum conservation in the lake and the lake outlet. This enables wider application of the model, to scenarios where simplifications made by previous authors are not valid. I follow Raymond and Nolan (2000) in considering the stability of drainage but take my analysis further to explain physically how and why some parameters affect stability and others do not.

The model consists of equations describing the time evolution of the height of a supraglacial lake's surface and the bottom surface of a rectangular channel, and further equations describing the hydraulics of water flow through the channel. It is developed in section 7.2. In section 7.3 I investigate the controls on drainage stability by examining my model equations analytically. In section 7.4 I corroborate findings of this analytical investigation by running numerical simulations of drainage using the model. In section 7.5, I discuss my findings in relation to future melt-extent change in Greenland and my new observations in East Antarctica.

7.2 Model formulation

The model geometry is shown in Fig. 7.3. A supraglacial lake drains through a channel incised into the ice. The model ignores the along-channel spatial dimension, assuming that the drainage of lake water is controlled by a single, stationary point in the channel near the lake, labelled as the lake outlet in Fig. 7.3.

7.2.1 Lake evolution

The lake has a volume V_L, a surface area A_L, and a depth h_L, related by the hypsometry parameterisation introduced in eqn. 2-35,

$$\left(\frac{h_L}{h_{Li}}\right)^{p_L} = \frac{V_L}{V_{Li}}.$$

7-1

Lake depth evolves with time, t, due to melt water input from its surroundings, Q_{in}, and outflow, Q, though a channel according to

$$\frac{dh_L}{dt} = \frac{1}{A_{Li}}\left(\frac{h_{Li}}{h_L}\right)^{p_L-1}[Q_{in} - Q],$$

7-2

where A_{Li}, V_{Li} and h_{Li} are the lake's reference area, volume and depth respectively, and are related by $A_{Li} = p_L\, V_{Li}/h_{Li}$. p_L is a lake shape parameter, $p_L = 1$ corresponds to a vertically-walled lake and increasing p_L corresponds to increasingly 'horn-shaped' lakes (Clarke, 1982). The meltwater input to the lake is assumed to originate from an area upglacier of the lake and I ignore melting of the lake bed, assuming a constant lake shape.
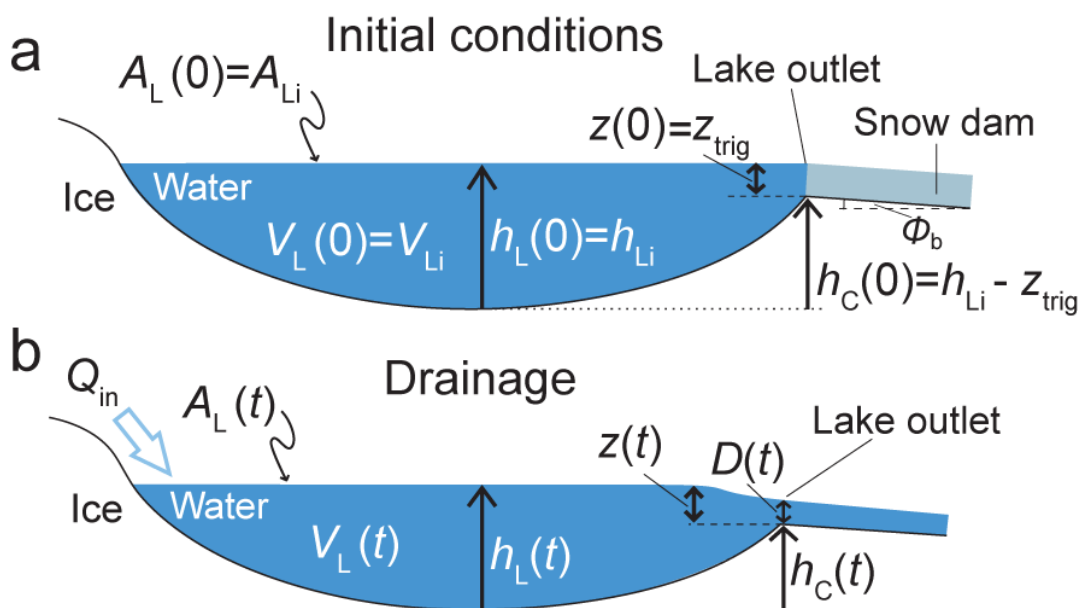

Fig. 7.3. Schematic of the surface lake drainage model geometry (a) before drainage (initial conditions) and (b) during drainage.

7.2.2 Bernouli's equation in the channel mouth

I consider the flow out of the lake into the channel mouth to be a potential flow to which Bernoulli's equation is applicable:

$$z + \frac{u^2}{2g} = \text{constant,}$$

<div align="right">7-3</div>

where u is the surface velocity of the flow and z is the height of the water above an arbitrary datum (e.g. Henderson, 1966). I use the height of the lake's bed for this datum and I denote the surface velocity of the water in the channel by v and the height of the channel bottom above the lake bed by h_c. Applying eqn. 7-3 to the surface of the water in the lake, where $u = 0$, and to the surface of the water flowing in the channel, where $u = v$, yields

$$h_L = (D + h_c) + \frac{v^2}{2g}.$$

<div align="right">7-4</div>

Next, I assume that the velocity of the water flowing in the channel is uniform and equal to the surface velocity v and that the channel has a rectangular cross-section with a constant width w. The discharge through the channel Q is therefore given by

$$Q = vwD.$$

<div align="right">7-5</div>
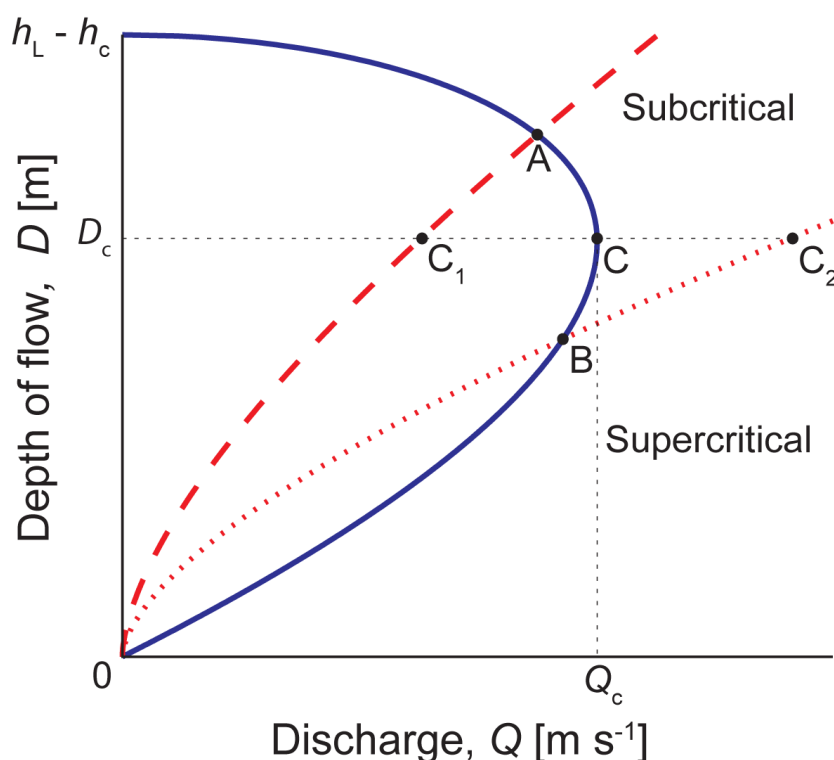
Fig. 7.4. Depth of flow, *D*, as a function of discharge, *Q*, from Bernoulli's equation (blue line) and Manning's equation (red dashed and dotted lines).

Hence, eqn. 7-4 can be written as

$$h_{\mathrm{L}} - h_{\mathrm{c}} = D + \frac{Q^2}{2gw^2D^2}.$$

7-6

The blue curve in Fig. 7.4 plots D vs. Q as defined by eqn. 7-6. The two branches of the curve with dD/dQ < 0 and dD/dQ > 0 correspond to subcritical and supercritical flow respectively (corresponding to F_{R} < 1 and F_{R} > 1, where the Froude number F_{R} is given by $F_{\mathrm{R}} = v(gD)^{-0.5}$) and meet at a critical point (C) where $D = D_{\mathrm{C}}$ and discharge is at a maximum, Q_{C}. Maximising Q with respect to D by differentiating eqn. 7-6 reveals how D_{C} is related to the lake height h_{L}, the height of the channel bottom h_{C} and Q_{C}

$$D_{\mathrm{c}} = \frac{2}{3}(h_{\mathrm{L}} - h_{\mathrm{c}}) \quad and \quad Q_{\mathrm{c}} = \sqrt{g\,w^2 D_{\mathrm{c}}^3}.$$

7-7

7.2.3 Force balance in the channel

To complete the model's description of water flow through the channel I balance the shear stress exerted by the moving water on the ice with the gravitational driving stress. I parameterise the shear stress with the Darcy-Weisbach equation,

$$\tau = \frac{1}{8}f_R\rho_w v^2,$$

7-8

where f_{R} is a friction constant and ρ_{w} is the density of water. In previous chapters I used Manning's equation to parameterise the balance of momentum in flowing water. My choice here of the Darcy-Weisbach equation simplifies the analysis of the model and does not qualitatively affect the model's behaviour. The gravitational driving stress, τ_{d}, depends on the along-channel slope ϕ_{b} and the depth of flow D:

$$\tau_{\mathrm{d}} = \rho_{\mathrm{w}}g\phi_{\mathrm{b}}D.$$

7-9

I assume the channel slope remains constant and uniform. Equating τ and τ_{d}, substituting in $Q = vwD$ and rearranging for Q yields an expression for the discharge in terms of the channel slope, the channel width, the depth of flow and the roughness of the channel:

$$Q = \sqrt{\frac{8g\phi_{\mathrm{b}}}{f_{\mathrm{R}}}}\,wD^{\frac{3}{2}}.$$

7-10

The red dashed curve in Fig. 7.4 plots this discharge–flow-depth relationship. This curve intercepts the blue curve derived from Bernoulli's equation (eqn. 7-6) at point A. This

point corresponds to the discharge Q and depth of flow D which simultaneously obeys both Bernoulli's equation and the force balance represented by eqn. 7-10.

7.2.4 Critical flow

Point A is on the subcritical branch of the Bernoulli curve (in blue), but, depending on model parameters, the intercept between the Bernoulli and force-balance curves can lie on the supercritical branch. The red dotted line in Fig. 7.4 plots the discharge–flow-depth relationship for a channel with a larger slope and a smaller roughness parameter than were used to plot the dashed line. It intercepts the Bernoulli curve at point B.

This leads to a slight complication in the model. When flow is supercritical at some position along a flowpath, hydrologists usually assume that discharge is controlled by a transition from sub- to super-critical flow somewhere upstream. At such a transition flow is critical, with discharge and flow depth given by maximising discharge with respect to flow depth (as I did to derive eqn. 7-7 for the special case of a rectangular channel). Indeed, artificial weirs are designed so that water flow over them is critical and the discharge can be easily calculated using the observed water depth upstream of the weir and eqn. 7-7. I adopt a similar approach here and assume that, when the solution to the Bernoulli and force balance equations indicate supercritical conditions, discharge is in fact provided by eqn. 7-7. Because the model has no along-channel spatial dimension, I am also assuming that the transition through critical flow occurs at the lake outlet (Fig. 7.3).

On which branch of the Bernoulli curve the solution lies, can be conveniently determined by evaluating where the force balance curve (red curves in Fig. 7.4) intercepts the line in $D = D_C$ (the horizontal dashed line Fig. 7.4 that passes through C_1, C and C_3). If this intercept occurs to the right of point C (e.g. at C_2) the flow is supercritical and the discharge at the lake outlet is the critical discharge Q_C, given by eqn. 7-7. Conversely, if the intercept is to the left of C (e.g. at C_1), flow is subcritical and the intercept between the force-balance and Bernoulli curves (e.g. A) provides the discharge at the lake outlet.

7.2.5 Channel incision

Heat transferred from the flowing water to the ice melts and enlarges the channel. I assume the lake temperature is 0°C, so that the only source of heat is frictional dissipation in the flowing water. Hence the mass of ice melted per unit length of the channel per unit time, m, is

$$m = \frac{\tau v w}{L}$$

7-11

(Walder and Costa, 1996). For simplicity I assume melt occurs in the channel bottom but not at the sides. This is motivated by other studies that make the same simplification (e.g. Mayer and Schuler, 2005; Vincent et al., 2010) and the fact that at present it is unclear how best to apportion melt between the channel bed and its side. Accordingly, the rate of change of the height of the channel bottom above the lake bed, h_c, is given by

$$\frac{dh_c}{dt} = -\frac{f_R \rho_w}{8 L \rho_i} v^3 \,.$$

7-12

Equations 7-2, 7-5, 7-6, 7-7, 7-10 and 7-12 complete the model:

$$\frac{dh_L}{dt} = \frac{1}{A_{Li}} \left(\frac{h_{Li}}{h_L}\right)^{p_L - 1} [Q_{in} - Q] \,,$$

7-13

$$Q = vwD,$$

7-14

$$h_L - h_c = D + \frac{Q^2}{2 g w^2 D^2} \,,$$

7-15

$$D_c = \frac{2}{3} (h_L - h_c),$$

7-16

$$Q_c = \sqrt{g\, w^2 D_c^3} \,,$$

7-17

$$Q = \sqrt{\frac{8 g \phi_b}{f_R}}\, w D^{\frac{3}{2}} \,,$$

7-18

$$\frac{dh_c}{dt} = -\frac{f_R \rho_w}{8 L \rho_i} v^3 .$$

7-19

These describe respectively the time evolution of lake level, Bernoulli's equation in the water flowing from the lake into the channel, the characteristics of critical flow, the balance of frictional and driving forces in the flowing water and the downward incision of the channel into the glacier surface.

7.3   Drainage stability

Before embarking on a numerical sensitivity analysis in the next section, I investigate model behaviour analytically. I will show that the surface drainage simulated by the model can be stable or unstable. Stable drainage remains bounded and often stops altogether before the lake has been emptied completely, while unstable drainage grows unboundedly with time, leading to complete emptying of the lake. In what follows I discuss the origin of these two styles of drainage, mathematically and physically. I go on to show how and why some model parameters affect drainage stability while other do not.

For this analysis I ignore the complication of a transition through critical flow controlling discharge in some cases (see previous section). This does not affect the findings of the present section qualitatively and comparison between these findings and the results of numerical simulations using the full model in the next section will highlight the role that critical flow plays in drainage.

I define z as the height difference between the lake's surface and the bottom of the channel (h_L - h_C) (see Fig. 7.3). Recasting eqns. 7-15 and 7-18 in terms of the flow velocity v (using eqn. 7-14) and rearranging both for the flow depth in the channel D results in

$$D = z - \frac{v^2}{2g},$$

7-20

$$D = \frac{v^2 f_R}{8g\phi_b}.$$

7-21

Eliminating D between the two equations above and rearranging yields the following expression relating the flow velocity to the difference z:

$$v^2 = z\frac{2g}{1 + \frac{f_R}{4\phi_b}}.$$

7-22

Eliminating v between this and eqn. 7-19 yields

$$\dot{h}_c = -\alpha z^{\frac{3}{2}},$$

7-23

where the dot above the h_C denotes a time derivative and

$$\alpha = \frac{f_R \rho_w}{8 L \rho_i} \left(\frac{2g}{1 + \frac{f_R}{4\phi_b}} \right)^{\frac{3}{2}}.$$

7-24

Eliminating D between eqn. 7-14 and eqn. 7-21 yields

$$Q = \frac{v^3 w f_R}{8g\phi_b},$$

7-25

and eliminating v between this expression and eqn. 7-22 shows how discharge Q depends on z:

$$Q = \beta z^{\frac{3}{2}},$$

7-26

where

$$\beta = \left(\frac{2g}{1 + \frac{f_R}{4\phi_b}} \right)^{\frac{3}{2}} \frac{w f_R}{8g\phi_b}.$$

7-27

Substituting this into eqn. 7-13 yields

$$\dot{h}_L = \frac{1}{A_{Li}} \left(\frac{h_{Li}}{h_L} \right)^{p_L - 1} \left[Q_{in} - \beta z^{\frac{3}{2}} \right],$$

7-28

The model has been reduced to a pair of ordinary differential equations (eqn. 7-23 and 7-28). The time evolution of z is found by differencing $\dot{h}_L$ and $\dot{h}_C$:

$$\dot{z} = \frac{1}{A_{Li}} \left(\frac{h_{Li}}{h_L} \right)^{p_L - 1} \left[Q_{in} - \beta z^{\frac{3}{2}} \right] + \alpha z^{\frac{3}{2}}.$$

7-29

This expression incorporates the two competing processes that control lake drainage in the model: lake-surface drawdown due to discharge through the channel, and downward incision of the channel into the glacier's surface due to the dissipation of heat in the flowing water. Armed with the two expressions above, the equation for the time evolution of h_c,

$$\dot{h}_c = -\alpha z^{\frac{3}{2}},$$

7-30

and the definitions of α and β,

$$\alpha = \left(\frac{2g}{1+\frac{f_R}{4\phi_b}}\right)^{\frac{3}{2}}\frac{f_R\rho_w}{8L\rho_i}, \qquad \beta = \left(\frac{2g}{1+\frac{f_R}{4\phi_b}}\right)^{\frac{3}{2}}\frac{wf_R}{8g\phi_b},$$

7-31

I continue the analysis by considering three simplified drainage scenarios.

7.3.1 Cylindrical lakes with no input

First I consider the drainage of a cylindrical lake ($p_L = 1$) which receives no input of water ($Q_{in} = 0$). Under these conditions eqn. 7-29 reduces to

$$\dot{z} = z^{\frac{3}{2}}\left(\alpha - \frac{\beta}{A_{Li}}\right).$$

7-32

Consider the situation shown in Fig. 7.3. A snow dam in the channel fails when the lake is a height z_{trig} above the bottom of the channel ($z = z_{trig}$) and lake drainage begins. This drainage initiation mechanism is supported by field observations of drainage in Greenland (I. Willis, personal communication).

Subsequent to this initiation eqn. 7-32 determines how z changes with time as the drainage progresses. In particular, it is the sign of the quantity in brackets in eqn. 7-32 that controls whether z increases or decreases with time. I define this quantity as

$$\Lambda = \alpha - \frac{\beta}{A_{Li}}.$$

7-33

If Λ is positive, $\dot{z}$ is also positive and z increases unstably with time. Physically, the channel is incised into the ice faster than the lake's surface is drawn down by the flood. A positive feedback is set up between z and $\dot{z}$, because discharge increases with z (eqn. 7-26). In this case discharge grows unboundedly with time, so I call this style of drainage unstable. Cylindrical lakes that drain unstably will always empty completely. In contrast, if $\Lambda < 0$, z and discharge always decreases with time. The physical explanation of this is that the lake surface is drawn down faster than the channel is incised downwards. Drainage that does not grow unboundedly with time I call stable. If Λ is sufficiently small, drainage will halt while there is still water in the lake.

The importance of the parameter Λ can been seen by integrating eqn. 7-32 to give the height difference z as a function of time:

$$z = \left(\frac{1}{\sqrt{z_{trig}}} - \Lambda\frac{t}{2}\right)^{-2}.$$

From eqn. 7-26, the discharge Q is therefore given by

$$Q = \beta \left(\frac{1}{\sqrt{z_{\text{trig}}}} - \Lambda \frac{t}{2} \right)^{-3}$$

When $\Lambda > 0$ the terms in brackets in both eqn. 7-34 and eqn. 7-35 decrease with time, hence z and Q increase with time. Conversely, when $\Lambda < 0$, z and Q decrease with time. Fig. 7.5 demonstrates this graphically. The figure shows the time evolution of discharge as defined by eqn. 7-35 for different values of the stability parameter Λ. Because Λ depends on the lake surface area, A_{Li} I have used this to vary Λ in Fig. 7.5. The larger the lake area the more unstable a lake is. The physical reason for this can be revealed by retracing how A_{Li} arrived in the definition of the stability parameter. In eqn. 7-13 it is in the denominator because the larger a lake's area, the slower its level changes due to a given discharge into the channel. Hence, for a given discharge (and associated channel-incision rate), the lake's surface drops more slowly if its area is large than if it is small.

The threshold between stability and instability ($\Lambda = 0$) corresponds to

$$\alpha = \frac{\beta}{A_{\text{Li}}},$$

or, after substituting in the definitions of α and β from eqn. 7-31,

$$\frac{A_{\text{Li}} \phi_{\text{b}}}{w} = \frac{L \rho_i}{g \rho_w}.$$

The quantities on the right of this expression are constants, so every lake has a critical surface area that is proportional to the channel's width and inversely proportional to its slope, ϕ_{b}, and independent of the hydraulic roughness of the ice. Or, to put it another way, drainage instability increases with lake area and channel slope, and decreases with channel width but does not depend on ice roughness.

Physically, increasing the channel slope ϕ_{b} has several effects, the net effect of which is more unstable drainage. Noting that the definitions of α and β (eqn. 7-31) show how varying model parameters affects the rate of channel incision and lake-surface drawdown respectively, one can retrace how ϕ_{b} arrived in the stability criterion. This exercise reveals that increasing ϕ_{b}, increases the water flow velocity, which increases the rates of channel incision and the rate of lake drawdown. However, in the case of the rate of lake drawdown this is slightly compensated for by a decrease in the depth of flow associated with the increase in slope and the hydraulics of open-channel flow as

described by the Darcy-Wiesbach equation. Hence, as channel slope increases, the incision rate increases more rapidly with increasing ϕ_b than does the rate of lake drawdown. Hence, the decrease in drainage stability with the channel slope.

A similar analysis explains the increase in drainage stability with the channel width w. Increasing this parameter does not affect the channel-incision rate, hence w does not appear in α. In contrast, it increases the rate of lake-surface drawdown by increasing the discharge through the channel for a given flow velocity (eqn. 7-14). Hence the increase in drainage stability with channel width.
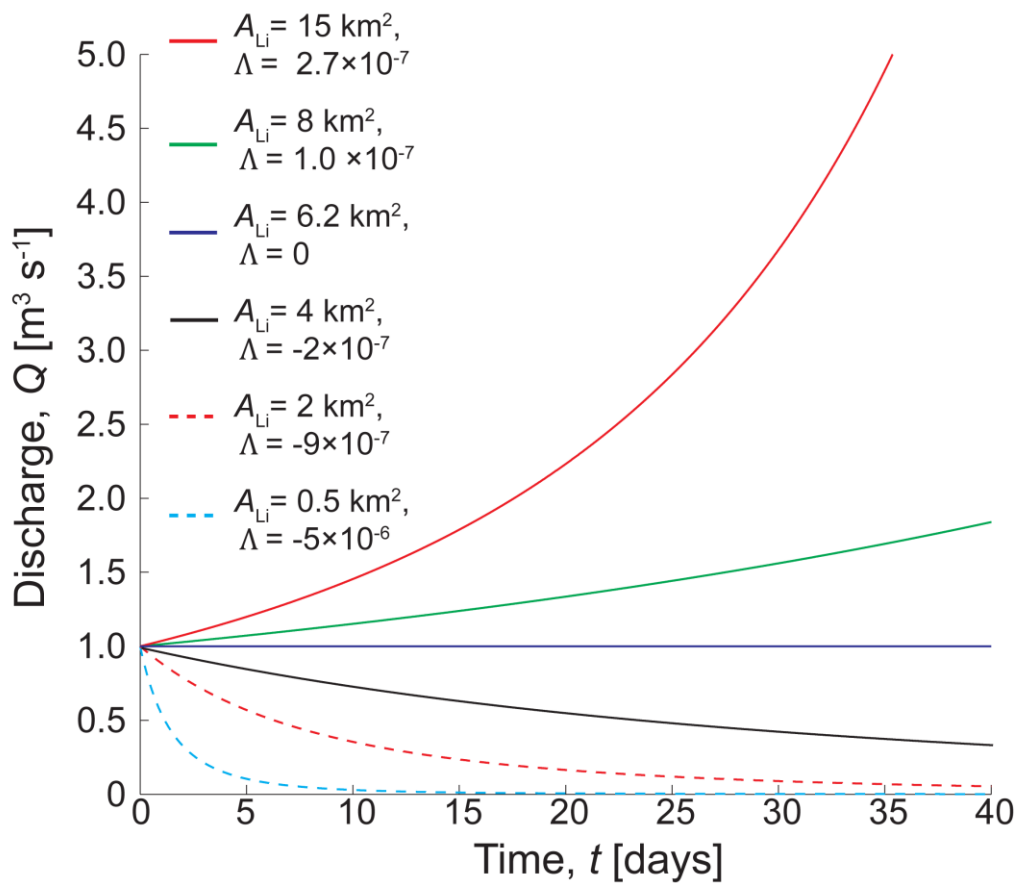

Fig. 7.5. Time evolution of discharge in the channel for six values of the stability parameter Λ, calculated using eqn. 7-35. The six stability parameters have been calculated using the initial lake areas, A_{Li}, shown and the following typical values for other parameters: f_R = 0.25, w_C = 2m ϕ_b = 0.01 and p_L = 1.

Perhaps surprisingly, the hydraulic roughness does not affect drainage stability. Decreasing the roughness increases the flow velocity, which affects both the channel incision rate and the rate of lake surface drawdown. As with increasing the channel slope, decreasing channel roughness decreases the depth of the flow in the channel, partially compensating for the increase in discharge from the faster-flowing water. However, the increased lake surface drawdown associated with this is exactly balanced by a decrease in channel incision rate due to a decrease in the shear stress applied by

the water on the channel and hence the transfer of heat from the water to the ice needed to incise the channel.

During stable drainage (when $\Lambda < 0$) the discharge asymptotically approaches zero as time passes. However, this does not always prevent the lake emptying completely. In some cases a lake can drain stably but still completely drain. To understand the conditions under which such stable but complete drainage can occur, I use the eqns. 7-30 and 7-32 to investigate how model solutions move through $h_C - z$ phase space.
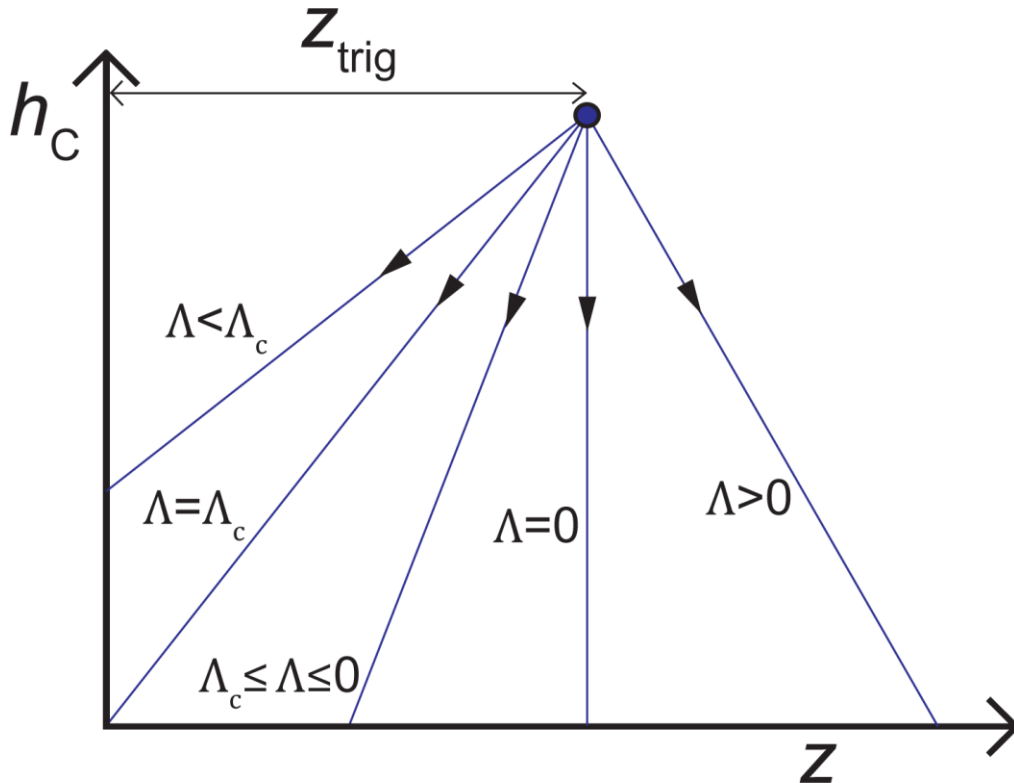

Fig. 7.6. Cartoon of trajectories in $h_C - z$ phase space corresponding to five different magnitudes for the stability parameter Λ relative to zero and to a critical magnitude Λ_C. The lake is cylindrical ($p_L = 1$).

Fig. 7.6 plots several possible trajectories in $h_C - z$ phase space for different values of $\Lambda > 0$. The gradient of the trajectories are found by dividing eqns. 7-30 by 7-32 to give

$$\frac{dh_C}{dz} = \frac{dh_C}{dt}\frac{dt}{dz} = -\frac{\alpha}{\Lambda}.$$

7-38

Again the significance of the stability parameter can be seen from the equation for the gradient and Fig. 7.6. When $\Lambda > 0$ trajectories have a negative gradient and, because h_C is always decreasing with time, the figure shows graphically that z always increases with time. When $\Lambda = 0$ the gradient is infinite; z does not change and the corresponding discharge time series is shown by the horizontal blue line in Fig. 7.5. When $\Lambda < 0$ the

gradient is positive and z decreases with time. The trajectory can intercept the vertical (h_C) axis, corresponding to drainage halting while there is still water in the lake, or intercept with the horizontal (z) axis, corresponding to stable but complete drainage.

The constant gradient of the trajectories and the initial position in $h_C - z$ phase space are both known (from Fig. 7.3 the initial height of the channel bottom is h_{Li} - z_{trig}) so I can calculate the final channel-bottom height h_{final} :

$$h_{final} = \left(h_{Li} - z_{trig}\right) + z_{trig}\frac{\alpha}{\Lambda}.$$

<div align="right">7-39</div>

The value of Λ that is just sufficient to empty the lake before discharge and z approach zero, Λ_C, is given by the above expression with h_{final} = 0:

$$\Lambda_C = -\frac{\alpha}{\left(\dfrac{h_{Li}}{z_{trig}} - 1\right)}.$$

<div align="right">7-40</div>

In summary, this analysis has shown that for a cylindrical lake with no water input (p_L = 1 and Q_{In} = 0) model drainage can evolve in one of three ways depending on the stability parameter Λ. When $\Lambda < -\alpha/(h_{Li} /z_{trig} - 1)$, lake drainage is stable and halts when there is still water in the lake. When $-\alpha/(h_{Li} /z_{trig} - 1) \leq \Lambda \leq 0$, drainage is still stable but results in complete drainage of the lake. And when $\Lambda > 0$, drainage is unstable with discharge and the height difference between the lake's surface and the channel bottom increasing unstably with time. The stability parameter Λ increases with the lake area and the channel slope, and decreases with channel width. It is independent of the hydraulic roughness of the channel.

7.3.2 Bowl-shaped or horn-shaped lakes with no water input

In general the surface areas of lakes surface area are not uniform. It often increases with depth. This is the scenario I now consider. It is manifested in the model by the lake shape parameter p_L having a value larger than 1. I still assume no input to the lake (Q_{in} = 0), so with $p_L > 1$ eqn. 7-29 becomes

$$\dot{z} = z^{\frac{3}{2}}\left(\alpha - \frac{\beta}{A_{Li}}\left(\frac{h_{Li}}{h_L}\right)^{p_L-1}\right).$$

<div align="right">7-41</div>

I define a modified stability parameter based on this equation:

$$\widetilde{\Lambda} = \alpha - \frac{\beta}{A_{Li}}\left(\frac{h_{Li}}{h_L}\right)^{p_L-1}.$$

7-42

This modified parameter is similar to Λ, but with the addition of the multiplicative term consisting of the ratio of the reference lake depth, h_{Li} and variable lake depth h_L, raised to the power of $(p_L - 1)$.

How does this new addition affect lake stability? Initially the lake depth is equal to its reference value h_{Li}, so the new stability parameter is identical to Λ; whether a lake is initially stable or unstable does not depend on its shape. However, as the lake drains, h_L decreases and the fraction in the brackets (h_{Li}/h_L) increases. Because $p_L - 1 > 0$, this causes the second term on the right of eqn. 7-42 (the term corresponding to the rate of lake drawdown) to increase and $\widetilde{\Lambda}$ to decrease. Inevitably, at some moment before the lake empties ($h_L = 0$), $\widetilde{\Lambda}$ will drop below zero and drainage will be stabilised. This is inevitable because as h_L approaches zero, $(h_{Li}/h_L)^{p_L-1}$ approaches infinity. This stabilisation can halt drainage altogether or, if it occurs after the channel has already been incised to the height of the lake bed ($h_C \leq 0$), merely slow the final stages of drainage. These two possibilities are illustrated in Fig. 7.7, which sketches how the model's trajectories in channel-bottom-height–lake-channel-height-difference ($h_C - z$) phase space change with the lake shape parameter p_L. Trajectories are evaluated by forward Euler time stepping of eqns. 7-30 and 7-41. Progressively lighter-blue coloured curves correspond to progressively larger values of p_L. When $p_L > 1$ trajectories are deflected from the straight trajectory corresponding to $p_L = 1$. This deflection increases as the lake depth decreases and does so earlier when p_L is higher. If p_L is sufficiently high, drainage is halted before the channel bottom is incised to the height of the lake bed ($h_C = 0$).

The physical interpretation of this is, as the lake depth decreases, the lake basin at the level of the lake's water surface narrows. Consequently, the rate of lake surface drawdown for a given discharge is increased without any corresponding change in the rate of channel incision. This acts to stabilise drainage by allowing the lake level to 'catch-up' with the bottom of the channel. The effect is more pronounced and the channel is caught-up with by lake level earlier, in drainage from more 'horn-shaped' lakes with higher p_L-values, as such lakes narrow more rapidly with depth.
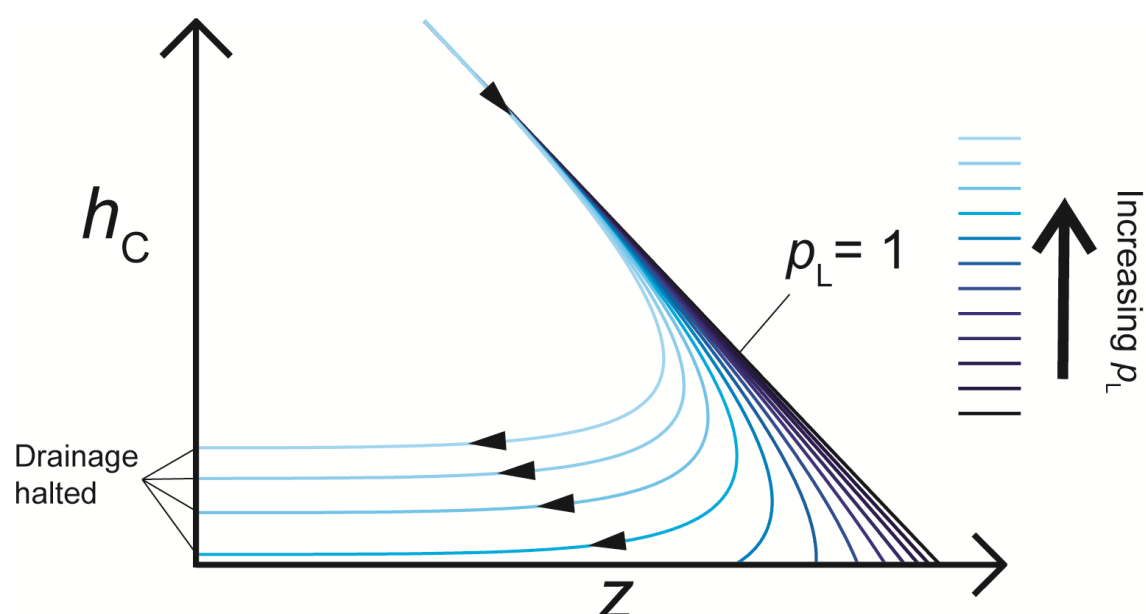
Fig. 7.7. Cartoon of trajectories in $h_C - z$ phase space corresponding to different lake-shape parameters p_L. In all cases the lake stability parameter $\widetilde{\Lambda}$ is initially large than 1. The black curve corresponds to $p_L = 1$ and curves coloured progressively lighter blue correspond to progressively higher values of p_L (intervals between p_L-values are all equal). In all cases when $p_L > 1$, drainage is slowed relative to the cylindrical lake (p_L=1). The curves corresponding to the four highest p_L-values intercept the h_c axis before h_c reaches zero i.e. drainage is halted before the lake empties.

7.3.3 Cylindrical lakes with a water input

I now return to cylindrical lakes ($p_L = 1$) and consider the effect of supplying the lake with water from its surroundings ($Q_{in} > 0$). In this scenario eqn. 7-29 becomes

$$\dot{z} = \frac{Q_{in}}{A_{Li}} + z^{\frac{3}{2}}\Lambda.$$

7-43

This equation indicates that, contrary to when there is no input to the lake, drainage cannot be halted before the lake empties. If $\Lambda > 0$, drainage is unstable and discharge increases unboundedly with time. If $\Lambda < 0$, eqn. 7-43 dictates that z will relax towards a positive value: $(-Q_{in}/A_{Li}\Lambda)^{2/3}$. From eqn. 7-30 a positive z corresponds to a negative $\dot{h}_C$, hence the channel continues to be incised downwards and the lake drains. This drainage remains stable, because $\Lambda < 0$, but results in the complete emptying of the lake.

I gain more insight into how the lake drains by comparing the discharge corresponding to a depth of flow $z = (-Q_{in}/A_{Li}\Lambda)^{2/3}$, with the input to the lake Q_{in}. From eqn. 7-26

$$Q = \beta z^{\frac{3}{2}},$$

<div align="right">**7-44**</div>

so the discharge after z has reached $(-Q_{in}/A_{Li}\Lambda)^{2/3}$ is

$$Q = -\beta \frac{Q_{in}}{A_{Li}\Lambda}.$$

<div align="right">**7-45**</div>

From the definition of Λ (eqn. 7-33), this becomes

$$Q = \frac{Q_{in}}{1 - \dfrac{\alpha A_{Li}}{\beta}}.$$

<div align="right">**7-46**</div>

From $\Lambda < 0$, it follows that $\alpha A_{Li}/\beta < 1$, and hence $0 < (1 - \alpha A_{Li}/\beta) < 1$. Therefore, from eqn. 7-46, the discharge through the channel Q is larger than the input Q_{in} and the lake drains as expected. Furthermore, the rate of lake surface drawdown, $\dot{h}_L$, equals $(Q_{in} - Q)/A_{Li}$, or, using eqn. 7-46,

$$\dot{h}_L = \frac{Q_{in}}{A_{Li}} \left(1 - \frac{1}{1 - \dfrac{\alpha A_{Li}}{\beta}} \right).$$

<div align="right">**7-47**</div>

The higher the input to the lake, the faster it drains. Physically this is because a higher input is capable of maintaining a higher depth of flow in the channel and this incises the channel more rapidly. This finding only holds for the case when $\Lambda < 0$ and the discharge is close to having relaxed to $((-Q_{in}/A_{Li}\Lambda)^{2/3})$. Later (in section 7.4.2) I will present results from numerical simulations that suggest the same mechanism operates more generally.

As Λ approaches zero, $(-Q_{in}/A_{Li}\Lambda)^{2/3}$ approaches infinity. Equation 7-43 still dictates that z relaxes towards $(-Q_{in}/A_{Li}\Lambda)^{2/3}$, so drainage becomes unstable when Λ reaches 0.

7.3.4 Summary

Lakes that do not receive a water input can drain stably or unstably. When stable, discharge decreases over time, as the lake level drops faster than the channel is incised, and can (but does not always) halt entirely before the lake is empty. When unstable, drainage grows unstably with time through a feedback between discharge and channel incision. Whether drainage is stable or unstable is determined by whether the 'stability parameter' is above or below zero. This parameter is a function of lake area, channel width and channel slope, but not the hydraulic roughness of the channel. For bowl- or horn-shaped lakes the stability parameter decreases as drainage progresses. This has the potential to halt initially unstable drainage before the lake empties. The situation is similar when the lake is supplied with an input of water from its surroundings except

that, even if drainage is stable, the lake will always drain completely. This is because the input maintains the height of the lake's surface above that of the bottom of the channel, so the channel continues to be incised downwards until the lake is empty.

7.4   Numerical simulations

To quantitatively demonstrate some of the mechanisms revealed by last section's analysis, here I present the results of numerical simulations of lake drainage using the full model, which takes account of whether flow is sub- or supercritical. In section 7.4.1 I present results from four simulations. Two of these simulate drainage from a cylindrical lake with no input and demonstrate the stable and unstable drainage anticipated by the analysis in section 7.3.1. The results of the remaining two simulations show how initially unstable drainage can be halted before the lake empties when the lake is not cylindrical and how a lake empties despite drainage being stable when it is supplied with an input of water.

In section 7.4.2 I present the results of a numerical sensitivity analysis. I investigate the sensitivity of simulated drainage to initial lake area, channel width, channel slope, the size of the snow dam when it fails and initiates drainage, lake shape, and lake input. I show that these results agree with the analytical results from the previous section.

At each time step the lake depth h_L and the height of the bottom of the channel h_C are evolved forward in time using the Forward Euler method with eqns. 7-13 and 7-19. Whether the flow is subcritical or controlled by a transition to supercritical flow, a property I hereafter refer to as the flow's criticality, is determined using the method described in section 7.2 and the depth of flow D and the discharge are determined using the appropriate method: eqn. 7-17 for critical flow and simultaneous solution of the Bernoulli and force-balance equations (eqns. 7-15 and 7-19) using Newton-Raphson for subcritical flow.

Simulations start with a full lake ($h_L = h_{Li}$) at $t = 0$ and terminate after either 1 model year has elapsed, the lake has emptied, $h_L \leq 0$ or discharge has become very low, $Q \leq Q_{min} = 2 \times 10^{-3}$ m^3 s^{-1}. Drainage is initiated by the mechanical failure of a dam of water-saturated snow in the channel. This is simulated by starting the simulation with the level of the bottom the channel a distance z_{trig} below the level of the lake's surface. Fig. 7.3a illustrates these initial conditions.

I consider a typical system and estimate the reference lake depth, h_{Li}, and the Darcy-Weisbach roughness coefficient, f_R, from published data. As shown in Fig. 7.8, fitting of eqn. 7-1 to hypsometry data from a lake in Greenland (Georgiou et al., 2009) yields $h_{Li} \approx 10$ m and $p_L \approx 1.5$. I use this value of h_{Li} throughout. Mernild et al. (2006) calculated Manning roughness coefficients, n', between 0.036 and 0.058 m$^{-1/3}$ s in

supraglacial streams. Their average value was $n' = 0.050$ m$^{-1/3}$ s. A Darcy-Weisbach roughness coefficient, f_R can be calculated from this using $f_R = 8gn'^2/R_H^{1/3}$ (see Clarke, 2003; his equation 24), where R_H is the hydraulic radius defined by eqn. 2-5. Given the range of Mernild et al.'s (2006) values for n', I choose $f_R = 0.25$ for my simulations.
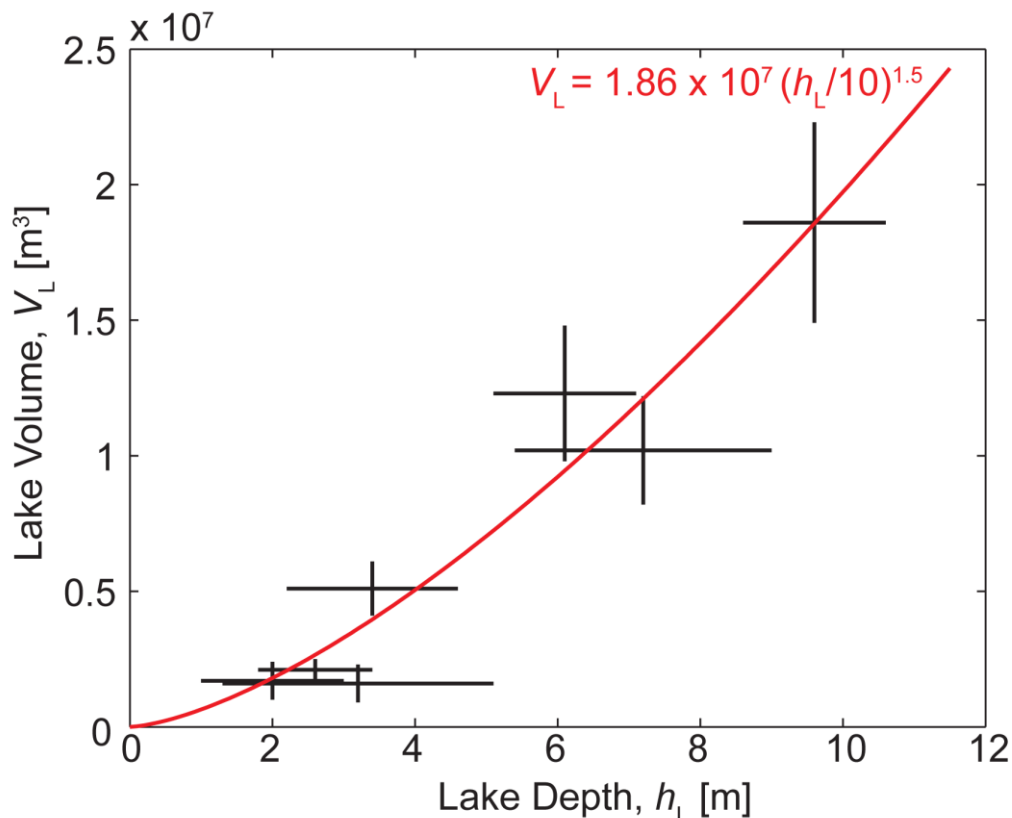

Fig. 7.8. Lake shape parameterisation. Crosses plot lake volume-depth data from Georgiou et al. (2009) with cross dimensions representing uncertainty (their table 2), and red line is the least-squares fit between eqn. 7-1 and this data.

7.4.1 Simulating stable and unstable drainage

Here I present results from four model simulations of lake drainage. Each demonstrates one of the ways in which lakes can drain, investigated in section 7.3.

Fig. 7.9 shows lake-level and channel-height time series and discharge hydrographs from two simulations. Both simulate a cylindrical lakes ($p_L = 1$) that receives no water input ($Q_{in} = 0$) and drains through 2-meter wide channels ($w_C = 2$). Drainage starts due to the failure of a 1 m high snow dam ($z_{trig} = 1$ m). The left-hand panels (Figs. 7.9a & 7.9c) display results from a simulation that used an initial lake area of 3 km^2 and a channel slope of 0.01, and the right-hand panels (Figs. 7.9b & 7.9d) plots results from a simulation that used a larger initial lake area of 6 km^2 and a steeper channel slope of 0.02.

Simulated drainage from the two lakes is markedly different. Drainage from the smaller lake with the less steep channel is initially 2.8 m^3 s^{-1} and decreases with time throughout the simulation (Fig. 7.9a). The lake level drops faster than the channel is incised (Fig. 7.9c) and after 200 days the simulation stops because the discharge goes below 2 × 10^{-3} m^3 s^{-1}. The lake level was reduced by less than a meter during drainage. In contrast, drainage from the larger of the two lakes with a steeper channel, is initially 3.3 m^3 s^{-1} and increases throughout the simulation (Fig. 7.9b) because the channel is incised
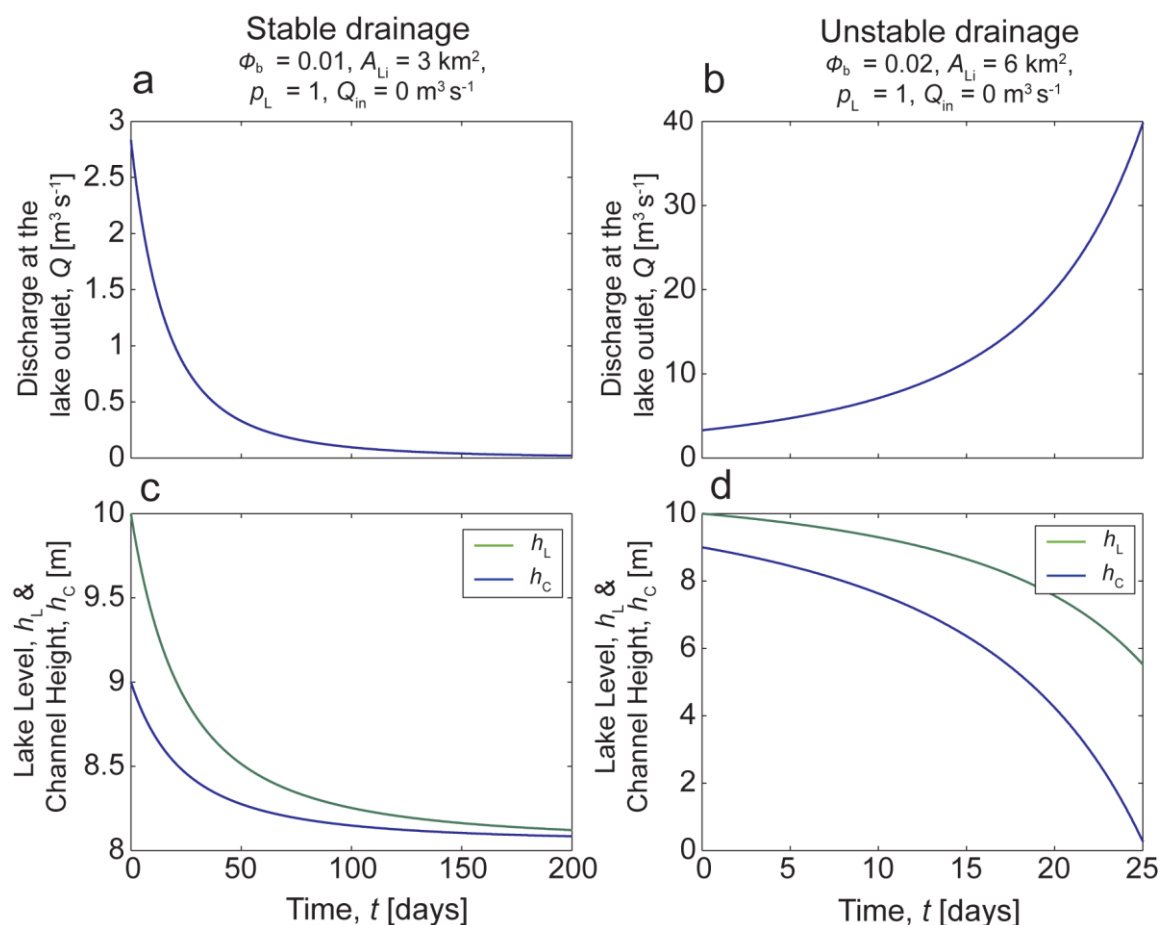

Fig. 7.9. Numerical model simulations demonstrating stable and unstable drainage. Top panels plot modelled hydrographs and bottom panels plot modelled lake level and channel height time series. From two lakes with different initial areas and channel slopes. The left-hand plots show results for a relatively small lake (A_{Li} = 3 km) with a relatively gently sloping channel (ϕ_b = 0.01). The right-hand plots show results for a larger lake (A_{Li} = 6 km) with a steeper channel (ϕ_b = 0.02). The small lake drains stably and the large lake drains unstably. In both cases lake input, Q_{in} = 0 m^3 s^{-1}, channel width, w_C = 2 m, initial height of the lake above the channel bottom, z_{trig} = 1 m and the hydraulic roughness coefficient used is f_R = 0.25.

faster than the lake level drops (Fig. 7.9d). After 25 days the channel bottom has reached the level of the lake bed and the complete emptying of the lake is inevitable. In the terminology introduced in the previous section, the smaller lake drains stably and the larger lake drains unstably.

This is consistent with my earlier analysis of stability. With an area of 3 km^2, a channel slope of 0.01 and a channel width of 2 m, the smaller lake has a stability parameter of Λ = -4.8 × 10^{-7} m$^{-1/2}$ s^{-1} (calculated from eqn. 7-33). The larger lake has Λ = 5.2 × 10^{-7} m$^{-1/2}$ s^{-1}. The criterion for stability is $\Lambda < 0$. Hence the smaller lake drains stably while the larger lake drains unstably. The criterion for incomplete drainage is $\Lambda < \Lambda_C$,
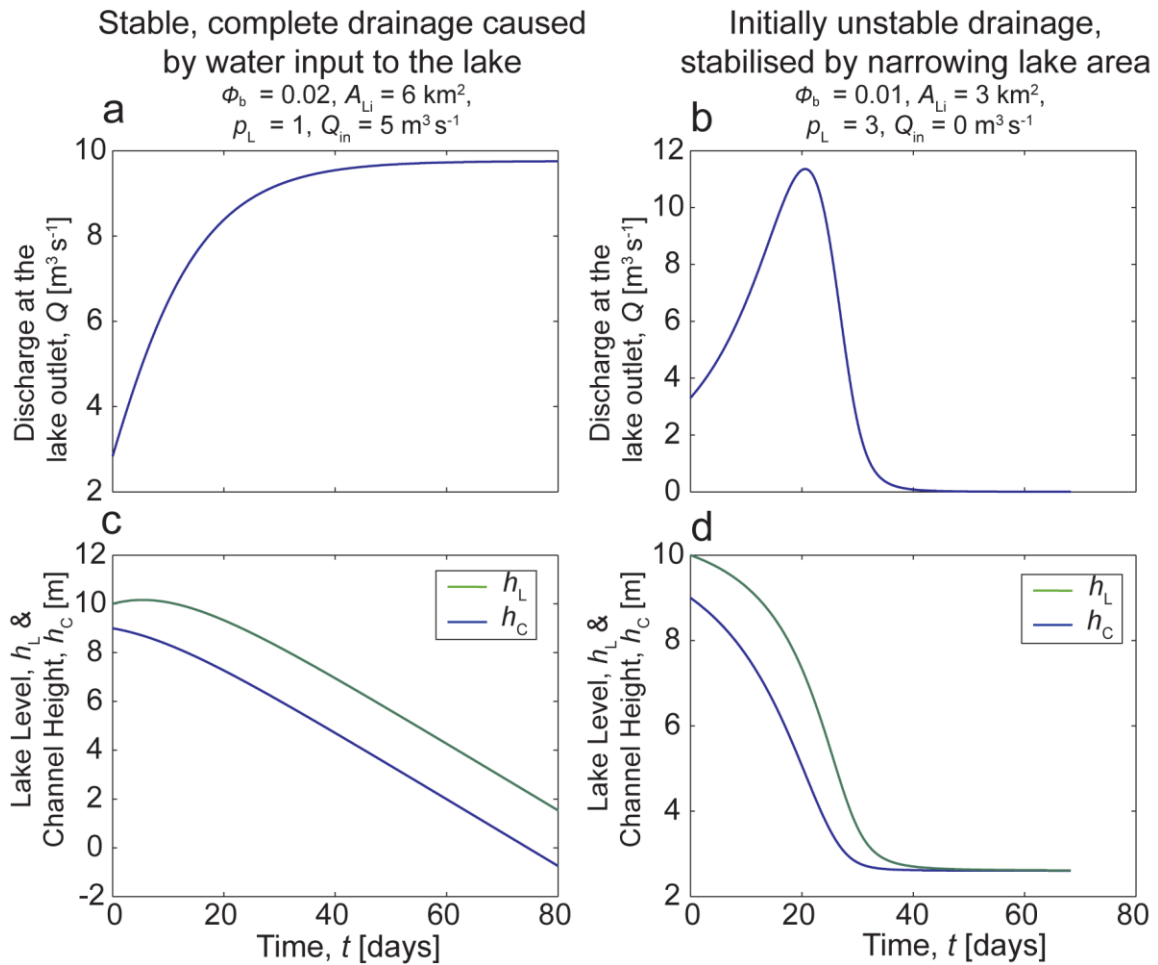

Fig. 7.10. Numerical model simualtions showing the effect of water input to the lake (Q_{in}>0) and a lake whose surface area decreses with depth (p_L>1), has on drainage. Layout is identical to Fig. 7.9. The left-hand plots show results for a small lake (A_{Li} = 3 km) with a gently sloping channel (ϕ_b = 0.01) that receives a water input of 5 m^3 s^{-1} from its surroundings. The right-hand plots show results for a larger lake (A_{Li} = 6 km) with a steeper channel (ϕ_b= 0.02) whose surface area decreases with depth, p_L = 3. In both cases channel width w_C = 2 m, initial height of the lake above the channel bottom z_{trig} = 1 m and the hydraulic roughness coefficient in the channel is f_R = 0.25.

where Λ_C (as calculated by eqn. 7-40) is -5.1×10^{-8} m$^{-1/2}$ s^{-1} for the smaller lake. This is indeed larger than Λ, hence the incomplete drainage of the smaller lake seen in Figs. 7.9a & 7.9c.

Fig. 7.10 shows lake-level and channel-height time series and discharge hydrographs from two more simulations using nearly the same parameters as the simulations discussed above. They use the same two lakes of contrasting sizes and with contrasting channel slopes. In the simulation of the smaller of the two lakes, the water input to the lake is increased to 5 m^3 s^{-1} (previously it was 0 m^3 s^{-1}). Figs. 7.10a & 7.10c plot the results. The plots show that the water input results in the discharge in the channel Q approaching a finite value – so drainage is stable – that is higher than the 5 m^3 s^{-1}. As a result the lake stably drains completely. This behaviour was predicted by the analysis in 7.3.3. From eqn. 7-45 Q should approach 9.7 m^3 s^{-1}. This agrees with the numerical results in Fig. 7.10a.

Results from a simulation using the larger of the two lakes are shown in Figs. 7.10b & 7.10d. In this simulation, by using a lake shape parameter of $p_L = 3$, the lake has been modified so that its surface area narrows as it drains. Discharge is initially 3.3 m^3 s^{-1} – the same as when $p_L = 1$ in the previous simulation using a lake of the same initial surface area. Initially discharge increases. However, after 20 days, discharge peaks and begins to fall. This drainage stabilisation occurs at the moment the modified stability parameter, $\widetilde{\Lambda}$, drops below zero (see eqn. 7-42). As described above, the physical explanation for the stabilisation is that the decreasing surface area of the lake increases the rate at which the lake's surface is drawn down, allowing the lake to catch up with the downward incision of the channel. In this simulation, this occurs at ~40 days.

7.4.2 Numerical sensitivity analysis

To complete the numerical investigation of the model, I now present the results of a numerical sensitivity analysis. The analysis is in three sections. In each I conduct multiple 1-year-long model simulations while varying model parameters systematically between simulations. After each simulation I record the final depth of the lake and the time taken to reach that depth.

In the first section, initial lake area, the channel slope and the height at which the snow dam fails are varied systematically while keeping other parameters constant. In the second, the same exercise is conducted with the initial lake area, the channel width and the lake shape parameter. In the third section, the initial lake area and the input to the lake are varied.

I present the results as filled contour maps representing the various 'parameter-spaces' that I explore. Each discrete point in a map corresponds to a simulation conducted using

a unique set of parameters. Each point is assigned a numerical value that derives from the results of its corresponding simulation. Filled contours are created using these grids of numbers using the 'contourf' command in the software package MATLAB.

Initial lake area, channel slope and dam failure height

Between 2005 and 2009, Selmes et al. (2011) observed maximum and mean Greenland lake areas of 17 and 0.8 km^2, so in simulations I vary the initial lake area A_{Li} between 0.05 and 30 km^2. Similarly, the channel slope ϕ_b is varied between 0.005 and 0.1 and the dam failure height z_{trig} between 0.1 and 3 m to bracket realistic ranges of these parameters. As before, the input to the lake is zero ($Q_{in} = 0$ m^3 s^{-1}) and the width of the channel is 2 m ($w_C = 2$ m).

Figs. 7.11a & 7.11b display the results from exploration of lake-area–channel-slope (A_{Li}–ϕ_b) parameter space. Filled contour maps display how the final lake height h_{final} and the time taken to reach this height T_0 vary with lake area A_{Li} and channel slope ϕ_b. In both plots, two regions are evident: one where $h_{final} > 0$ m and T_0 is not defined, corresponding to incomplete drainage and another where $h_{final} = 0$ m and $13 \leq T_0 \leq 365$ days, corresponding to complete drainage.

Also plotted in Figs. 7.11a & 7.11b is the critical channel slope required for drainage to be unstable as a function of lake area (the solid green curve), evaluated using eqn. 7-37. Below this *critical slope curve*, drainage is stable and above it drainage is unstable. This curve and the boundary between incomplete and complete drainage (visible as the boundary of where T_0 is defined in Fig. 7.11) are nearly aligned – unstable drainage often leads to complete emptying of the lake and vice versa. However, they do not align exactly. This is shown more clearly in Fig. 7.12. In one region of parameter space, adjacent to the critical-slope curve and coloured red in Fig. 7.12, drainage is stable but results in the complete emptying of the lake. This drainage possibility was discussed in section 7.3.1. It occurs when the stability parameter Λ is negative but close to zero (more precisely when $-\alpha/(h_{Li}/z_{trig} - 1) \leq \Lambda \leq 0$). Because drainage is stable, discharge decreases with time, but it does so too slowly to halt drainage before the lake empties. In another region of parameter space, coloured yellow in Fig. 7.12, drainage is unstable but does not result in the emptying of the lake. This is an artefact of the finite length of simulations (1 year). In these simulations discharge from the lake is increasing with time because $\Lambda > 0$, but only very slowly because Λ is small. Hence, after one model year, water still remains in the lake.

In Fig. 7.11a and Fig. 7.12 the boundary of the region in parameter space corresponding to simulations that involve critical flow is visible in Fig. 7.11a as a kink in the otherwise
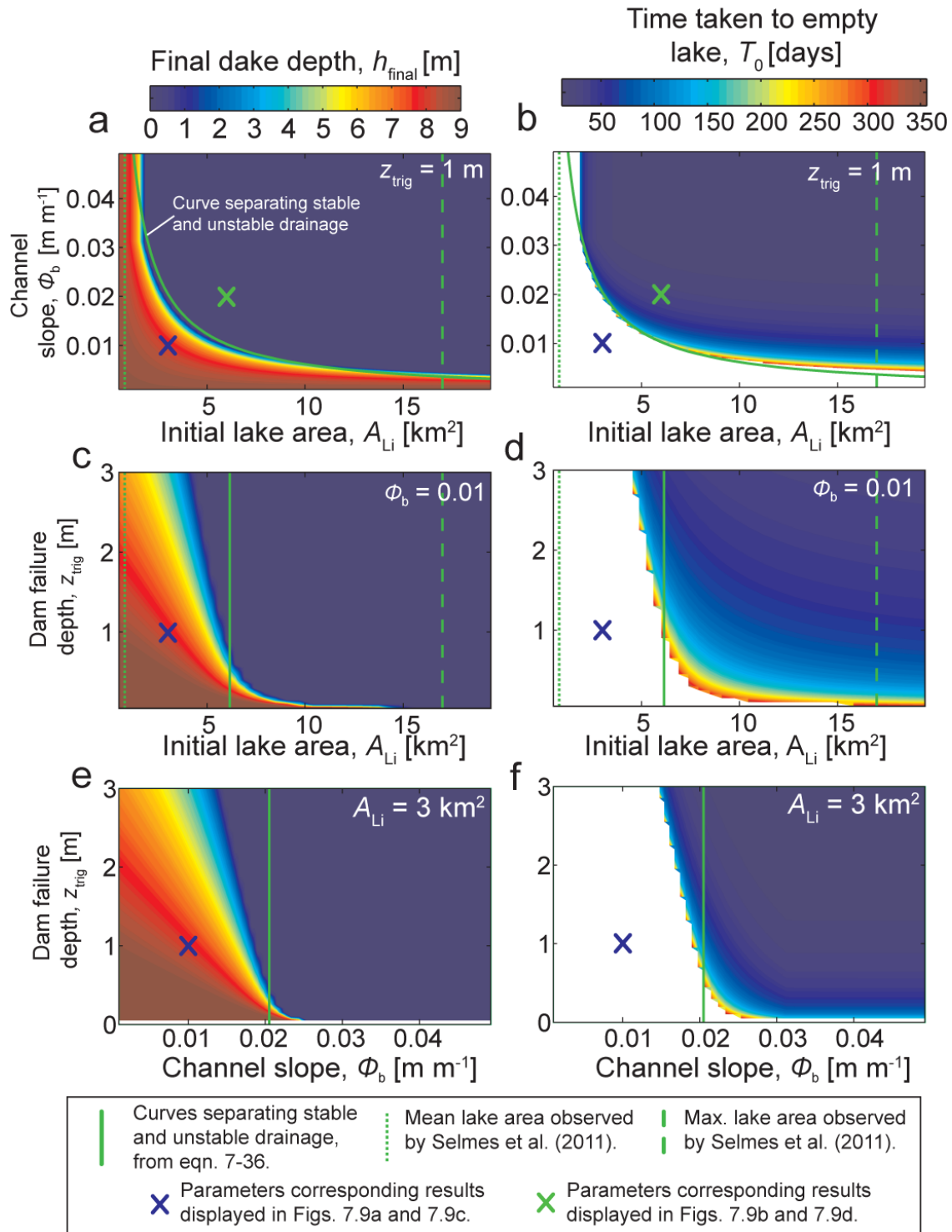
Fig. 7.11. Exploration of three 2-parameter spaces: (a & b) channel-slope – lake-area, ϕ_b–A_{Li}, space, (c & d) snow-dam-failure-height–lake-area, z_{trig}–A_{Li}, space and (e & f) snow-dam-failure-height–channel-slope, z_{trig}–ϕ_b, space. Filled contour maps show how final lake depth (left column), the time taken to empty the lake (right column) vary with these parameters. In all simulatiosn $Q_{in} = 0$ m^3 s^{-1}, $w_C = 2$ m and $p_L = 1$. Solid green lines separate regions corresponding to stable and unstable drainage (plotted using eqn. 7-36). Green dotted and dashed lines in (a–d) indicate the mean and maximum areas of lakes in Greenland between 2005 and 2009 reported by Selmes et al. (2011). Crosses indicate locations in each parameter space of simulations whose time series are shown in Fig. 7.9.

smooth contours at $\phi_b \approx 0.032$. Above this value, where flow is critical, drainage is not a function of the channel slope ϕ_b. This is expected from the model equations, neither eqn. 7-17 nor eqn. 7-18, which describe the hydrology in the channel when the flow is critical, involve ϕ_b.

The second and third rows of maps in Fig. 7.11 display results from explorations of snow-dam-failure-height–lake-area (z_{trig}–A_{Li}) parameter space and snow-dam-failure-height–channel-slope (z_{trig}–ϕ_b) parameter space. In these sets of simulations I used a channel slope of $\phi_b = 0.01$ and initial lake areas of $A_{Li} = 10$ km^2 respectively. From the analytical investigation of the model I expect drainage stability to be unaffected by snow-dam height, z_{trig}, in a cylindrical lake. However, from Fig. 7.6 and eqn. 7-39, I would expect z_{trig} to affect the depth the lake reaches before drainage stops during stable drainage and how long it takes unstable drainage to empty the lake. In other words, I expect z_{trig} to affect the size of the red and yellow regions in Fig. 7.12. Figs. 7.11c and 7.11e show this. The green solid curve separates parameter values that result in stable drainage (to the left of the curve) from those that lead to unstable drainage (to the right of the curve). Increasing z_{trig}, increases the range of lake areas (Fig. 7.11c) and channel slopes (Fig. 7.11c) that result in stable and complete drainage. Similarly, when z_{trig} is small (<0.6 m) decreasing it further increases the range of lake areas and channel slopes that result in unstable drainage that does not have sufficient time to empty the lake before the end of the 1-year-long simulation.
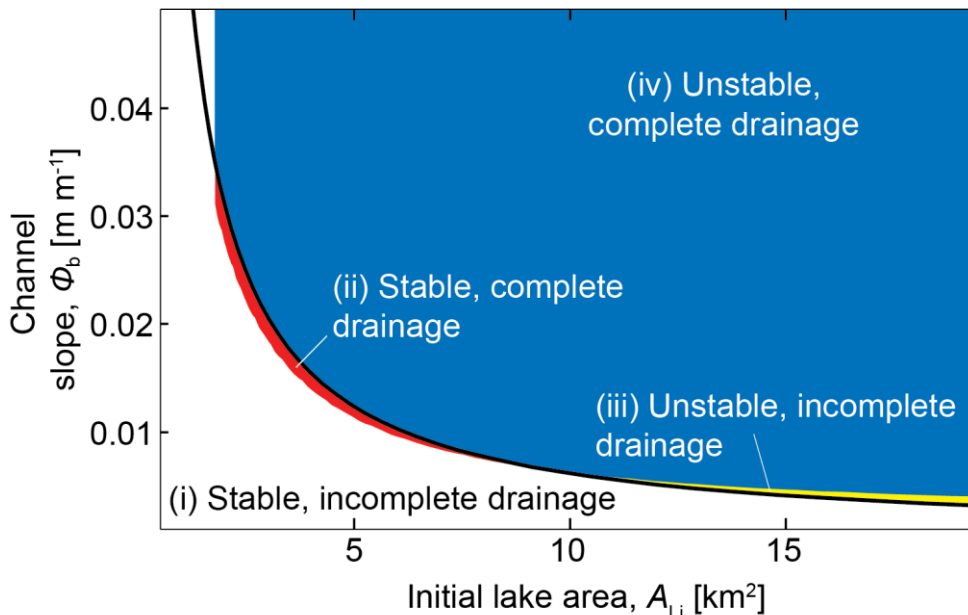
**Fig. 7.12. Schematic of the results displayed in Fig. 7.11 showing four possible ways in which a lake can drain: (i) stably, leaving water in the lake (in white); (ii) stably, but emptying the lake completely (in red); (iii) unstably, but leaving water in the lake (in yellow); and (iv) unstably, emptying the lake completely. The black curve separates stable and unstable drianage (eqn. 7-36).**
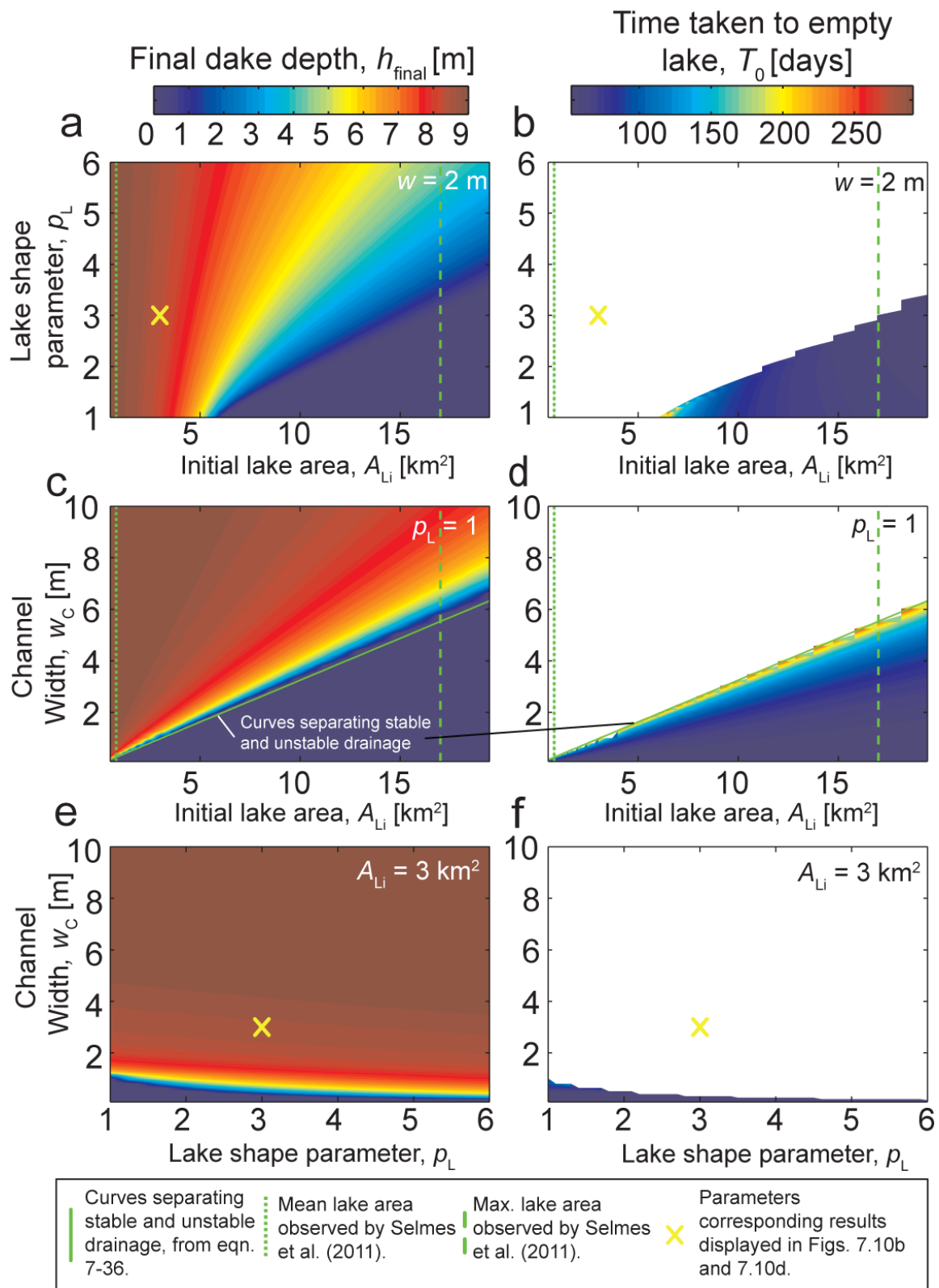
Fig. 7.13. Exploration of three 2-parameter spaces: (a & b) lake-shape-parameter–lake-area, p_L–A_{Li}, space, (c & d) channel-width–lake-area, w_C–A_{Li}, space and (e & f) channel-width–lake-shape-parameter, w_C–p_L, space. Layout is identical to Fig. 7.11. In all simulations $\phi_b = 0.05$ and $Q_{in} = 0$ m³ s⁻¹ and $z_{trig} = 1$ m. Yellow crosses indicate the location in the corresponding parameter space of the simulation whose results are displayed in Figs. 7.10b and 7.10d.

Channel width and lake shape

The layout of Fig. 7.13 is identical to Fig. 7.11, but the three 2-parameter spaces explored are: (i) lake-shape-parameter–initial-lake-area (p_L–A_{Li}); (ii) channel-width– initial-lake area (w_C–A_{Li}); and channel-width–lake-shape-parameter (w_C–p_L). During all simulations, the channel slope ϕ_b is 0.01 and the lake receives no input (Q_{in} = 0 m^3 s^{-1}). The chosen ranges of the channel width w_C and the lake shape parameter p_L ($0.1 \leq w \leq$ 10 m; $1 \leq p_L \leq 6$) bracket the poorly constrained distributions of real w_C and p_L values.

Considering the top two maps in Fig. 7.13 first; the results show that high values of the lake shape parameter p_L, corresponding to narrow 'horn-shaped' lakes, result in a higher final lake depth. This is due to the mechanisms first discussed in section 7.3.2, depicted in Fig. 7.7, and simulated in section 7.4.1. When p_L > 1 the area of the lake-water's surface decreases as drainage progresses. This stabilises drainage by increasing the rate at which the lake level drops and can halt drainage by allowing the lake's surface to catch-up with the channel as it is incised downwards through the ice.

Similarly, the two plots on the middle row in Fig. 7.13, that display the channel-width– initial-lake-area (w_C–A_{Li}) parameter space, show how the final lake depth (when drainage is incomplete) and the time taken to empty the lake (when drainage is complete) both increase with the channel width w_C. This is a manifestation of the stabilising effect of increasing w_C discussed in section 7.3.2. The wider the channel the higher the discharge through the channel for a given flow velocity. As the rate at which the lake level decreases depends on the discharge, while the channel-incision rate depends on the flow velocity, increasing w_C increases drainage stability. To confirm this association between these numerical results and the findings of section 7.3.2, the analytically-derived critical channel-width needed for stable drainage is plotted as a function of lake area as the solid green curve in Figs. 7.13a & 7.13d (this was calculated using eqn. 7-36). The curve is closely aligned with the boundary in the numerical results between incomplete and complete drainage. This is most clearly seen in Fig. 7.13d.

The lower two plots in Fig. 7.13 display the channel-width–lake-shape-parameter (w_C–p_L) parameter space. For the chosen ranges of the model parameters the channel width has a stronger effect on drainage than the lake shape. Fig. 7.13e shows the stabilising effect of increasing the channel width. The stabilising effect of increasing p_L is also just discernible but is more clearly shown in Fig. 7.13a.

Lake input

Finally, simulations are conducted to explore the lake-input–lake-area (Q_{in}–A_{Li}) parameter space and the lake-input–channel-slope (Q_{in}–ϕ_b) parameter space. As discussed in section 7.3.2, when $Q_{in} > 0$ m^3 s^{-1}, discharge can never go to zero because the input maintains the lake level above the height of the channel. All drainage will result in the emptying of the lake, no matter how stable it is (i.e. how small the stability parameter is). Consequently, the details of the Q_{in}–A_{Li} and Q_{in}–ϕ parameter-space contour maps in Fig. 7.14 depend on the length of simulations; a non-zero final lake height reflects how far drainage has progressed during the 1-year-long simulation, rather than the lake level reached before discharge has gone to zero. Nonetheless, Fig. 7.14 corroborates my earlier finding (see section 7.3.3) that increasing the input to the lake speeds up drainage, decreasing the final lake height (Figs. 7.14a and 7.14c) and,
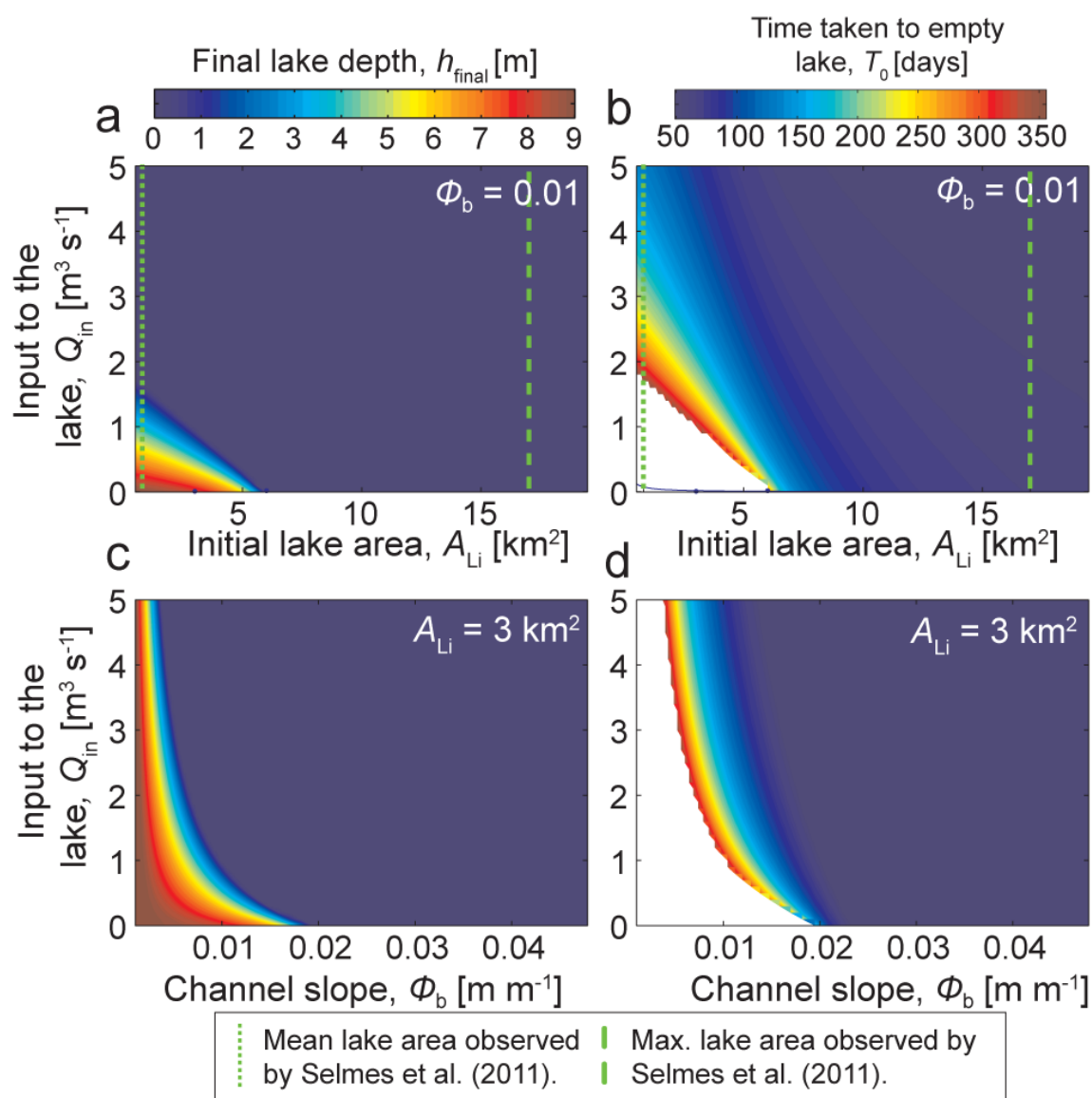

Fig. 7.14. Exploration of Q_{in}–A_{Li} and Q_{in}–ϕ_b parameter spaces. Layout is identical to Fig. 7.11. In all simulations $p_L = 1$, $w_C = 2$ m and $z_{trig} = 1$ m.

when drainage is complete, the time it takes the lake to empty. For the case when the stability parameter $\Lambda < 0$, I proved analytically that increasing Q_{in} speeds-up drainage by maintaining a higher depth of flow in the channel. This causes the channel to be incised more rapidly and the lake to empty more quickly. These numerical results suggest the same mechanism operates when $\Lambda > 0$.

7.5   Discussion

I have developed a model of surface drainage of supraglacial lakes and considered the case where drainage starts when a snow dam in a pre-existing channel fails when the lake's surface is some height above the bottom of the channel. In the model, how drainage develops over time depends on a competition between the drawdown of the lake's surface and the downward incision of the bottom of the channel into the ice. Because these two processes depend on various model parameters, drainage can develop stably or unstably. During stable drainage, discharge remains bounded and during unstable drainage, discharge increases unboundedly with time. These two styles of drainage often (but not always) correspond respectively to complete and incomplete emptying of a lake.

When a lake receives no input of water from its surroundings – a situation that is arguably unlikely in reality – stable drainage can lead to the discharge out of the lake going to zero and drainage stopping before the lake has emptied. I have called this stable, incomplete drainage. Alternatively, stable drainage can empty the lake completely if the discharge does not decrease with time sufficiently rapidly after it is initiated by snow-dam failure. This I call stable, complete drainage. Mathematically, unstable drainage will always result in the complete emptying of a lake as discharge increases unboundedly with time. However, numerical simulations have shown that, in some cases, unstable drainage increases very slowly and after a one-year-long simulation model lakes still have not emptied completely. As this drainage time is much longer than a single melt season, in reality, drainage from such lakes would be stable for all practical purposes.

The stability, or otherwise, of drainage depends on some model parameters and not others. Instability increases with the lake area and the channel slope, and decreases with the channel width. Lake hypsometry also affects drainage stability, with lakes that get narrower with depth promoting stability. Neither the hydraulic roughness of the channel, the height of snow-dam in the channel nor the initial depth of the lake affects drainage stability.

Drainage of a lake that does receive an input of water from its surroundings can also be characterised as stable or unstable, but regardless of stability, drainage will always empty it completely. When draining stably discharge from a lake increases as the rate of water supply to the lake is increased.

One aspect of drainage that I have only touched upon is what controls how long it takes for a lake to drain. The analysis suggests that the higher the input the faster a lake drains and it also revealed a physical explanation for this (which strictly only applies when drainage is stable). Furthermore, numerical simulations in section 7.4.2 suggest that lakes with larger initial lake areas drain faster. Although it is clear from the analysis in section 7.3.1 that increasing a lake's area increases the rate of change of discharge out of the lake, I have not been able to show analytically under what circumstances this increase can overcome the increase in total lake volume associated with an increase in lake area. A fuller physical understanding of the dependence of the time required to empty a lake on its initial area may come from further analysis of the model (possibly by integrating eqn. 7-35 over time). This will be pursued elsewhere.

This investigation has revealed some potentially important mechanisms that may control the movement of water across the surface of glaciers and ice sheets. However, some limitations of the model prevent the quantitative application of my findings to real systems.

For example, the model ignores lake sensible heat, solar radiation and along-channel spatial variation. Lake sensible heat and solar radiation may affect channel incision by warming of the flowing water significantly above $0\ ^{\circ}\mathrm{C}$ and developing the model to include along-channel spatial variation may reveal dynamics associated with a melt–slope–discharge feedback. If the model is to gain any predictive power, its mechanisms and unconstrained physical parameters must be validated against data from in situ hydrological measurements of surface drainage. In particular, the thermal and hydraulic roughness coefficient f_R needs to be calibrated and the model's sensitivity to this parameter quantified.

I have assumed a constant channel width. Although previous work has justified this with observations of deep, vertical-walled supraglacial channels (e.g. Vincent et al., 2010; Mayer and Schuler, 2005), this assumption is probably invalid when channel width is less than the flow depth and a physical explanation for these observations is presently lacking. Related to this is an alternative drainage initiation mechanism to snow-dam failure: a slow lake-bank over-topping. After initial sheet flow, a channel would form through a feedback between melt and flow-depth. Two-dimensional modelling of the channel formation process is possible and may illuminate the controls on channel width.

Despite limitations, some qualitative features of model behaviour may be realistic. Moreover, as mean and maximum lake areas observed by Selmes et al. (2011) bracket the transition between stability and instability in model parameter-space, these results may have implications in the Greenland Ice Sheet.

A concern among glaciologists is that atmospheric warming could increase the area of the ice sheet populated by supraglacial lakes, resulting in a corresponding increase in the area of the bed that receives injections of melt water from the surface. This in turn could affect ice dynamics (e.g. Lüthje et al., 2006).

Lüthje et al. (2006) suggest that, as lakes populate a larger area of the ice sheet, they will form at higher altitudes where they will tend to be larger because of the lower mean ice surface slopes at higher elevations. In terms of the supraglacial drainage simulated by my model, such a shift in elevation corresponds to movement through the model's parameter space, the details of which remain to be determined. For example, an increase in mean lake area may increase the propensity of lakes to drain unstably, increasing the relocation of surface water to lower elevations and partially mitigating the effect of atmospheric warming on basal meltwater injection from the surface. However, decreasing average surface slopes will tend to have the opposite effect. Alternatively, lake area and channel slope may be entirely controlled by large-scale surface roughness, itself controlled by local surface processes and ice dynamics. How other model parameters (e.g. lake shape, channel width and lake input) may change is similarly unclear.

Quantitative assessment of the impact of change in Greenland on surface drainage will require model development, to avoid some model limitations, and calibration, by applying it to present-day Greenland and comparing its predictions to observed lake stability. Observations could involve a remote sensing survey of surface-draining lakes similar to recent studies by Selmes et al.'s (2011) and Johansson et al.'s (2012) that have focused on the drainage of lakes through the ice sheet to its bed.

In East Antarctica, new observations of extensive surface drainage (Fig. 7.2) allow speculation on mechanisms affecting drainage stability. The most rapid drainage appears to originate from several of the largest lakes positioned just above the grounding line on the ice sheet flank where ice surface slope is steepest. This is consistent with the results of the model.

It is unclear whether lakes are advected with ice flow or if they form in topographic depressions whose locations are dictated by ice dynamics and remain geographically stationary. Lake advection may be favoured by intense solar radiation, as lake position

relative to the ice is reinforced by differential ablation between the low albedo lake and the surrounding ice.

If lake-bed ablation decreases with water depth, lake walls would steepen as shallower areas preferentially ablate, corresponding to a decrease in the lake parameter p_L and drainage stability. Furthermore, if lakes do advect with ice flow, the ice surface will steepen and (possibly) its catchment area will increase over time, as it approaches the grounding line. This would also decrease the stability of drainage. Lakes may be formed in the blue-ice area (to the lower right of Fig. 7.2a) and advected towards the grounding line over many years, becoming increasingly unstable until input is sufficient to cause the rapid drainage observed in Fig. 7.2b.

Whether lakes are advected or not, variation in lake input will affect the timing and rate of lake drainage. Such mechanisms may help explain the large inter-annual variability seen in drainage extent and will be investigated further elsewhere using the model developed in this chapter.

7.6   Conclusions

This work is the first attempt to model the surface drainage of supraglacial lakes on ice sheets. Despite simplifying assumptions made during its derivation, the model yields qualitative results that highlight and physically explain potentially important controls on drainage. Lakes are more prone to drain unstably, which often results in their complete emptying, when initial lake area, lake input and channel slope are larger. These findings could have implications for predictions of the response of ice sheets to atmospheric warming and for our understanding of previously unobserved hydrological systems in East Antarctica. Further work will aim to quantitatively assess these implications through model development and calibration.

Chapter 8 **Conclusions**

In this thesis I have investigated theoretically several aspects of ice-dammed lake drainage. A persistent theme of the work has been an attempt to unravel the links between environmental parameters and the magnitude and timing of lake drainage. This theme has led me to extend Fowler's (1999) theoretical investigation of subglacial jökulhlaups and to apply similar physics to an analogous lake drainage phenomenon: the surface drainage of supraglacial lakes.

Chapter 2 introduced the mathematics that underlies the rest the thesis. Particularly important to introduce was Fowler's modifications to Nye's (1976) classic jökulhlaup theory. Throughout the rest of the thesis I referred to the model that resulted from these modifications as the Nye-Fowler model.

In Chapter 3, my first extension of Fowler's work used the Nye-Fowler model to investigate the environmental controls on the size and timing of cycles of subglacial floods. This involved pinning down, more thoroughly than Fowler (1999) did, under what conditions his model simulates periodic, stable flood cycles.

Next I examined how the size of simulated jökulhlaups changes with the rate of meltwater input to the model. The results of my simulations suggest that this depends on how this meltwater is distributed around the system. If climatic warming leads to an increase in the rate of meltwater input to an ice-dammed lake, results suggest that floods may occur more frequently or increase in magnitude or both. Results also suggest that, if the same climatic warming also leads to an increase in the meltwater input to the bed of the glacier that dams the lake, floods may still occur more frequently but decrease in magnitude. Any predictions of change in jökulhlaup systems associated with climatic warming in mountainous regions should consider these findings, as well as changes in the geometry of glaciers, that I have not investigated.

The mechanistic link between jökulhlaups and environmental parameters that I examined in Chapter 3 is based around Fowler's (1999) idea of a moving subglacial water divide that exists between floods. In particular, the moving divide links the rate of meltwater input to the system to the depth at which an ice-dammed lake begins to drain – I have called the latter the flood-initiation threshold. This link was exploited in Chapter 4 to establish how well simple models can predict the date of an upcoming jökulhlaup. I used hydrological and meteorological data from Merzbacher Lake, Kyrgyzstan to optimise several flood-date-prediction models of varying complexity and found that including weather in the determination of the flood-initiation threshold significantly

improved the reliability of flood-date predictions. This empirically reinforces the assertion made by previous authors (e.g. Ng et al., 2007; Ng and Liu, 2009) and examined theoretically in Chapter 3, that variability in the timing and size of jökulhlaups can be, at least partially, attributed to climatic variability.

In Chapter 5 I extended the Nye-Fowler model by coupling it to models of a distributed linked-cavity subglacial drainage system and glacier sliding. The cavities could exchange water with the channel along its length and the glacier's sliding velocity was a function of the water pressure in the cavities. Simulating flood cycles with the model allowed me to investigate how the drainage of a marginal lake affects the hydraulics of the distributed cavity system and the rate at which the glacier slides, and how the cavities affects lake drainage. The results showed that temporal changes in the glacier's sliding velocity during simulated flood cycles are due to temporal changes in the depth of the marginal lake. Continuing the theme of environmental controls on jökulhlaup systems, I showed that decreasing the background meltwater input to the cavity system increases the magnitude of these temporal changes in sliding velocity and the size of floods.

While conducting the simulations of flood cycles presented in Chapter 3 and Chapter 5, I had to be careful not to allow my model lake to empty because the Nye-Fowler model cannot simulate the open-channel flow which results when this happens in real systems. To address this shortcoming, in Chapter 6 I added to the model a description of open-channel flow. Hence I was able to simulate flood cycles that involve periods of open-channel flow. This is valuable because the majority of observed jökulhlaups end with a period of open-channel flow. Considering the effect of open-channel flow on the water-balance of jökulhlaup lakes could improve reconstructions of lake depth and some details of an existing reconstruction of Merzbacher Lake's depth could be explained by invoking mechanisms revealed by solving the model numerically.

In Chapter 7 I turned my attention to the drainage of supraglacial lakes across the surface of glaciers and ice sheets. Much of the same physics that apply to subglacial jökulhlaups can be applied to surface drainage. Both types of drainage involve the enlargement of drainage pathways through the melting of ice caused by frictional dissipation of heat in flowing water. Hence, the positive feedback between discharge and channel enlargement revealed first by Nye's (1976) analysis of subglacial jökulhlaups, potentially also applies to the surface drainage of supraglacial lakes.

The model I developed in Chapter 7 demonstrates that when a supraglacial lake drains through a channel that is incised through an ice-sheet's surface a competition between the drawdown of the surface of the lake and the incision of the channel determines if a lake drains stably or unstably – that is, if discharge from a lake always increases with

time or always decreases with time. Analysis of the model shows how various environmental factors control drainage stability. Unstable lakes tend to empty more quickly and more completely, so the model's predictions of the controls on drainage stability may have implications in real systems. Systematic changes in lake characteristics caused by environmental changes may affect their propensity to drain and relocate water across the surface of ice sheets.

The work presented in this thesis has increased our understanding of several aspects of ice-dammed lake drainage, but it has also highlighted many areas in which further work is needed. I have outlined some of these during Chapters 3 to 7. However, I want to end this thesis by suggesting two further areas of theoretical work based on the Nye-Fowler model that are worthwhile and by arguing that the time has come for an attempt to verify this model's behaviour against field observations.

Firstly, future theoretical work could apply the Nye-Fowler model to the drainage of subglacial floods beneath ice sheets. Evatt et al.'s (2006) work has already shown that the model can be used to simulate this, despite the complication of coupling between drainage and the dynamics of the overlying ice. Their work also suggests that drainage from subglacial lakes is inherently unstable and jökulhlaup-like in nature.

Since Evatt et al.'s (2006) model-based study, observational surveys of Antarctic subglacial lake drainage have collected a large amount of data pertaining to the timing, magnitude and spatially-complex nature of drainage events (e.g. Smith et al., 2009). One thing these observations reveal is that lakes are hydraulically connected to one another. It appears that lakes connect together to form extensive multi-lake drainage systems. Some questions worth asking are: How are the dynamics of such a multi-lake system different from those of a single-lake system focussed on by Evatt et al. (2006)? Can the drainage of a downstream lake induce the drainage of an upstream lake? And, under the right conditions, can water from a downstream lake drain to an upstream lake? The last question is particularly interesting because people tasked with interpreting observations of contemporaneous, but spatially separated, temporal changes in Antarctica's surface elevation frequently assume that lake drainage always occurs in a downstream direction.

Modelling could address these questions. An attempt to do this was made Peters et al. (2009) using a version of the Nye equations, but their simulations could not capture, even qualitatively, observed features of sub-ice-sheet lake drainage involving more than two lakes. In this thesis I have developed a numerical method that can solve the mass and momentum balance equations of the full Nye-Fowler model as a boundary value problem (the relaxation method; section 2.2.5). So, using the Nye-Fowler model, two

lakes could be coupled together, with the upper and lower pressure boundary conditions on a subglacial channel defined by the pressure of an upstream lake and a downstream lake respectively. Water exchange between the channel and both lakes would change with time and determine the drainage or otherwise of the lakes. Using the model to simulate the coevolution of a channel and more than one lake, one could attempt to reproduce observations of multi-lake drainage and determine under what conditions lakes could drain in an upstream direction.

The second way in which modelling using the Nye-Fowler model could be advanced would aim to address an assumption that underlies many aspects of the model's behaviour that this thesis and previous work have uncovered. The model assumes that a channel always exists beneath an ice dam, even when water discharge is low between floods. There are at least two approaches one could take in removing this potentially unrealistic assumption.

In Chapter 5 I allowed water to flow through two drainage systems simultaneously, but I assumed that both systems existed throughout simulated flood cycles. Future modelling could allow one system to dominate when the hydrological conditions dictate this, for example when discharge is low the channel could collapse leaving only a drainage system that is favoured in low discharge condition. One issue is the question of how to allow the channel to reform when hydrological conditions change, for example in response to a lake filling.

An alternative approach is to model multiple drainage systems using one continuous physical description of drainage. Schoof (2010), Hewitt et al. (2012) and Schoof et al. (2012) have pursued this. Combining my investigation of jökulhlaups with their work could allow a channel to evolve from a low discharge system during the early stages of lake drainage. It would be interesting to see if the dynamics of divide migration, which were revealed by my analysis in Chapter 3 and have proved so important for linking environmental factors and jökulhlaup characteristics, manifest in any way in such a model.

Given how much we now know about how the theoretical Nye-Fowler model behaves, it is time for an attempt to verify this behaviour against observations.

This thesis contributes to several other studies that have used versions of Fowler's (1999) model (very similar to my "Nye-Fowler model") to investigate jökulhlaup-related phenomenon. Evatt (2006) demonstrated that assuming the water in a subglacial channel is always at the pressure-melting point is often appropriate. Evatt and Fowler (2006) have shown that the model can be usefully applied to the drainage of subglacial lakes beneath ice sheets and above I have suggested ways in which this can be extended

in future work. And Fowler (2009) has shown that model simulations can produced realistic hydrographs.

We understand the model reasonably well and are poised to apply it to other glacial-hydrological systems, but key aspects of its behaviour remain unverified observationally. In particular, divide formation and migration, which underlie many of my findings in this thesis, have not been observed in the field. By injecting dye into, and measuring the water pressure at the bottom of bore-holes drilled to the base of an ice dam in a marginal-lake jökulhlaup system, one may be able to verify that water can flow upstream towards a marginal lake between floods, demonstrating divide formation. Repeat measurements may even reveal temporal changes in drainage associated with changes in lake depth, hinting at divide migration.

Successful verification of the behaviour of the Nye-Fowler model against observations of a real jökulhlaup system would bolster efforts to apply the model to other glacio-hydraulic systems and increase the applicability of my theoretical findings to the study of real ice-dammed lake drainage.

Bibliography

Aitkenhead, N. (1957) Observations on the drainage of a glacier-dammed lake in Norway. *Journal of Glaciology*, 3(27), 607–609.

Aizen, V.B. and E.M. Aizen (1998) Estimation of glacial runoff to the Tarim River, central Tien Shan. In HeadWater'98, 191–198. Meran/Merano, Italy: IAHS.

Aizen, V. B. and E. M. Aizen. 1998. Estimation of glacial runoff to the Tarim River, central Tien Shan: HeadWater'98, 191–98.

Aizen, V. B., E. M. Aizen and V. A. Kuzmichonok (2007) Glaciers and hydrological changes in the Tien Shan: simulation and prediction. *Environmental Research Letters*, 2(4). doi:10.1088/1748-9326/2/4/045019.

Anderson, R.S., S.P. Anderson, K.R. MacGregor, E.D. Waddington, S. O'Neel, C.A. Riihimaki, & M.G. Loso (2004) Strong feedbacks between hydrology and sliding of a small alpine glacier. *Journal of Geophysical Research*, 109, F03005.doi:10.1029/2004JF000120.

Anderson, S.P., J.S. Walder, R.S. Anderson, E.R. Kraal, M. Cunico, A.G. Fountain, and D.C. Trabant (2003) Integrated hydrologic and hydrochemical observations of Hidden Creek Lake jökulhlaups, Kennicott glacier, Alaska. *Journal of Geophysical Research*, 108(F1), 6003, doi:10.1029/2002JF000004

Anderson, R. S., J. S. Walder, S. P. Anderson, D. C. Trabant and A. G. Fountain (2005) The dynamic response of Kennicott Glacier, Alaska, USA, to the Hidden Creek Lake outburst flood. *Annals of Glaciology*, 40, 237–242.

Bajracharya, B.B, A.B. Shrestha and L. Rajbhandari (2007) Glacial Lake Outburst Floods in the Sagarmatha Region. *Mountain Research and Development*. 27(4), 336–344.

Bajracharya, S.R. and P. Mool (2009) Glaciers, glacial lakes and glacial lake outburst floods in the Mount Everest region, Nepal. *Annals of Glaciology*, 50, 81-86.

Barnett, T.P., J.C. Adam and D.P. Lettenmaier (2005) Potential impacts of a warming climate on water availability in snow-dominated regions. *Nature*, 438, 303-309.

Bartholomaus, T. C., R. S. Anderson and S. P. Anderson (2008) Response of glacier basal motion to transient water storage. *Nature Geoscience*, 1, 33–37.

Bartholomaus, T.C., R.S. Anderson and S.P. Anderson (2011) Growth and collapse of the distributed subglacial hydrologic system of Kennicott Glacier, Alaska, USA, and its effects on basal motion. *Journal of Glaciology*, 57(206), 985–1002.

Bartholomew, I., P. Nienow, D. Mair, A. Hubbard, M. A. King and A. Sole (2010) Seasonal evolution of subglacial drainage and acceleration in a Greenland outlet glacier. *Nature Geoscience*, 3, 408–411.

Bartholomew, I. D., P. Nienow, A. Sole, D. Mair, T. Cowton, M. A. King and S. Palmer (2011a) Seasonal variations in Greenland Ice Sheet motion: Inland extent and behaviour at higher elevations. *Earth and Planetary Science Letters*, 307, 271–278.

Bartholomew, I., P. Nienow, A. Sole, D. Mair, T. Cowton, S. Palmer and J. Wadham (2011b) Supraglacial forcing of subglacial drainage in the ablation zone of the Greenland ice sheet. *Geophysical Research Letters*, 38.

Bell, R. E., M. Studinger, C. A. Shuman, M. A. Fahnestock and I. Joughin (2007) Large subglacial lakes in East Antarctica at the onset of fast-flowing ice streams. *Nature*, 445, 904–907.

Benn, D.I. and D.J.A. Evans (2008) Glaciers and glaciation. Hodder Arnold, London.

Benn, D.I., N.R.J. Hulton and R.H. Mottram (2007) 'Calving laws', 'sliding laws' and the stability of tidewater glaciers, *Annals of Glaciology*, 46, 123–130.

Bindoff, N.L. J. Willebrand, V. Artale, A. Cazenave, J.M. Gregory, S. Gulev, K. Hanawa, K.; C. Le Quere, S. Levitus, Y. Nojiri, C.K. Shum, L.D. Talley, A.S. Unnikrishnan (2007) Observations: oceanic climate change and sea level. In: Solomon, S. D. Qin, M. Manning, Z. Chen, M. Marquis, K.B. Averyt, M. Tignor, H.L. Miller (eds.) Climate change 2007: the physical science basis. Contribution of Working Group I to the Fourth Assessment Report of the Intergovernmental Panel on Climate Change. Cambridge, Cambridge University Press, 385–428.

Bindschadler, R (1983) The importance of pressurized subglacial water in separation and sliding at the glacier bed. *Journal of Glaciology*, 29(101), 3-19.

Björnsson, H. (1992) Jökulhlaups in Iceland: Characteristics, prediction and simulation. *Annals of Glaciology*, 16, 95–106.

Björnsson, H. (1998) Hydrological characteristics of the drainage system beneath a surging glacier. *Nature*, 395, 771–774.

Björnsson, H. (2002) Subglacial lakes and jökulhlaups in Iceland. *Global and Planetary Change*, 35(3), 255-271.

Björnsson, H. (2004) Glacial lake outburst floods in mountain environments. In: Owens, P., and O. Slaymaker (eds.) Mountain Geomorphology, London, Edward Arnold, 165–184.

Björnsson, H. (2009) Jökulhlaups in Iceland: sources, release and drainage. In: Burr, D.M., P.A Carling, and V.R. Baker (Eds.) Megaflooding on Earth and Mars. Cambridge University Press.

Boulton, G.S., R. Lunn, P. Vidstrand and S. Zatsepin (2007a) Subglacial drainage by groundwater-channel coupling, and the origin of esker systems: Part 1—glaciological observations. *Quaternary Science Reviews,* 26(7), 1067–1090.

Boulton, G.S., R. Lunn, P. Vidstrand and S. Zatsepin (2007b). Subglacial drainage by groundwater–channel coupling, and the origin of esker systems: part II—theory and simulation of a modern system. *Quaternary Science Reviews*, 26(7), 1091–1105.

Burke, M.J., J. Woodward, A.J. Russell and P.J. Fleisher (2009) Structural controls on englacial esker sedimentation: Skeioararjokull, Iceland. *Annals of Glaciology*, 50, 85–92.

Capps, D.M., B. Rabus, J.J. Clague, D.H. and Shugar (2010) Identification and characterization of alpine subglacial lakes using interferometric synthetic aperture radar (InSAR): Brady Glacier, Alaska, USA. *Journal of Glaciology*, 56(199), 861–870.

Carrivick, J.L. (2007) Hydrodynamics and geomorphic work of jökulhlaups (glacial outburst floods) from Kverkfjoll volcano, Iceland. *Hydrological Processes*, 21, 725–740.

Carter, S.P., D.D. Blankenship, M.E. Peters, D.A. Young, J.W. Holt and D.L. Morse (2007) Radar-based subglacial lake classification in Antarctica. *Geochemical Geophysical Geosystems*, 8(3), Q03016, doi:10.1029/2006GC001408.

Cenderelli, D.A. & E.E. Wohl (2003) Flow hydraulics and geomorphic effects of glacial-lake outburst floods in the Mount Everest region, Nepal. *Earth Surface Processes and Landforms*, 28(4), 385–407.

Chen, Y., C. Xu, Y. Chen, W. Li, and J. Liu (2010) Response of glacial-lake outburst floods to climate change in the Yarkant River basin on northern slope of Karakoram Mountains, China. *Quaternary International*, 226(1), 75–81.

Chow, V.T. (1959). Open-channel hydraulics. McGraw-Hill.

Clague, J.J. and W.H. Mathews (1973) The magnitude of jökulhlaups. *Journal of Glaciology*, 12(66), 501–504.

Clarke, G.K.C. (1982) Glacier Outburst Floods from Hazard Lake, Yukon Territory, and the Problem of Flood Magnitude Prediction. *Journal of Glaciology*, 28(98), 3–21.

Clarke, G.K.C. (2003) Hydraulics of subglacial outburst floods: new insights from the Spring-Hutter formulation. *Journal of Glaciology*, 49(165), 299–313.

Clarke, G.K.C. (2005) Subglacial processes. *Annual Reviews of Earth and Planetary Science*, 33, 247–276.

Creyts, T.T. and G.K.C. Clarke (2010) Hydraulics of subglacial supercooling: Theory and simulations for clear water flows. *Journal of Geophysical Research*, 115, F03021, doi:10.1029/2009JF001417.

Creyts, T.T. and C.G. Schoof (2009) Drainage Through Subglacial Water Sheets. *Journal of Geophysical Research*, 114, F04008, doi:10.1029/2008JF001215.

Collins, S.G. and G.K.C. Clarke (1977) History and Bathymetry of a surge-dammed lake. *Arctic*, 30(4), 217–24.

Costa, J.E. and R.L. Schuster (1988) The Formation and Failure of Natural Dams. *Geological Society of America Bulletin*, 100(7), 1054–1068.

Cuffey, K. and W.S.B. Paterson (2010) The Physics of Glaciers. Butterworth-Heinemann/Elsevier.

Das, S.B., I. Joughin, M.D. Behn, I.M. Howat, M.A. King, D. Lizarralde and M.P. Bhatia (2008) Fracture propagation to the base of the Greenland Ice Sheet during supraglacial lake drainage. *Science*, 320, 778–781.

Drazin, P. G. (1992) Nonlinear systems. Cambridge University Press.

Ding, Y. And J. Liu (1992) Glacial lake outburst flood disasters in China. *Annals of Glaciology*, 16, 180–184.

Dussaillant, A., G. Benito, W. Buytaert, P. Carling, C. Meier and F. Espinoza (2010) Repeated glacial-lake outburst floods in Patagonia: an increasing hazard? *Natural Hazards*, 54, 469–481.

Echelmeyer, K., T.S. Clarke and W.D. Harrison (1991) Surficial glaciology of Jakobshavns Isbræ, West Greenland: Part I. Surface morphology. *Journal of Glaciology*, 37(127), 368–382.

Eisen, O., W.D. Harrison, C.F. Raymond, K.A. Echelmeyer, G. A. Bender and J. L. D. Gorda (2005) Variegated Glacier, Alaska, USA: a century of surges. *Journal of Glaciology*, 51, 399–406.

Engeset, R.V., T.V. Schuler and M. Jackson (2005) Analysis of the first jökulhlaup at Blåmannsisen, northern Norway, and implications for future events. *Annals of Glaciology*, 42, 2005, 42, 35–41.

Evatt, G.W. 2006. Jökulhlaups and subglacial floods. (D.Phil. thesis, Oxford University.)

Evatt, G.W., A.C. Fowler, C.D. Clark, and N.R.J. Hulton (2006) Subglacial floods beneath ice sheets. *Philosophical Transactions of the Royal Society A: Mathematical, Physical and Engineering Sciences*, 364(1844), 1769–1794.

Fahnestock, M.A., W. Abdalati and C.A. Shuman (2002) Long melt seasons on ice shelves of the Antarctic Peninsula: an analysis using satellite-based microwave emission measurements. *Annals of Glaciology*, 34, 127–133.

Flowers, G.E., & G.K.C. Clarke (2002). A multicomponent coupled model of glacier hydrology: 1. Theory and synthetic examples. *Geophysical Research Letters*, 107(2287), doi:10.1029/2001JB001122.

Flowers, G.E., H. Björnsson, F. Pálsson and G.K.C. Clarke (2004) A coupled sheet-conduit mechanism for jökulhlaup propagation. *Geophysical Research Letters*, 31(5). L05401. 10.1029/2003GL019088.

Fountain, A.G. (1993) Geometry and flow conditions of subglacial water at South Cascade Glacier, Washington State, USA; an analysis of tracer injections. *Journal of Glaciology*, 39(131), 143–156.

Fountain, A.G. and J.S. Walder (1998) Water flow through temperate glaciers. *Reviews of Geophysics*, 36, 299–328.

Fowler, A.C. and E. Schiavi (1998) A theory of ice-sheet surges. *Journal of Glaciology*, 44, 104–118.

Fowler, A.C. (1986) A Sliding Law for Glaciers of Constant Viscosity in the Presence of Subglacial Cavitation. *Proceedings of the Royal Society of London Series a-Mathematical Physical and Engineering Sciences*, 407, 147–170.

Fowler, A.C. (1987a) Sliding with Cavity Formation. *Journal of Glaciology*, 33(115), 255–267.

Fowler, A.C. (1987b) A theory of glacier surges. *Journal of Geophysical Research-Solid Earth and Planets*, 92, 9111–9120.

Fowler, A.C. (1999) Breaking the seal at Grimsvötn, Iceland. *Journal of Glaciol*ogy, 45(151), 506–516.

Fowler, A.C. (2009) Dynamics of subglacial floods. *Proceedings of the Royal Society a-Mathematical Physical and Engineering Sciences*, 465, 1809–1828.

Fowler, A.C. (2010) Weertman, Lliboutry and the development of sliding theory. *Journal of Glaciology*, 56(200), 965–972.

Fowler, A.C. and E. Schiavi (1998). A theory of ice-sheet surges. *Journal of Glaciology*, 44(146), 104–118.

Fowler, A.C. and F.S.L. Ng (1996) The role of sediment transport in the mechanics of jökulhlaups. *Annals of Glaciology*, 22, 255–259.

Fricker, H.A. and T. Scambos (2009) Connected subglacial lake activity on lower Mercer and Whillans Ice Streams, West Antarctica, 2003–2008. *Journal of Glaciology*, 55(190), 303–315.

Fricker, H.A., T. Scambos, R. Bindschadler, and L. Padman, (2007). An active subglacial water system in West Antarctica mapped from space. *Science*, 315(5818), 1544–1548.

Fricker, H.A., T. Scambos, S. Carter, C. Davis, T. Haran, and I. Joughin (2010) Synthesizing multiple remote-sensing techniques for subglacial hydrologic mapping: application to a lake system beneath MacAyeal Ice Stream, West Antarctica. *Journal of Glaciology*, 56(196), 187–199.

Gagliardini, O., D. Cohen, P. Raback and T. Zwinger (2007) Finite-element modeling of subglacial cavities and related friction law. *Journal of Geophysical Research-Earth Surface*, 112, F02027, doi:10.1029/2006JF000576.

Georgiou, S., Shepherd, A., McMillan, M., & Nienow, P. (2009). Seasonal evolution of supraglacial lake volume from ASTER imagery. *Annals of Glaciology*, 50(52), 95-100.

Glen, J.W. (1954). The stability of ice-dammed lakes and other water-filled holes in glaciers. Journal of Glaciology, 2(15), 316–18.

Glen, J.W. (1955). The creep of polycrystalline ice. Proceedings of the Royal Society of London. *Series A. Mathematical and Physical Sciences*, 228(1175), 519–538.

Gudmundsson, M.T., F. Sigmundsson and H. Björnsson (1997) Ice-volcano interaction of the 1996 Gjalp subglacial eruption, Vatnajokull, Iceland. *Nature*, 389, 954–957.

Henderson, F.M. (1966) Open Channel Flow. Macmillan.

Hewitt, K., and Liu, J. (2010). Ice-dammed lakes and outburst floods, Karakoram Himalaya: historical perspectives on emerging threats. *Physical Geography*, 31(6), 528-551.

Hewitt, I.J. (2011) Modelling distributed and channelized subglacial drainage: the spacing of channels. Journal of Glaciology, 57(202), 302–314.

Hewitt, I.J. and A.C. Fowler (2008) Seasonal waves on glaciers. *Hydrological Processe*s, 22, 3919–3930.

Hewitt, I.J., C. Schoof, and M.A. Werder (2012) Flotation and free surface flow in a model for subglacial drainage. Part 2. Channel flow. *Journal of Fluid Mechanics*, 702, 157–187.

Higgins, A.K. (1970). On some ice-dammed lakes in the Frederikshåb district, south-west Greenland. Meddelelser Fra Dansk Geologisk Forening, 19, 378–97.

Hooke, R. (1984) On the role of mechanical energy in maintaining subglacial water conduits at atmospheric pressure. *Journal of Glaciology*, 30(105), 180–187.

Hooke, R.L., T. Laumann and J. Kohler (1990) Sub glacial water pressures and the shape of subglacial conduits. *Journal of Glaciology*, 36(122), 67–71.

Huss, M., A. Bauder, M. Werder, M. Funk and R. Hock (2007) Glacier-dammed lake outburst events of Gornersee, Switzerland. *Journal of Glaciology*, 53(181), 189–200.

Iken, A. (1981) The Effect of the Subglacial Water-Pressure on the Sliding Velocity of a Glacier in an Idealized Numerical-Model. *Journal of Glaciology,* 27(97), 407–421.

Iken, A., and M. Truffer (1997) The relationship between subglacial water pressure and velocity of Findelengletscher, Switzerland, during its advance and retreat. *Journal of Glaciology*, 43(144), 328–338.

Isenko, E., R. Naruse, and B. Mavlyudov (2005) Water temperature in englacial and supraglacial channels: Change along the flow and contribution to ice melting on the channel wall. *Cold regions science and technology*, 42(1), 53–62.

Jóhannesson, T. 2002. Propagation of a subglacial flood wave during the initiation of a jökulhlaup. *Hydrological Sciences Journal*, 47(3), 417–434.

Johansson, A.M., P. Jansson, and I.A. Brown (2012) Spatial and temporal variations in lakes on the Greenland Ice Sheet. *Journal of Hydrology*, 476, 314–320.

Joughin, I., S.B. Das, M.A. King, B.E. Smith, I.M. Howat and T. Moon (2008) Seasonal speedup along the western flank of the Greenland Ice Sheet. *Science*, 320, 781–783.

Kalnay, E., M. Kanamitsu, R. Kistler, W. Collins, D. Deaven, L. Gandin, M. Iredell, S. Saha, G. White, J. Woollen, Y. Zhu, M. Chelliah, W. Ebisuzaki, W. Higgins, J. Janowiak, K. C. Mo, C. Ropelewski, J. Wang, A. Leetmaa, R. Reynolds, R. Jenne and D. Joseph (1996) The NCEP/NCAR 40-year reanalysis project. *Bulletin of the*

American Meteorological Society, 77(3), 437–471.

Kamb, B. and E. LaChapelle (1964) Direct observations of the mechanism of glacier sliding over bedrock. *Journal of Glaciology*, 5, 159–172.

Kamb, B. (1987) Glacier Surge Mechanism Based on Linked Cavity Configuration of the Basal Water Conduit System. *Journal of Geophysical Research-Solid Earth and Planets*, 92, 9083–9100.

Kerr, F.A. (1934) The ice dam and floods of the Talsekwe, British Columbia. *Geographical Review*, 643–645.

Kanamaru, T. (2007) Van der Pol oscillator. *Scholarpedia*, 2(1), 2202. [website last visited on 18th December 2012: http://www.scholarpedia.org/article/Van_der_Pol_Oscillator].

Kehrwald, N.M., L.G. Thompson, Y. Tandong, E. Mosley-Thompson, U. Schotterer, V. Alfimov, J. Beer, J. Eikenberg, and M.E. Davis (2008) Mass loss on Himalayan glacier endangers water resources. *Geophysical Research Letters*, 35(22), L22503, doi:10.1029/2008GL035556.

Kingslake, J. and F. Ng. (2013) Modelling the coupling of flood discharge with glacier flow during jökulhlaups. *Annals of Glaciology*, 54(63), 25–31.

Kistler, R., E. Kalnay, W. Collins, S. Saha, G. White, J. Woollen, M. Chelliah, W. Ebisuzaki, M. Kanamitsu, V. Kousky, H. van den Dool, R. Jenne and M. Fiorino (2001) The NCEP-NCAR 50-year reanalysis: Monthly means CD-ROM and documentation. *Bulletin of the American Meteorological Society*, 82(2), 247–267.

Komori, J. 2008. Recent expansions of glacial lakes in the Bhutan Himalayas. *Quaternary International*, 184(1) 177–186.

Krawczynski, M.J., M.D. Behn, S.B. Das and I. Joughin (2009) Constraints on the lake volume required for hydro-fracture through ice sheets. *Geophysical Research Letters*, 36, L10501, doi:10.1029/2008GL036765.

Kuzmichenok, V.A. (1984) K voprosu ob obrabotke materialov topograficheskikh s'emok dna glyatsial'nykh ozer [Questioning the treatment of materials from topographical surveys of glacial lakebeds]. In: Dikikh, A.N. (eds.) *Gliatsiologicheskie Issledova-niya v Tsentral'nom Tyan-Shane* [Glaciological studies in central Tien Shan], 130–137, Frunze, IlimPress.

Liestøl, O. (1956) Glacier Dammed Lakes in Norway. *Norsk Geografisk Tidsskrift* [Norwegian Journal of Geography]. 15(3-4), 122–149.

Liu, J.S. (1992) Jökulhlaups in the Kunmalike River, Southern Tien-Shan Mountains, China. *Annals of Glaciology*, 16, 85–88.

Liu, J.S and Y. Fukushima (1999) Recent change and prediction of glacier-dammed lake outburst floods from Kunmalik River in southern Tien Shan, China. *IAHS-AISH publication*, 99–107.

Livingstone, S.J., C.D. Clark, J.A. Piotrowski, M. Tranter, M.J. Bentley, A. Hodson, D.A. Swift and J. Woodward (2012) Theoretical framework and diagnostic criteria for the identification of palaeo-subglacial lakes. *Quaternary Science Review*s, 53, 88–110.

Lliboutry, L. (1958) Contribution a la theorie du frottement du glacier sur son lit (Contribution to the theory of friction on the bed of the glacier). *Comptes Rendus Hebdomadaires des Seances de l'Academie des Sciences*, 247, 318–320.

Lliboutry, L. (1964) Sub-glacial `Supercavitation' as a Cause of the Rapid Advances of Glaciers. *Nature*, 202, 77–77.

Lliboutry, L. (1968) General theory of subglacial cavitation and sliding of temperate glaciers. *Journal of Glaciology*, 7, 21–58.

Lüthje, M., L.T. Pedersen, N. Reeh, and W. Greuell (2006) Modelling the evolution of supraglacial lakes on the West Greenland ice-sheet margin. *Journal of Glaciology*, 52(179), 608–618.

Maag, H. U. (1969). Ice dammed lakes and marginal glacial drainage on Axel Heiberg Island, Canadian Arctic Archipelago. Montreal: McGill University.

Magnússon, E., H. Björnsson, H. Rott and F. Pálsson (2010) Reduced glacier sliding caused by persistent drainage from a subglacial lake. *Cryosphere*, 4(1), 13–20.

Magnússon, E., H. Björnsson, H. Rott, M. J. Roberts, F. Pálsson, M. T. Gudmundsson, R. A. Bennett, H. Geirsen & E. Sturkell (2011) Localized uplift of Vatnajökull, Iceland: subglacial water accumulation deduced from InSAR and GPS observations. *Journal of Glaciology*, 57(203), 475–484.

Magnússon, E., H. Rott, H. Björnsson and F. Pálsson (2007) The impact of jökulhlaups on basal sliding observed by SAR interferometry on Vatnajökull, Iceland. *Journal of Glaciology*, 53(181), 232–240.

Mair, D., P. Nienow, M. Sharp, T. Wohlleben, and I. Willis (2002) Influence of subglacial drainage system evolution on glacier surface motion: Haut Glacier d'Arolla, Switzerland. *Journal of geophysical research*, 107(13), doi:10.1029/2001JB000514.

Mamatkanov, D.M. and D. Mingtszyan (2011) Water and hydropower resources of the Sarydjaz-Kumaryk river and prospects of their use. AASA Regional Workshop on "The Roles of Academies of Sciences in Water and Energy Problems in Central Asia and Ways for Their Solution". Tuzova T.V. and D. A.Z. Bishkek.

Mathews, W.H. (1973). Record of two jokullhlaups. *From the Symposium on the hydrology of glaciers*. *International Association of Scientific Hydrology*. 95, 99–110.

Mavlyudov, B.R. (1997) Drainage of ice-dammed Mertzbacher Lake, Tien Shan. *Mater. Glyatsiol. Issled.*, 81, 61–65.

May, R.M. (1976). Simple mathematical models with very complicated dynamics. Nature, 261(5560), 459–467.

Mayer, C. and T.V. Schuler (2011) Breaching of an ice dam at Qorlortossup tasia, south Greenland. *Annals of Glaciology*, 42, 297–302.

Mayer, C., A. Fowler, A. Lambrecht and K. Scharrer (2011) A surge of North Gasherbrum Glacier, Karakoram, China. *Journal of Glaciology*, 57(205), 904–916.

Mayer, C., A. Lambrecht, W. Hagg, A. Helm and K. Scharrer (2008) Post-drainage ice dam response at Lake Merzbacher, Inylchek glacier, Kyrgyzstan. *Geografiska Annaler Series a-Physical Geography*, 90A, 87–96.

McAdams, W.H. (1953) Heat Transmission. McGraw-Hill.

Mernild, S.H., B. Hasholt and G.E. Liston (2006) Water flow through Mittivakkat Glacier Ammassalik Island, SE Greenland, *Geografisk Tidsskrift (Danish Journal of Geography)*, 106(1), 25–43.

Narama, C., M. Duishonakunov, A. Kaab, M. Daiyrov and K. Abdrakhmatov (2010) The 24 July 2008 outburst flood at the western Zyndan glacier lake and recent regional changes in glacier lakes of the Teskey Ala-Too range, Tien Shan, Kyrgyzstan. *Natural Hazards and Earth System Sciences*, 10, 647–659.

Ng, F. S. L. (1994) Modelling the evolution of subglacial outburst floods. Final-year undergraduate project report in BSc Engineering Science degree, University of Oxford.

Ng, F.S.L. (1998) Mathematical modelling of subglacial drainage and erosion. (D.Phil. thesis, Oxford University.)

Ng, F.S. (2000). Canals under sediment-based ice sheets. *Annals of Glaciology*, 30(1), 146–152.

Ng, F. and H. Björnsson (2003) On the Clague-Mathews relation for jökulhlaups. *Journal of Glaciology*, 49(165), 161–172.

Ng, F. and S. Liu (2009) Temporal Dynamics of a Jökulhlaup System. *Journal of Glaciology*, 55(192), 651–665.

Ng, F., S. Liu, B. Mavlyudov and Y. Wang (2007) Climatic control on the peak discharge of glacier outburst floods. *Geophysical Research Letters*, 34, L21503, doi:10.1029/2007GL031426.

Nienow, P., M. Sharp, and I. Willis (1998) Seasonal changes in the morphology of the subglacial drainage system, Haut Glacier d'Arolla, Switzerland. *Earth Surface Processes and Landforms*, 23(9), 825–843.

Novak, S. and R.G. Frehlich (1982) Transition to chaos in the Duffing oscillator. *Physical Review A*, 26(6), 3660.

Nye, J. F. (1953) The flow law of ice from measurements in glacier tunnels, laboratory experiments and the Jungfraufirn borehole experiment. *Proceedings of the Royal Society of London. Series A. Mathematical and Physical Sciences*, 219(1139), 477–489.

Nye, J. (1976) Water Flow in Glaciers: Jökulhlaups, Tunnels and Veins. *Journal of Glaciology*, 17(76), 181–207.

Palmer, S., A. Shepherd, P. Nienow and I. Joughin (2011) Seasonal speedup of the Greenland Ice Sheet linked to routing of surface water. *Earth and Planetary Science Letters*, 302, 423–428.

Pimentel, S. and G.E. Flowers (2011) A numerical study of hydrologically driven glacier dynamics and subglacial flooding. *Proceedings of the Royal Society A: Mathematical, Physical and Engineering Science*, 467(2126), 537–558.

Parlitz, U., & Lauterborn, W. (1987). Period-doubling cascades and devil's staircases of the driven van der Pol oscillator. *Physical Review A*, 36(3), 1428.

Post, A. And L.R. Mayo (1971) Glacier dammed lakes and outburst floods in Alaska. US Geological Survey.

Pritchard, H.D., R.J. Arthern, D.G. Vaughan, and L.A. Edwards (2009) Extensive dynamic thinning on the margins of the Greenland and Antarctic ice sheets. *Nature*, 461(7266), 971–975.

Raymond, C.F., and M. Nolan (2000) Drainage of a glacial lake through an ice spillway. *IAHS publication*, 199–210.

Reynolds, J.M. (1981) Lakes on George VI Ice Shelf, Antarctica. *Polar record*, 20(128), 425–432.

Richardson, S.D. and J.M. Reynolds (2000) An overview of glacial hazards in the Himalayas. *Quaternary International*, 65-6, 31–47.

Rignot, E. and P. Kanagaratnam (2006) Changes in the velocity structure of the Greenland Ice Sheet. *Science*, 311(5763), 986–990.

Riesen, P., S. Sugiyama and M. Funk (2010) The influence of the presence and drainage of an ice-marginal lake on the flow of Gornergletscher, Switzerland. *Journal of Glaciology*, 56(196), 278–286.

Riesen, P., T. Strozzi, A. Bauder, A. Wiesmann and M. Funk (2011) Short-term surface ice motion variations measured with a ground-based portable real aperture radar interferometer. *Journal of Glaciology*, 57(201), 53–60.

Roberts, M.J. (2005) Jökulhlaups: a reassessment of floodwater flow through glaciers. Reviews of. Geophysics, 43, RG1002, doi:10.1029/2003RG000147.

Roberts, M.J., F. Palsson, M.T. Gudmundsson, H. Björnsson, and F.S. Tweed (2005) Icewater interactions during floods from Grænalón glacier-dammed lake, Iceland. *Annals of Glaciology*, 40, 133–138.

Roberts, M.J., F.S. Tweed, A.J. Russell, O. Knudsen and T.D. Harris (2003) Hydrologic and geomorphic effects of temporary ice-dammed lake formation during jökulhlaups. *Earth Surface Processes and Landforms*, 28(7), 723–737.

Röthlisberger, H. (1972) Water Pressure in Intra- and subglacial Channels. *Journal of Glaciology*, 11(62), 177-203.

Russell, A.J., M.J. Roberts, H. Fay, P.M. Marren, N.J. Cassidy, F.S. Tweed and T. Harris (2006) Icelandic jökulhlaup impacts: Implications for ice-sheet hydrology, sediment transfer and geomorphology. *Geomorphology*, 75, 33–64.

Scambos, T.A., C. Hulbe, M. Fahnestock and J. Bohlander (2000) The link between climate warming and break-up of ice shelves in the Antarctic Peninsula. *Journal of Glaciology*, 46(154), 516–530.

Scambos, T., C. Hulbe and M. Fahnestock (2003) Climate-induced ice shelf disintegration in the Antarctic Peninsula. *Antarctic Peninsula Climate Variability: Historical and Paleoenvironmental Perspectives, Antarctic Research Series*, 76, 79–92.

Scambos, T., H.A. Fricker and J. Bohlander (2009) Ice shelf disintegration by plate bending and hydro-fracture: Satellite observations and model results of the 2008 Wilkins ice shelf break-ups. *Earth and Planetary Science Letters*, 280(1-4), 51–60.

Scambos, T., J. Bohlander, and B. Raup (1996) Images of Antarctic ice shelves. [2002-2010] Boulder, Colorado, USA: National Snow and Ice Data Center. Digital media. http://nsidc.org/data/iceshelves_images/

Schoof, C. (2005) The effect of cavitation on glacier sliding. *Proceedings of the Royal Society a-Mathematical Physical and Engineering Sciences*, 461, 609–627.

Schoof, C. (2010). Ice-sheet acceleration driven by melt supply variability. *Nature*, 468(7325), 803–806.

Schoof, C., I.J. Hewitt and M.A. Werder (2012) Flotation and open water flow in a model for subglacial drainage. Part 1. Distributed drainage. Journal of Fluid Mechanics. 702, 126–156.

Schuler, T.V. and U.H. Fischer (2009) Modeling the diurnal variation of tracer transit velocity through a subglacial channel. *Journal of Geophysical Research*, 114, F04017, doi:10.1029/2008JF001238.

Selmes, N., T. Murray and T.D. James (2011) Fast draining lakes on the Greenland Ice Sheet. *Geophysical Research Letters*, 38, L15501, doi:10.1029/2011GL047872.

Sergienko, O. and D.R. Macayeal (2005) Surface melting on Larsen ice shelf, Antarctica. *Annals of Glaciology*, 40, 215–218.

Sergienko, O.V. and C.L. Hulbe (2011) 'Sticky spots' and subglacial lakes under ice streams of the Siple Coast, Antarctica. *Annals of Glaciology*, 52(58), 18–22.

Sergienko, O.V., D.R. MacAyeal and R.A. Bindschadler (2007) Causes of sudden, short-term changes in ice-stream surface elevation. Geophysical Research Letters, 34(22). L22503, doi:10.1029/2007GL031775.

Sharp, M. (2005) Subglacial Drainage, Encyclopedia of Hydrological Sciences: John Wiley & Sons, Ltd.

Shen, Y., G. Wang, C. Shao, W. Mao, and S. Wang (2007) Response of glacier flash flood to climate warming in the Tarim River Basin, *Advances in Climate Change Research*, 3, 51–56.

Shepherd, A., A. Hubbard, P. Nienow, M. King, M. McMillan & I. Joughin (2009) Greenland ice sheet motion coupled with daily melting in late summer. *Geophysical Research Lette*rs, 36, L01501, doi:10.1029/2008GL035758.

Shi, Y.F., Y.P. Shen and R.J. Hu (2002) Preliminary study on signal, impact and foreground of climatic shift from warm-dry to warm-humid in northwest China (in Chinese), *Journal of Glaciology and Geocryology*, 24, 219–226.

Siegert, M.J., S. Carter, I. Tabacco, S. Popov and D.D. Blankenship (2005) A revised inventory of Antarctic subglacial lakes. *Antarctic Science*, 17(3), 453–460.

Smart, C.C. (1986) Some observations on subglacial ground-water flow. *Journal of Glaciology*. 32(111), 232–234.

Smith, B. E., H.A. Fricker, I.R. Joughin and S. Tulaczyk (2009). An inventory of active subglacial lakes in Antarctica detected by ICESat (2003-2008). *Journal of Glaciology*, 55(192), 573–595.

Spring, U. and K. Hutter (1981) Numerical-Studies of Jökulhlaups. *Cold Regions Science and Technology*, 4(3), 227–244.

Spring, U. and K. Hutter (1982) Conduit flow of a fluid through its solid phase and its application to intraglacial channel flow. *International Journal of Engineering Science*, 20(2), 327-363.

Stearns, L. A., B. E. Smith and G. S. Hamilton (2008) Increased flow speed on a large East Antarctic outlet glacier caused by subglacial floods. *Nature Geoscience*, 1(12), 827–831.

Sugiyama, S., A. Bauder, M. Huss, P. Riesen and M. Funk (2008) Triggering and drainage mechanisms of the 2004 glacier-dammed lake outburst in Gornergletscher, Switzerland. *Journal of Geophysical Research-Earth Surface*, 113, F04019, doi:10.1029/2007JF000920.

Sugiyama, S., A. Bauder, P. Riesen and M. Funk (2010) Surface ice motion deviating toward the margins during speed-up events at Gornergletscher, Switzerland. *Journal of Geophysical Research-Earth Surface*, 115, F03010, doi:10.1029/2009JF001509.

Sugiyama, S., A. Bauder, P. Weiss and M. Funk (2007) Reversal of ice motion during the outburst of a glacier-dammed lake on Gornergletscher, Switzerland. *Journal of Glaciology*, 53(181), 172–180.

Sundal, A. V., A. Shepherd, P. Nienow, E. Hanna, S. Palmer and P. Huybrechts (2009) Evolution of supra-glacial lakes across the Greenland Ice Sheet. Rem. Sens. Enviro, 113, 2164–2171

Sundal, A. V., A. Shepherd, P. Nienow, E. Hanna, S. Palmer and P. Huybrechts (2011) Melt-induced speed-up of Greenland ice sheet offset by efficient subglacial drainage. *Nature*, 469(7331), 521–524.

Tedesco, M. Lüthje, K. Steffen, N. Steiner, X. Fettweis, I. Willis, N. Bayou, and A. Banwell (2012) Measurement and modeling of ablation of the bottom of supraglacial lakes in western Greenland, Geophysical Research Letters, 39, L02502, doi:10.1029/2011GL049882.

Thorarinsson, S (1953) Some new aspects of the Grimsvötn problem. *Journal of Glaciology*, 2(14), 267–75.

Thorarinsson, S. (1939) The ice-dammed lakes of Iceland, with particular reference to their values as indicators of glacier oscillations. *Geografiska Annaler*, 21(3-4), 216-242.

Truffer, M. and A. Iken (1998) The sliding velocity over a sinusoidal bed at high water pressure. *Journal of Glaciology*, 44(147), 379–382.

Tweed, F.S. (2000). Jökulhlaup initiation by ice-dam flotation: the significance of glacier debris content. *Earth Surface Processes and Landforms*, 25(1), 105–108.

Tweed, F.S. and A.J. Russell (1999) Controls on the formation and sudden drainage of glacier-impounded lakes: implications for jökulhlaup characteristics. *Progress in Physical Geography*, 23, 79–110.

Uppala, S.M., P.W. Kallberg, A.J. Simmons, U. Andrae, V.D. Bechtold, M. Fiorino, J.K. Gibson, J. Haseler, A. Hernandez, G.A. Kelly, X. Li, K. Onogi, S. Saarinen, N. Sokka, R.P. Allan, E. Andersson, K. Arpe, M.A. Balmaseda, A.C.M. Beljaars, L. Van De Berg, J. Bidlot, N. Bormann, S. Caires, F. Chevallier, A. Dethof, M. Dragosavac, M. Fisher, M. Fuentes, S. Hagemann, E. Holm, B.J. Hoskins, L. Isaksen, P. Janssen, R. Jenne, A.P. McNally, J.F. Mahfouf, J.J. Morcrette, N.A. Rayner, R.W. Saunders, P. Simon, A. Sterl, K.E. Trenberth, A. Untch, D. Vasiljevic, P. Viterbo and J. Woollen (2005) The ERA-40 re-analysis. *Quarterly Journal of the Royal Meteorological Society*, 131, 2961–3012.

van den Broeke, M. (2005) Strong surface melting preceded collapse of Antarctic Peninsula ice shelf. *Geophysical Research Letters*, 32, L12815, doi:10.1029/2005GL023247.

Vincent, C., S. Auclair and E. Le Meur (2010) Outburst flood hazard for glacier-dammed Lac de Rochemelon, France. *Journal of Glaciology*, 56(195), 91–100.

Vuichard, D. & M. Zimmermann, 1986, The Langmoche Flash-Flood, Khumbu Himal, Nepal, *Mountain Research and Development*, 6(1), 90–94.

Walder, J.S. and J.E. Costa (1996) Outburst floods from glacier-dammed lakes: The effect of mode of lake drainage on flood magnitude. *Earth Surface Processes and Landforms*, 21, 701–723.

Walder, J.S. (1986) Hydraulics of Subglacial Cavities. *Journal of Glaciology*, 32(112), 439–445.

Walder, J.S. and C.L. Driedger (1994) Rapid Geomorphic Change Caused by Glacial Outburst Floods and Debris Flows Along Tahoma Creek, Mount Rainier, Washington, USA. Arctic and Alpine Research, 26(4), 319–327.

Walder, J.S. and J. E. Costa (1996) Outburst floods from glacier-dammed lakes: The effect of mode of lake drainage on flood magnitude. *Earth Surface Processes and Landforms*, 21(8), 701–723.

Walder, J. and B. Hallet (1979) Geometry of former subglacial water channels and cavities. *Journal of Glaciology*, 23(89), 335–346.

Walder, J.S., D.C. Trabant, M. Cunico, S.P. Anderson, R.S. Anderson, A.G. Fountain and A. Malm (2005) Fault-dominated deformation in an ice dam during annual filling and drainage of a marginal lake. *Annals of Glaciology*, 40(1), 174–178.

Weertman, J. (1957) On the sliding of glaciers. *Journal of Glaciology*, 3(21), 33–38.

Weertman, J. (1962) Catastrophic glacier advances. In: *Symposium of Obergurgl,* edited by *Ward. W, IAHS Publication*, 38, 31–39 .

Weertman, J. (1967) An examination of the Lliboutry theory of sliding. *Journal of Glaciology*, 6(46), 489–494.

Werder, M.A. and M. Funk (2009) Dye tracing a jökulhlaup: II. Testing a jökulhlaup model against flow speeds inferred from measurements. Journal of Glaciology, 55(193), 899–908.

Werder, M.A., A. Bauder, M. Funk and H.R. Keusen (2010) Hazard assessment investigations in connection with the formation of a lake on the tongue of Unterer Grindelwaldgletscher, Bernese Alps, Switzerland. *Natural Hazards and Earth System Sciences*, 10, 227–237.

Whalley, W.B. (1971) Observations of the Drainage of an Ice-Dammed Lake — Strupvatnet, Troms, Norway, *Norsk Geografisk Tidsskrift* (*Norwegian Journal of Geography*), 25(3-4), 165–174.

Winberry, J. P., S. Anandakrishnan and R.B. Alley (2009) Seismic observations of transient subglacial water-flow beneath MacAyeal Ice Stream, West Antarctica. *Geophysical Research Letters*, 36, L11502, doi:10.1029/2009GL037730.

Wingham, D. J., M.J. Siegert, A. Shepherd, and A.S. Muir (2006) Rapid discharge connects Antarctic subglacial lakes. *Nature*, 440(7087), 1033–1036.

Wright, A., and M.J. Siegert (2011) The identification and physiographical setting of Antarctic subglacial lakes: an update based on recent discoveries. *Geophysical monograph*, 192, 9–26.

Yen, B. C. (2002). Open channel flow resistance. *Journal of Hydraulic Engineering*, 128(1), 20–39.

Young, H. D., R.A. Freedman and L. Ford (2006). University physics (Vol. 1). Addison-Wesley Longman.

Zwally, H.J., W. Abdalati, T. Herring, K. Larson, J. Saba and K. Steffen (2002) Surface melt-induced acceleration of Greenland ice-sheet flow. *Science*, 297, 218–222